THE DEVELOPMENT OF SUPPORTED GOLD CATALYSTS FOR SELECTIVE HYDROGENATION APPLICATIONS

FERNANDO CÁRDENAS-LIZANA

A dissertation submitted for the degree of Doctor of Philosophy

Heriot-Watt University

School of Engineering and Physical Sciences

April 2009

Abstract

An alternative cleaner route for the production of aromatic amino-compounds under mild reaction conditions (P = 1 atm; 393 K ≤ T ≤ 573 K) *via* the continuous gas phase reduction of aromatic nitro derivates has been investigated over (oxide and/or carbon) supported Au, Ag, Pd, Ni, Ni-Pd, Au-Pd and Au-Ni catalysts. Taking the hydrogenation of *p*-chloronitrobenzene as a model reaction, Pd/Al_2O_3 promoted the exclusive production of nitrobenzene and aniline, *i.e.* hydrodechlorination with subsequent $-NO_2$ group reduction prevailed. In contrast, *p*-chloroaniline was the only product detected over a series of supported Ni catalysts. This is the first time that such product exclusivity has been achieved in gas phase operation. The synthesis of bimetallic $Pd\text{-}Ni/Al_2O_3$ (prepared *via* co-impregnation) proved effective to enhance catalytic activity while maintaining 100% selective $-NO_2$ reduction, a result ascribed to bimetallic particle formation as established by TPR, H_2 chemisorption and XRD analyses. Nevertheless, the three systems (supported Pd, Ni and Pd-Ni) suffered a loss of activity with time-on-stream. Monometallic Au catalysts promoted the exclusive and time invariant formation of *p*-chloroaniline. The incorporation of Au (as a modifier) with Pd *via* reductive deposition to form $Au\text{-}Pd/Al_2O_3$ (Pd/Au=10 mol/mol) did not influence catalytic performance, which was equivalent to that delivered by Pd/Al_2O_3, *i.e.* aniline was the predominant product. On the other hand, the inclusion of Pd (as a promoter) with Au (at Au/Pd≥20) *via* co-impregnation and/or co-deposition precipitation resulted in increased hydrogenation rate while retaining exclusivity to *p*-chloroaniline, an effect resulting from a surface Pd-Au synergism demonstrated by DRIFTS analysis. With the goal of elevating the catalytic activity of Au, the possible role of the oxide (Al_2O_3 *vs.* TiO_2) support to modify catalytic response was considered. Au/TiO_2 delivered a higher specific rate that was attributed to a combination of smaller Au particle size (with higher number of defects) and possible *p*-chloronitrobenzene activation *via* interaction(s) with TiO_2 surface oxygen vacancies. This work was extended to decouple the individual contribution of each factor by (i) considering a series of oxide supports that exhibited a range of acid-base and redox surface properties, *i.e.* Al_2O_3, TiO_2, Fe_2O_3 and CeO_2 and (ii) controlling the Au particle size using two synthesis methods (deposition-precipitation and impregnation). The results demonstrated that specific activity increased with decreasing particle size (from 9 to 3 nm), regardless of the nature of the support. Furthermore, in the case of Au/Fe_2O_3, XRD and TPR analyses have established that Au can promote the partial reduction of the

support (from α-Fe_2O_3 to Fe_3O_4), an effect more pronounced for smaller Au particles (< 5 nm) where H_2-TPD suggests the participation of spillover hydrogen in this reduction step. A similar effect was also found for the TiO_2 allotropic phase transition (from anatase to rutile), which can occur at lower temperatures due to the presence of Au, as demonstrated by DRS UV-vis, XRD and BET measurements.

Having established that supported Au is effective in promoting the exclusive reduction of *p*-chloronitrobenzene to *p*-chloroaniline, hydrogenation selectivity was proved further by considering the reduction of *m*-dinitrobenzene. The reaction products, *i.e. m*-nitroanline (partial -NO_2 reduction) and *m*-phenylenediamine (complete -NO_2 reduction) are both high value intermediates in the fine chemical industry but existing routes can not achieve high selectivity to either product. It is shown that the nature of the oxide support (for TiO_2-rutile, TiO_2-anatase, Al_2O_3, CeO_2, Fe_2O_3) does not have a direct effect on the rate of nitro-group reduction, which is controlled by Au particle size where a mean size of 5 nm was found to be critical in that with larger particles, nitro-group reduction rate was structure insensitive. In contrast, the nature of the support has a direct effect on the selectivity response. Au/TiO_2 and Au/Fe_2O_3 promoted the exclusive hydrogenation of *m*-dinitrobenzene to *m*-nitroaniline, Au/CeO_2 delivered *m*-phenylenediamine as the sole product and Au/Al_2O_3 generated a mixture of both products. This response can be accounted for on the basis of a modification to the electronic character of the Au nanoclusters induced by the acid-base Lewis properties of the support that impacts on the adsorption/activation of *m*-dinitrobenzene. A similar alteration of the electronic nature of Au can also be induced by alteration of the Au particle size or the introduction of a second metal (Ni). Taking the same reaction over Au/Al_2O_3, Ni/Al_2O_3 and Au-Ni/Al_2O_3, it is established that it is possible to control product composition in terms of partial (over Au) or complete nitro-group reduction (over Ni) or a combination of both (over Au-Ni), which can be attributed to a surface Au-Ni synergism as suggested by XPS and EDX mapping measurements. In order to assess the impact of annealing treatment on catalytic response, the analysis was extended to the preparation and application of an Au-Ni/Al_2O_3 alloy, formation of which is demonstrated by XRD, DRS UV-Vis and HRTEM. While alumina supported bimetallic and alloy both promoted the formation of both *m*-nitroaniline and *m*-phenylenediamine *via* a predominantly stepwise reduction mechanism, the annealed (alloy) system delivered rate constants up to two orders of magnitude lower. In the final section of this thesis, the catalytic behaviour of supported (TiO_2) Au and Ag is

compared in the selective hydrogenation of a series of *para*-substituted nitroarenes. While both catalysts promoted the exclusive nitro-group reduction, Ag/TiO_2 delivered lower reaction rates. The reaction mechanism has been probed by adopting the Hammett approach, where the linear correlation and positive slopes (higher for Au than Ag) associated with the Hammett plots are consistent with an electron withdrawing substituent activation effect, *i.e.* nucleophilic attack and a more effective reactant activation over Au/TiO_2.

The results presented in this thesis demonstrate, for the first time, that catalytic hydrogenation over gold-based catalysts in continuous flow gas operation is a viable, clean high throughput route to aromatic amines. The findings of this thesis show that Au on reducible supports with $d_{Au} < 5$ nm is the optimum monometallic formulation while $-NO_2$ group reduction rate and/or selectivity can be controlled (or tuned) by (i) changing the acid-base Lewis character of the support, (ii) modifying Au dispersion or (iii) incorporation of Pd or Ni as promotors. This work represents a critical advancement in the sustainable production of high value fine chemicals.

SCOPE OF THE PROJECT

GAS PHASE HYDROGENATION

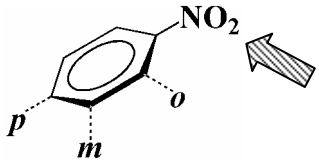

CONTACT TIME CONSTANT

V *Catalyst Bed* → Catalyst; Diluent

Q *Organic Reactant* → Reactant; Solvent

Q *Gas (Hydrogen)*

CHLORONITROBENZENE

Metal

- Ni **(*Ch. 1*)**
- Pd
- Ni–Pd **(*Ch. 2*)**
- **Au (*Ch. 3*)**
  - Au-Pd (1:10)
  - Au-Pd (10:1) **(*Ch. 4*)**

Support

- *Oxides* (No H_2 uptake)
  - Non- / Reducible **(*Ch. 5*)**
    - Support *vs.* Au-Size **(*Ch. 6*)**
    - Nature of Support **(*Ch. 7*)**
    - Particle Size **(*Ch. 8*)**

DINITROBENZENE

Au-Ni (1:10)

- Bimetallic **(*Ch.9*)**
- Alloy **(*Ch. 10*)**

SUBSTITUTED NITROCOMPOUNDS

Au *vs.* Ag **(*Ch. 11*)**

Dedication

To my grandfather D. Luis Lizana López

Acknowledgements

This thesis is the result of a series of conversations over the past three and a half years with my supervisor Professor Mark A. Keane. Through his inquisitive questions, Mark always found a path to take me closer to the reality I had initially perceived, enabling me to grasp its complex nature. I truly admire his ability to merge critique with an immediate empathy and commitment towards students engaged in struggle along with his professional integrity. His rich academic knowledge combine with a sharp wit and incredible imagination to challenge conventional wisdom always inspire me. In spite of his busy agenda, Mark was always there to offer direction and quiet encouragement.

This research was possible by the financial support from the Engineering and Physical Sciences Research Council (EPSRC) through Grant 0231 110525, and the steadfast support of my family and friends.

I was privileged to work in the laboratory with my colleague and friend, the soon to be, Dr. Santiago Gómez Quero. It is impossible for me to reference the knowledge and insights gained from our endless dialogues. His advice on results interpretation, productive comments and willingness to discuss ideas influenced my approach and contributed directly to this research. I am indebted to Santi for his patience, extraordinary kindness and unconditional support creating a relaxed work environment and enhancing the PhD experience.

I would specially like to thank my close friend and flatmate James Cassidy for his positive attitude, always refreshing, and the steady encouragement provided during each stage of the completion of this thesis.

Special tanks to my fellow researchers at the Chemistry Department Lucía Romero Pérez and Patricia Leyva Bailén, whose friendship and cheerful character animated my years at Heriot-Watt University. I am also grateful to the several students I have the pleasure to work with and from whom this research has benefited: Dimitra Gouliari, Craig Burnett, Maria-Luz Pérez Cuevas, Fisher Millard, Noémie Perret, Antonio Nieto-Marquez Ballesteros, Etienne Crop, Zahara Martínez de Pedro, Elena Díaz Nieto, Leslie-Ann Josephine Wong Fo Sue, Darion Turner, Sofia Marin Mallo and Jassiel Rolando Rodríguez Barreras, they are appreciated for their individual contributions.

Many thanks to the staff in the Chemical Engineering Department at Heriot-Watt University and whose support have made it more than a temporary place of study for students, like myself, from different parts of the world. I would especially like to thank Marian K. Millar for her assistance with XRD and SEM measurements and Ronald Millar, Curtis L. Abbott and Cameron Smith for helping with acquisition and maintenance of the experimental facilities. Also thanks to Ross Blackley in the Chemistry Department at St. Andrews University, whose assistance in TEM analysis and experience in data analysis/interpretation enriched this research.

Finally, I am forever grateful to my parents, Fernando Cárdenas Naranjo and Araceli Lizana Maldonado, whose foresight and values cemented the path for a privileged education, and to my sister Maria Jesús Cárdenas Lizana who kindly offer guidance and unconditional support at each turn of the road.

Table of Contents

List of Tables

List of Figures

Nomenclature

List of Symbols

$\bar{d}_s = d_p = d_{TEM}$	Surface area-weighted metal diameter (using TEM); (nm)
d_{hkl}	Metal particle size (using Scherrer equation); (nm)
n_z $(z = Ni, Pd)$	Moles of metal (z) in the catalyst bed; (moles)
F	Inlet molar aromatic feed rate; (moles h^{-1})
F_{-NO_2}	Inlet -NO_2 molar flow; (mol_{-NO_2} h^{-1})
$(n)_{out}/(n)_{in}$	Moles of reactant in the exit relative to inlet stream
$x_{p\text{-CNB}}$	Fractional (degree of) *p*-chloronitrobenzene conversion
$x_{m\text{-DNB}}$	Fractional (degree of) *m*-dinitrobenzene conversion
x_{-NO_2}	Fractional (degree of) nitro-group reduction
x_{mh}	Fractional (degree of) conversion after m h on-stream
x_0	Initial fractional conversion
S_H	Selectivity of compound H
S_0	Initial selectivity
β	Time scale fitting parameter
k	Pseudo-first order rate constant; (mol mol^{-1}_{metal} h^{-1})
k'	Specific pseudo-first order rate constant; (mol m^{-2}_{metal} h^{-1})
S_{Au}	Specific gold surface area; (m^2_{Au} g^{-1}_{Au})
A_{max}	Maximum absorption band (in DRS UV-vis analysis)
T_{max}	Temperature associated with maximum H_2 consumption/ desorption (in temperature programmed reduction/desorption)
ρ	Reaction constant in the Hammett Equation
σ_I	Empirical parameter in the Hammett Equation

List of Acronyms

CNB	Choronitrobenzene
CAN	Choroaniline
DCNB	Dichloronitrobenzene
DCAN	Dichloroaniline
BNB	Bromonitrobenzene
BAN	Bromoaniline
DNB	Dinitrobenzene
NAN	Nitroaniline
PDM	Phenylenediamine
NT	Nitrotoluene
CB	Chlorobenzene
AN	Aniline
NB	Nitrobenzene
BZ	Benzene
AC	Activated Carbon
ECP	Electrochemical Potential
ICP-OES	Inductively Coupled Plasma-Optical Emission Spectrometry
TPR	Temperature Programmed Reduction
TCD	Thermal Conductivity Detector
TEM	Transmission Electron Microscopy
EDX	Energy Dispersive X-Ray
IFFT	Inverse Fast Fourier Transform
HAADF	High Angle Annular Dark Field
EFTEM	Energy Filtered Transmission Electron Microscopy
DRS/DR UV-vis	Diffuse reflectance UV-vis
XRD	Powder X-ray Diffraction
JCPDS-ICDD	Joint Committee on Powder Diffraction Standards-

	-International Centre for Diffraction Data
TPD	Temperature Programmed Desorption
XPS	X-ray Photoelectron Spectroscopy
FTIR	Fourier Transform Infrared Spectroscopy
DRIFTS	Diffuse Reflectance Infrared Fourier Transform Spectroscopy
HDC	Hydrodechlorination
TOF	Turnover frequency
DP	Deposition-Precipitation
IMP	Impregnation

List of Publications by the Candidate

1) F. Cárdenas-Lizana, S. Gómez-Quero and M. A. Keane, Clean Production of Chloroanilines by Selective Gas Phase Hydrogenation over Supported Ni Catalysts, Appl. Catal. A: Gen., 334, 199 (2008)

2) F. Cárdenas-Lizana, S. Gómez-Quero and M. A. Keane, Ultra-Selective Gas Phase Hydrogenation of Aromatic Nitro Compounds over Au/Al_2O_3, Catal. Commun., 9, 475 (2008)

3) F. Cárdenas-Lizana, S. Gómez-Quero and M. A. Keane, Exclusive Production of Chloroaniline from Chloronitrobenzene over Au/TiO_2 and Au/Al_2O_3, ChemSusChem, 1, 215 (2008)

4) F. Cárdenas-Lizana, S. Gómez-Quero, A. Hugon, L. Delannoy, C. Louis and M. A. Keane, Pd-Promoted Selective Gas Phase Hydrogenation of *p*-Chloronitrobenzene over Alumina Supported Au, J. Catal., 262, 235 (2009)

5) F. Cárdenas-Lizana, S. Gómez-Quero and M. A. Keane, Gas Phase Hydrogenation of *m*-Dinitrobenzene over Alumina Supported Au and Au-Ni Alloy, Catal. Lett., 127, 25 (2009)

6) F. Cárdenas-Lizana, S. Gómez-Quero, N. Perret and M. A. Keane, Support Effects in the Selective Gas Phase Hydrogenation of *p*-Chloronitrobenzene over Gold, Gold Bulletin, *in press*

7) F. Cárdenas-Lizana, S. Gómez-Quero, C. Amorim and M. A. Keane, Gas Phase Hydrogenation of *p*-Chloronitrobenzene over $Pd\text{-}Ni/Al_2O_3$, Manuscript ready for submission

8) F. Cárdenas-Lizana, S. Gómez-Quero, N. Perret and M. A. Keane, Controlled Nitro-Group Reduction in the Conversion of *m*-Dinitrobenzene over Oxide Supported Gold: Role of the Support, Manuscript ready for submission

9) F. Cárdenas-Lizana, S. Gómez-Quero, C. J. Baddeley and M. A. Keane, Tunable Gas Phase Hydrogenation of *m*-Dinitrobenzene over Alumina Supported Au and Au-Ni, Manuscript ready for submission

10) F. Cárdenas-Lizana, S. Gómez-Quero and M. A. Keane, Gold Particle Size Effects in the Gas Phase Hydrogenation of Dinitrobenzene over Au/TiO_2, Manuscript in preparation

11) F. Cárdenas-Lizana, Z. M. De Pedro, S. Gómez-Quero and M. A. Keane, Gas Phase Hydrogenation of Nitroarenes: A Comparison of the Catalytic Action of Titania Supported Gold and Silver, Manuscript in preparation

Oral Presentations

1) "Use of Gold Catalysts to Promote the Ultra-Selective Sustainable Production of Aromatic Amines". IChemE Conference on Applied Catalysis: Towards Sustainable Chemical Industry; Bath, November 2008.

2) "Gas Phase Hydrogenation of Nitroarenes over Supported Au Catalysts: A Consideration of Particle Size and Support Effects". 5th International Conference on Environmental Catalysis; Belfast, August 2008.

3) "Role of the Support in the Selective Hydrogenation of Aromatic Nitrocompounds over Gold". 9th UK Particle Technology Forum; Edinburgh, June 2008.

4) "Ultra-Selective Hydrogenation Using Supported Gold Catalysts". SURCAT Ecosse Conference; Aberdeen, April 2008.

5) "Exclusive Production of Haloamines in the Gas Phase Hydrogenation over Supported Au". Chemical Engineering Department (Heriot-Watt University) Seminar Series; Edinburgh, November 2007.

6) "Clean Production of Chloroaniline by Selective Gas Phase Hydrogenation over Supported Gold Catalysts". SURCAT Ecosse Conference; St Andrews, May 2007.

7) "Gas Phase Hydrogenation of *p*-Chloronitrobenzene over Alumina Supported Au, Ni and Pd Catalysts". ScotCHEM Materials Conference; Edinburgh, March 2007.

Awards

1) November 2008 - Prize for the Best Oral Presentation in: IChemE Conference on Applied Catalysis: Towards Sustainable Chemical Industry.

2) June 2008 - 2nd Prize in the Young Researcher's Award Competition: IChemE Particle Technology Group.

3) October 2007 - 2nd Year Engineering and Physical Science (Heriot-Watt University) Research Student Prize.

Chapter 1

Clean Production of Chloroanilines by Selective Gas Phase Hydrogenation over Supported Ni Catalysts

Environmental legislation as applied to chemical processing is increasingly stringent. This has lead to a pressing demand for the development of sustainable manufacturing processes. In this Chapter, the application of oxide and carbon supported Ni catalysts in the continuous gas phase hydrogenation of *para*-chloronitrobenzene (model reactant) is considered as an alternative route to commercially important haloamines. The catalysis results are linked to critical catalyst characterization.

1.1 Introduction

The role of catalysis in the development of clean chemical production with limited hazardous/toxic by-products is now well established as an essential element of sustainable processing [1,2]. Aromatic haloamines are extensively used as intermediates in the manufacture of pesticides, herbicides, pigments, pharmaceuticals and cosmetic products [3,4]. *p*-Chloroaniline (*p*-CAN), a high production volume compound [3], can be synthesised *via* Fe promoted reduction of *p*-chloronitrobenzene (*p*-CNB) in acid media (Béchamp reaction) or by selective hydrogenation using transition-metal catalysts. Industrial implementation of the Béchamp reaction is no longer viable due to the generation of significant amounts of toxic metal waste which requires costly and laborious separation and disposal [5]. Liquid phase catalytic hydrogenation has emerged as a cleaner alternative to the Béchamp process with higher associated product yields [6]. However, the economic benefits are dependent on catalyst performance, where unwanted C-Cl bond hydrogenolysis is difficult to fully circumvent. Reaction selectivity is critical as *p*-CNB hydrotreatment can generate a range of intermediates and by-products as shown in **Figure 1.1**, which presents the reaction pathways proposed for batch liquid phase hydrogenation [7-13]. The reduction of *p*-CNB to *p*-CAN involves the formation of nitroso- and hydroxylamine-intermediates (Path I) that can participate in side reactions [14]. The formation of dimeric azoxybenzene (Path II) and azobenzene (Path III) results from condensation-reduction involving *p*-CAN where conversion of

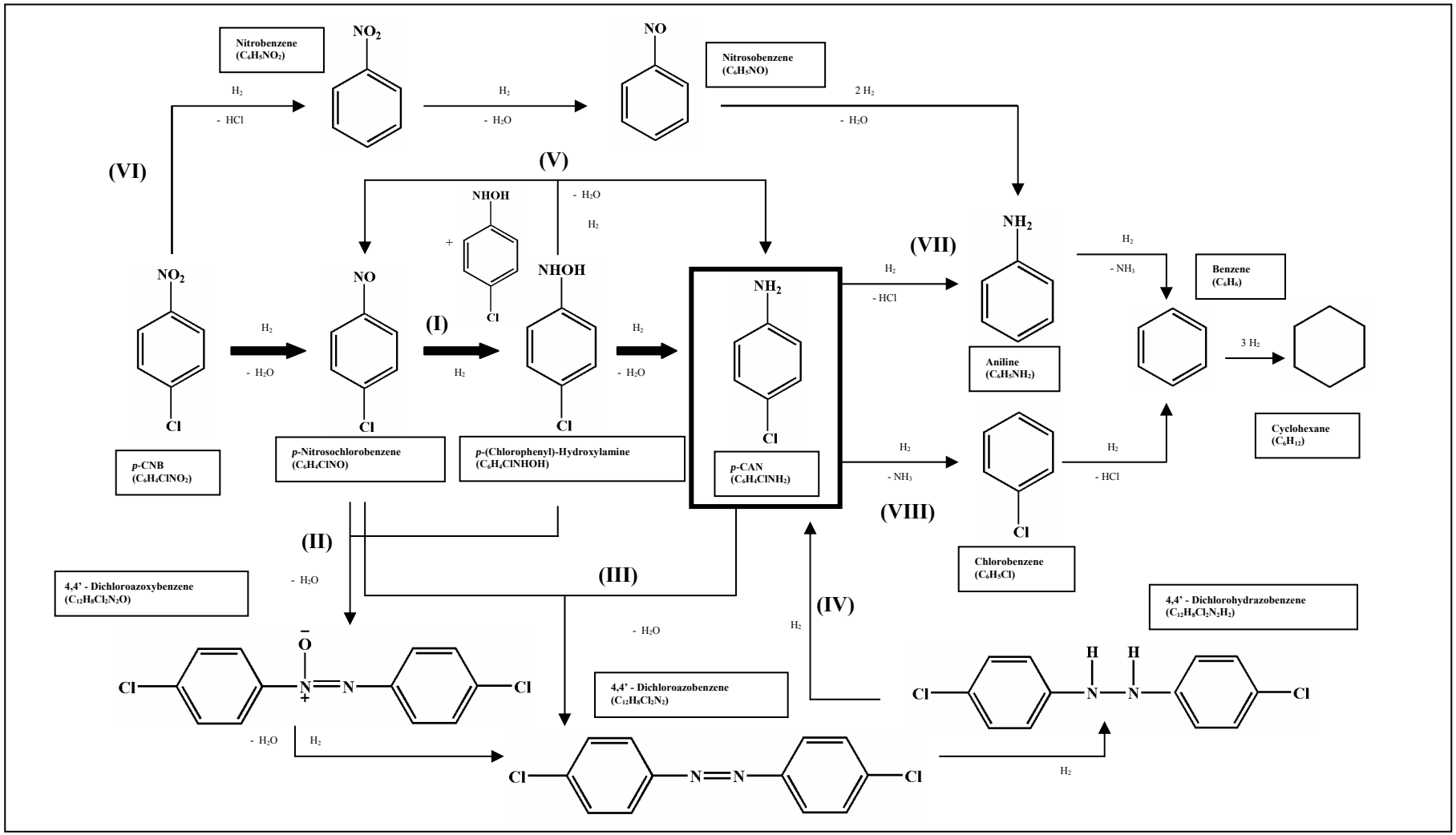

Figure 1.1: Reaction pathways associated with the hydrogen mediated conversion of *p*-CNB. The targeted route (I) to *p*-CAN is represented by bold arrows.

the hydrazobenzene intermediate to *p*-CAN (Path IV) is favoured in basic media [15]. Azoxybenzene/azobenzene formation, as highly toxic compounds, must be avoided in the clean production of *p*-CAN. Disproportionation of the hydroxylamine intermediate to *p*-nitrosochlorobenzene and *p*-CAN requires significant formation of *p*-(chorophenyl)-hydroxylamine (Path V). Hydrogenolysis of the halosubstituent with subsequent formation of aniline (AN), benzene (BZ) and/or cyclohexane can occur either *via* the reduction of nitrobenzene (NB) (Path VI) or as a result of the further conversion of *p*-CAN (Paths VII and VIII). The authors have failed to unearth any study dealing with the gas phase hydrogenation of *p*-CNB. Taking an overview of the existing literature on (homogeneous and heterogeneous) discontinuous liquid systems, elevated pressures (≥ 5 atm) and/or temperatures (up to 542 K) are required where C-Cl bond cleavage is an issue, contributing significantly to the overall pathway for reaction over monometallic Ni [9-11,14,16,17], Pd [12,13,15,18-20], Pt [7,8,21-25] and Ru [19,26] and bimetallic [8,9,11,12,16,17,19,21-23,27] catalysts. Preliminary results for batch liquid phase reaction over Ag [28] and Au [29] show promise in terms of achieving high selectivity. Several factors have been proposed to influence activity/selectivity that are dependent on catalyst structure (alloying, metal/support interactions and metal dispersion) [7-13,16,17,19,21-27,30] where variations in process variables such as solvent polarity [9,10,15,18] and *p*-CNB concentration [7-9,22,24-26] have a lesser effect. Coq *et al.* investigated the catalytic response for a series of supported Pt catalysts, focusing on the role of particle size [7], support/metal precursor [25] and the effect of adding a second metal (Sn, Pb, Ge, Al and Zn) [8], and concluded that *p*-CAN selectivity is sensitive to dispersion and the introduction of a second metal, a response that extends to Ru catalysts [26]. Han *et al.*, have noted that the presence of an electron deficient promoter serves to promote selective *p*-CNB conversion over heterogeneous [21-23] and homogeneous [24] Pt catalysts. Chloronitroarene isomers have exhibited different reactivities, ascribed to steric/electronic factors [13,15,17,21,23,30,31], while the nature of the halogen also impacts on selectivity [31-34]. Photocatalytic and electrochemical reduction of *p*-CNB have been the subject of patent literature [5,35,36] where these approaches again involve batch operation but the available results are insufficient to permit a full evaluation of the associated efficiencies relative to catalytic hydrogenation.

In this report, we present for the first time the results of a feasibility study to examine the viability of Ni promoted gas phase hydrogenation of *p*-CNB as a cleaner

route to *p*-CAN. We have established exclusive formation of *p*-CAN (at 393 K and atmospheric pressure) for reaction over Ni supported on Al_2O_3, SiO_2, activated carbon (AC) and graphite in continuous gas flow operation. Our results can provide the basis for the development of a clean high throughput route for the production of *p*-CAN.

1.2 Experimental

1.2.1 Catalyst Preparation

The SiO_2 (fumed) and Al_2O_3 supports were supplied by Sigma-Aldrich and used as received. The AC (G-60, 100 mesh) was obtained from NORIT (UK) and the graphite (synthetic 1–2 μm powder) from Sigma-Aldrich. The Ni-loaded samples were prepared by impregnation where a 2-butanolic $Ni(NO_3)_2$ solution (0.6 cm^3 g^{-1}) was added drop wise at 353 K to the substrate with constant agitation (500 rpm). The impregnated samples were oven dried at 393 K for 12 h. The Ni content (accurate to within ± 2 %) was measured by inductively coupled plasma-optical emission spectrometry (ICP-OES, Vista-PRO, Varian Inc.) from the diluted extract in HF. A Pd/Al_2O_3 catalyst also prepared by impregnation was examined for comparative purposes. Prior to use in catalysis, the catalyst precursors were sieved (ATM fine test sieves) into a batch of 75 μm average particle diameter.

1.2.2 Catalyst Characterization

BET surface area, temperature programmed reduction (TPR) and H_2 chemisorption were determined using the commercial CHEM-BET 3000 (Quantachrome) unit. The samples were loaded into a U-shaped Pyrex glass cell (10 cm × 3.76 mm i.d.) and heated in 17 cm^3 min^{-1} (Brooks mass flow controlled) 5% v/v H_2/N_2 at 10 K min^{-1} and 2 K min^{-1} to a final temperature of 523 K and 723 K for Pd/Al_2O_3 and supported Ni, respectively. The effluent gas passed through a liquid N_2 trap and changes in H_2 consumption were monitored by a thermal conductivity detector (TCD) with data acquisition/manipulation using the TPR Win™ software. The reduced samples were maintained at the final reduction temperature for at least 1 h in a constant flow of H_2, swept with a 65 cm^3 min^{-1} flow of N_2 for 1.5 h, cooled to room temperature and subjected to H_2 chemisorption using a pulse (50 μl) titration procedure. After H_2 chemisorption the supported Ni samples were reoxidised in air (17 cm^3 min^{-1}) and subjected to a second TPR step, conditions as above. BET areas were recorded with a

30% v/v N_2/He flow; pure N_2 (99.9%) served as the internal standard. At least 2 cycles of nitrogen adsorption-desorption in the flow mode were employed to determine total surface area using the standard single point method. BET surface area and H_2 uptake values were reproducible to within ± 5% and the values quoted in this paper are the mean. XRD analysis (recorded on a Philips X'Pert instrument using nickel filtered Cu Kα radiation) established that the supported Ni and Pd phases exhibit an exclusive cubic symmetry: peaks at 44.5°, 51.8° and 76.3° for Ni corresponding to (111), (200) and (220) planes; peaks at 40.1°, 46.7°, 68.1°, and 82.15° for Pd corresponding to (111), (200), (220), and (311) planes. Supported metal particle size was determined by transmission electron microscopy: JEOL 2000 TEM microscope operated at an accelerating voltage of 200 kV. The catalyst samples were dispersed in 1-butanol by ultrasonic vibration, deposited on a lacey-carbon/Cu grid (300 Mesh) and dried at 383 K for 12 h. At least 600 individual metal particles were counted for each catalyst and the surface area-weighted metal diameter ($\bar{d}_s$) was calculated from

$$\bar{d}_s = \sum_i n_i d_i^3 \Big/ \sum_i n_i d_i^2 \qquad \textbf{(1.1)}$$

where n_i is the number of particles of diameter d_i.

1.2.3 Catalysis Procedure

Reactions were carried out under atmospheric pressure, in situ immediately after activation, in a fixed bed vertical continuous glass reactor (l = 60 cm, i.d. = 15 mm) at T = 393 K. The catalytic reactor, and operating conditions to ensure negligible heat/mass transport limitations, have been fully described elsewhere [34,37,38] but some features, pertinent to this study, are given below. A layer of borosilicate glass balls served as preheating zone, ensuring that the reactant was vaporised and reached the reaction temperature before contacting the catalyst. Isothermal conditions (± 1 K) were ensured by diluting the catalyst bed with ground glass (75 μm). Reaction temperature was continuously monitored by a thermocouple inserted on a thermowell within the catalyst bed. The reactant was delivered to the reactor *via* a glass/teflon air-tight syringe and teflon line using a microprocessor controlled infusion pump (Model 100 kd Scientific) at a fixed calibrated flow rate. A co-current flow of aromatic and ultra pure H_2 was maintained at a $GHSV = 2\times10^4$ h^{-1} with an inlet aromatic molar flow = 0.4 mmol h^{-1}, where the H_2 content was up to 95 times in excess of the stoichiometric requirement, the flow rate of

which was monitored using a Humonics (Model 520) digital flowmeter. The molar metal (n_{Ni} or n_{Pd}) to inlet molar aromatic feed rate (F) spanned the range 3×10^{-3} – 136×10^{-3} h. In a series of blank tests, passage of each reactant in a stream of H_2 through the empty reactor or over the support alone did not result in any detectable conversion. The reactor effluent was frozen in a liquid nitrogen trap for subsequent analysis which was made using a Perkin-Elmer Auto System XL chromatograph equipped with a programmed split/splitless injector and a flame ionization detector, employing a DB-1 50 m × 0.20 mm i.d., 0.33 μm film thickness capillary column (J&W Scientific), as described in detail elsewhere [39]. A halogen (in the form of HX) mass balance was performed by passing the effluent gas through an aqueous NaOH trap (7.0×10^{-4} mol dm^{-3}, kept under constant agitation at 400 rpm) with independent pH (Hanna HI Programmable Printing pH Bench-Meter) analysis. Repeated (up to five separate) catalytic runs with different samples from the same batch of catalyst delivered product compositions that were reproducible to within ± 8%. *p*-CNB (Aldrich, ≥99.9% w/w purity), *p*-BNB (Aldrich, 99% w/w purity), NB (Fluka, >99.0% v/v), CB (Sigma-Aldrich, 99.0% v/v), *p*-CAN (Aldrich, >+99.0 % w/w), *o*-CNB (Fluka, >99.0% w/w), *m*-CNB (Fluka, >98.0% w/w) and the solvents (propanol: Aldrich, 99.7 % v/v, butanol: Riedel-de Haën, ≥99.5% v/v; pentanol: Fluka, >98.0% v/v and hexanol: Aldrich, 98.0 % v/v) were used without further purification.

1.3 Result and Discussion

1.3.1 Catalyst Characterization

Table 1.1: Metal loading, temperature programmed reduction (TPR) characteristics, BET surface area, H_2 uptake and surface area weighted mean metal particle size ($\bar{d}_S$).

	Metal loading (% w/w)	TPR T_{max} (K)[a]	TPR T_{max} (K)[b]	BET area ($m^2\ g^{-1}$)	H_2 uptake ($\mu mol\ g^{-1}$)	($\bar{d}_s$) (nm)
Ni/Al_2O_3	6.1	**595**, 723	490	166	4	30
Ni/SiO_2	5.2	525, **559**, 583	388	187	16	35
Ni/Graphite	7.6	**584**, 625	386	10	13	46
Ni/AC	7.1	**592**, 622	356	885	17	43
Pd/Al_2O_3	6.9	377[c], **523**	-	173	24	20

[a] T_{max} associated with the dominant TPR peak for the reduction of the catalyst precursors is given in bold
[b] T_{max} associated with TPR of reoxidised samples
[c] negative TPR peak associated with Pd hydride decomposition

The metal loading, BET surface area, H_2 chemisorption uptake and mean metal particle size for the catalysts used in this study are given in **Table 1.1**. We have chosen a similar metal loading (6±2% w/w) on an array of supports, ranging from conventional Al_2O_3 and SiO_2 to high surface area activated carbon and low surface area graphite with which to assess *p*-CNB hydrogenation activity/selectivity response. The temperature programmed reduction (TPR) profiles generated for Ni/Al_2O_3 (Ia), Ni/SiO_2 (IIa), Ni/Graphite (IIIa), Ni/AC (IVa) and Pd/Al_2O_3 (V) can be compared in **Figure 1.2**, which also includes the TPR responses for the reoxidised supported Ni catalysts (profiles Ib-IVb). Hydrogen consumption during the initial TPR exceeded (by a factor of 1.1-1.5) that required for the reduction of the supported precursor. This "over consumption" can be attributed to hydrogen spillover during TPR as has been established previously [40,41]. The characteristic temperatures (T_{max}) for maximum H_2 consumption are recorded in **Table 1.1**; the TPR conditions match those used for actual catalyst activation prior to reaction. The TPR profiles associated with the direct reduction of the supported Ni catalysts are characterised by a sharp H_2 consumption peak with a secondary higher temperature peak and a subsequent return to baseline. A similar two stage reduction of nickel has been reported elsewhere for oxide [32,42] and carbon [43,44] supported systems where differences in TPR T_{max} values result from metal/support effects [45,46]. The principal TPR peak (T_{max} = 559-595 K) recorded in this study can be attributed to the decomposition of nickel nitrate to NiO with a subsequent reduction of NiO to Ni^0 responsible for the higher T_{max} peak. González-Marcos *et al.* [47], studying an impregnated (5% w/w) Ni/SiO_2, correlated their single H_2 consumption peak at 601 K to $Ni(NO_3)_2$ decomposition while Rynkowski *et al.*[48] and Diaz and co-workers [49] ascribed TPR peaks at *ca.* 723 K (5% w/w Ni/SiO_2) and 651 K (15% w/w Ni/SiO_2), respectively, to NiO reduction. It is notable that the second TPR peak for Ni/Al_2O_3 extends into the final isothermal hold, which we take to be indicative of a stronger NiO/support interaction [50]. Zaki [51] proposed the presence of partially electron-deficient Ni species that exhibit strong electronic interaction with Al_2O_3. TPR of the reoxidised samples generated a single reduction peak where the significantly higher T_{max} (490 K) for Ni/Al_2O_3 (profile Ib) provides further evidence for a stronger Ni-Al_2O_3 interaction. The TPR profile for Pd/Al_2O_3 is characterized by a sharp negative peak (at 377 K) with an ill-defined (positive) H_2 consumption at 523 K. The negative peak can be attributed to H_2 release resulting from β-Pd hydride decomposition[52-57].

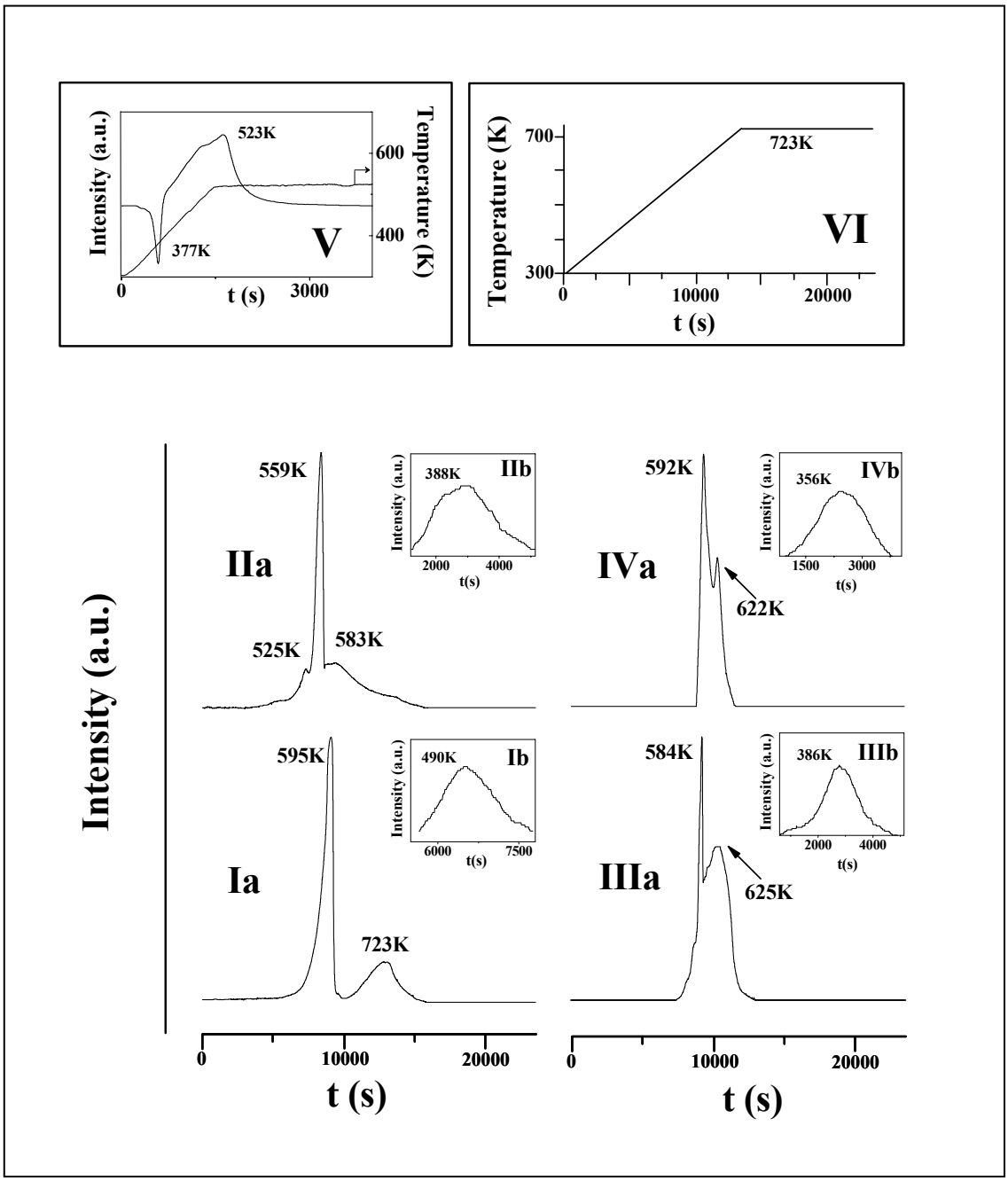

Figure 1.2: TPR profiles for (a) precursor (unreduced) and (b) reoxidised (I) Ni/Al_2O_3, (II) Ni/SiO_2, (III) Ni/graphite, (IV) Ni/activated carbon and (V) the Pd/Al_2O_3 precursor; (VI) temperature programmed ramp employed during TPR of supported Ni catalysts.

Palladium hydride formation is known to occur at room temperature when the H_2 partial pressure exceeds 0.013 atm [58]; room temperature Pd precursor reduction to zero valent Pd has been established elsewhere [59-61]. The occurrence of H_2 consumption at 523 K suggests a secondary reduction of the Pd precursor that is stabilised to some degree by the Al_2O_3 support [61,62]. Based on the TPR analysis, the final reduction temperatures for supported Ni and Pd/Al_2O_3 were set at 723 K and 523 K, respectively.

Representative TEM images are presented in **Figure 1.3** and illustrate metal dispersion and particle morphology. A range of Ni particle sizes is in evidence with a surface area weighted mean Ni particle size that is larger for the carbon relative to the oxide supported systems (**Table 1.1**). Previous studies [63,64] have revealed that supported Ni catalysts prepared by $Ni(NO_3)_2$ impregnation exhibit a wide size distribution post TPR when compared with preparation by the more controlled deposition-precipitation route, which generates smaller average Ni particle diameters. It should be noted that Ni/Al_2O_3, which bore the smallest mean Ni particle size and should accordingly exhibit the highest H_2 uptake, actually delivered the lowest chemisorption value (**Table 1.1**). We tentatively attribute this to metal-support interaction(s) that result(s) in suppressed H_2 uptake but this effect is not without precedent. Hoang-Van *et al.* [65] reported smaller Ni particle sizes associated with Al_2O_3 as support when compared with SiO_2 and TiO_2 where a strong metal-support interaction caused a decrease in hydrogen chemisorption. A similar inhibition of H_2 uptake on Ni/Al_2O_3 was observed by Bartholomew *et al.* [66]. In addition, Ding *et al.* [67] using Ni/Al_2O_3 catalysts prepared by co-precipitation and impregnation reported a suppression of H_2 chemisorption on smaller metal particles and attributed this to stronger metal-support interaction. The smaller mean Pd particle size recorded in **Table 1.1** can be ascribed, at least in part, to a lower reduction temperature [57].

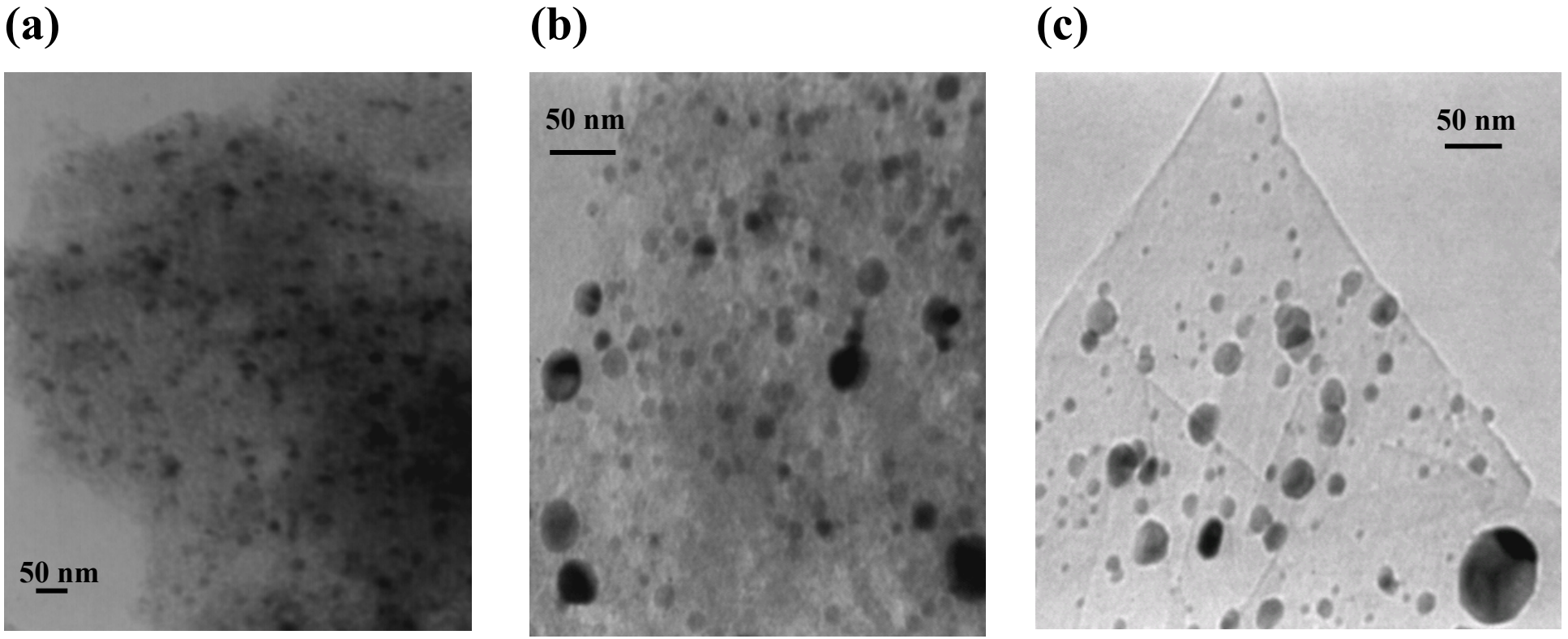

Figure 1.3: Representative TEM images of (a) Ni/Al_2O_3, (b) Ni/AC and (c) Ni/graphite.

1.3.2 Catalyst activity/selectivity.

Hydrogenation of *p*-CNB at 393 K over supported Ni generated *p*-CAN as the only product with no evidence of dechlorination or ring reduction. Fractional *p*-CNB conversion ($x_{p\text{-}CNB}$) is illustrated as a function of time-on-stream for two representative cases in **Figure 1.4** where the temporal drop in activity can be expressed in terms of the empirical relationship [32,68]

$$\frac{(x_{p-CNB} - x_0)}{(x_{5h} - x_0)} = \frac{\Delta t}{(\beta + \Delta t)} \qquad \textbf{(1.2)}$$

where x_{5h} represents fractional conversion after 5 h on-stream and β is a time scale fitting parameter. Fit convergence yields values for x_0, the initial fractional conversion. A pseudo-first order kinetic treatment has been applied previously [32,34] for the catalytic hydrodehalogenation of haloarenes under plug-flow conditions where hydrogen was maintained far in excess; the following reactor/kinetic expression applies

$$\ln(1 - x_0)^{-1} = k\left(\frac{n_{Ni}}{F}\right) \qquad \textbf{(1.3)}$$

The parameter F is the inlet hourly molar *p*-CNB feed rate and n_{Ni} represents moles of Ni in the catalyst bed; n_{Ni}/F has the physical significance of contact time. The linear relationships between $\ln(1\text{-}x_0)^{-1}$ and n_{Ni}/F, shown in **Figure 1.5**, confirm the applicability of pseudo-first order kinetics.

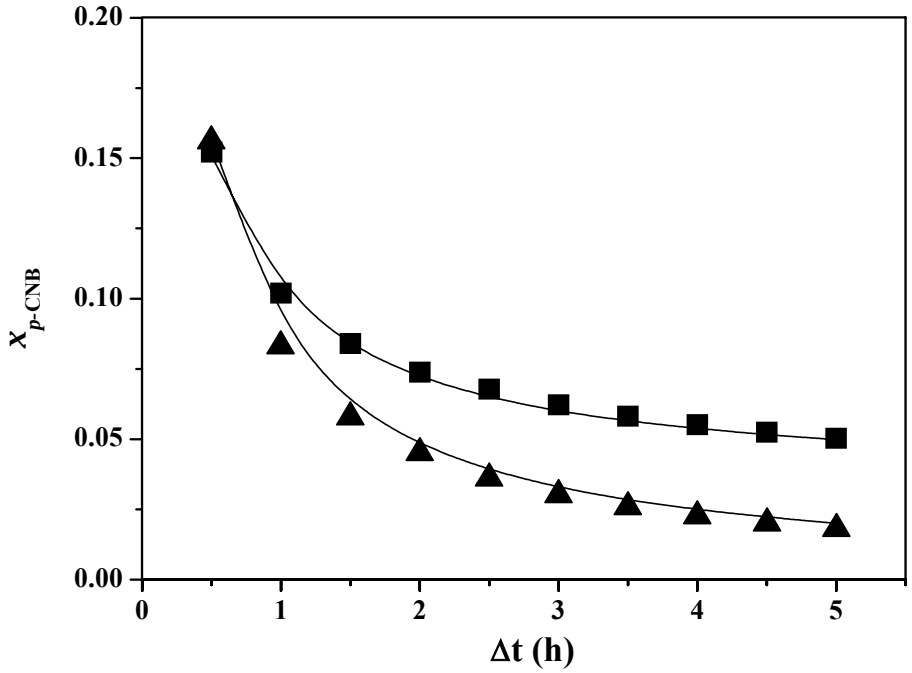

Figure 1.4: Variation of *p*-CNB fractional conversion ($x_{p\text{-}CNB}$) with time-on-stream over Ni/Al_2O_3 (*p*-CNB/Ni= 24 $mol_{p\text{-}CNB}$ mol_{Ni}^{-1} h^{-1}, ▲) and Ni/Graphite (*p*-CNB/Ni= 9 $mol_{p\text{-}CNB}$ mol_{Ni}^{-1} h^{-1}, ■): lines represent fit to Equation (1.2).

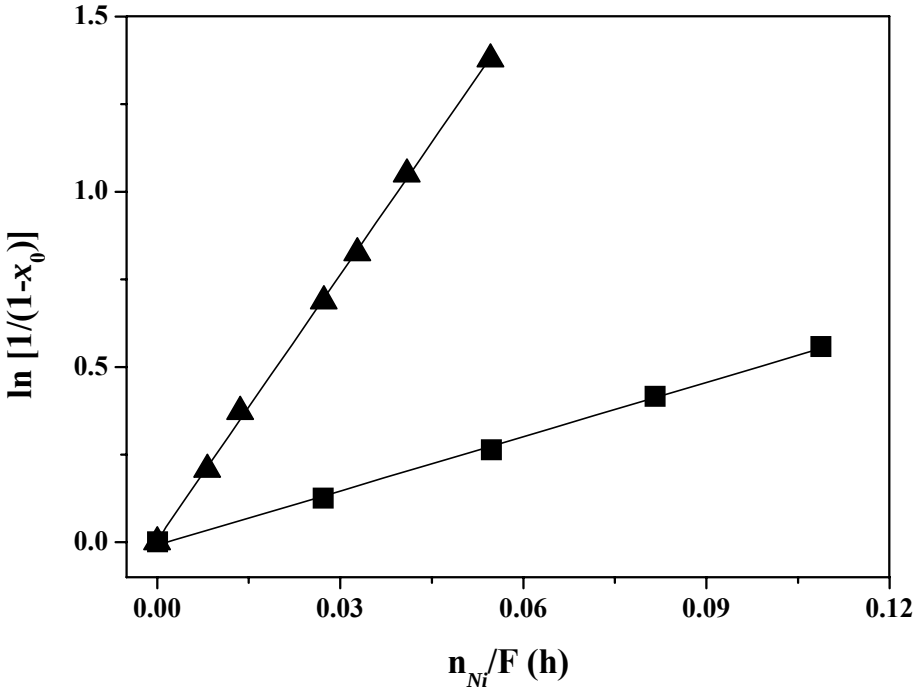

Figure 1.5: Pseudo-first order kinetic plots for the hydrogenation of *p*-CNB over Ni/Al_2O_3 (▲) and Ni/Graphite (■).

Table 1.2: Pseudo-first order rate constants (k) and reaction products (with selectivities) obtained in the hydrogenation of a range of arene reactants over supported Ni and Pd catalysts.

Catalyst	Reactant	Solvent	Product(s) (Selectivity %)	Rate Constant k (h^{-1})
Ni/Al_2O_3	*p*-CNB	Butanol	*p*-CAN (100)	25
Ni/SiO_2	*p*-CNB	Butanol	*p*-CAN (100)	20
Ni/Graphite	*p*-CNB	Butanol	*p*-CAN (100)	5
Ni/AC	*p*-CNB	Butanol	*p*-CAN (100)	16
Ni/Al_2O_3	CB	Butanol	BZ (100)	1
Ni/Al_2O_3	*p*-CAN	Butanol	AN (55) CB (45)	4
Ni/Al_2O_3	NB	Butanol	AN (100)	58
Ni/Al_2O_3	*p*-CNB	Propanol	*p*-CAN (100)	26
Ni/Al_2O_3	*p*-CNB	Pentanol	*p*-CAN (100)	22
Ni/Al_2O_3	*p*-CNB	Hexanol	*p*-CAN (100)	17
Pd/Al_2O_3	*p*-CNB	Butanol	NB (98) AN (2)	68
Ni/Al_2O_3	*o*-CNB	Butanol	*o*-CAN (100)	22
Ni/Al_2O_3	*m*-CNB	Butanol	*m*-CAN (100)	24
Ni/Al_2O_3	*p*-BNB	Butanol	*p*-BAN (100)	20

The extracted pseudo-first order rate constants for the supported Ni catalysts are presented in **Table 1.2**, where the following activity sequence is established: Ni/Al_2O_3 > Ni/SiO_2 > Ni/AC > Ni/Graphite. Converting the raw pseudo-first order rate constants to specific rates, Ni/Al_2O_3 (19×10^{-3} $mol_{p\text{-}CNB}$ h^{-1} m_{Ni}^{-2}) delivered a greater than threefold higher specific activity compared with Ni/Graphite (6×10^{-3} $mol_{p\text{-}CNB}$ h^{-1} m_{Ni}^{-2}), indicative of a support effect. The latter may be manifested in variations of mean Ni size (and size distribution), electronic interactions which impact on Ni site electron density and possible reactant activation. In liquid phase reactions, Kratky and co-workers [13] have observed that CNB reduction is sensitive to the nature of the support and metal particle size. Han *et al.* [22], using a series of oxide (TiO_2, γ-Al_2O_3 and ZrO_2) supported Pt catalysts, ascribed the highest *p*-CAN yield delivered by Pt/TiO_2 to strong metal/support interactions. Xiong *et al.* [69] attributed a higher hydrogenation rate over Ni/TiO_2, when compared with Ni/ZrO_2 and Ni/SiO_2, to a polarization of the N=O bond induced by oxygen vacancies associated with TiO_x. A similar support effect was

proposed by Coq *et al.* for the enhancement of activity and selectivity to *p*-CAN over a series of supported Pt catalysts [25]. The same group also reported that *p*-CAN selectivity is sensitive to metal dispersion where *p*-CAN exhibited a lower adsorption strength relative to *p*-CNB on larger Al_2O_3 supported Pt particles (1-12 nm) [7]. In our study, Pd/Al_2O_3 exhibited a higher overall activity, a response that is expected based on the available literature on liquid phase systems but which is explicitly established here for gas phase reaction. However, reaction over Pd/Al_2O_3 generated NB as the predominant product with a secondary AN formation (see **Table 1.2**), *i.e.* Path (VI) (see **Figure 1.1**) was preferred where C-Cl hydrogen scission and subsequent $-NO_2$ reduction prevailed. Significant hydrodehalogenation activity has, however, been established for supported Pd with specific rates that were higher by up to three orders of magnitude compared with supported Ni catalysts [34].

The Ni/Al_2O_3 sample was adopted as a model catalyst to assess halo/nitro-arene reactivity and probe selectivity responses; the results are given in **Table 1.2**. Conversion of chlorobenzene (CB) generated benzene (BZ) as the sole product, *i.e.* 100% selectivity with respect to hydrodechlorination but at an appreciably lower (by a factor of 25) rate when compared with that recorded for the *p*-CNB reaction. The exclusivity in terms of *p*-CNB $\rightarrow$ *p*-CAN over supported Ni must result from a more facile reduction of the nitro group. Indeed, Ni/Al_2O_3 also exhibited 100% selectivity in terms of $-NO_2$ reduction for the conversion of NB (to AN) where the rate constant ratio for selective $-NO_2$ reduction (NB$\rightarrow$AN) relative to C-Cl hydrogenolysis (CB $\rightarrow$BZ) approached 60. It is significant that there was a greater than twofold increase in NB hydrogenation rate relative to the conversion of *p*-CNB, *i.e.* the Cl substituent has a deactivating effect. In contrast, the presence of electron-withdrawing groups has been found to result in higher hydrogenation activity in liquid phase applications, which was taken to be consistent with the involvement of a negatively charged intermediate [70]. In our study, under the same reaction conditions *p*-CAN underwent hydrogenolytic cleavage of the –Cl or $-NH_2$ substituents to generate AN and CB with no evidence of BZ formation. The higher selectivity to AN suggests that *p*-CAN conversion preferably followed Path VII over Path VIII (**Figure 1.1**), *i.e.* aromatic dechlorination is favoured over deamination. Reaction exclusivity also extends to the hydrogenation of *p*-bromonitrobenzene (*p*-BNB) where *p*-bromoaniline (*p*-BAN) was formed with 100% selectivity but at a lower rate than the *p*-CNB reaction, suggesting a greater deactivating effect by the Br substituent. The hydrogenation of both *ortho*- and *meta*- CNB isomers was also 100%

selective with respect to the corresponding haloaniline isomer with no obvious dependency of rate on isomer structure (**Table 1.2**). Steric hindrance has been reported to result in a significantly lower conversion of *o*-CNB in batch liquid phase operation [13,18,23]. The aromatic feed was introduced to the reactor as an alcohol solution and subsequently vaporised before contacting the catalyst. Exclusive selectivity in terms of -NO_2 group reduction was maintained with no appreciable dependence of rate on the nature of the alcohol solvent, albeit there was a measurable drop in activity in going from butanol/propanol to hexanol. In gas phase hydrogenation, solvent effects have been attributed to a competitive adsorption of solvent and reactant on the catalyst surface [71,72]. In this instance, the alcohol solvent served as a carrier and did not have a major involvement in determining reaction rate. However, significant solvent effects have been noted for the liquid phase hydrogenation of *p*-CNB [10,15,18] with higher conversions established with increasing solvent (alcohol) polarity [9]. The temporal plots given in **Figure 1.4** reveal a short term decline in fractional conversion. The catalyst exhibited a continual decline in activity with extended reaction times but the exclusive formation of *p*-CAN was maintained to ultimately deliver a production of 40 $g_{p\text{-}CAN}\ g_{Ni}^{-1}$ after 9 h on-stream. Work is now underway to identify the source of the catalyst deactivation and to assess the viability of catalyst regeneration and alternative catalyst formulations that will deliver time invariant activity while maintaining the product exclusivity that we report here.

1.4 Conclusions

We have established that oxide and carbon supported Ni (6±2% w/w) promote the hydrogenation of *p*-CNB to *p*-CAN with 100% selectivity in gas phase continuous operation under mild reaction conditions (393 K and 1atm). A support effect is established where Ni/Al_2O_3 delivered the highest specific reaction rate; activity increased in the order Ni/Graphite < Ni/AC < Ni/SiO_2 < Ni/Al_2O_3. The Ni/Al_2O_3 catalyst required a higher reduction temperature, exhibited suppressed H_2 uptake and, on the basis of TEM analysis, bore a smaller mean Ni particle diameter, effects that we attribute to stronger Ni/support interactions. While Pd/Al_2O_3 was significantly more active, it generated NB as the principal product (*via* hydrodechlorination) with subsequent hydrogenation to give AN as a secondary product. Reaction exclusivity in terms of -NO_2 reduction over supported Ni extends to CNB isomers and the conversion of a brominated analogue. The aromatic ring halogen substituent has a deactivating

effect which serves to lower -NO_2 reduction. These results demonstrate for the first time the viability of continuous gas phase catalytic hydrogenation of *p*-CNB for the direct (and clean) production of *p*-CAN. However, the catalysts suffer time on-stream loss of activity (while still retaining exclusive selectivity), an effect that will be the subject of future research.

1.5 References

[1.1] M. M. Kirchhoff, Resour., Conserv. Recycling, 44, 237 (2005)

[1.2] P. T. Anastas, M. M. Kirchhoff, T. C. Williamson, Appl. Catal. A: Gen., 221, 3 (2001)

[1.3] G. Konnecker, A. Boehncke, S. Schmidt, Fresenius Environ. Bull., 12, 589 (2003)

[1.4] A. Boehnecke, J. Kielhorn, G. Konnecker, C. Pohlenz-Michel, I. Mangelsdorf, CICADS Report 48, W.H.O., Geneva, 2003, p. 78.

[1.5] Y. D. Smirnov, L. A. Fedorova, A. P. Tomilov, Russ. J. Electrochem., 33, 1168 (1997)

[1.6] K. R. Westerterp, K. B. van Gelder, H. J. Janssen, M. H. Oyevaar, Chem. Eng. Sci., 43, 2229 (1988)

[1.7] B. Coq, A. Tijani, F. Figuéras, J. Mol. Catal., 68, 331 (1991)

[1.8] B. Coq, A. Tijani, F. Figuéras, J. Mol. Catal., 71, 317 (1992)

[1.9] Y.-Z. Chen, Y.-C. Chen, Appl. Catal. A: Gen., 115, 45 (1994)

[1.10] Y.-C. Liu, C.-Y. Huang, Y.-W. Chen, Ind. Eng. Chem. Res., 45, 62 (2006)

[1.11] Y.-C. Liu, Y.-W. Chen, Ind. Eng. Chem. Res., 45, 2973 (2006)

[1.12] Z. Yu, S. Liao, Y. Xu, B. Yang, D. Yu, J. Chem. Soc., Chem. Commun., 11, 1155 (1995)

[1.13] V. Kratky, M. Kralik, M. Mecarova, M. Stolcova, L. Zalibera, M. Hronec, Appl. Catal. A: Gen., 235, 225 (2002)

[1.14] V. I. Savchenko, T. V. Denisenko, S. Y. Sklyar, V. D. Simonov, Russ. J. Inorg. Chem., 11, 2149 (1975)

[1.15] I. A. Ilchenko, A. V. Bulatov, I. E. Uflyand, V. N. Sheinker, Kinet. Catal., 32, 691 (1991)

[1.16] N. P. Sokolova, A. A. Balandin, N. P. Maksimova, Z. M. Skul'skaya, Russ. Chem. Bull., 15, 1824 (1966)

[1.17] O. P. Savvateev, M. V. Klyuev, J. Appl. Chem. USSR, 63, 1485 (1990)

[1.18] I. E. Uflyand, I. A. Ilchenko, V. N. Sheinker, A. V. Bulatov, Transition Met. Chem., 16, 293 (1991)

[1.19] Z. Yu, S. Liao, Y. Xu, B. Yang, D. Yu, J. Mol. Catal. A: Chem., 120, 247 (1997)

[1.20] M. L. Kantam, T. Bandyopadhyay, A. Rahman, N. M. Reddy, B. M. Choudary, J. Mol. Catal. A: Chem., 133, 293 (1998)

[1.21] X.-X. Han, R.-X. Zhou, G.-H. Lai, X.-M. Zheng, React. Kinet. Catal. Lett., 83, 55 (2004)

[1.22] X.-X. Han, R.-X. Zhou, G.-H. Lai, X.-M. Zheng, Catal. Today, 93-95, 433 (2004)

[1.23] X.-X. Han, R.-X. Zhou, G.-H. Lai, B.-H. Yue, X.-M. Zheng, J. Mol. Catal. A: Chem., 209, 83 (2004)

[1.24] X.-X. Han, R.-X. Zhou, X.-M. Zheng, H. Jiang, J. Mol. Catal. A: Chem., 193, 103 (2003)

[1.25] B. Coq, A. Tijani, R. Dutartre, F. Figuéras, J. Mol. Catal., 79, 253 (1993)

[1.26] A. Tijani, B. Coq, F. Figuéras, Appl. Catal., 76, 255 (1991)

[1.27] P. Lu, N. Toshima, Bull. Chem. Soc. Jpn., 73, 751 (2000)

[1.28] Y. Chen, C. Wang, H. Liu, J. Qiu, X. Bao, Chem. Commun., 42, 5298 (2005)

[1.29] Y. Chen, J. Qiu, X. Wang, J. Xiu, J. Catal., 242, 227 (2006)

[1.30] X. Yan, J. Sun, Y. Wang, J. Yang, J. Mol. Catal. A: Chem., 252, 17 (2006)

[1.31] J. R. Kosak, in: W.H. Jones (Ed.), Catalysis in Organic Synthesis, Academic Press, New York, 1980, p. 107.

[1.32] K. V. Murthy, P. M. Patterson, M. A. Keane, J. Mol. Catal. A: Chem., 225, 149 (2005)

[1.33] C. Park, C. Menini, J. L. Valverde, M. A. Keane, J. Catal., 211, 451 (2002)

[1.34] M. A. Keane, Appl. Catal. A: Gen., 271, 109 (2004)

[1.35] T. Zhang, L. You, Y. Zhang, Dyes and Pigments, 68, 95 (2006)

[1.36] E. Wagner-Czauderna, E. Orlowska, M. K. Kalinowski, Pol. J. Chem., 72, 2127 (1998)

[1.37] M. A. Keane, P. M. Patterson, J. Chem. Soc., Faraday Trans., 92, 1413 (1996)

[1.38] G. Tavoularis, M. A. Keane, J. Chem. Technol. Biotechnol., 74, 60 (1999)

[1.39] G. Yuan, M. A. Keane, Chem. Eng. Sci., 58, 257 (2003)

[1.40] M. A. Keane, G. Tavoularis, React. Kinet. Catal. Lett., 78, 11 (2003)

[1.41] E.-J. Shin, A. Spiller, G. Tavoularis, M. A. Keane, Phys. Chem. Chem. Phys., 1, 3173 (1999)

[1.42] C. Louis, Z. X. Cheng, M. Che, J. Phys. Chem., 97, 5703 (1993)

[1.43] L. M. Gómez-Sainero, A. Cortés, X. L. Seoane, A. Arcoya, Ind. Eng. Chem. Res., 39, 2849 (2000)

[1.44] M. Cerro-Alarcón, B. Bachiller-Baeza, A. Guerrero-Ruiz, I. Rodríguez-Ramos, J. Mol. Catal. A: Chem., 258, 221 (2006)

[1.45] C. Li, Y.-W. Chen, Thermochim. Acta, 256, 457 (1995)

[1.46] A. Jasik, R. Wojcieszak, S. Monteverdi, M. Ziolek, M. M. Bettahar, J. Mol. Catal. A: Chem., 242, 81 (2005)

[1.47] M. P. González-Marcos, J. I. Gutiérrez-Ortiz, C. González-Ortiz de Elguea, J. R. González-Velasco, J. Mol. Catal. A: Chem., 120, 185 (1997)

[1.48] J. Rynkowski, D. Rajski, I. Szyszka, J. R. Grzechowiak, Catal. Today, 90, 159 (2004)

[1.49] A. Diaz, D. R. Acosta, J. A. Odriozola, M. Montes, J. Phys. Chem. B, 101, 1782 (1997)

[1.50] A. Jones, B. McNicol, Temperature-Programmed Reduction for Solid Materials Characterization, Marcel Dekker, Inc., New York, 1986, p. 121.

[1.51] M I Zaki, Stud. Surf. Sci. Catal., 100, 569 (1996)

[1.52] N. Lingaiah, P. S. Sai Prasad, P. Kanta Rao, F. J. Berry, L. E. Smart, Catal. Commun., 3, 391 (2002)

[1.53] M. Bonarowska, B. Burda, W. Juszczyk, J. Pielaszek, Z. Kowalczyk, Z. Karpiński, Appl. Catal. B: Environ., 35, 13 (2001)

[1.54] N. K. Nag, J. Phys. Chem. B, 105, 5945 (2001)

[1.55] M. Bonarowska, J. Pielaszek, V. A. Semikolenov, Z. Karpiński, J. Catal., 209, 528 (2002)

[1.56] G. Neri, M. G. Musolino, C. Milone, D. Pietropaolo, S. Galvagno, Appl. Catal. A: Gen., 208, 307 (2001)

[1.57] L. M. Gómez-Sainero, X. L. Seoane, J. L. G. Fierro, A. Arcoya, J. Catal., 209, 279 (2002)

[1.58] J. E. Benson, H. S. Hwang, M. Boudart, J. Catal., 30, 146 (1973)

[1.59] C.-B. Wang, H.-K. Lin, C.-M. Ho, J. Mol. Catal. A: Chem., 180, 285 (2002)

[1.60] G. M. Tonetto, D. E. Damiani, J. Mol. Catal. A: Chem., 202, 289 (2003)

[1.61] T. Fujitani, E. Echigoya, Nippon Kagaku Kaishi, 261 (1991)

[1.62] F. Pinna, F. Menegazzo, M. Signoretto, P. Canton, G. Fagherazzi, N. Pernicone, Appl. Catal. A: Gen., 219, 195 (2001)

[1.63] M. A. Keane, Can. J. Chem., 72, 372 (1994)

[1.64] G. Pina, C. Louis, M. A. Keane, Phys. Chem. Chem. Phys., 5, 1924 (2003)

[1.65] C. Hoang-Van, Y. Kachaya, S. J. Teichner, Y. Arnaud, J. A. Dalmon, Appl. Catal., 46, 281 (1989)

[1.66] C. H. Bartholomew, R. B. Pannell, J. L. Butler, D. G. Mustard, Ind. Eng. Chem. Prod. Res. Dev., 20, 296 (1981)

[1.67] L. Ding, Z. J. Zhang, Y. Zheng, Z. Zhang, Z. Ring, J. Chen, Int. J. Chem. React. Eng., 4, A3 (2006)

[1.68] S. Jujjuri, E. Ding, E. L. Hommel, S. G. Shore, M. A. Keane, J. Catal., 239, 486 (2006)

[1.69] J. Xiong, J. X. Chen, J. Y. Zhang, Catal. Commun., 8, 345 (2007)

[1.70] B. Coq, F. Figuéras, Coord. Chem. Rev., 178-180, 1753 (1998)

[1.71] A. Guevara, R. Bacaud, M. Vrinat, Appl. Catal. A: Gen., 253, 515 (2003)

[1.72] E.-J. Shin, M. A. Keane, J. Catal., 173, 450 (1998)

Chapter 2

Gas Phase Hydrogenation of *p*-Chloronitrobenzene over Pd-Ni/Al_2O_3

In the previous Chapter, reaction exclusivity in terms of -NO_2 group reduction over Ni/Al_2O_3 was established at relatively low reactant conversions. In this Chapter, the catalytic action of alumina supported mono- (Pd and Ni) and bi-metallic (Pd-Ni/Al_2O_3 prepared by (co-)impregnation is considered in the gas phase hydrogenation of *p*-chloronitrobenzene in order to establish a promotional/synergistic effect of Pd with Ni.

2.1 Introduction

Aromatic amino compounds find widespread use in the chemical industry primarily as intermediates but also as reactants [1], *e.g.* anisidines in the production of pigments and azo dyes and aniline (AN) in rubbers, herbicides and amino resins. The traditional production routes, *via* the reduction of nitroarenes in the presence of Fe (Béchamp process) or sulfides, are no longer viewed as sustainable because of the formation of iron oxide sludges (250-500 $g\,mol^{-1}_{-NO_2}$), elemental sulphur and sulphur-containing organic by-products [2]. Selective catalytic hydrogenation over supported transition metals represents a cleaner alternative but the formation of undesired toxic azo [3] and azoxy [4] derivatives is still a decided drawback. Nitroarene hydrogenation has typically been conducted in liquid phase batch systems, where the use of H_2 gas [5-9] or hydrogen abstracted from a donor molecule [10] has been considered. There have also been some recent reports of the gas phase hydrogenation of nitrobenzene (NB) over Cu/SiO_2 [6] and Pt/ZSM-5 [11]. In this study, we examine the selective hydrogenation of *p*-chloronitrobenzene (*p*-CNB) where *p*-chloroaniline (*p*-CAN), as the target product, is an important intermediate in the production of a range of fine chemicals [1]. There are two main reaction pathways associated with the catalytic hydrogenation of *p*-CNB, as illustrated in **Figure 2.1**.

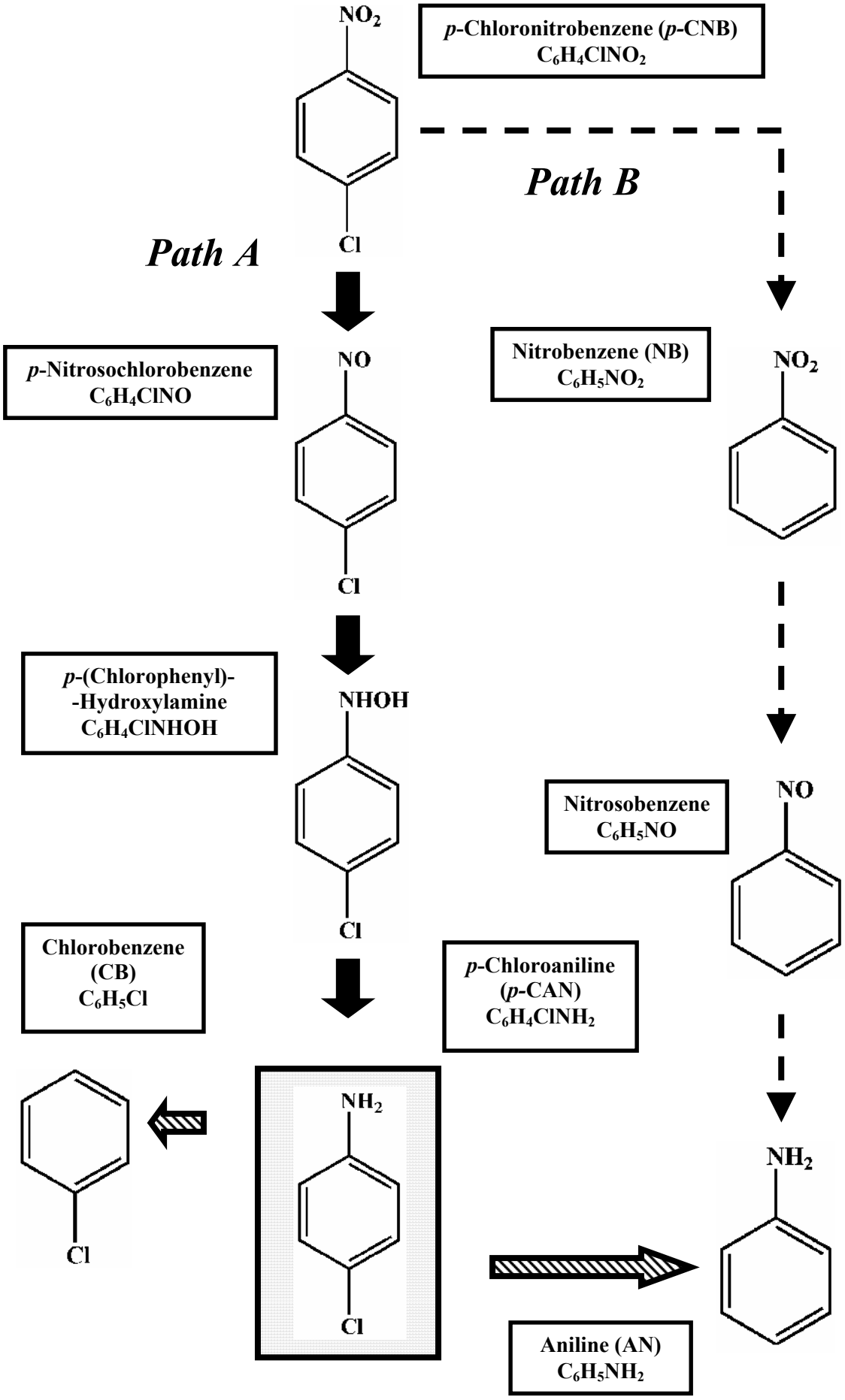

Figure 2.1: Reaction pathways associated with the hydrogen mediated conversion of *p*-CNB.

Path A involves -NO_2 group reduction, *via* nitrosochloro- and hydroxylamine-intermediates, to yield the target *p*-CAN, which can then undergo further hydrodechlorination (HDC) and/or hydrodenitrogenation to generate AN and/or chlorobenzene (CB). In Path B, *p*-CNB undergoes HDC (to NB) and further hydrogenation (to AN) *via* the nitrosobenzene intermediate. Both mechanisms have been proposed for gas and liquid phase operation over supported metals [12-20]. High *p*-CNB conversions have been invariably accompanied by significant dechlorination [21], where C-Cl scission can be influenced to differing degrees by metal dispersion [19,21], metal-support interactions [8,22] and the use of additives [21,23]. The incorporation of a second metal, in the case of unsupported (Pt-Ni [10], Ru-Pt [24], Ru-Pd [24] and Ni-Fe-P [25]) and supported (Pt-M/TiO_2 (M=Cr, Mn, Fe, Co, Ni and Cu) [26]) systems, has been demonstrated to impact on the catalytic response in batch liquid phase hydrogenation. The preparation of supported bimetallic catalysts can involve either the concurrent or successive incorporation of both metals precursors onto the support [27]. In this study we consider the catalytic action of Pd-Ni/Al_2O_3 prepared by co-impregnation.

The existing literature [14-18,25,28-34] on *p*-CNB hydrogenation (in batch liquid phase operation) over Ni and/or Pd catalysts is summarized in **Table 2.1**; where feasible, we relate our results to the trends that emerge from the tabulated reports. It can be seen that those studies involving reaction over Ni catalysts typically necessitated elevated pressure (≥ 5 atm) and/or temperature (up to 542 K) while reactions over the more active Pd catalysts were conducted under milder operating conditions. The incorporation of Ru [17,35], Rh [35], Sn^{4+} [36], Cu [37], Co [37] and Pt [38] with Pd in liquid phase reactions has been reported to inhibit the dechlorination step. Nevertheless, Vishwanathan *et al.* [39] observed an equivalent selectivity response in the gas phase hydrogenation of *o*-CNB over Pd/Al_2O_3 with and without Li, Na, K and Cs addition. Lu and Thoshima [34] studied the liquid phase hydrogenation of a series of *p*-substituted nitro derivates over poly(*N*-vinyl-2-pyrrolidone)-protected Ni-Pd colloids and reported increased activity that was dependent on the bimetallic nano-cluster composition. Our study represents the first comprehensive analysis of gas phase *p*-CNB hydrogenation over supported (Al_2O_3) Pd-Ni. Catalytic activity/selectivity is correlated to catalyst characterisation, which draws on TPR, H_2 chemisorption, XRD, and TEM-EDX analyses.

Table 2.1: Compilation of the literature dealing with batch liquid phase reduction of *p*-CNB over Ni and Pd catalysts.

Catalyst (% w/w)	Solvent	Conditions	Rate	Remarks	Ref
Raney Ni Ni/Kieselguhr (50) Ni/Asbestos (50)	EtOH	T = 298-542 K; P = 50-130 atm	4.9×10^{-5} - 5.5×10^{-3} $mol_{p\text{-}CNB}\ g_{catalyst}^{-1}\ min^{-1}$[a]	$NiCl_2$ formation lowers selectivity to *p*-CAN. Catalyst reactivation accompanied by increased C-Cl cleavage ($21 \le Y_{p\text{-}CAN} \le 99$)	[28]
Raney Ni	*i*-PrOH	T = 328 K; P = 1 atm	0.1 - 0.2 $mol_{H2}\ mol_{p\text{-}CNB}^{-1}\ min^{-1}$[a]	Preferential formation of aniline at high *p*-CNB conversion[b]	[29]
Ni-Cr (≤50 Ni)	*i*-PrOH	T= 293-333 K; P = 1 atm	1×10^{-3} $mol_{H2}\ mol_{Ni}^{-1}\ s^{-1}$	Ni-Cr more active than Raney Nickel but promotes *p*-CAN dechlorination to a greater extent[b]	[30]
Nickel Boride	EtOH	T = 363-393 K; P = 5 - 8 atm	1.0 - 4.8 $mmol_{p\text{-}CNB}\ g_{Ni}^{-1}\ min^{-1}$	Level of dechlorination affected by Mo addition. Solvent affected selectivity and rate (EtOH>MeOH>cyclohexane>methylacetate)[b]	[14]
Ni-Fe-P amorphous alloy ($15 \le Ni \le 55$; $P = 34$; $11 \le Fe \le 51$)	EtOH	T = 383 K; P = 10 atm	33.6 - 93.3 $mmol_{H2}\ g_{Ni}^{-1}\ h^{-1}$	Fe-Ni electron donation promoted *p*-CNB hydrogenation, lowerd *p*-CAN dehalogenation. Best results achieved with Ni-Fe-P compared with Raney Nickel, Ni-P and Fe-P ($63 \le X \le 100$; $63 \le Y_{p\text{-}CAN} \le 98$)	[25]
Ni-P-B amorphous alloy ($29 \le Ni \le 83$; $P = 7$; $9 \le B \le 64$)	EtOH	T = 393 K; P = 12 atm	$\ge 6.1\times10^{-6}$ $mol_{p\text{-}CNB}\ g_{catalyst}^{-1}\ s^{-1}$	Induction period observed. Electronic transfer (B→Ni→P) modified Ni active sites, raising activity. Activity was solvent dependant: MeOH>EtOH ($93 \le Y_{p\text{-}CAN} \le 99$)	[15]
La-NiB (La/Ni = 10)	MeOH	T = 393 K; P = 12 atm	5.2×10^{-5} $mol_{p\text{-}CNB}\ g_{Ni}^{-1}\ s^{-1}$	Activity and selectivity to *p*-CAN decreased in the order: LaNiB>NiB>Raney Nickel. La promoter served to modify Ni electronic structure ($80 \le X \le 100$; $92 \le S_{p\text{-}CAN} \le 99$)	[16]
Pd (II) Chelates/Sibunite (0.13-0.60)	EtOH	T = 318 K; P = 1 atm	5 – 149 $mol_{H2}\ mol_{Pd}^{-1}\ min^{-1}$	Isomer effect: *p*-CAN formed with highest selectivity. Highest activity achieved with the most polar solvent (EtOH).	[31,32]
Pd/PVP (poly-(N-vinyl- -2-pyrrolidone)) Pd-Ru/PVP Pd-Rh/PVP	MeOH	T = 338 K; P = 1 atm	1.6 - 94.4 $mol_{H2}\ mol_{Pd}^{-1}\ min^{-1}$	Second metal enhanced *p*-CAN selectivity and lowered rate. Small amount of base also increased haloaniline selectivity. ($1 \le X \le 100$; $0 \le S_{p\text{-}CAN} \le 94$)	[17]
Pd/Charcoal (1.02) Pd/Sulphonated poly(styrene -*co*-divinylbenzene) (0.98)	MeOH	T = 298 K; P = 5 atm	0.2 - 0.4 $mol_{H2}\ mol_{Pd}^{-1}\ s^{-1}$[c]	Isomer effect; activity decreased in the order *m*-CNB>*p*-CNB>*o*-CNB for polymer supported Pd and *p*-CNB>*o*-CNB>*m*-CNB for Pd/C. *p*-CAN was further converted to aniline.	[18]
Pd/MCM-41	THF	T = 298 K; P = 1 atm	1.1×10^{-4} $mol_{p\text{-}CNB}\ g_{catalyst}^{-1}\ min^{-1}$[a]	($Y_{p\text{-}CAN} \le 77$)	[33]
Pd-Ni colloids	EtOH	T = 303 K; P = 1 atm	-[d]	Exclusive formation of aniline[b]	[34]

[a]calculated from source data; [b]conversion, selectivity and/or yield of *p*-CAN not provided; [c]rate derived from time required for 50% theoretical stoichiometric hydrogen consumption
[d]no rate data reported; X = Conversion of *p*-CNB (%); S_x = Selectivity with respect to compound x (%); Y_x = Yield of compound x (%)

Table 2.2: Metal loading, BET surface area, temperature programmed reduction (TPR) characteristics, H_2 chemisorption and range of Pd/Ni surface atomic ratios obtained from TEM-EDX analyses.

Catalyst	Metal loading (wt. %)	BET area ($m^2\ g^{-1}$)	TPR T_{max} (K)[a]	H_2 chemisorption ($\mu mol\ mg_{Pd}^{-1}$)	Pd/Ni surface atomic ratio
Pd/Al_2O_3	6.9	173	387[b], **560**, 723	0.3	-
Ni/Al_2O_3	6.1	166	**715**	-[c]	-
Pd/Al_2O_3+Ni/Al_2O_3(1:3)	6.4	168	383[b], **457**, **641**, 723	0.4	-
Pd/Al_2O_3+Ni/Al_2O_3(1:1)	6.6	172	383[b], **444**, **630**, 723	0.3	-
Pd/Al_2O_3+Ni/Al_2O_3(3:1)	6.8	170	392[b], **598**, 723	0.3	-
Pd-Ni/Al_2O_3(1:3)	7.8	162	354[b], **428**, 630, 723	0.3	0.2 – 19
Pd-Ni/Al_2O_3(1:1)	7.7	168	354[b], **429**, 723	0.6	0.6 – 24
Pd-Ni/Al_2O_3(3:1)	8.1	168	354[b], **426**, 723	0.8	1 - 31

[a]principal H_2 consumption peak(s) are given in bold
[b]negative TPR peak associated with Pd hydride decomposition
[c]$H_{2\ uptake}$ = 0.07 $\mu mol\ mg_{Ni}^{-1}$

2.2 Experimental

2.2.1 Materials and Catalyst Preparation

The Al_2O_3 support (Puralox) was obtained from Condea Vista Co. and used as received. Alumina supported Pd (6.9 % w/w), Ni (6.1 % w/w) and three Pd-Ni bimetallics (Pd:Ni mole ratios = 1:3, 1:1 and 3:1, total metal loading 7.8-8.1 % w/w) were prepared by standard wetness impregnation of Al_2O_3 where aqueous solutions of $Pd(NO_3)_2$ and/or $Ni(NO_3)_2$ were added drop wise at 353 K to the substrate with constant agitation (500 rpm). The impregnated solids were oven dried at 383 K for 16 h and sieved (ATM fine test sieves) into a batch of 75 μm average particle diameter. Physical mixtures of reduced passivated Pd/Al_2O_3+Ni/Al_2O_3 (Pd:Ni mole ratios = 1:3, 1:1 and 3:1) were also examined. The metal loadings (reproducible to within ± 4%) were determined by inductively coupled plasma-optical emission spectrometery (ICP-OES, Vista-PRO, Varian Inc.) and are given in **Table 2.2**.

2.2.2 Characterization Analyses

The temperature programmed reduction (TPR) response, BET area and H_2 chemisorptions were recorded using the commercial CHEMBET 3000 (Quantachrome Instruments) unit. The samples were loaded into a U-shaped Pyrex glass cell (100 mm × 3.76 mm i.d.) and heated in 17 cm^3 min^{-1} (Brooks mass flow controlled) 5% v/v H_2/N_2 to 723 K at 10 K min^{-1}. The effluent gas passed through a liquid N_2 trap and changes in H_2 consumption were monitored by TCD with data acquisition/manipulation using the TPR Win^{TM} software. The reduced samples were swept with 65 cm^3 min^{-1} N_2 for 1.5 h, cooled to room temperature and subjected to H_2 chemisorption using a pulse (50 μl) titration procedure. The maximum partial pressure of H_2 in the sample cell (0.001 atm) was well below the pressure required (0.013 atm) for β-phase Pd hydride formation at room temperature [40]. Hydrogen pulse introduction was repeated until the signal area was constant, indicating surface saturation. BET areas were recorded with a 30% v/v N_2/He flow; pure N_2 (99.9%) served as the internal standard. At least two cycles of N_2 adsorption-desorption in the flow mode were used to determine total surface area using the standard single point method. BET surface area and H_2 uptake values were reproducible to within ± 5 % and the values quoted in this paper are the mean. Powder X-ray diffractograms were recorded on a Bruker/Siemens D500 incident X-ray diffractometer using Cu Kα radiation. The samples were scanned at a rate of 0.02º $step^{-1}$

over the range $20^o \leq 2\theta \leq 90^o$ (scan time = 5 s $step^{-1}$). Diffractograms were identified using the JCPDS-ICDD reference standards, *i.e.* γ-Al_2O_3 (10-0425), Pd (05-0681) and Ni (04-0850). Transmission electron microscopy analysis was conducted using a JEOL JEM 2011 HRTEM unit with a UTW energy dispersive X-ray detector (EDX) detector (Oxford Instruments) operated at an accelerating voltage of 200 kV and using Gatan DigitalMicrograph 3.4 for data acquisition/manipulation. Samples for analysis were prepared by dispersion in acetone and deposited on a holey carbon/Cu grid (300 Mesh). Up to 400 individual metal particles were counted for each catalyst and the surface area-weighted metal diameter (d_{TEM}) was calculated from

$$d_{TEM} = \frac{\sum_i n_i d_i^3}{\sum_i n_i d_i^2} \qquad (2.1)$$

where n_i is the number of particles of diameter d_i.

2.2.3 Catalytic Procedure

The gas phase hydrogenation of *p*-CNB at 393 K and atmospheric pressure was conducted *in situ* immediately after activation in a fixed bed micro-reactor, operating under conditions that ensured negligible heat/mass transport limitations, as has been described in detail elsewhere [41,42]. The *p*-CNB reactant was fed (F = 0.4 mmol h^{-1}) by means of a microprocessor controlled infusion pump (Model 100, kd Scientific) *via* a glass/teflon air tight syringe and a teflon line to the reactor in a stream of ultra pure H_2, the flow rate of which was monitored using a Humonics 520 digital flow meter: *GHSV* = 2×10^4 h^{-1}. The n_{metal}/F ratio, where n_{metal} denotes the number of moles of metal (Pd and/or Ni) in the catalyst bed, spanned the range 3×10^{-3} – 55×10^{-3} mol_{metal} h $mol_{p\text{-}CNB}^{-1}$. The reactor effluent was frozen in a liquid nitrogen trap for subsequent analysis, which was made by capillary GC as described previously [43,44]. The relative peak area % was converted to mol % using regression equations based on detailed calibration. Repeated catalytic runs with different samples from the same batch of catalyst delivered product compositions that were reproducible to within ± 8 %. The fractional *p*-CNB conversion ($x_{p\text{-}CNB}$) is given by

$$x_{p-CNB} = \frac{[p\text{-CNB}]_{In} - [p\text{-CNB}]_{Out}}{[p\text{-CNB}]_{In}} \quad (2.2)$$

and the fractional selectivity with respect to *p*-CAN ($S_{p\text{-}CAN}$) was obtained from

$$S_{p-CAN} = \frac{[p\text{-CAN}]_{Out}}{[p\text{-CNB}]_{In} - [p\text{-CNB}]_{Out}} \quad (2.3)$$

For comparison purposes, the gas phase HDC of CB was carried out at 393 K where $n_{Pd}/F = 13\times10^{-3}$ - 32×10^{-3} mol_{Pd} h mol_{CB}^{-1}. A chlorine mass balance (in the form of HCl product) was performed by passing the effluent gas through an aqueous NaOH trap ($7.0 \times 10^{-4} - 8.0 \times 10^{-3}$ mol dm^{-3}), kept under constant agitation (≥ 300 rpm) and monitoring continuously the pH change by means of a Hanna HI Programmable Printing pH Bench-Meter. The concentration of HCl generated was also measured by titrimetric analysis of the NaOH trap solution using a Metrohm (Model 728) Autotitrator ($AgNO_3$, combined Ag electrode); Cl mass balance was complete to better than ± 10%. The reactants: *p*-CNB and CB (Sigma-Aldrich, ≥ 98 %) and the solvent (*1*-butanol: Riedel-de Haën, ≥ 99.5 %) were used as received and the gases (H_2, He and N_2) employed were of ultra high purity (99.999%).

2.3 Results and Discussion

The metal loading and BET areas of the mono- and bi-metallic catalysts considered in this study are given in **Table 2.2**. A decrease in surface area was observed for each supported catalyst relative to the starting Al_2O_3 support (190 m^2 g^{-1}), a response that can be attributed to a partial pore filling by the metal component.

2.3.1 Mono-Metallic Systems: Pd/Al_2O_3 and Ni/Al_2O_3

2.3.1.1 Catalyst Characterization

The TPR responses recorded for the mono-metallic Pd/Al_2O_3 and Ni/Al_2O_3 catalysts are given in **Figure 2.2** as profiles A and B, respectively. The temperatures associated with maximum hydrogen consumption and release (T_{max}) during TPR are presented in **Table 2.2**.

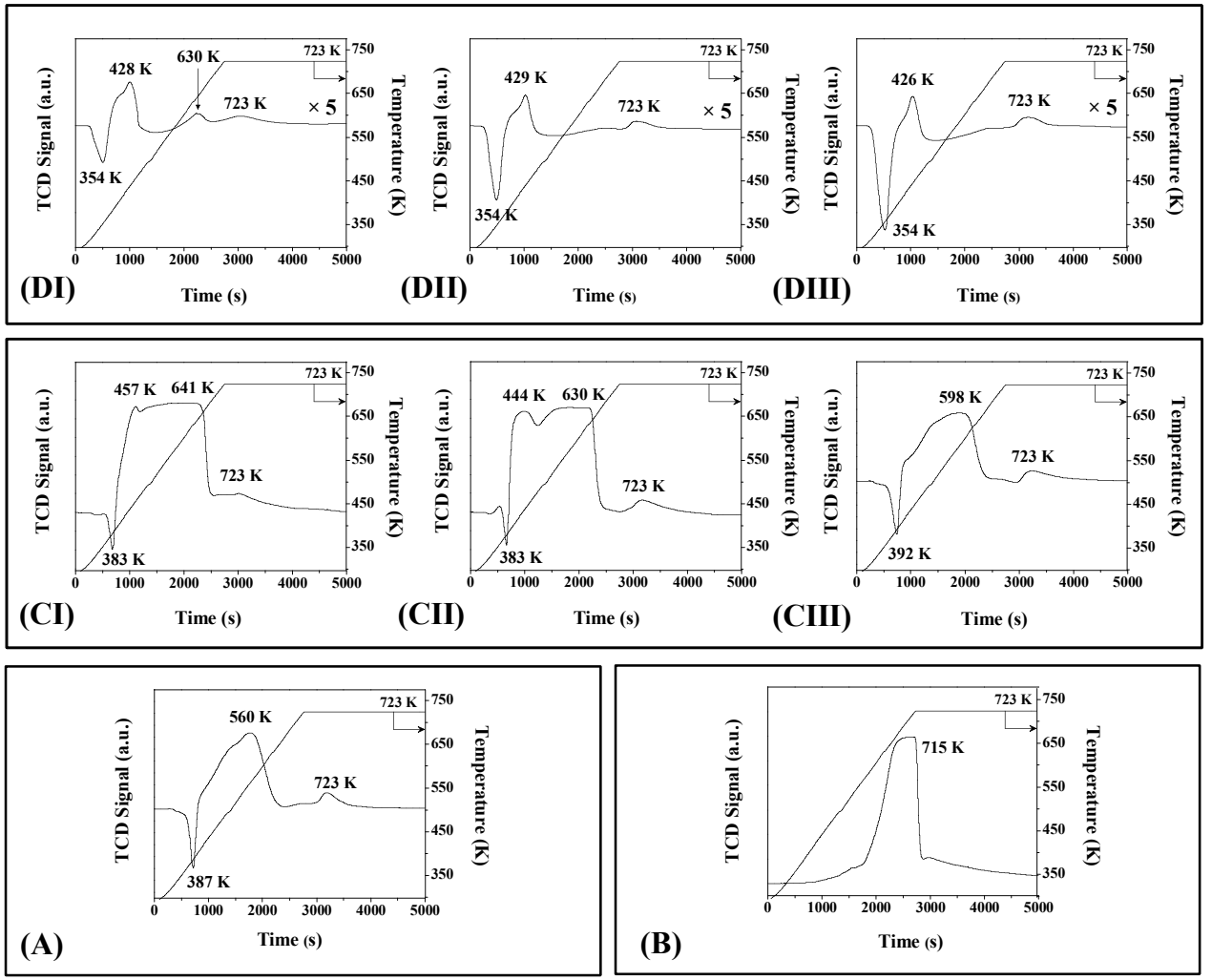

Figure 2.2: TPR profiles (to 723 K) generated for (A) Pd/Al_2O_3 and (B) Ni/Al_2O_3, (C) Pd/Al_2O_3+Ni/Al_2O_3 physical mixtures and (D) Pd-Ni//Al_2O_3 where Pd:Ni mole ratios = (I) 1:3, (II) 1:1 and (III) 3:1.

The TPR profile for Pd/Al_2O_3 is characterized by a negative peak at 387 K, which can be attributed to H_2 release due to the decomposition of β-phase Pd hydride [45-47]. It is well established that Pd can absorb H_2 at room temperature to form a hydride [40,48,49] where the H_2 partial pressure exceeds 0.013 atm [40]. The absence of a positive peak during TPR in advance of H_2 release presupposes the existence of a metallic phase prior to the commencement of the temperature ramp. Indeed, palladium nitrate decomposes readily to form PdO [50] and room temperature reduction of supported PdO to Pd has been reported elsewhere [51,52]. Shi and Jang [53] have demonstrated the reduction of alumina supported $Pd(NO_3)_2$ to Pd metal during H_2 plasma treatments at room temperature, a result that was confirmed by TPR measurements. Hydride formation involves the diffusion of hydrogen in the Pd crystallite structure to occupy the available octahedral "holes" in the metal lattice, where hydrogen solubility (H_{ab}/Pd ratio) is affected by electronic and structural factors [54,55]. The ratio of the number of Pd atoms in the bulk crystal relative to the number of surface Pd atoms decreases with decreasing particle size to reach a limiting case (< 2.5 nm) where H_{ab}/Pd approaches zero [48,55]. An upper H_{ab}/Pd value of 0.7 has been established for bulk Pd [56,57]. Based on the TPR response, our recorded H_{ab}/Pd (= 0.20) is consistent with values quoted in the literature for related supported Pd systems [58,59]. In addition to H_2 release/hydride decomposition, the Pd reduction profile also exhibited a broad positive peak with an associated T_{max} at *ca.* 560 K and a lesser H_2 consumption during the isothermal hold (at 723 K), suggesting support interaction(s) that serve(s) to stabilize the Pd precursor, necessitating higher reduction temperatures. This is consistent with previous reports wherein H_2 consumption at elevated temperatures (573–723 K) was recorded for the TPR of Pd/Al_2O_3 [60-62]. The reduction of Ni/Al_2O_3 generated a broad positive reduction peak with T_{max} at 715 K that we associate with the reduction of the precursor to metallic nickel. Indeed, the reduction of supported nickel nitrate to Ni^0 post TPR at $T \leq 723$ K has been reported for carbon [60,63] and oxide [60,64] supported systems.

The XRD patterns for the passivated/reduced mono-metallic samples are given in **Figure 2.3** and confirm the presence of Pd^0 and Ni^0 post-TPR. The three peaks that characterize Pd/Al_2O_3 (profile V) at 40.1°, 46.7° and 68.1° correspond, respectively, to (111), (200) and (220) Pd planes and are consistent with an exclusive cubic symmetry. The reflection (at 44.5°) recorded for Ni/Al_2O_3 (profile VI) corresponds to the (111) plane of metallic nickel, also consistent with cubic symmetry.

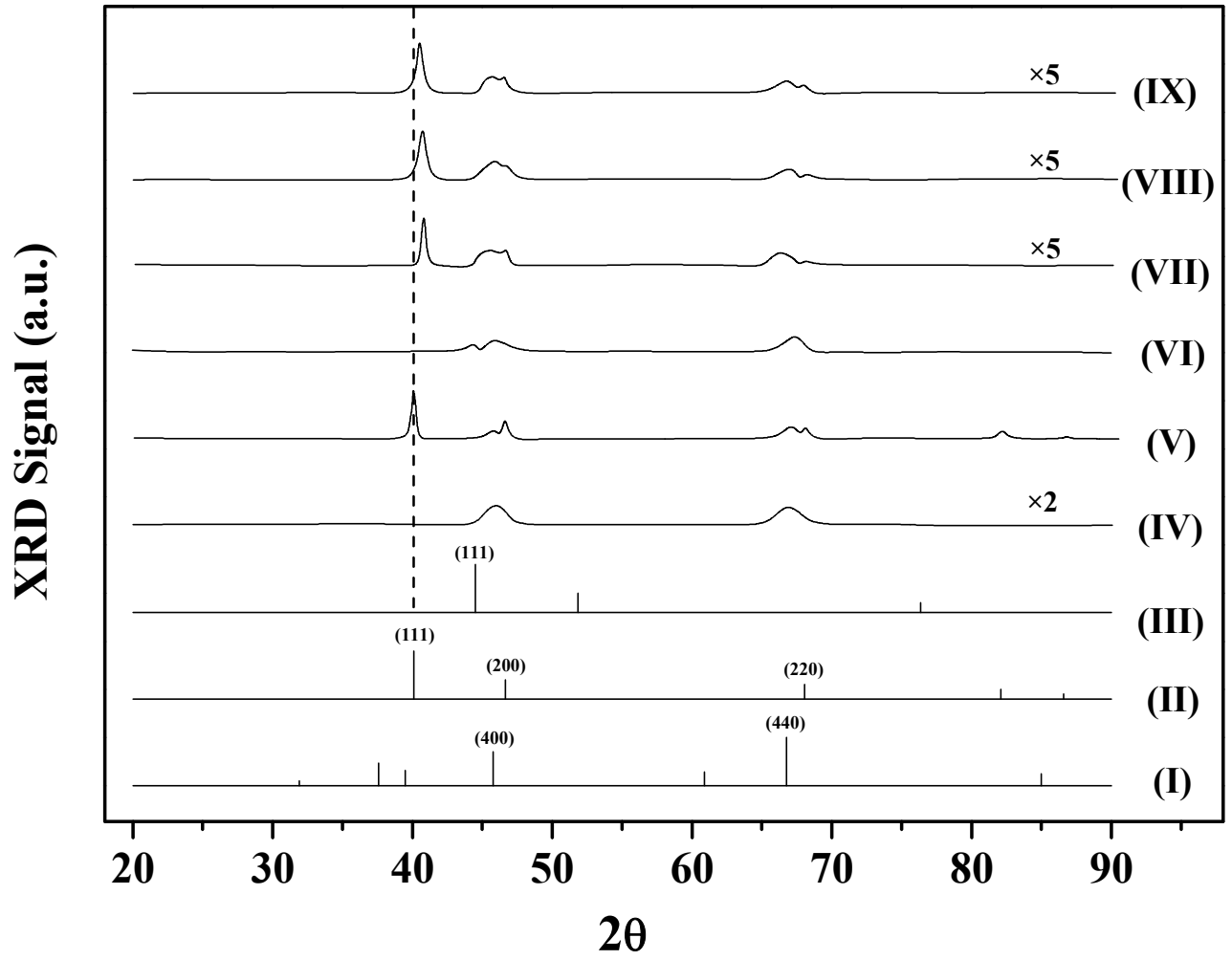

Figure 2.3: XRD patterns associated with JCPDS-ICDD references ((I) γ-Al_2O_3 (10-0425), (II) Pd (05-0681) and (III) Ni (04-0850)), (IV) Al_2O_3 support and passivated/reduced (V) Pd/Al_2O_3, (VI) Ni/Al_2O_3, (VII) Pd-Ni/Al_2O_3(1:3), (VIII) Pd-Ni/Al_2O_3(1:1) and (IX) Pd-Ni/Al_2O_3(3:1). *Note*: dashed line serves to illustrate the position of the main reflection (at 40.1°) corresponding to the (111) plane of metallic Pd.

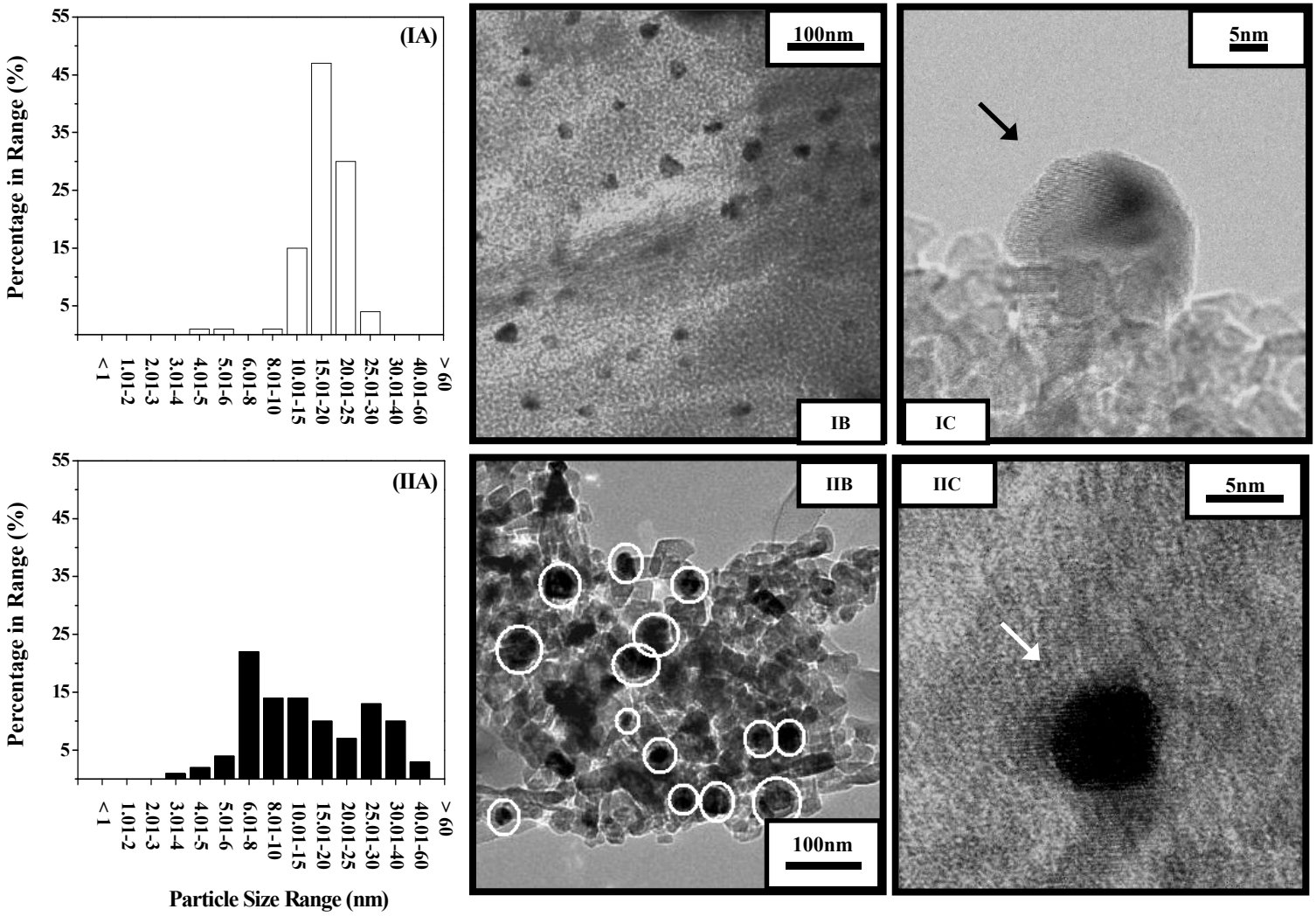

Figure 2.4: Metal particle size distribution (A) and representative TEM images of passivated/reduced (I) Pd/Al_2O_3 and (II) Ni/Al_2O_3; Ni particles are encircled in the lower magnification image (IIB); arrows indicate isolated (IC) Pd and (IIC) Ni particles in the higher magnification images.

In addition, the x-ray patterns for both mono-metallic systems present two broad signals in the 2θ range 40º-70º, corresponding to the (400) and (440) planes characteristics of cubic γ-Al_2O_3 (see profile IV for the starting support). The markers included in **Figure 2.3** illustrate the position of the XRD peaks for cubic γ-Al_2O_3, Pd and Ni (profiles I, II and III, respectively), taken from the JCPDS-ICDD reference standards (card number 10-0425, 05-0681 and 04-0850, respectively).

The H_2 chemisorption values (post-TPR) are given in **Table 2.2**, where the specific H_2 uptake on Pd/Al_2O_3 was significantly higher (by a factor of 4) than that recorded for Ni/Al_2O_3. Hydrogen chemisorption is related to metal particle size and the representative TEM images presented in **Figure 2.4** serve to illustrate the nature of particle morphology and dispersion associated with Pd/Al_2O_3 (I) and Ni/Al_2O_3 (II); EDX analysis also confirmed the presence of metallic Pd and Ni. The Pd and Ni particles exhibit a pseudo-spherical morphology where Pd/Al_2O_3 presented a narrower size distribution (see histogram IA) when compared with Ni/Al_2O_3. The broader distribution of Ni particle diameters (see histogram IIA) is in agreement with reports in the literature [65,66] dealing with oxide supported Ni prepared by impregnation. The surface area-weighted mean particle sizes (from TEM analysis) for Pd/Al_2O_3 (20 nm) and Ni/Al_2O_3 (30 nm) are consistent with the lower hydrogen chemisorption values measured for Ni/Al_2O_3. It should, however, be noted that limited H_2 chemisorption on Ni/Al_2O_3 has been reported previously [67,68] and linked to the presence of strong Ni/support interactions that inhibit H_2 uptake but the same effect does not seem to prevail in the case of Pd/Al_2O_3 [58,69].

2.3.1.2 Catalyst Activity/Selectivity

The hydrotreatment of *p*-CNB over both mono-metallic catalysts only generated products resulting from -NO_2 group reduction (*p*-CAN) and/or HDC (NB and AN). This response alone is significant in that the formation of toxic azo- [70] and/or azoxy-derivates [14,31,32] over nickel borides [14] and carbon supported Pd [31,32,70] has been reported for liquid phase operation. Representative time-on-stream conversion profiles are shown in **Figure 2.5**(A) where a temporal decline in activity is in evidence for both systems. Deactivation during the hydrogenation of nitroarenes has been linked to coke deposition and/or a poisoning effect of water vapour (as by-product).

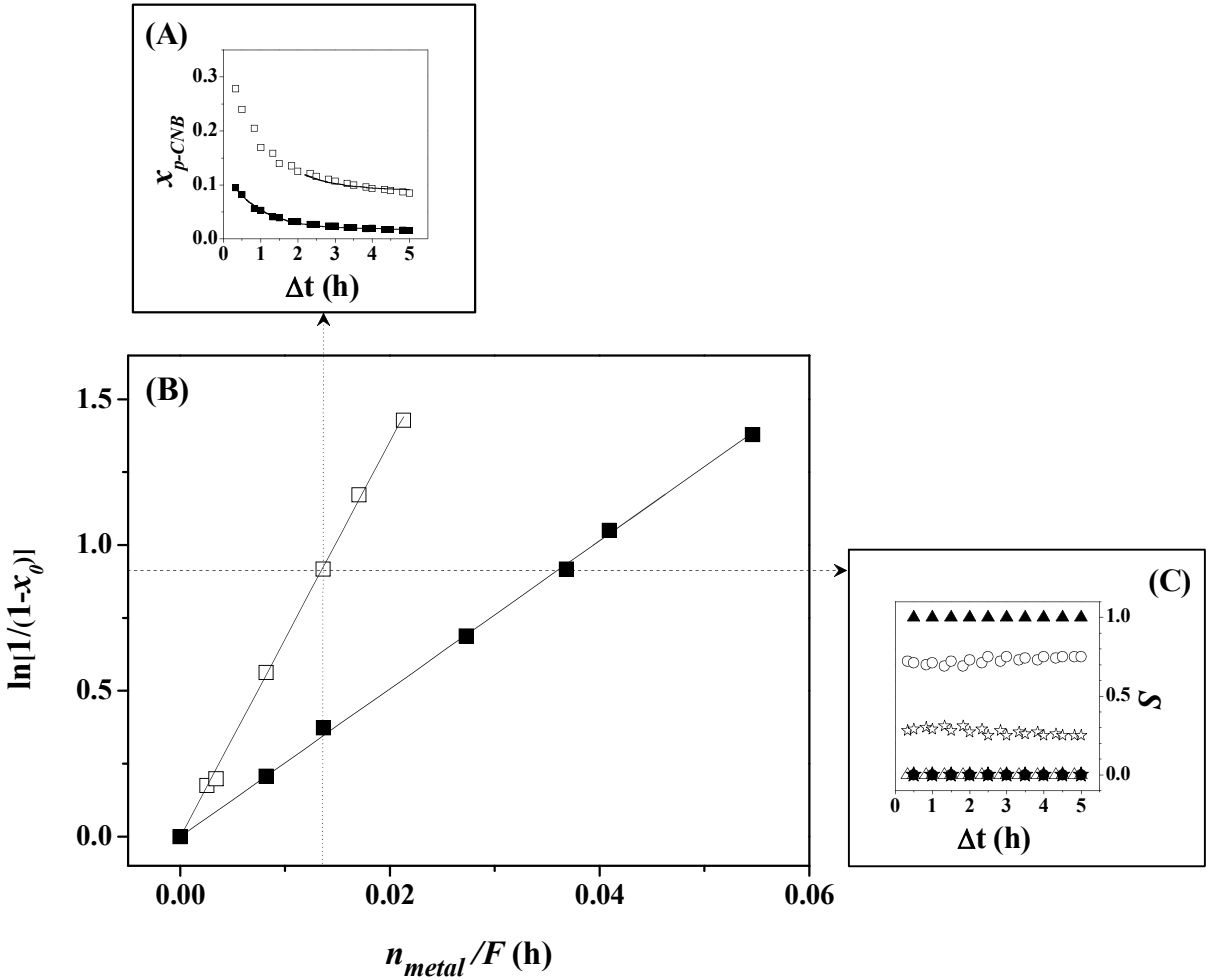

Figure 2.5: Catalytic response exhibited by Pd/Al_2O_3 (open symbols) and Ni/Al_2O_3 (solid symbols) in terms of (A) temporal variation of *p*-CNB fractional conversion ($x_{p\text{-}CNB}$), (B) pseudo-first-order kinetic plots and (C) temporal variation of selectivity with respect to *p*-CAN (▲,Δ), NB (★,☆) and AN (●,○) at the same initial conversion (x_0 = 0.6): T = 393 K.

Vishwanathan *et al.* [39] studied the gas phase hydrogenation of *o*-CNB over Pd/Al_2O_3 and reported a loss of activity, which they ascribed to coking. Sangeetha *et al.* [71,72] investigated the hydrogenation of NB in gas phase operation over hydrotalcite-supported Pd and associated catalyst deactivation to the formation of H_2O by-product but the authors did not elaborate further. The time on-stream loss of activity can also be the result of metal poisoning by chlorine [73,74], which has been suggested to (a) increase surface acidity favouring coke formation and (b) promote metal leaching and/or agglomeration.

An initial activity (x_0) was obtained from the fit of the temporal data to [75,76]

$$\frac{(x_{p\text{-}CNB} - x_0)}{(x_{5h} - x_0)} = \frac{\Delta t}{(\beta + \Delta t)} \qquad \textbf{(2.4)}$$

where x_{5h} represents fractional conversion after 5 h on-stream and β is a time scale fitting parameter. A pseudo-first order kinetic treatment where hydrogen was maintained far in excess has been applied in related systems [60,77]

$$\ln(1 - x_0)^{-1} = k\left(\frac{n_{metal}}{F}\right) \qquad \textbf{(2.5)}$$

where the ratio n_{metal}/F has the physical significance of contact time. The linear relationships between $\ln(1\text{-}x_0)^{-1}$ and n_{metal}/F (see **Figure 2.5**(B)) confirm the applicability of this approach and the extracted pseudo-first order rate constants are presented in **Table 2.3**. The Pd catalyst delivered a higher overall *p*-CNB consumption rate when compared with Ni. This is consistent with the studies presented in **Table 2.1** for the (liquid phase) hydrogenation of *p*-CNB where higher hydrogenation rates over supported Pd [18] relative to Ni [14,16] have been reported. In contrast to fractional conversion, reaction selectivity for both catalysts was time invariant (see **Figure 2.5**(C)) where the product distribution generated by Pd/Al_2O_3 and Ni/Al_2O_3 was markedly different. At the same initial conversion, Ni/Al_2O_3 promoted the exclusive formation of *p*-CAN (Path A in **Figure 2.1**) whereas Pd generated NB and AN as products of HDC and hydrogenation (Path B in **Figure 2.1**).

Table 2.3: Pseudo-first order rate constants (k) and reaction products (with selectivities) obtained in the hydrogen treatment of *p*-chloronitrobenzene and hydrodechlorination of chlorobenzene over alumina supported mono- and bi-metallic Ni and/or Pd catalysts.

Catalyst	Hydrogenation of *p*-chloronitrobenzene		Hydrodechlorination of chlorobenzene
	k ($mol_{p\text{-}CNB}\ h^{-1}\ mol_{Pd}^{-1}$)	Product(s) (Selectivity %)[a]	k ($mol_{Cl}\ h^{-1}\ mol_{Pd}^{-1}$)
Pd/Al_2O_3	68	NB(62) AN(38)	21
Ni/Al_2O_3	[b]	*p*-CAN (100)	[c]
Pd/Al_2O_3+Ni/Al_2O_3(1:3)	66	NB(62) AN(38)	-
Pd/Al_2O_3+Ni/Al_2O_3(1:1)	61	NB(61) AN(39)	20
Pd/Al_2O_3+Ni/Al_2O_3(3:1)	61	NB(62) AN(38)	-
Pd-Ni/Al_2O_3(1:3)	68	*p*-CAN(100)	4
Pd-Ni/Al_2O_3(1:1)	140	*p*-CAN(100)	7
Pd-Ni/Al_2O_3(3:1)	83	*p*-CAN(100)	10

[a]inlet $n_{Pd}/F = 3\times10^{-3}\ mol_{Pd}\ h\ mol_{p-CNB}^{-1}$

[b]$k = 25\ mol_{p\text{-}CNB}\ h^{-1}\ mol_{Ni}^{-1}$

[c]inactive

There was no evidence of any dechlorination over Ni/Al_2O_3 whereas both products resulting from reaction over Pd/Al_2O_3 involved a HDC step. This response was probed further by considering the HDC of chlorobenzene (CB) over both catalysts, where benzene was the only reaction product detected; the results are included in **Table 2.3**. Under the same reaction conditions, Ni/Al_2O_3 was inactive whereas Pd/Al_2O_3 delivered a significant HDC rate. Such as a response finds agreement in the literature [78] where up to three orders of magnitude higher HDC rates have been quoted for supported Pd (relative to Ni) in liquid [79] and gas [80] phase operation. The lack of HDC activity observed for Ni/Al_2O_3 in the treatment of CB is consistent with the exclusive formation of *p*-CAN (from *p*-CNB), ***i.e.*** HDC is not favoured over Ni. In contrast, C-Cl scisson predominates for reactions over Pd/Al_2O_3.

2.3.2 Physical Mixtures: Pd/Al_2O_3+ Ni/Al_2O_3

2.3.2.1 Catalyst Characterization

The TPR profiles (CI-CIII in **Figure 2.2**) generated for the Pd/Al_2O_3+Ni/Al_2O_3(1:3), Pd/Al_2O_3+Ni/Al_2O_3(1:1) and Pd/Al_2O_3+Ni/Al_2O_3(3:1) physical mixtures exhibit a negative peak at T_{max} close to that observed in the single component Pd/Al_2O_3 TPR with an equivalent H_{ab}/Pd. This response is diagnostic of Pd and Ni segregation in the physical mixtures. At higher temperatures, the TPR profiles for the mixtures present a complex reduction behaviour that is quite distinct from that which should result from a simple combination of the profiles recorded for Pd/Al_2O_3 (profile A) and Ni/Al_2O_3 (profile B). We take this to be evidence for a facilitated reduction of the metal precursors in the physical mixtures with a shift in H_2 consumption to lower temperatures. Each mixture is characterised by a broad region of H_2 consumption during the temperature ramp where the associated T_{max} values decreased with increasing Pd content. This can be attributed to a contribution from reactive hydrogen dissociated on zero valent Pd, which spills over onto Ni/Al_2O_3. Hydrogen spillover, *i.e.* migration of atomic hydrogen formed *via* dissociative adsorption on metal sites, has been established in the case of Pd/Al_2O_3 [81]. The spillover phenomenon typically applies to transfer of hydrogen from a supported metal site to the carrier, but there is also evidence for the migration of dissociated hydrogen species from bulk [57] or supported [82,83] metals to a second (contiguous) phase that is in physical contact, *i.e.* across a solid-solid physical boundary. The hydrogen chemisorption values given in **Table 2.2** are consistent with a composite uptake due to

the individual Pd and Ni components in the mixture, again in keeping with the segregation of both metals.

2.3.2.2 Catalyst Activity/Selectivity

The catalytic response recorded for the Pd/Al_2O_3+Ni/Al_2O_3 physical mixtures was probed under reaction conditions where the Pd content in the catalyst bed was kept constant and the Pd:Ni mol ratio was varied (from 1:3 to 3:1) with the addition of different amounts of Ni/Al_2O_3. It must be noted that under these conditions, Ni/Al_2O_3 exhibited negligible activity in the hydrogenation of *p*-CNB, *i.e.* where $n_{Ni}/F < 0.008$ mol_{Ni} h $mol_{p\text{-}CNB}^{-1}$ (see **Figure 2.5**). The results given in **Table 2.3** demonstrate that, under these conditions, the specific activity (expressed as *p*-CNB consumption per mol of Pd) over the three Pd/Al_2O_3+Ni/Al_2O_3 combinations was similar and equivalent to that recorded for Pd/Al_2O_3. Moreover, in terms selectivity, the three physical mixtures promoted the formation of NB and AN (Path B in **Figure 2.1**) with a product distribution very close to that obtained over Pd/Al_2O_3. This response suggests that the incorporation of Ni/Al_2O_3 as a physical mixture with Pd/Al_2O_3 does not influence overall catalytic performance, which is controlled by the Pd component. This result extends to the HDC of CB where the specific rate recorded for Pd/Al_2O_3+Ni/Al_2O_3(1:1), selected as a representative physical mixture, was equivalent to that for Pd/Al_2O_3.

2.3.3 Bimetallic Catalysts: Pd-Ni/Al_2O_3

2.3.3.1 Catalyst Characterization

The TPR profiles (DI-DIII) generated for the three Pd-Ni/Al_2O_3 samples are presented in **Figure 2.2**. In comparison with the response of the equivalent physical combinations (profiles CI-CIII), the co-impregnated systems exhibit an increased displacement of the reduction peaks to lower temperatures. This response is diagnostic of a direct interaction between Ni and Pd that serves to modify reduction behaviour. Our results find agreement with published work [84] where it was noted that TPR profile of Pd-Ni/Al_2O_3 (prepared by stepwise impregnation) did not correspond to a combination of the TPR profiles of the mono-metallic samples. Comparing the TPR response of Pd-Ni/Al_2O_3 with the corresponding physical mixtures, differences in the intensity and position (by *ca.* 30 K) of the negative peak, due to Pd hydride decomposition, are observed. A displacement in the temperature of hydride decomposition in the case of Pd-Au/SiO_2 [54] and Pd-Re/Al_2O_3 [55,85] has been linked to the formation of

bimetallic clusters. Moreover, the Pd hydride composition (H_{ab}/Pd) in Pd-Ni/Al_2O_3 differed significantly from that recorded for Pd/Al_2O_3 (0.20) where H_{ab}/Pd decreased with decreasing Pd content, *i.e.* Pd-Ni/Al_2O_3(3:1) = 0.13 > Pd-Ni/Al_2O_3(1:1) = 0.11 > Pd-Ni/Al_2O_3(1:3) = 0.10. A decrease in H_{ab}/Pd has been associated with a reduction in the number of lattice "cavities" in the Pd phase (see section 2.3.1.1). Such an effect can be the result of (a) a reduction in the Pd crystallite size [58] or (b) formation of bimetallics by inclusion of Ni in the Pd lattice [86]. Barlag *et al.* [87] have established that H_2 solubility in Pd-Ni decreases when increasing Ni content, which can account for the lower H_{ab}/Pd that we record for our bimetallic systems. A positive signal at T_{max} = 427 ± 2 K is also observed in the TPR profiles for the three bimetallics. This response can be attributed to a combined reduction of Ni and Pd where the presence of both metals has significantly modified their respective reducibility resulting in a more facile activation. This effect finds some agreement in the work of Śrębowata *et al.* [88] who observed a decrease (by *ca.* 50 K) in the reduction temperature of Pd-Ni supported on carbon (relative to the mono-metallic systems), which was attributed to the action of dissociated hydrogen on zero valent Pd. Massard *et. al* [89] and Noronha *et al.* [84] have concluded that the incorporation of Pd with Ni on alumina facilitates Ni reduction with a shift in the requisite reduction temperature by *ca.* 30 K [89] and 260 K [84]. Feeley and Sachtler have likewise reported [90] a similar effect for the TPR of Ni and Pd-Ni supported on Y zeolites, where the bimetallic exhibits greater reducibility and a shift in the characteristic reduction peak by up to 120 K. Karthikeyan and co-workers [91] investigated HY zeolite supported Pd and Pd-Ni, noting a decrease in Pd reduction temperature with increasing Ni concentration that resulted in the formation of bimetallic Ni-Pd nano-particles (on the basis of TEM and XPS analysis).

The hydrogen chemisorption measurements given in **Table 2.2** demonstrate that the Pd rich bimetallics exhibited a substantial increase in H_2 uptake relative to Pd/Al_2O_3 or Ni/Al_2O_3. Moreover, the higher uptake compared with the corresponding physical mixtures is indicative of interaction between Pd and Ni. Malinowski and co-workers [85] also recorded an increase in H_2 uptake (and decrease in CO adsorption) with increased Pd content in Pd-Re/Al_2O_3 and attributed this to the formation of bimetallic Pd-Re clusters. Miyata *et al.* [92] have reported a significant increase in H_2 uptake on Pd-$Ni_{0.5}$/$Mg_{2.5}$(Al)O (relative to $Ni_{0.5}$/$Mg_{2.5}$(Al)O and Pd/Mg_3(Al)O), which they explained on the basis of a synergism between Pd and Ni that enhanced hydrogen uptake due to bimetal formation.

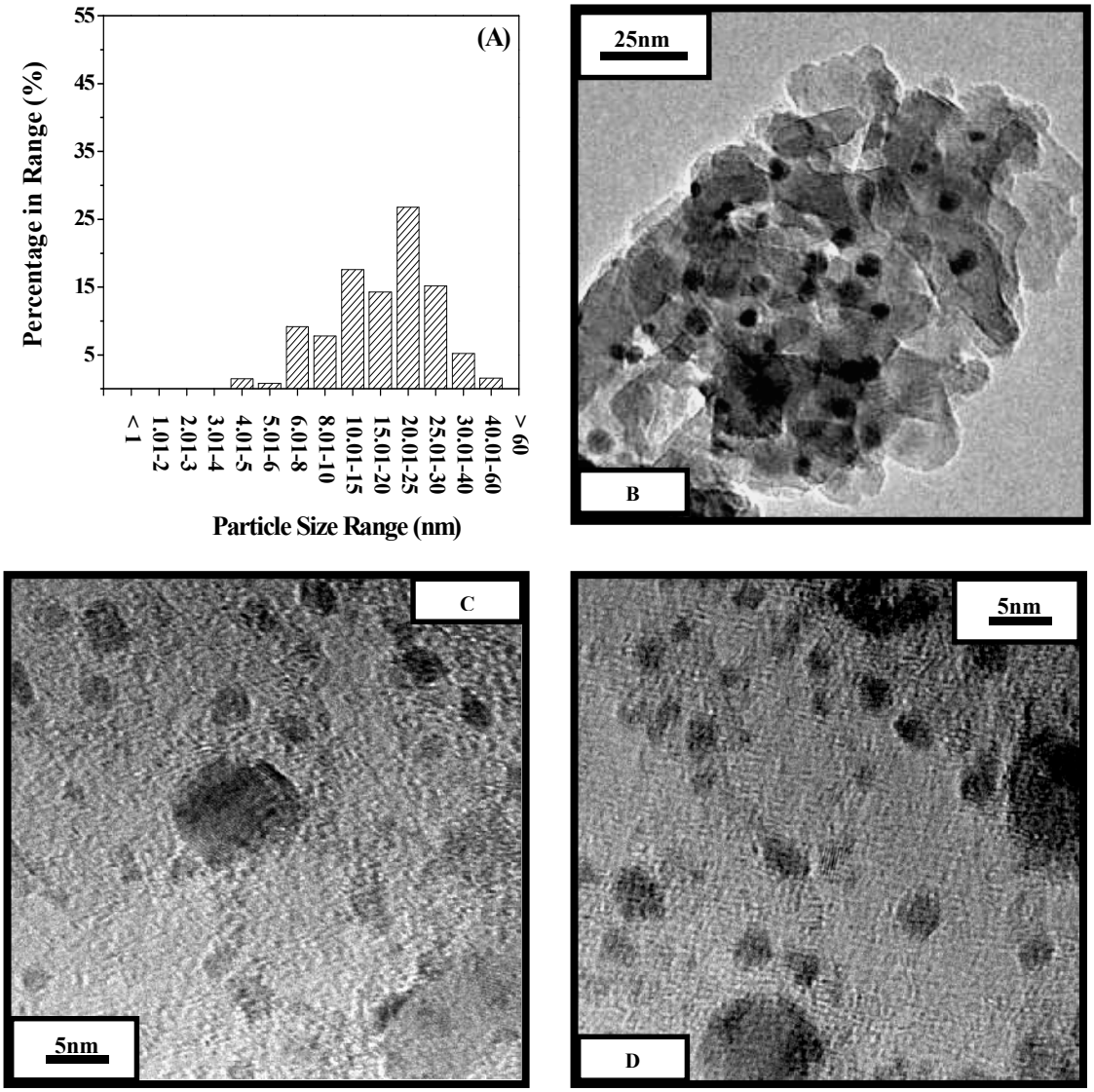

Figure 2.6: Metal particle size distribution (A) and representative (medium (B) and high magnification (C and D)) TEM images of passivated/reduced Pd-Ni/Al_2O_3(1:1).

Representative medium (B) and high (C and D) resolution TEM images of Pd-Ni/Al_2O_3(1:1) (selected as a representative bimetallic) are presented in **Figure 2.6** where it can be seen that the metal particles present a pseudo-spherical morphology. The catalyst is characterized by a size distribution (see histogram A) which overlaps that obtained with both mono-metallic catalysts and the surface area weighted mean metal particle diameter (27 nm) falls between the values obtained for Pd/Al_2O_3 (20 nm) and Ni/Al_2O_3 (30 nm). A comprehensive TEM-EDX analysis of the bimetallics revealed (for sample areas $\geq$ 315 nm^2) a non-uniform distribution of the Pd and Ni on the surface; the range of surface Pd/Ni atomic ratios are given in **Table 2.2**. The tabulated Pd/Ni ratios suggest a significant surface enrichment by Pd. In the EDX analysis performed on Pd-Ni/Al_2O_3(3:1), we could not find any area that was rich in Ni, *i.e.* Pd/Ni atomic ratio

≥ 1. Moreover, in the case of Pd-Ni/Al_2O_3(1:1) and Pd-Ni/Al_2O_3(1:3), surface Pd predominated. These findings are in line with the work of Miegge *et al.* [93] who have reported a segregation of Pd on the surface of bimetallic (Ni rich) Pd_1Ni_{99} and Pd_5Ni_{95}. Furthermore, Renouprez *et al.* [94] in their XPS analysis of Pd-Ni/SiO_2 observed that the surface Pd content exceeded the bulk value. The XRD patterns generated for the bimetallic catalysts (profiles VII-IX in **Figure 2.3**) exhibit peaks at 40.1°, 46.7°, 68.1° that correspond to metallic Pd (see JCPDS-ICDD reference standard of Pd in profile II). There is a detectable displacement of the (111) main plane (at 40.1°) of metallic Pd (see dashed line), which has been associated in the literature [95] with the formation of a bimetallic Pd-Ni phase. Ramos-Sánchez *et al.* [96] have recently reported a shift in the Pd XRD signal to higher 2θ values, for unsupported PdNi and ascribed this to the presence of bimetallic Pd-Ni nano-particles. The combination of TPR (in terms of hydride composition), H_2 chemisorption and XRD analyses points to the formation of bimetallic nano-scale particles in Pd-Ni/Al_2O_3 where there is evidence (from TEM-EDX analysis) of surface Pd enrichment.

2.3.3.2 Catalyst Activity/Selectivity

The results presented in section 2.3.2.2. demonstrated that (at the same Pd content) there was no difference between the catalytic response delivered by Pd/Al_2O_3 and Pd/Al_2O_3+Ni/Al_2O_3. The characterization results for Pd-Ni/Al_2O_3 suggest the formation of bimetallic Ni-Pd particles, which should result in distinct catalytic behaviour. In order to asses this, the three bimetallic catalysts were tested under the same conditions (constant Pd content) as those employed for the physical mixtures. The results presented in **Table 2.3** show that the bimetallics (where Pd:Ni = 1:1 and 3:1) exhibited higher specific hydrogenation rates than any of the mono-metallics and/or physical combinations. The selectivity response is striking in that while NB and AN were the products generated over Pd/Al_2O_3+Ni/Al_2O_3, the three Pd-Ni/Al_2O_3 catalysts promoted the sole formation of *p*-CAN. The catalytic action of the supported bimetallic systems resulted in ultra-selectivity in terms of -NO_2 group reduction (the targeted Path A, **Figure 2.1**), which represents a dramatic switch from the composite HDC/hydrogenation (Path B, **Figure 2.1**) that characterised the physical mixtures. This is consistent with the catalytic HDC of CB (see **Table 2.3**), where a lower HDC activity was recorded over the three Pd-Ni/Al_2O_3 catalysts relative to Pd/Al_2O_3; HDC inhibition was a feature of increasing Ni content. We associate this catalytic response with the bimetallic character of the active sites in Pd-Ni/Al_2O_3. Indeed, it has been observed that

mono- and bi-metallic clusters can exhibit quite distinct catalytic activities [88,97-99] and/or selectivities [23,26,88] in hydrogenation reactions. This response has been found to extend to the hydrogenation of nitroarenes in liquid phase operation over unsupported Pd-Ni ([34], see **Table 2.1**) and other Ni- [10,25,100] and/or Pd-containing bimetallics [24] and ascribed to electron transfer [10,25], re-dispersion [25,100] and/or synergistic [24] effects resulting from the incorporation of the second metal. We have provided, in this report, the first evidence of distinct bimetallic catalytic behaviour in the gas phase hydrogenation of a nitro-haloarene.

It can be seen from **Table 2.3** that Pd-Ni/Al_2O_3(1:1) represents the superior formulation in terms of achieving the highest *p*-CAN yield. This result finds support in published literature [34] where hydrogenation rate in the batch treatment of nitroarenes over Pd-Ni nano-colloids was found to be dependent on bimetallic composition with an optimum achieved at Pd:Ni = 1:1 and ascribed to an ensemble (or geometric) effect. Our initial findings can form the basis for the design of effective catalysts for selective hydrogenation directed at the sustainable production of commercially important amines. Future work will focus on alternative bimetallic preparations (*e.g.* consecutive impregnation and co-precipitation/deposition) and application in related hydrogenation processes with the goal of optimising catalyst structure in order to increase activity while retaining the reaction exclusivity reported in this study.

2.4 Conclusions

The hydrogenation of *p*-CNB in continuous gas phase operation over alumina supported mono- (Pd and Ni) and bi-metallic (co-impregnated Pd-Ni/Al_2O_3 and physical mixtures of Pd/Al_2O_3+Ni/Al_2O_3) catalysts has been investigated for the first time. Pd/Al_2O_3 and Pd/Al_2O_3+Ni/Al_2O_3 delivered equivalent hydrogenation rates and promoted a composite HDC/hydrogenation with the formation of NB and AN. In contrast, reaction over Ni/Al_2O_3 generated *p*-CAN as the sole product, *i.e.* 100% selective hydrogenation, but at a significantly lower *p*-CNB consumption rate. Pd-Ni/Al_2O_3 resulted in the exclusive formation of *p*-CAN (at a significantly higher rate than Ni/Al_2O_3) where the highest *p*-CAN yield was obtained at Pd:Ni = 1:1. These results are consistent with a decreasing level of HDC activity as established for the conversion of CB, *i.e* Pd/Al_2O_3 ≈ Pd/Al_2O_3+Ni/Al_2O_3 > Pd-Ni/Al_2O_3. We ascribe the distinct catalytic response exhibited by Pd-Ni/Al_2O_3 to Pd/Ni interactions with evidence

for bimetallic particle formation on the basis of TPR, H_2 chemisorption and XRD analyses. Our findings demonstrate the feasibility of bimetallic (Pd-Ni) catalyst application in the sustainable clean production of aromatic amines in continuous gas phase operation.

2.5 References

[2.1] P. F. Vogt, J. J. Gerulis, Ullmann's Encyclopedia of Industrial Chemistry. "Aromatic Amines", Wiley-VCH Verlag GmbH & Co. KGaA, Weinheim, 2005.

[2.2] R. A. Sheldon, H. van Bekkum, Fine Chemicals through Heterogeneous Catalysis."Aromatic Nitro Compounds", Wiley-VCH, Weinheim (Germany), 2001.

[2.3] F. Zhao, R. Zhang, M. Chatterjee, Y. Ikushima, M. Araib, Adv. Synth. Catal., 346, 661 (2004)

[2.4] C.-H. Li, Z.-X. Yu, K.-F. Yao, S.-F. Jib, J. Liang, J. Mol. Catal. A: Chem., 226, 101 (2005)

[2.5] L. Zhao, J. Chen, J. Zhang, J. Mol. Catal. A: Chem., 246, 140 (2006)

[2.6] S. Diao, W. Qian, G. Luo, F. Wei, Y. Wang, Appl. Catal. A: Gen., 286, 30 (2005)

[2.7] X.-X. Han, R.-X. Zhou, G.-H. Lai, X.-M. Zheng, Catal. Today, 93-95, 433 (2004)

[2.8] B. Coq, A. Tijani, R. Dutartre, F. Figuéras, J. Mol. Catal., 79, 253 (1993)

[2.9] M. M. Telkar, J. M. Nadgeri, C. V. Rode, R. V. Chaudhari, Appl. Catal. A: Gen., 295, 23 (2005)

[2.10] S. K. Ghosh, M. Mandal, S. Kundu, S. Nath, T. Pal, Appl. Catal. A: Gen., 268, 61 (2004)

[2.11] T. Komatsu, T. Hirose, Appl. Catal. A: Gen., 276, 95 (2004)

[2.12] F. Cárdenas-Lizana, S. Gómez-Quero, M. A. Keane, Catal. Commun., 9, 475 (2008)

[2.13] C. Xi, H. Cheng, J. Hao, S. Cai, F. Zhao, J. Mol. Catal. A: Chem., 282, 80 (2008)

[2.14] Y.-Z. Chen, Y.-C. Chen, Appl. Catal. A: Gen., 115, 45 (1994)

[2.15] Y.-C. Liu, C.-Y. Huang, Y.-W. Chen, Ind. Eng. Chem. Res., 45, 62 (2006)

[2.16] Y.-C. Liu, Y.-W. Chen, Ind. Eng. Chem. Res., 45, 2973 (2006)

[2.17] Z. Yu, S. Liao, Y. Xu, B. Yang, D. Yu, J. Mol. Catal. A: Chem., 120, 247 (1997)

[2.18] V. Kratky, M. Kralik, M. Mecarova, M. Stolcova, L. Zalibera, M. Hronec, Appl. Catal. A: Gen., 235, 225 (2002)

[2.19] B. Coq, A. Tijani, F. Figuéras, J. Mol. Catal., 68, 331 (1991)

[2.20] V. L. Khilnani, S. B. Chandalia, Org. Proc. Res. Dev., 5, 257 (2001)

[2.21] X. D. Wang, M. H. Liang, J. L. Zhang, Y. Wang, Curr. Org. Chem., 11, 299 (2007)

[2.22] J. Xiong, J. X. Chen, J. Y. Zhang, Catal. Commun., 8, 345 (2007)

[2.23] X.-X. Han, R.-X. Zhou, X.-M. Zheng, H. Jiang, J. Mol. Catal. A: Chem., 193, 103 (2003)

[2.24] M. Liu, W. Yu, H. Liu, J. Zheng, J. Colloid Interface Sci., 214, 231 (1999)

[2.25] X. Yan, J. Sun, Y. Wang, J. Yang, J. Mol. Catal. A: Chem., 252, 17 (2006)

[2.26] X.-X. Han, R.-X. Zhou, G.-H. Lai, B.-H. Yue, X.-M. Zheng, J. Mol. Catal. A: Chem., 209, 83 (2004)

[2.27] O. S. Alexeev, B. C. Gates, Ind. Eng. Chem. Res., 42, 1571 (2003)

[2.28] N. P. Sokolova, A. A. Balandin, N. P. Maksimova, Z. M. Skul'skaya, Russ. Chem. Bull., 15, 1824 (1966)

[2.29] V. I. Savchenko, T. V. Denisenko, S. Y. Sklyar, V. D. Simonov, Russ. J. Inorg. Chem., 11, 2149 (1975)

[2.30] O. P. Savvateev, M. V. Klyuev, J. Appl. Chem. USSR, 63, 1485 (1990)

[2.31] I. A. Ilchenko, A. V. Bulatov, I. E. Uflyand, V. N. Sheinker, Kinet. Catal., 32, 691 (1991)

[2.32] I. E. Uflyand, I. A. Ilchenko, V. N. Sheinker, A. V. Bulatov, Transition Met. Chem., 16, 293 (1991)

[2.33] M. L. Kantam, T. Bandyopadhyay, A. Rahman, N. M. Reddy, B. M. Choudary, J. Mol. Catal. A: Chem., 133, 293 (1998)

[2.34] P. Lu, N. Toshima, Bull. Chem. Soc. Jpn., 73, 751 (2000)

[2.35] Z. Yu, S. Liao, Y. Xu, B. Yang, D. Yu, J. Chem. Soc., Chem. Commun., 11, 1155 (1995)

[2.36] Q. Xu, X.-M. Liu, J.-R. Chen, R.-X. Li, X.-J. Li, J. Mol. Catal. A: Chem., 260, 299 (2006)

[2.37] Y. Gao, F. Wang, S. Liao, D. Yu, React. Kinet. Catal. Lett., 64, 351 (1998)

[2.38] X. Yang, H. Liu, H. Zhong, J. Mol. Catal. A: Chem., 147, 55 (1999)

[2.39] V. Vishwanathan, V. Jayasri, P. M. Basha, N. Mahata, L. M. Sikhwivhilu, N. J. Coville, Catal. Commun., 9, 453 (2008)

[2.40] J. E. Benson, H. S. Hwang, M. Boudart, J. Catal., 30, 146 (1973)

[2.41] G. Tavoularis, M. A. Keane, J. Chem. Technol. Biotechnol., 74, 60 (1999)

[2.42] M. A. Keane, D. Y. Murzin, Chem. Eng. Sci., 56, 3185 (2001)

[2.43] G. Tavoularis, M. A. Keane, J. Mol. Catal. A: Chem., 142, 187 (1999)

[2.44] G. Tavoularis, M. A. Keane, Appl. Catal. A: Gen., 182, 309 (1999)

[2.45] N. Lingaiah, P. S. Sai Prasad, P. Kanta Rao, F. J. Berry, L. E. Smart, Catal. Commun., 3, 391 (2002)

[2.46] M. Bonarowska, J. Pielaszek, V. A. Semikolenov, Z. Karpiński, J. Catal., 209, 528 (2002)

[2.47] L. M. Gómez-Sainero, X. L. Seoane, J. L. G. Fierro, A. Arcoya, J. Catal., 209, 279 (2002)

[2.48] N. K. Nag, J. Phys. Chem. B, 105, 5945 (2001)

[2.49] G. Neri, M. G. Musolino, C. Milone, D. Pietropaolo, S. Galvagno, Appl. Catal. A: Gen., 208, 307 (2001)

[2.50] R. Gopinath, N. S. Babu, J. V. Kumar, N. Lingaiah, P. S. S. Prasad, Catal. Lett., 120, 312 (2008)

[2.51] G. M. Tonetto, D. E. Damiani, J. Mol. Catal. A: Chem., 202, 289 (2003)

[2.52] C.-B. Wang, H.-K. Lin, C.-M. Ho, J. Mol. Catal. A: Chem., 180, 285 (2002)

[2.53] C. Shi, B. W.-L. Jang, Ind. Eng. Chem. Res., 45, 5879 (2006)

[2.54] M. Bonarowska, J. Pielaszek, W. Juszczyk, Z. Karpiński, J. Catal., 195, 304 (2000)

[2.55] S. B. Ziemecki, J. B. Michel, G. A. Jones, React. Sol., 2, 187 (1986)

[2.56] E. J. A. X. van de Sandt, A. Wiersma, M. Makkee, H. van Bekkum, J. A. Moulijn, Appl. Catal. A: Gen., 155, 59 (1997)

[2.57] C. Amorim, M. A. Keane, J. Colloid Interface Sci., 322, 196 (2008)

[2.58] S. Gómez-Quero, F. Cárdenas-Lizana, M. A. Keane, Ind. Eng. Chem. Res., 47, 6841 (2008)

[2.59] S. Jujjuri, E. Ding, S. G. Shore, M. A. Keane, J. Mol. Catal. A: Chem., 272, 96 (2007)

[2.60] F. Cárdenas-Lizana, S. Gómez-Quero, M. A. Keane, Appl. Catal. A: Gen., 334, 199 (2008)

[2.61] V. Ferrer, A. Moronta, J. Sánchez, R. Solano, S. Bernal, D. Finol, Catal. Today, 107-108, 487 (2005)

[2.62] N. S. Babu, N. Lingaiah, R. Gopinath, P. S. S. Reddy, P. S. S. Prasad, J. Phys. Chem. C, 111, 6447 (2007)

[2.63] N. Lingaiah, Md. A. Uddin, A. Muto, T. Iwamoto, Y. Sakata, Y. Kusano, J. Mol. Catal. A: Chem., 161, 157 (2000)

[2.64] T. Shido, M. Lok, R. Prins, Top. Catal., 8, 223 (1999)

[2.65] M. A. Keane, Can. J. Chem., 72, 372 (1994)

[2.66] P. Burattin, M. Che, C. Louis, J. Phys. Chem. B 101, 7060 (1997)

[2.67] G. L. Xu, K. Y. Shi, Y. Gao, H. Y. Xu, Y. D. Wei, J. Mol. Catal. A: Chem., 147, 47 (1999)

[2.68] C. Hoang-Van, Y. Kachaya, S. J. Teichner, Y. Arnaud, J. A. Dalmon, Appl. Catal., 46, 281 (1989)

[2.69] G. Yuan, M. A. Keane, Chem. Eng. Sci., 58, 257 (2003)

[2.70] G. Zhang, L. Wang, K. Shen, D. Zhao, H. S. Freeman, Chem. Eng. J., 141, 368 (2008)

[2.71] P. Sangeetha, P. Seetharamulu, K. Shanthi, S. Narayanan, K.S. Rama Raob, J. Mol. Catal. A: Chem., 273, 244 (2007)

[2.72] P. Sangeetha, K. Shanthi, K. S. R. Rao, B. Viswanathan, P. Selvam, Appl. Catal. A: Gen., 353, 160 (2009)

[2.73] S. Ordóñez, E. Díaz, F. V. Díez, H. Sastre, React. Kinet. Catal. Lett., 90, 101 (2007)

[2.74] E. López, S. Ordóñez, F. V. Díez, Appl. Catal. B: Environ., 62, 57 (2006)

[2.75] F. Cárdenas-Lizana, S. Gómez-Quero, M. A. Keane, ChemSusChem, 1, 215 (2008)

[2.76] F. Cárdenas-Lizana, S. Gómez-Quero, A. Hugon, L. Delannoy, C. Louis, M. A. Keane, J. Catal., 262, 235 (2009)

[2.77] F. Cárdenas-Lizana, S. Gómez-Quero, N. Perret, M. A. Keane, Gold Bulletin, in press (2009)

[2.78] B. Aristazábal, C. A. González, I. Barrio, M. Montes, C. M. de Correa, J. Mol. Catal. A: Chem., 222, 189 (2004)

[2.79] L. M. Gómez-Sainero, A. Cortés, X. L. Seoane, A. Arcoya, Ind. Eng. Chem. Res., 39, 2849 (2000)

[2.80] M. A. Keane, Appl. Catal. A: Gen., 271, 109 (2004)

[2.81] G. Yuan, M. A. Keane, Catal. Today, 88, 27 (2003)

[2.82] F. Benseradj, F. Sadi, M. Chater, Appl. Catal. A: Gen., 228, 135 (2002)

[2.83] M. A. Keane, G. Tavoularis, React. Kinet. Catal. Lett., 78, 11 (2003)

[2.84] F. B. Noronha, M. C. Durão, M. S. Batista, L. G. Appel, Catal. Today, 85, 13 (2003)

[2.85] A. Malinowski, W. Juszczyk, M. Bonarowska, J. Pielaszek, Z. Karpiński, J. Catal., 177, 153 (1998)

[2.86] T. B. Flanagan, D. Wang, H. Noh, J. Alloys Compd., 253-254, 216 (1997)

[2.87] H. Barlag, L. Opara, H. Züchner, J. Alloys Compd., 330, 434 (2002)

[2.88] A. Śrębowata, W. Juszczyk, Z. Kaszkur, Z. Karpiński, Catal. Today, 124, 28 (2007)

[2.89] R. Massard, D. Uzio, C. Thomazeau, C. Pichon, J. L. Rousset, J. C. Bertolini, J. Catal., 245, 133 (2007)

[2.90] J. S. Feeley, W. M. H. Sachtler, Catal. Lett., 9, 377 (1991)

[2.91] D. Karthikeyan, N. Lingappan, B. Sivasankar, N. J. Jabarathinam, Ind. Eng. Chem. Res., 47, 6538 (2008)

[2.92] T. Miyata, D. Li, M. Shiraga, T. Shishido, Y. Oumi, T. Sano, K. Takehira, Appl. Catal. A: Gen., 310, 97 (2006)

[2.93] P. Miegge, J. L. Rousset, B. Tardy, J. Massardier, J. C. Bertolini, J. Catal., 149, 404 (1994)

[2.94] A. Renouprez, J. F. Faudon, J. Massardier, J. L. Rousset, P. Delichère, G. Bergeret, J. Catal., 170, 181 (1997)

[2.95] K.-W. Wang, S.-R. Chung, C.-W. Liu, J. Phys. Chem. C, 112, 10242 (2008)

[2.96] G. Ramos-Sánchez, H. Yee-Madeira, O. Solorza-Feria, Int. J. Hydrogen Energy, 33, 3596 (2008)

[2.97] V. I. Pârvulescu, V. Pârvulescu, U. Endruschat, G. Filoti, F. E. Wagner, C. Kübel, R. Richards, Chem. Eur. J., 12, 2343 (2006)

[2.98] B. Pawelec, A. M. Venezia, V. La Parola, S. Thomas, J. L. G. Fierro, Appl. Catal. A: Gen., 283, 165 (2005)

[2.99] G. Yuan, C. Louis, L. Delannoy, M. A. Keane, J. Catal. , 247, 256 (2007)

[2.100] X. Yang, H. Liu, Appl. Catal. A: Gen., 164, 197 (1997)

Chapter 3

Ultra-selective Gas Phase Catalytic Hydrogenation of Aromatic Nitro Compounds over Au/Al_2O_3

Catalyst deactivation was observed for the reduction of *p*-chloronitrobenzene over supported Ni, Pd and Ni-Pd systems, where a predominant C-Cl scission was promoted for reaction over Pd/Al_2O_3. The alternative use of Au/Al_2O_3 and the possible effect of Au to modify supported Pd is considered in this Chapter for the hydrogenation of a series of substituted nitroarenes.

3.1 Introduction

The multiple applications of amino derivates in the manufacture of pesticides, herbicides, pigments, pharmaceuticals and cosmetics has led to increased commercial importance for the selective hydrogenation of aromatic nitro-compounds [1]. Conventional synthesis *via* Fe promoted reduction in HCl (the Béchamp process) produces a sludge containing the target product and toxic by-products, which require costly and difficult downstream separation/waste treatment steps where low overall product yields have limited the viability of this production route [2]. In an attempt to overcome these limitations, "green syntheses" based on noble metal catalysts are currently under investigation. The catalytic hydrotreatment of nitroarenes over standard metal (Pd or Pt) catalysts can deliver high conversion but 100 % selectivity to the corresponding amino compound has not been achieved. The inefficiency of these catalysts is particularly marked in the case of aromatic halonitro-compounds where hydrogenolytic C-X cleavage is also promoted [3]. A number of parameters have been shown [3,4] to influence selectivity in batch liquid systems, notably metal particle size and loading, support, solvent and the incorporation of a second metal. Gold catalysts have been successfully employed in H_2 mediated reactions, particularly the hydro-treatment of CO, CO_2, NO_x, alkenes, alkynes, alkadienes, α,β-unsaturated aldehydes and ketones [5,6]. Recent results for the discontinuous liquid phase reduction of nitroarenes over Au supported on SiO_2 [7], TiO_2 [8], Fe_2O_3 [8] and MCM supported Au-Pt [9] show promise.

A search through the open literature has failed to unearth any study using gold catalysts in the gas phase hydrogenation of nitroarenes. Gold delivers lower hydrogenation activity when compared to conventional transition metal, a response that has been attributed to less effective activation/dissociation of H_2 [10,11]. However, it has been shown [5] that supported Au exhibits enhanced selectivity in the hydrotreatment of polyfunctional reactants. Molecular hydrogen does not chemisorb on bulk Au [5,12] but weakly interacts at 78 K (desorbing at 125 K) on Au atoms of low coordination number [13]. The capacity of supported Au to dissociatively chemisob H_2 has been proposed to depend on Au particle size, morphology and support interactions [10,14,15], with a measurable uptake on Au < 10 nm [5,6]. Bokhoven *et al.* [16] attributed hydrogen uptake on Au/Al_2O_3 to dissociative adsorption at Au corner and edge positions. Touroude *et al.* [11] recorded higher crotonaldehyde hydrogenation rates over Au/TiO_2 for Au particles ~2 nm and proposed, as rate-determining, H_2 dissociation on Au edge and corner sites. Moreover, Claus and co-workers [10] reported increasing acrolein hydrogenation activity (by a factor of 2) with decreasing particle size (4-8 nm) over Au/ZrO_2 and concluded that reaction rate is enhanced over smaller particles with a preponderance of defect sites. Spillover hydrogen can also contribute to catalytic hydrogenation and Yates *et al.* [17] have recently reported H atom spillover from H_2 dissociation on TiO_2 supported Au (2-3 nm) at 295 K. The oxidation state of catalytically active gold is still unresolved in the literature [18] where zero valent [19] and cationic Au [20] have been proposed to promote hydrogenation. In the present work, we assess for the first time the catalytic action of Al_2O_3 supported Au, Pd and Au-Pd in the gas phase hydrogenation of a range of polyfunctional nitro-derivates.

3.2 Experimental

3.2.1 Catalyst Preparation and Activation

The Al_2O_3 support (Puralox) was obtained from Condea Vista Co. and used as received. The Au/Al_2O_3 (1 mol %) and Pd/Al_2O_3 (6.6 mol %) samples were prepared by standard wetness impregnation of Al_2O_3 with a $HAuCl_4$ solution (Aldrich, 0.0025 g cm^{-3}, pH = 2) and a 2-butanolic $Pd(NO_3)_2$ solution, respectively. The catalyst precursors were dried in a flow of He at 383 K for 3 h and sieved into a batch of 75 μm average particle diameter. $Au\text{-}Pd/Al_2O_3$ (10/1 Pd/Au mol ratio) was prepared by contacting pre-reduced and passivated in 1% v/v O_2/He Pd/Al_2O_3 with $HAuCl_4$. The Au/Al_2O_3 and $Au\text{-}Pd/Al_2O_3$ samples were stored (under He) in the dark at 277 K. The metal loadings were

determined (to within ± 2 %) by inductively coupled plasma-optical emission spectrometry (ICP-OES, Vista-PRO, Varian Inc.) from the diluted extract of aqua regia. A physical mixture of reduced/passivated Pd/Al_2O_3 + Au/Al_2O_3 (10/1 Pd/Au mol ratio) was also examined.

3.2.2 Catalyst Characterization

BET surface area, temperature programmed reduction (TPR) and H_2 chemisorption were determined using the commercial CHEM-BET 3000 (Quantachrome) unit. The samples were loaded into a U-shaped Pyrex glass cell (10 cm ×. 3.76 mm i.d.) and heated in 17 cm^3 min^{-1} (Brooks mass flow controlled) 5% v/v H_2/N_2 to 603 K at 2 K min^{-1}. The effluent gas passed through a liquid N_2 trap and changes in H_2 consumption were monitored by TCD with data acquisition/manipulation using the TPR Win™ software. The reduced samples were maintained at the final temperature for at least 1 h in a steady flow of H_2, swept with a 65 cm^3 min^{-1} flow of N_2 for 1.5 h, cooled to room temperature and subjected to H_2 chemisorption using a pulse (50 μl) titration procedure. BET areas were recorded with a 30% v/v N_2/He flow using pure N_2 (99.9%) as internal standard. At least 2 cycles of nitrogen adsorption-desorption in the flow mode were employed to determine total surface area using the standard single point method. BET surface area and H_2 uptake values were reproducible to within ± 5%; the values quoted in this communication are the mean. Particle size and shape were assessed by transmission electron microscopy analysis; JEOL-2000 TEM/STEM microscope equipped with a UTW energy dispersive X-ray (EDX) detector (Oxford Instruments) operated at an accelerating voltage of 200 kV. The specimens were prepared by ultrasonic dispersion in 2-butanol, deposited on a lacey-carbon/Cu grid (300 Mesh) and dried at 383 K for 12 h.

3.2.3 Catalysis Procedure

Reactions were carried out under atmospheric pressure, *in situ* immediately after activation, in a fixed bed vertical continuous glass reactor (l = 600 mm; i.d. = 15 mm) over the temperature range 393 K ≤ T ≤ 523 K. The catalytic reactor, and operating conditions to ensure negligible heat/mass transport limitations, have been fully described elsewhere [21]. Isothermal reaction conditions (± 1 K) were ensured by diluting the catalyst bed with ground glass (75 μm). Temperature was continuously monitored by a thermocouple inserted in a thermowell within the catalyst bed. The

reactant was delivered to the reactor *via* a glass/teflon air-tight syringe and teflon line using a microprocessor controlled infusion pump (Model 100 kd Scientific) at a fixed calibrated flow rate. A co-current flow of aromatic and ultra pure H_2 (< 1% v/v Aromatic/H_2) was maintained at a $GHSV = 2 \times 10^4$ h^{-1} with a molar metal (n) to inlet molar aromatic feed rate (F) ratio that spanned the range $9\times10^{-4} – 435\times10^{-4}$ h; inlet -NO_2 flow = 0.1-0.4 mmol h^{-1}. The H_2 content was up to 55 times in excess of the stoichiometric requirement, the flow rate of which was monitored using a Humonics (Model 520) digital flowmeter. In a series of blank tests, passage of each reactant in a stream of H_2 through the empty reactor or over the support alone, *i.e.* in the absence of Pd and/or Au, did not result in any detectable conversion. The reactor effluent was frozen in a liquid N_2 trap for subsequent analysis which was made using a Perkin-Elmer Auto System XL gas chromatograph equipped with a programmed split/splitless injector and a flame ionization detector, employing a DB-1 50 m × 0.20 mm i.d., 0.33 μm film thickness capillary column (J&W Scientific). A halogen (in the form of HCl) mass balance was performed by passing the effluent gas through an aqueous NaOH trap (7.0×10^{-4} mol dm^{-3}, kept under constant agitation at 400 rpm) with pH (Hanna HI Programmable Printing pH Bench-Meter) analysis. Repeated (up to five separate) catalytic runs with different samples from the same batch of catalyst delivered product compositions that were reproducible to within ± 8%. The nitroarene reactants, *p*-CNB, *o*-CNB, *m*-CNB, nitrobenzene (NB), *p*-nitrotoluene (*p*-NT), *p*-bromonitrobenzene (*p*-BNB), 2,4-dichloronitrobenzene (2,4-DCNB), 3,4-DCNB, 3,5-DCNB (all from Aldrich, ≥ 98.0 %) and the 1-butanol solvent (Riedel-de Häen, ≥ 99.5 %), were used without further purification.

3.3 Result and Discussion

3.3.1 Catalyst Characterization

The metal loading, T_{max} associated with maximum H_2 consumption/release during TPR activation, H_2 uptake and BET areas recorded for the mono- (Pd/Al_2O_3 and Au/Al_2O_3) and bi-metallic ($Au\text{-}Pd/Al_2O_3$) catalysts are given in **Table 3.1**. The temperature programme reduction (TPR) profile for Pd/Al_2O_3 (profile I, **Figure 3.1**) is characterized by a negative peak (H_2 release at 344 K), which can be attributed to the decomposition of β-phase Pd hydride [22]. Room temperature reduction of PdO has been established when the gas phase H_2 partial pressure exceeds 15 Torr [23].

Table 3.1: Metal loading, temperature programmed reduction (TPR) T_{max}, BET surface area, H_2 uptake and Pd hydride composition (H_{ab}/Pd) associated with the three catalyst systems.

	Metal loading (mol %)	TPR T_{max} (K)	BET area ($m^2\ g^{-1}$)	$H_{2\ uptake}$ ($\mu mol\ g^{-1}$)	H_{ab}/Pd ($\mu mol_H\ \mu mol_{Pd}^{-1}$)
Pd/Al_2O_3	6.6	344	130	24	0.18
Au/Al_2O_3	1.0	434	161	0.4	-
$Au\text{-}Pd/Al_2O_3$	Pd (6.6) Au (0.7)	349	130	25	0.19

The hydrogen content in the Pd hydride, represented by the ratio of the number of moles of hydrogen desorbed per total mol of Pd (H_{ab}/Pd = 0.18, see **Table 3.1**) is in good agreement with values quoted in the literature for supported Pd where an upper limit of H_{ab}/Pd = 0.76 has been established for bulk Pd [24]. In addition to H_2 release/hydride decomposition, H_2 consumption at temperatures above 573 K has been reported for Pd/Al_2O_3 due to a reduction of the Pd precursor [25] and this can be linked to the broad ill-defined H_2 uptake shown in **Figure 3.1**. The TPR for Au/Al_2O_3 is characterised by a single positive peak (H_2 consumption at 434 K, see profile II in **Figure 3.1**) which can be ascribed to the reduction of Au^{3+} to Au^0 in accordance with the assignment of Gluhoi *et al.* [26]. Au/Al_2O_3 prepared by deposition-precipitation generated single peaks at 465 K [27] and 503 K [18]. The reduction profile recorded for $Au\text{-}Pd/Al_2O_3$ (profile III in **Figure 3.1**) is dominated by a negative peak at 349 K which can again be attributed to Pd hydride decomposition. The associated T_{max} and Pd hydride composition in the bimetallic are equivalent to that recorded for Pd/Al_2O_3 (**Table 3.1**), suggesting limited interaction between the two metals. The absence of any hydrogen consumption peak in the TPR of $Au\text{-}Pd/Al_2O_3$ demonstrates that the pre-reduced Pd facilitates Au precursor reduction, as noted by Bonarowska *et al.* [28] for $Au\text{-}Pd/SiO_2$ prepared by reductive deposition of gold onto pre-reduced Pd. However, in the latter study an increase in Pd hydride decomposition temperature (up to 15 K) and a lower H_{ab}/Pd was observed as a result of Au-Pd interaction. The H_2 uptake recorded for Au/Al_2O_3 (0.4 $\mu mol\ g^{-1}$) is close to the instrumental detection limits. Indeed, the general consensus that emerges from the literature is that the H_2 chemisorptive capacity of Au is limited [5]. Uptake on Pd/Al_2O_3 is close that for $Au\text{-}Pd/Al_2O_3$, *i.e.* H_2 chemisorption on Pd was unaffected by the presence of Au, again suggesting negligible Au-Pd surface interactions.

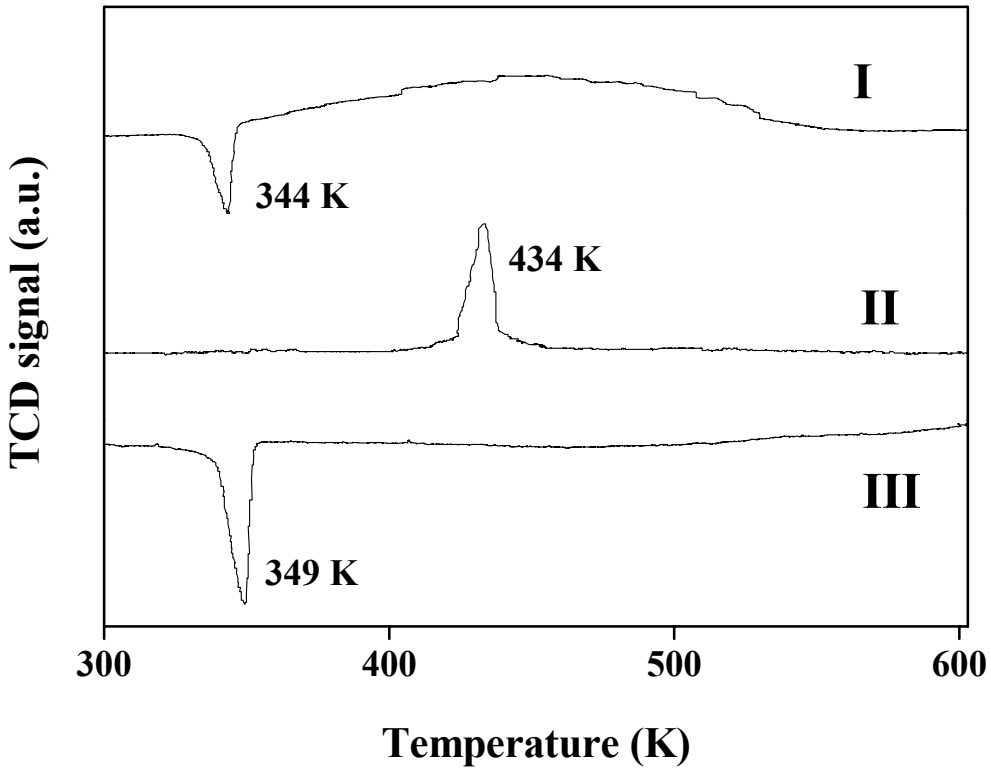

Figure 3.1: TPR profiles for (I) Pd/Al_2O_3, (II) Au/Al_2O_3 and (III) $Au\text{-}Pd/Al_2O_3$.

The representative TEM images of Pd/Al_2O_3 given in **Figure 3.2**(a) reveals pseudo-spherical particles in the overall size range 2-8 nm. A spherical morphology also characterises the supported Au (see **Figure 3.2**(b)) as has been noted elsewhere [29]; Au particles were also in 2-8 nm size range**.**

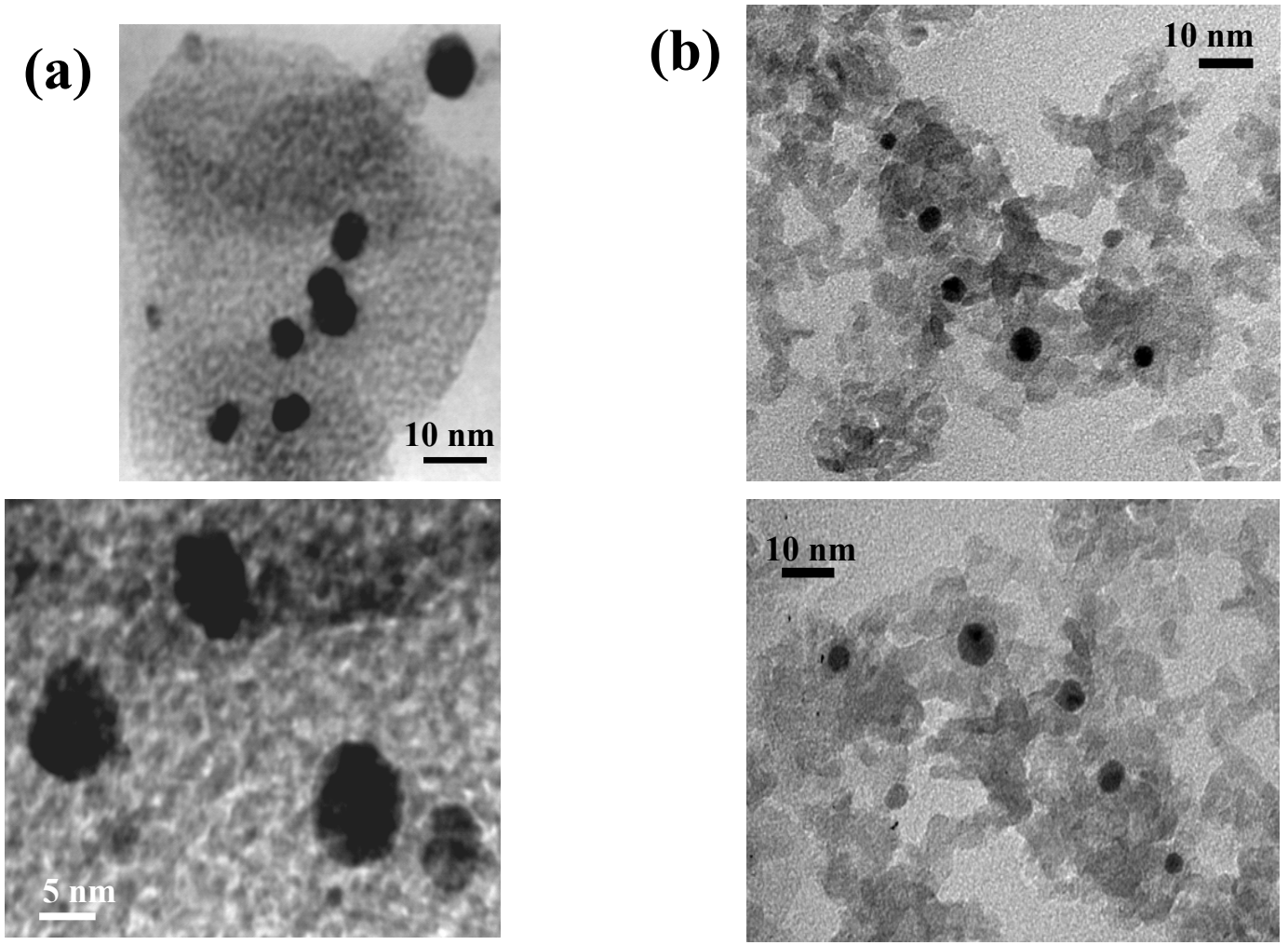

Figure 3.2: Representative TEM images of (a) Pd/Al_2O_3 and (b) Au/Al_2O_3.

3.3.2 Catalyst activity/selectivity

3.3.2.1 Hydrogenation of p-CNB

Time on-stream fractional *p*-CNB conversion ($x_{p\text{-}CNB}$) is shown in **Figure 3.3**; the temporal drop in activity can be expressed in terms of the empirical relationship [30]

$$\frac{(x_{p\text{-}CNB} - x_0)}{(x_{3h} - x_0)} = \frac{\Delta t}{(\beta + \Delta t)} \qquad (3.1)$$

where x_{3h} represents fractional conversion after 3 h on-stream and β is a time scale fitting parameter. Fit convergence yields values for x_0, the initial fractional conversion, a measure of initial activity. It should be noted from the outset that Au/Al_2O_3 was significantly less active than the Pd-containing catalysts, necessitating higher reaction temperature to achieve comparable conversions. The temporal profiles for Pd/Al_2O_3 and $Au\text{-}Pd/Al_2O_3$ converge to give similar initial conversions where the bimetallic delivered slightly higher conversions at extended reaction times. In contrast, Au/Al_2O_3 showed a time invariant conversion.

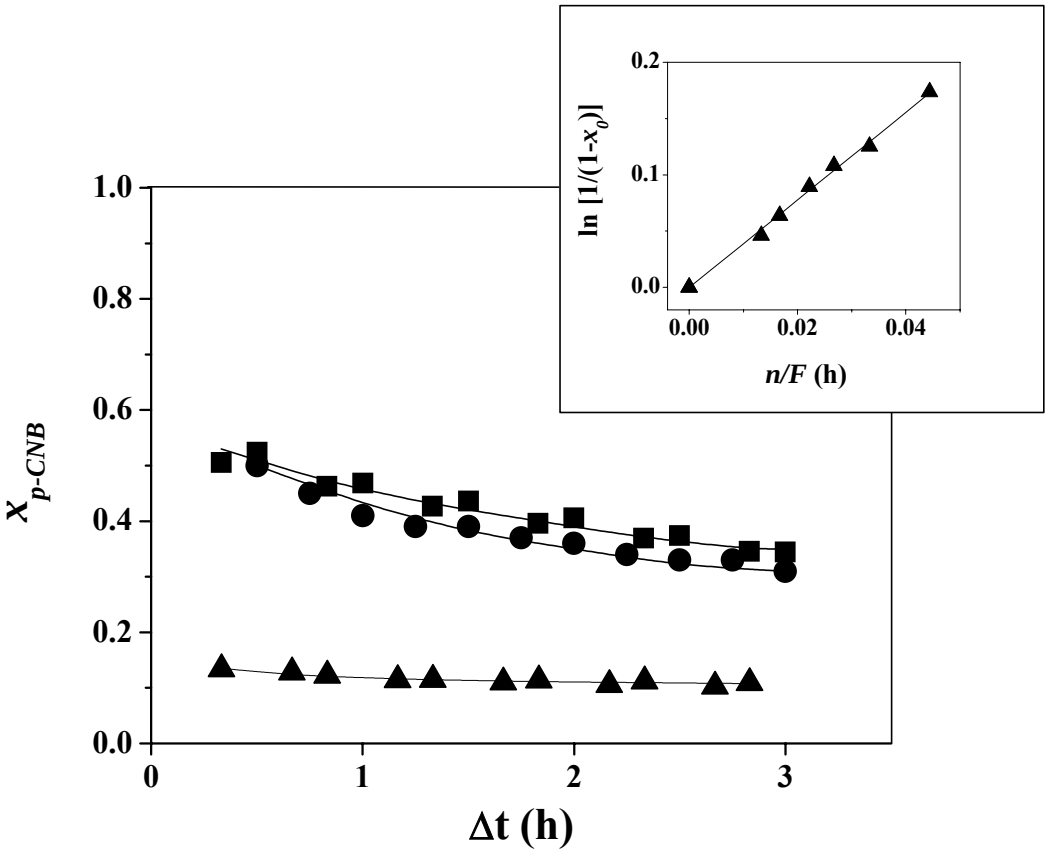

Figure 3.3: Variation of *p*-CNB fractional conversion (x_{p-CNB}) with time-on-stream over Pd/Al_2O_3 (●) and $Au\text{-}Pd/Al_2O_3$ (■) at T = 453 K and Au/Al_2O_3 (▲) at T = 473 K: inlet *p*-CNB/metal = 75 $mol_{p\text{-}CNB}$ mol_{metal}^{-1} h^{-1}; lines represent fit to Equation (3.1). Inset: Pseudo-first order kinetic plot for the hydrogenation of *p*-CNB over Au/Al_2O_3 at T = 453 K.

A pseudo-first order kinetic treatment for reaction under plug-flow conditions where H_2 was maintained far in excess, yields the following reactor/kinetic expression

$$\ln(1-x_0)^{-1} = k\left(\frac{n}{F}\right) \qquad (3.2)$$

The parameter F represents the inlet hourly molar *p*-CNB feed rate and n represents moles of metal in the catalyst bed; the parameter n/F has the physical significance of contact time. The representative linear relationship between $\ln(1-x_0)^{-1}$ and n/F, shown as an inset to **Figure 3.3**, confirms the applicability of pseudo-first order kinetics. The extracted pseudo-first order rate constants are presented in **Table 3.2**, which includes initial selectivity values obtained at the same initial conversion.

Table 3.2: Pseudo-first order rate constants (k) and reaction products (with selectivities) obtained in the hydrogenation of *p*-CNB at T = 523 K (Au/Al_2O_3) and T = 453 K (Pd/Al_2O_3, $Au\text{-}Pd/Al_2O_3$ and $Au/Al_2O_3 + Pd/Al_2O_3$) under conditions of equal initial activity ($x_0 \sim 0.2$).

Catalyst	Rate Constant $k\ (h^{-1})$	Product(s) (% selectivity)
Pd/Al_2O_3	89	AN (52) NB (48)
Au/Al_2O_3	16	*p*-CAN (100)
$Au\text{-}Pd/Al_2O_3$	87	AN (50) NB (50)
$Pd/Al_2O_3 + Au/Al_2O_3$	89	AN (45) NB (55)

Even at the higher reaction temperature (523 K as opposed to 453 K), Au/Al_2O_3 delivered an appreciably lower (by a factor of six) rate constant. This lower hydrogenation activity can be linked to the lower H_2 uptake relative to that recorded for the Pd-containing catalysts (**Table 3.1**). Fierro *et al.* [31], investigating the hydrogenation of naphthalene in the presence of dibenzothiophene a series of alumina supported catalysts, reported a reaction rate decrease in the order Pd-Au>Pd>Au, which was ascribed to enhanced surface Pd^0 associated with the bimetallic, *i.e.* formation of smaller Pd particles in Au-Pd. In this study, the incorporation of Au, either chemically ($Au\text{-}Pd/Al_2O_3$) or as a physical mixture (Au/Al_2O_3+Pd/Al_2O_3) had no significant influence on catalytic activity; the rate constants approached that generated for Pd/Al_2O_3 (**Table 3.2**). Our characterization measurements did not show any significant

difference in terms of H_2 uptake or Pd hydride composition due to the incorporation of Au which would suggest negligible Au-Pd interaction, a response that is borne out by the catalytic activity values.

The entries in **Table 3.2** also demonstrate that the presence of Au had little effect on reaction selectivity in the case of Au-Pd/Al_2O_3 and Au/Al_2O_3+Pd/Al_2O_3; selectivity is governed by the Pd component. Hydrogenation of *p*-CNB over Pd-containing catalysts generated NB and aniline (AN) *via* hydrodechlorination (HDC) and subsequent hydrogenation, respectively. The dependence of product selectivity (with respect to NB, AN and *p*-CAN) on (initial) conversion is presented in **Figure 3.4**(a). The selectivity profiles overlap for Pd/Al_2O_3, Au-Pd/Al_2O_3 and Au/Al_2O_3+Pd/Al_2O_3, suggesting a common reaction pathway. Nitrobenzene was the predominant product at low x_{p-CNB} with decreasing selectivity and an increasing preference for the production of AN at higher conversions, *i.e.* C-Cl hydrogen scission and subsequent -NO_2 reduction ultimately prevailed. Supported Pd is well established in the literature as an effective hydrodechlorination catalyst [32]. Nevertheless, dechlorination efficiency has been shown to be influenced by the addition of Au to supported Pd. Bonarowska and co-workers [33], studying the hydrodechlorination of CFC-12 over carbon-supported Pd-Au reported a higher selectivity towards the formation of difluoromethane that was dependent on the degree of Pd-Au "alloying". We did not observe any significant selectivity variation due to incorporation of Au in Pd/Al_2O_3. However, Au/Al_2O_3 solely promoted the formation of *p*-CAN from *p*-CNB (see **Table 3.2**), *i.e.* 100% selectivity with respect to -NO_2 reduction. The distinct reaction pathway favoured by Au/Al_2O_3 as opposed to the "Pd catalysts", which accounts for the observed selectivity trends is given in **Figure 3.4**(b).

This is the first report of an exclusive hydrogenation of *p*-CNB to *p*-CAN for continuous gas phase reaction over supported Au. Reaction exclusivity was maintained over the temperature range 393 K $\leq T \leq$ 523 K and the associated Arrhenius plot is shown as an inset to **Figure 3.5**. The resultant apparent activation energy (49 kJ mol^{-1}) falls within the range (25 kJ - 60 kJ mol^{-1}) of values quoted in the literature for reaction over Ni [34] and Pt [35] catalysts in batch liquid systems. The temporal profile given in **Figure 3.3** demonstrated that there was no short term deactivation of Au/Al_2O_3. In order to explicitly establish catalyst stability, the reaction was carried out over a prolonged

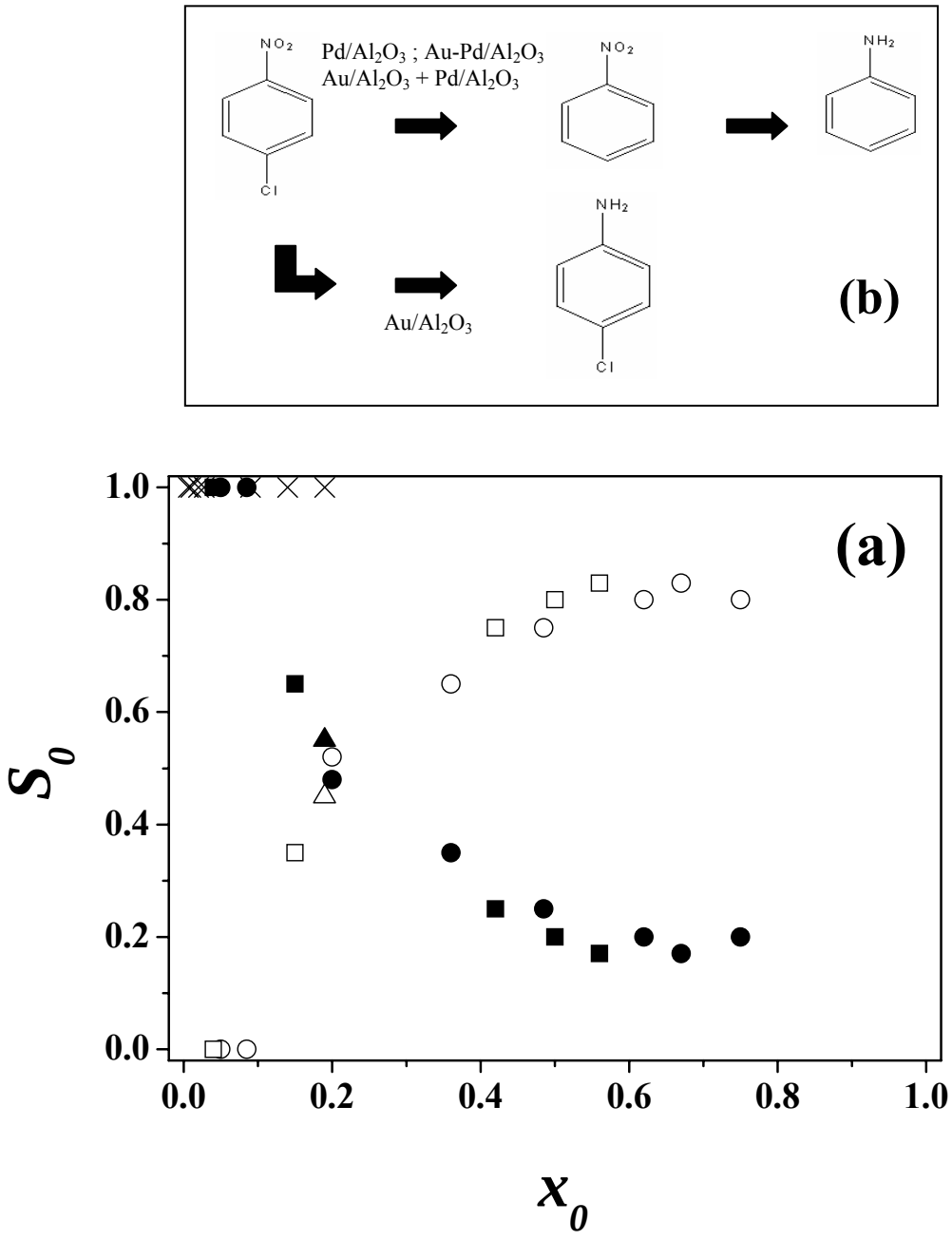

Figure 3.4: (a) Variation of *p*-CAN (×), NB (solid symbols) and AN (open symbols) initial selectivity (S_0) with initial *p*-CNB fractional conversion (x_0) for reaction over Au/Al_2O_3 (×), Pd/Al_2O_3 (●,○), $Au\text{-}Pd/Al_2O_3$ (■,□) and $Au/Al_2O_3 + Pd/Al_2O_3$ (▲,Δ). (b) Reaction pathways associated with the conversion of *p*-CNB over the four catalyst systems.

period of time. The results are presented in **Figure 3.5** where the ratio of *p*-CNB in the exit ($(n)_{out}$) relative to that in the inlet ($(n)_{in}$) stream is plotted as a function of time. Following an initial induction period, the catalyst showed a constant conversion for up to 80 h on-stream. Moreover, reaction exclusivity (to *p*-CAN) was maintained throughout this extended run.

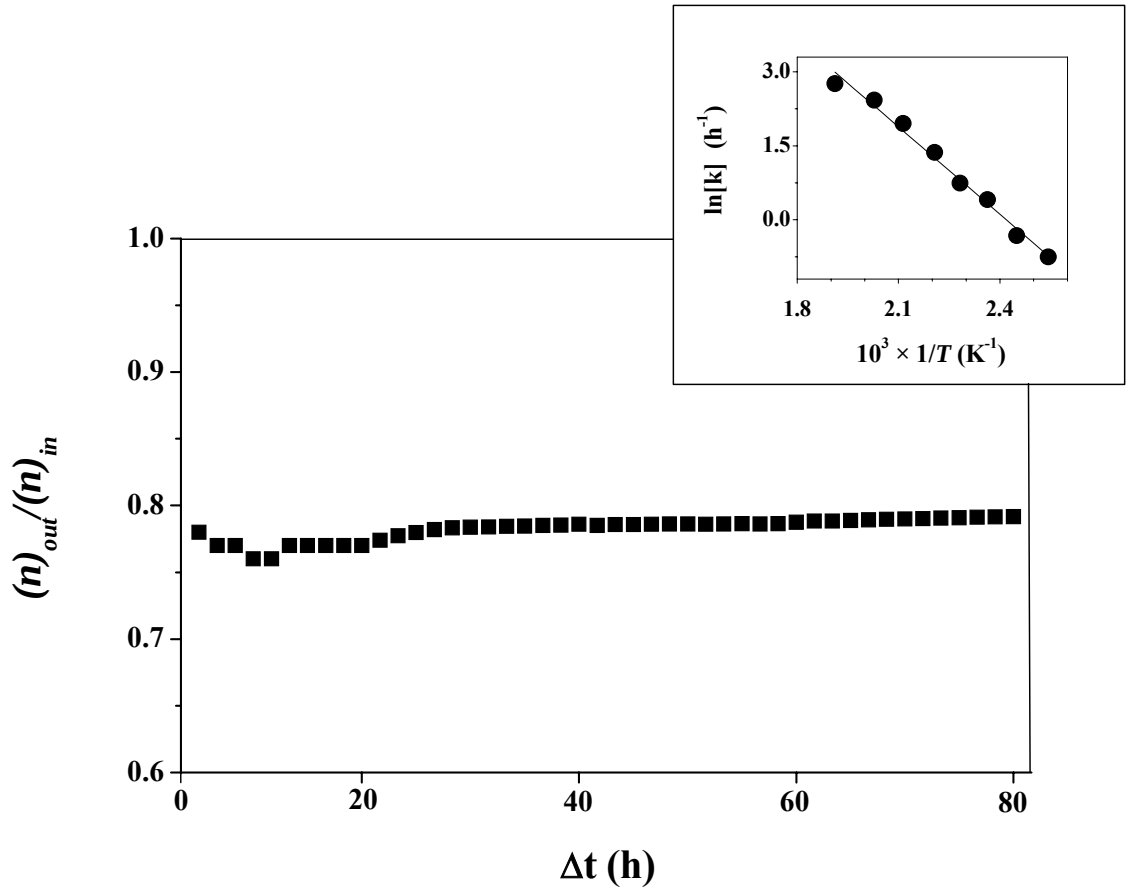

Figure 3.5: **Ratio of *p*-CNB in the exit stream ($(n)_{out}$) relative to that in the inlet stream ($(n)_{in}$) for reaction over Au/Al_2O_3 at T = 473 K. Inset: Arrhenius plot for hydrogenation of *p*-CNB to *p*-CAN.**

Nitro group reduction was further evaluated by considering the hydrotreatment of a series of nitrohaloarenes at a fixed inlet hourly $-NO_2$/Au mol ratio and the resultant pseudo-first order rate constants (at 453 K) are presented in **Table 3.3**. Conversion of all the reactants generated the corresponding amino compound as the sole product, *i.e.* 100% selective $-NO_2$ reduction in every case. The tabulated results support the following sequence of increasing $-NO_2$ reduction rate: NT < NB ≤ CNB/BNB < DNB. This trend is indicative of an electron withdrawing substituent activation effect, which is consistent with the involvement of a negatively charged intermediate as has been proposed elsewhere [4]. The higher rate constant obtained for the conversion of *o*- and *p*-CNB relative to *m*-CNB suggests that inductive rather steric effects determine hydrogenation rate over Au/Al_2O_3. The three dichloro-isomers exhibited equivalent rate constants that were an order of magnitude higher than that obtained for the mono-haloarene reactants.

Table 3.3: Pseudo-first order rate constants (k) and reaction products obtained in the hydrotreatment of a range of nitroarenes over Au/Al_2O_3 ($75\ mol_{-NO_2}\ mol_{Au}^{-1}\ h^{-1}$) at T = 453 K.

Reactant	Rate Constant k (h^{-1})	Product(s)
p-Nitrotoluene (*p*-NT)	No conversion	
Nitrobenzene (NB)	2	AN
m-Chloronitrobenzene (*m*-CNB)	2	*m*-CAN
p-Bromonitrobenzene (*p*-BNB)	4	*p*-BAN
p-Chloronitrobenzene (*p*-CNB)	4	*p*-CAN
o-Chloronitrobenzene (*o*-CNB)	9	*o*-CAN
2,4-Dichloronitrobenzene (2,4-DNB)	90	2,4-DCAN
3,4-Dichloronitrobenzene (3,4-DNB)	90	3,4-DCAN
3,5-Dichloronitrobenzene (3,5-DNB)	90	3,5-DCAN

3.4 Conclusions

The results presented in this Chapter support the following conclusions:

i. Au/Al_2O_3 promotes the gas phase continuous hydrogenation of *p*-CNB solely to *p*-CAN (393 K $\leq T \leq$ 523 K, ΔE_a = 49 kJ mol^{-1}) where reaction exclusivity has been established for up to 80 h on-stream with no detectable catalyst deactivation.

ii. Under the same reaction conditions, Pd/Al_2O_3 delivers a higher reaction rate than Au/Al_2O_3 catalyst but generates NB and AN as products with an appreciable time on-stream loss of activity.

iii. The incorporation of Au, either chemically ($Au\text{-}Pd/Al_2O_3$) or as a physical mixture (Au/Al_2O_3+Pd/Al_2O_3) did not influence *p*-CNB hydrogenation activity or selectivity which was equivalent to that delivered by Pd/Al_2O_3. TPR analysis and H_2 uptake measurements suggest negligible Au-Pd interaction.

iv. The hydrogenation of a series of mono- and di-substituted nitroarenes resulted in the exclusive formation of the corresponding aminoarene over Au/Al_2O_3 with

the following sequence of increasing rate, NT < NB ≤ CNB/BNB < DNB, consistent with an electron withdrawing substituent activation effect.

3.5 References

[3.1] R. S. Downing, P. J. Kunkeler, H. van Bekkum, Catal. Today, 37, 121 (1997)

[3.2] K. R. Westerterp, K. B. van Gelder, H. J. Janssen, M. H. Oyevaar, Chem. Eng. Sci., 43, 2229 (1988)

[3.3] X. D. Wang, M. H. Liang, J. L. Zhang, Y. Wang, Curr. Org. Chem., 11, 299 (2007)

[3.4] B. Coq, F. Figuéras, Coord. Chem. Rev., 178-180, 1753 (1998)

[3.5] P. Claus, Appl. Catal. A: Gen., 291, 222 (2005)

[3.6] A. S. K. Hashmi, G. J. Hutchings, Angew. Chem. Int. Ed., 45, 7896 (2006)

[3.7] Y. Chen, J. Qiu, X. Wang, J. Xiu, J. Catal., 242, 227 (2006)

[3.8] A. Corma, P. Serna, Science, 313, 332 (2006)

[3.9] T. Joseph, K. V. Kumar, A. V. Ramaswamy, S. B. Halligudi, Catal. Commun., 8, 629 (2007)

[3.10] C. Mohr, H. Hofmeister, P. Claus, J. Catal., 213, 86 (2003)

[3.11] R. Zanella, C. Louis, S. Giorgio, R. Touroude, J. Catal., 223, 328 (2004)

[3.12] L. Barrio, P. Liu, J. A. Rodríguez, J. M. Campos-Martín, J. L. G. Fierro, J. Chem. Phys., 125, 164715 (2006)

[3.13] L. Stobiński, L. Zommer, R. Duś, Appl. Surf. Sci., 141, 319 (1999)

[3.14] B. Campo, M. Volpe, S. Ivanova, R. Touroude, J. Catal., 242, 162 (2006)

[3.15] C. Milone, R. Ingoglia, L. Schipilliti, C. Crisafulli, G. Neri, S. Galvagno, J. Catal., 236, 80 (2005)

[3.16] E. Bus, J. T. Miller, J. A. van Bokhoven, J. Phys. Chem. B, 109, 14581 (2005)

[3.17] D. A. Panayotov, J. T. Yates, J. Phys. Chem. C, 111, 2959 (2007)

[3.18] C. K. Costello, J. Guzman, J. H. Yang, Y. M. Wang, M. C. Kung, B. C. Gates, H. H. Kung, J. Phys. Chem. B, 108, 12529 (2004)

[3.19] S. Panigrahi, S. Basu, S. Praharaj, S. Pande, S. Jana, A. Pal, S. K. Gosh, T. Pal, J. Phys. Chem. C, 111, 4596 (2007)

[3.20] X. Zhang, H. Shi, B. Q. Xu, Angew. Chem. Int. Ed., 44, 7132 (2005)

[3.21] G. Tavoularis, M. A. Keane, J. Chem. Technol. Biotechnol., 74, 60 (1999)

[3.22] N. K. Nag, J. Phys. Chem. B, 105, 5945 (2001)

[3.23] V. Ferrer, A. Moronta, J. Sánchez, R. Solano, S. Bernal, D. Finol, Catal. Today, 107-108, 487 (2005)

[3.24] M. Boudart, H. S. Hwang, J. Catal., 39, 44 (1975)

[3.25] F. Pinna, F. Menegazzo, M. Signoretto, P. Canton, G. Fagherazzi, N. Pernicone, Appl. Catal. A: Gen., 219, 195 (2001)

[3.26] A. C. Gluhoi, X. Tang, P. Marginean, B. E. Nieuwenhuys, Top. Catal., 39, 101 (2006)

[3.27] Y.-J. Chen, C.-T. Yeh, J. Catal., 200, 59 (2001)

[3.28] M. Bonarowska, J. Pielaszek, W. Juszczyk, Z. Karpiński, J. Catal., 195, 304 (2000)

[3.29] G. C. Bond, C. Louis, D. T. Thompson, Catalysis by Gold, Imperial College Press, London, 2006.

[3.30] G. Yuan, C. Louis, L. Delannoy, M. A. Keane, J. Catal. , 247, 256 (2007)

[3.31] B. Pawelec, E. Cano-Serrano, J. M. Campos-Martin, R. M. Navarro, S. Thomas, J. L. G. Fierro, Appl. Catal. A: Gen., 275, 127 (2004)

[3.32] F. J. Urbano, J. M. Marinas, J. Mol. Catal. A: Chem., 173, 329 (2001)

[3.33] M. Bonarowska, J. Pielaszek, V. A. Semikolenov, Z. Karpiński, J. Catal., 209, 528 (2002)

[3.34] Y.-Z. Chen, Y.-C. Chen, Appl. Catal. A: Gen., 115, 45 (1994)

[3.35] B. Coq, A. Tijani, F. Figuéras, J. Mol. Catal., 68, 331 (1991)

Chapter 4

Pd-Promoted Selective Gas Phase Hydrogenation of *p*-Chloronitrobenzene over Alumina Supported Au

Nitro group reduction exclusivity (at low conversions) is a feature of catalysis by supported Au while Pd delivered higher activity but promoted hydrodechlorination. In this Chapter the possible role of Pd as an Au promoter (in terms of increased catalytic activity) in the selective hydrogenation of *p*-chloronitrobenzene has been investigated.

4.1 Introduction

Halogenated aromatic amines, with multiple applications in the manufacture of pesticides, herbicides, pigments, pharmaceuticals and cosmetics, are commercially important target products [1]. Existing routes, notably the Béchamp process (Fe promoted reduction in acid media), produce toxic by-products with low overall product yields [2] and there is now a pressing demand for a cleaner technology. We have recently demonstrated that the gas phase hydrogenation of *p*-chloronitrobenzene over Au supported on alumina [3,4] and titania [4] was 100% selective in terms of $-NO_2$ group reduction to *p*-chloroaniline over a prolonged (up to 80 h) time on-stream. However, the level of *p*-chloronitrobenzene conversion was appreciably lower than that delivered by supported Pd, which generated nitrobenzene and aniline (non-selective hydrogenation) as the principal products with a significant temporal loss of activity [3]. Indeed, two possible reaction pathways are associated with the hydrogenation of *p*-chloronitrobenzene [3,5], as shown in **Figure 4.1**. Path A involves hydrodechlorination to nitrobenzene, which can be further hydrogenated to aniline *via* the nitrosobenzene intermediate. In Path B, the $-NO_2$ group is initially hydrogenated to yield the target product (*p*-chloroaniline), which can undergo subsequent hydrodechlorination to aniline. Both mechanisms have been reported for gas and/or liquid phase catalytic operation over supported metals [3,6-13].

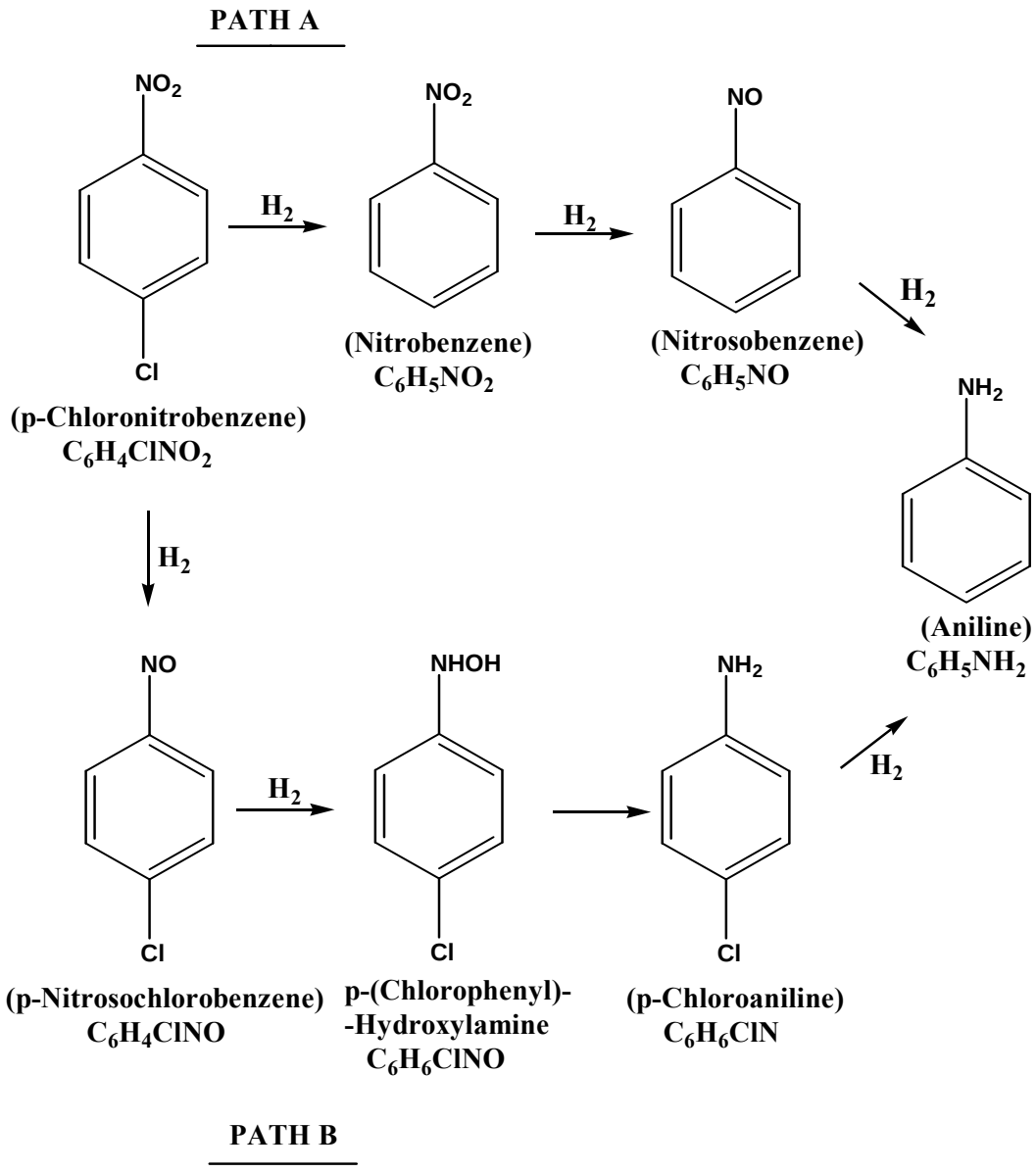

Figure 4.1: Reaction pathways associated with the hydrogen mediated conversion of *p*-chloronitrobenzene.

Dechlorination at high conversions is a feature of reactions promoted by supported Ni [7,8], Pd [11,14], Pt [12,13,15], Ru [16], bi-metallic La-NiB [9], Pd-Ru [10], Pd-Pt [10], Pt-M (M = Cr, Mn, Fe, Co, Ni and Cu) [17] and Pt-M (M = Sn, Pb, Ge, Al, Zn) [18] catalysts. Xu *et al.* [19] have reported that the incorporation of Sn^{4+} in Pd/Al_2O_3 served to limit the degree of *p*-chloronitrobenzene dechlorination in batch liquid reaction and attributed this effect to interaction between Sn^{4+} and the $-NO_2$ group that increased the polarity of the N=O bond and promoted reduction. However, higher conversions of *p*-chloronitrobenzene were accompanied by a decrease in selectivity to

p-chloroaniline. The main goal of our work is to direct the reaction along Path B, elevating the level of *p*-chloroaniline production without the formation of aniline in continuous flow operation.

Catalytic hydrogenation over supported Au has been proposed to depend on the preparation method [20], metal particle size/morphology [21] and support surface chemistry [22]. The optimum supported Au particle size is still a matter of some debate but it is commonly accepted that, in order to achieve high activity, the presence of particles smaller than *ca.* 5 nm is crucial. An increase in Au dispersion, with a consequent decrease in Au particle size, increases the proportion of surface low coordination sites on which H_2 can dissociate [23,24]. Nevertheless, there is some evidence of a lower limit in terms of Au particle size (*ca.* 2 nm), below which activity decreases due to quantum effects [25,26]. The ultimate degree of dispersion is dependent on catalyst synthesis and Okumura *et al.* [27] obtained, in the case of (*ca.* 1 % w/w) Au/Al_2O_3 prepared by deposition-precipitation (DP) and impregnation (IMP), an order of magnitude difference in the mean Au diameter (DP = 3 nm, IMP = 37 nm). Grisel *et al.* [28] also recorded an appreciably smaller Au particle size (3-5 nm) by DP synthesis when compared with IMP. Catalytic activity may also be enhanced through the use of promoters, which can serve to modify the electronic properties of the active site [29]. In the case of Au catalysis, the number of studies that have considered the use of promoters in hydrogenation reactions is very limited but we can flag the work of Gluhoi *et al.* [30,31] who demonstrated enhanced activity in NO reduction over Al_2O_3-supported combinations of Au with CeO_x and LiO_2, ascribing the promotional effect of the metal oxides to the formation of small and thermally stable Au particles. Moreover, Nutt *et al.* [32] reported enhanced activity in the hydrogen mediated dechlorination of C_2HCl_3 over $Au\text{-}Pd/Al_2O_3$ when compared with Pd/Al_2O_3 which they attributed to Au/Pd interactions, an effect that extended to unsupported Au/Pd nanoparticles [33].

With a view to elevating the catalytic activity of Au, we have considered the possible role of Pd, with high activity in gas phase $-NO_2$ group reduction [3,5,34-36], as a promoter. In this paper, we examine, for the first time, the catalytic action of Pd promoted Au/Al_2O_3 ($Au/Pd \geq 8$) in the selective reduction of *p*-chloronitrobenzene to *p*-chloroaniline. We also assess the feasibility of increasing hydrogenation rate, while maintaining exclusivity in terms of $-NO_2$ reduction, by controlling Au particle size during catalyst preparation and compare IMP and DP as two distinct synthesis routes.

4.2 Experimental

4.2.1 Catalyst Preparation and Activation

The monometallic Au and bimetallic Pd-Au catalysts were prepared by deposition-precipitation (DP) with urea [37] and impregnation (IMP) in excess solvent using Al_2O_3 (AluC Degussa, 110 m^2 g^{-1}) as support. In the case of the DP synthesis, a suspension of the support (3 g) in distilled water (100 cm^3) was placed in an ultrasound bath in order to disperse the support particles. The suspension was then placed in a reactor, 190 cm^3 of distilled water was added and the mixture was heated to 353 K at which point 6 cm^3 of a solution of $HAuCl_4$ (10 g dm^{-3}), corresponding to the desired Au loading (1 % w/w), was added with a *ca.* 100-fold excess of urea. The pH of the suspension (initially *ca.* 2.5) progressively increased to reach *ca.* 7 after 16 h. The solids obtained were separated by centrifugation, washed three times with deionized water (with centrifugation between each washing) and dried under vacuum at 298 K for 12 h. For the bimetallic catalysts, an adequate volume of a solution of $PdCl_2$ (1 g dm^{-3}) was added to the gold solution to give nominal atomic Au/Pd ratios = 5, 10 and 20. Because of the formation of soluble Pd^{2+} amino species during DP with urea, the experimentally determined (see **Table 4.1**) metal loadings corresponded to Au/Pd ratios = 8, 20 and 88, respectively.

In the synthesis by IMP, Al_2O_3 (3 g) was dispersed in 25 cm^3 distilled water in a round bottomed flask (100 cm^3), appropriate volumes of $HAuCl_4$ (10 g dm^{-3}) and (in the case of the bimetallic) $PdCl_2$ (1 g dm^{-3}) were added to achieve a Au/Pd ratio equal to 20 and the resulting slurry was vigorously stirred for 10 min. Excess water was removed on a rotary evaporator at 353 K over 1 h and then dried under vacuum at 298 K for 12 h. Two reference monometallic Pd/Al_2O_3 samples were also prepared by DP (320 ppm Pd, < 200 ppm Cl) and IMP (297 ppm Pd, 630 ppm Cl), *i.e.* with a Pd loading corresponding to that in the Pd-Au samples where Au/Pd = 20. In the case of Pd–IMP, 3 g Al_2O_3 were dispersed in 29 cm^3 distilled water, 1.25 cm^3 $PdCl_2$ (1 g dm^{-3}) solution were added and the resulting slurry was stirred vigorously for 1 h. Excess water was removed on a rotary evaporator at 353 K over a 1 h period and the sample was dried at 393 K for 12 h. In the preparation of Pd–DP, 3 g Al_2O_3 were dispersed in 150 cm^3 distilled water at room temperature to which 1.25 cm^3 of a $PdCl_2$ (1 g dm^{-3}) solution was added with continuous stirring. Because of the formation of soluble Pd^{2+} species when urea is used, Na_2CO_3 was employed as the precipitating agent. The pH was

increased by the dropwise addition of a Na_2CO_3 (1 M) solution until it reached 10.5 and the suspension was stirred for 1 h at room temperature; the solid was recovered, washed and dried as above.

After preparation, the samples were stored at 298 K under vacuum (in the dark) in a desiccator. The metal loading was determined (to within ± 2 %) by inductively coupled plasma-optical emission spectrometry (ICP-OES, Vista-PRO, Varian Inc.) from the diluted extract of aqua regia. The Cl content was measured by silver potentiometric titration after combustion in a Schöniger flask. Prior to use in catalysis, the samples (sieved into a batch of 75 μm average diameter) were activated in 60 cm^3 min^{-1} H_2 at 3 K min^{-1} to 573 K (Au/Al_2O_3) or 773 K (Pd/Al_2O_3 and $Pd\text{-}Au/Al_2O_3$), which was maintained for 2.5 h. After activation, the samples were passivated in 1% v/v O_2/He at room temperature for off-line analysis. Physical mixtures of reduced/passivated Pd-DP+Au-DP and Pd-IMP+Au-IMP (Au/Pd atomic ratio = 20) were also examined.

4.2.2 Catalysis Characterization

BET surface area, temperature programmed reduction (TPR) and H_2 chemisorption were determined using the commercial CHEM-BET 3000 (Quantachrome) unit. The samples were loaded into a U-shaped Pyrex glass cell (10 cm ×. 3.76 mm i.d.) and heated in 17 cm^3 min^{-1} (Brooks mass flow controlled) 5% v/v H_2/N_2 to 573 K (Au/Al_2O_3) or 773 K (Pd/Al_2O_3 and $Pd\text{-}Au/Al_2O_3$) at 3 K min^{-1}. The effluent gas passed through a liquid N_2 trap and changes in H_2 consumption were monitored by TCD with data acquisition/manipulation using the TPR Win™ software. The reduced samples were maintained at the final temperature for 2.5 h in a constant flow of H_2, swept with 65 cm^3 min^{-1} N_2 for 1.5 h, cooled to room temperature and subjected to H_2 chemisorption using a pulse (10 μl) titration procedure. BET areas were recorded with a 30% v/v N_2/He flow using pure N_2 (99.9%) as internal standard. At least 2 cycles of N_2 adsorption-desorption in the flow mode were employed to determine total surface area using the standard single point method. BET surface areas and H_2 uptake values were reproducible to within ± 5%; the values quoted represent the mean. TEM analysis was performed using a JEOL 100 CX II microscope where the average metal particle sizes were established from a measurement of up to 1000 particles. The size limit for the detection of gold particles on Al_2O_3 is *ca.* 1 nm. Infrared spectroscopy was performed with an IFS 66V Bruker spectrometer using a DRIFTS

cell. The catalyst precursors (10-20 mg) were reduced *in situ* by TPR (conditions as described above). The cell was then purged with He at 298 K before introducing a flow (50 cm^3 min^{-1}) of 1% v/v CO in He. The spectrum recorded under He was used as reference and the intensity of the spectrum under CO/He is expressed as Log (I_{CO}/I_{ref}).

4.2.3 Catalyst Procedure

Reactions were carried out under atmospheric pressure at T = 393 K, *in situ* immediately after activation, in a continuous fixed bed vertical glass reactor (l = 600 mm; i.d. = 15 mm). The catalytic reactor and operating conditions to ensure negligible heat/mass transport limitations, have been fully described elsewhere [38] but some features, pertinent to this study, are given below. A layer of borosilicate glass beads served as a preheating zone, ensuring that the *p*-chloronitrobenzene was vaporized and reached reaction temperature before contacting the catalyst. Isothermal conditions (± 1 K) were ensured by diluting the catalyst bed with ground glass (75 μm); the ground glass was mixed thoroughly with catalyst before insertion into the reactor. Reaction temperature was continuously monitored by a thermocouple inserted in a thermowell within the catalyst bed. The reactant was delivered to the reactor *via* a glass/teflon air-tight syringe and teflon line using a microprocessor controlled infusion pump (Model 100 kd Scientific) at a fixed calibrated flow rate. A co-current flow of *p*-chloronitrobenzene and ultra pure H_2 (< 1% v/v *p*-chloronitrobenzene/H_2) was maintained at a $GHSV = 2 \times 10^4$ h^{-1} with an inlet *p*-chloronitrobenzene molar flow (F) over the range 0.1-0.4 mmol h^{-1}, where the H_2 content was up to 200 times in excess of the stoichiometric requirement (P_{H_2} = 0.92 atm), the flow rate of which was monitored using a Humonics (Model 520) digital flowmeter. The molar metal (n) to inlet *p*-chloronitrobenzene feed rate ratio spanned the range 1×10^{-3}–14×10^{-3} h. In a series of blank tests, passage of *p*-chloronitrobenzene in a stream of H_2 through the empty reactor or over the support alone, *i.e.* in the absence of Pd, Au or Pd-Au, did not result in any detectable conversion. The reactor effluent was frozen in a liquid nitrogen trap for subsequent analysis, which was made using a Perkin-Elmer Auto System XL gas chromatograph equipped with a programmed split/splitless injector and a flame ionization detector, employing a DB-1 50 m × 0.20 mm i.d., 0.33 μm film thickness capillary column (J&W Scientific), as described elsewhere [39]. A chlorine (in the form of HCl) mass balance was performed by passing the effluent gas through an aqueous NaOH trap (7.0×10^{-4} mol dm^{-3}, kept under constant agitation at 400 rpm) with independent pH (Hanna HI Programmable Printing pH Bench-Meter) analysis. Repeated

(up to five separate) catalytic runs with different samples from the same batch of catalyst delivered product compositions that were reproducible to within ± 8%. *p*-Chloronitrobenzene (Aldrich, ≥99.9% w/w purity) and the 1-butanol solvent (Riedel-de Häen, ≥ 99.5 %) were used as supplied without further purification.

4.3 Result and Discussion

4.3.1 Catalyst Characterization

4.3.1.1 TPR, H_2 Chemisorption and TEM Analysis

The BET surface areas of the activated catalysts (see **Table 4.1**) were close to that of the Al_2O_3 support (110 m^2 g^{-1}). The TPR activation profiles for Au/Al_2O_3 prepared by DP (profile I) and IMP (profile V) are presented in **Figure 4.2**; the temperatures associated with maximum H_2 consumption (T_{max}) are given in **Table 4.1**. Hydrogen consumption during TPR matched (to within ± 8%) that required for the reduction of the supported Au precursors. The reduction profile for Au–DP is characterised by a single positive peak at 450 K, which is consistent with the TPR results for Au/Al_2O_3 prepared by DP that have been reported in the literature [40-43]. The occurrence of a single TPR peak has been attributed to Au^{3+} reduction to Au^0 [42,44]. TPR of our Au-IMP sample generated a single T_{max} at 494 K, which is in good agreement with the work of Baatz and Prüße [41] and Gluhoi *et al.* [43]. Bus and co-workers [45], in their analysis of Au/Al_2O_3 prepared by IMP using time-resolved *in situ* XAS, established the presence of Al_2O_3-supported oxidic or hydroxidic Au^{3+} species in the precursor that were reduced to Au^0 in H_2 at 440 K. The higher reduction temperature recorded for Au–IMP compared with Au–DP may be related to the greater residual Cl (see **Table 4.1**) associated with the former, which can affect the reducibility of Au(III) [45-49]. Moreover, the mobility of the Cl containing precursor after impregnation is known to induce Au sintering during activation [50-52]. This can account for the larger mean Au particle size in the Au-IMP sample (see **Table 4.1**). Representative TEM images are included in **Figure 4.3**, which serve to illustrate the nature of the metal dispersion in these catalysts. It can be seen that the Au component is present as discrete particles with a quasi-spherical morphology.

Table 4.1: Metal content, residual Cl content, T_{max} and associated H_2 consumption during TPR, H_2 chemisorption values, metal particle size (d_p) and BET surface areas for the mono- and bimetallic catalysts prepared by deposition/precipitation (DP) and impregnation (IMP).

Catalyst	Au (% w/w)	Au/Pd	Cl content (ppm)	TPR T_{max} (K)	TPR H_2 consumption (μmol $g_{catalyst}^{-1}$)	H_2 uptake (μmol g_{Au}^{-1})	d_p (nm)	BET Area (m^2 $g_{catalyst}^{-1}$)
Au-DP	0.88	-	<200	450	62	33	2.9	112
Pd/Au-DP	0.87	88	<200	453	62	47	1.9[a]	97
Pd/Au-DP	0.87	20	300	454 (434)[b]	68	84 (62)[b]	2.0[a]	100 (98)[b]
Pd/Au-DP	0.95	8	1381	491	75	109	2.7[a]	98
Au-IMP	0.81	-	9800	494	62	38	4.5	104
Pd/Au-IMP	0.87	20	14300	471 (444)[c]	68	30 (23)[c]	5.3[a]	92 (95)[c]

[a] refers to total metal (Au and Pd) mean particle size
[b] results for the physical mixture of Pd-DP + Au-DP (see Experimental section)
[c] results for the physical mixture of Pd-IMP + Au-IMP (see Experimental section)

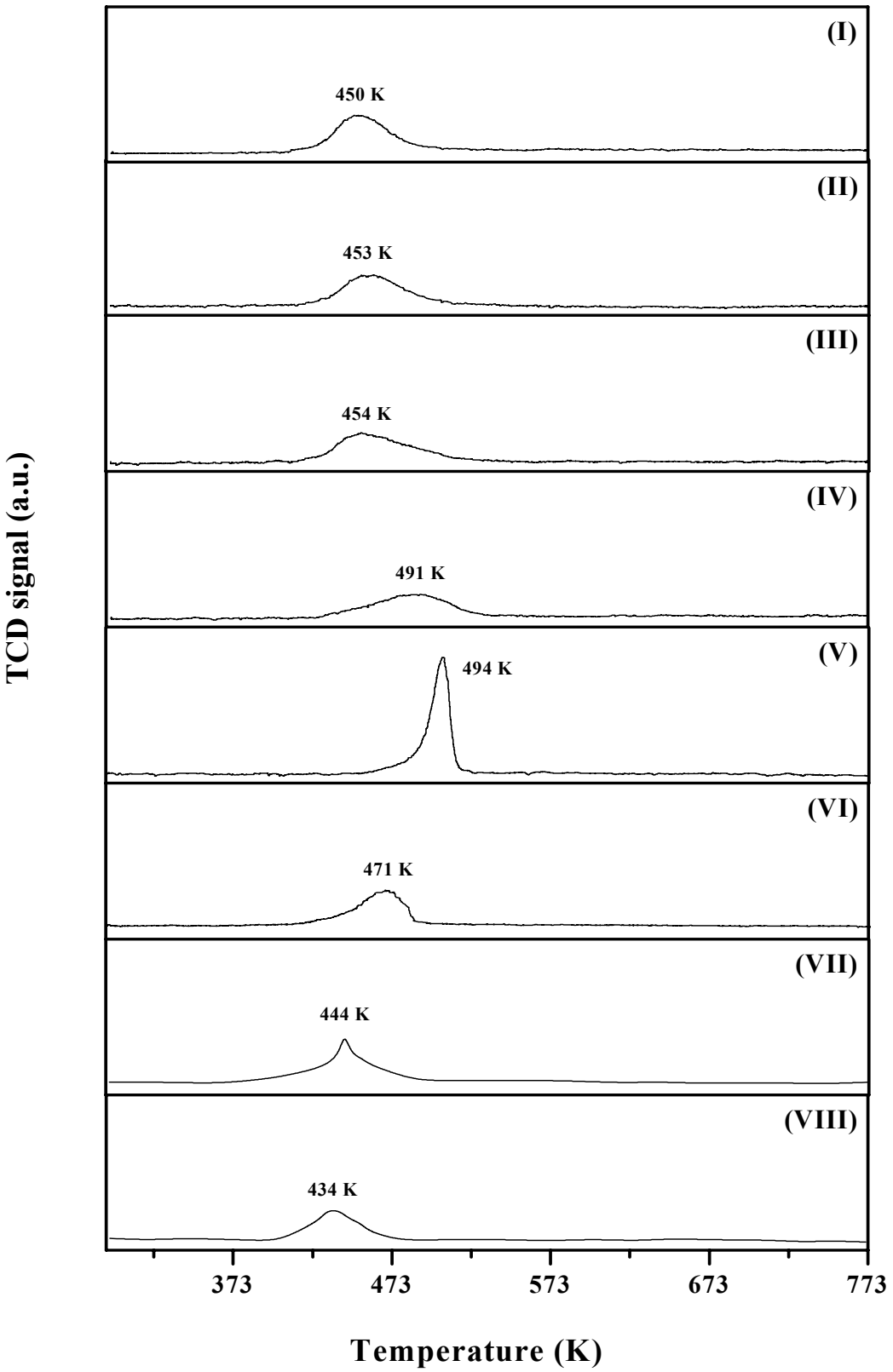

Figure 4.2: TPR profiles for: (I) Au-DP; (II) Pd/Au-DP (Au/Pd = 88); (III) Pd/Au-DP (Au/Pd = 20); (IV) Pd/Au-DP (Au/Pd = 8); (V) Au-IMP; (VI) Pd/Au-IMP (Au/Pd = 20); (VII) Au-IMP + Pd–IMP (Au/Pd = 20); (VIII) Au-DP + Pd-DP (Au/Pd = 20).

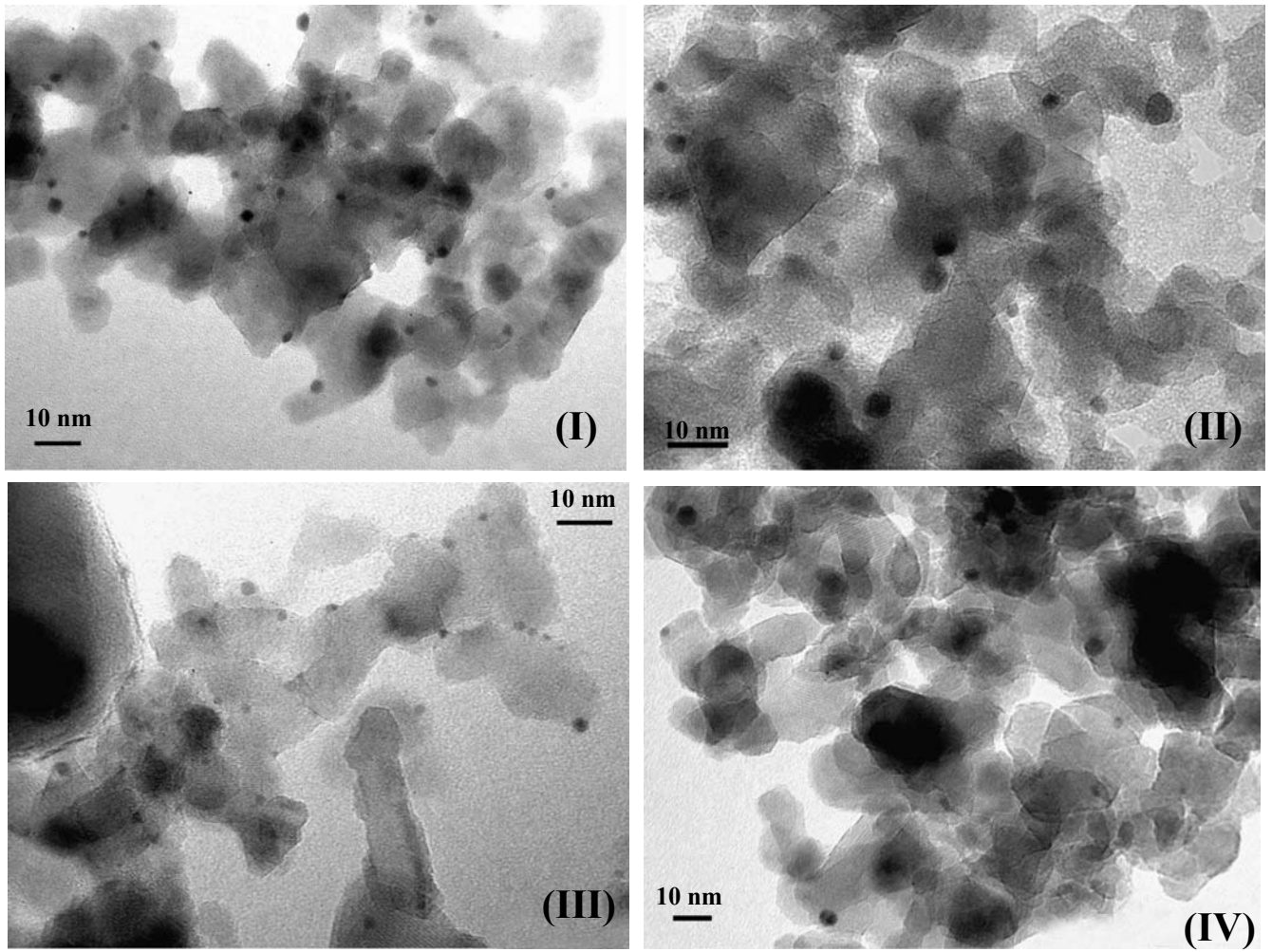

Figure 4.3: Representative TEM images of (I) Au-DP, (II) Au-IMP, (III) Pd/Au-DP (Au/Pd = 20) and (IV) Pd/Au-IMP (Au/Pd = 20).

Taking the Pd/Au–DP samples (see **Figure 2**, profiles II, III and IV), a progressive shift of the reduction peak to higher temperatures was observed with increasing Pd content. In previous studies [3,5], we have recorded a negative peak (H_2 release at 340-380 K) during the TPR of Pd/Al_2O_3 that we attributed to the decomposition of β-Pd hydride formed by the absorption of H_2 on zero valent Pd when the H_2 pressure exceeds 0.02 atm [53]. In the case of our Pd/Au samples, there was no detectable H_2 release but this can be due to the low Pd content. In addition to H_2 release/hydride decomposition, Pd/Al_2O_3 has been reported to exhibit H_2 consumption where $T > 573$ K due to the reduction of oxidized Pd species that interact strongly with the support [54]. The broad peaks observed for Pd/Au-DP (453-491 K) may be the result of a composite reduction of both metals, suggesting some interaction between Au and Pd species that modifies their respective reducibility. Hosseini *et al.* [55], using co-deposited $Au-Pd/TiO_2$ noted a shift in the reduction peak for PdO (with the introduction of Au) from 433 (100 Pd atom %) to 373 K (33 Pd atom %). In the TPR of Pd/Au-IMP (profile VI), the reduction peak appears at a lower temperature than that recorded for Au-IMP. This response is the direct opposite of that observed for the DP systems, possibly suggesting a different degree of interaction between Au and Pd in the IMP sample, which may be affected by the Cl content. The TPR profiles generated for both physical mixtures (profiles VII and VIII) exhibit a similar response in that the onset of H_2 consumption during reduction was shifted to lower temperatures (with a lower T_{max}, see **Table 4.1**) than that observed for the Au/Al_2O_3 systems. The inclusion of Pd/Al_2O_3 in the mixture must serve to facilitate the reduction of Au/Al_2O_3, possibly through the involvement of spillover hydrogen generated by the Pd component.

Hydrogen uptake (see **Table 4.1**) on both Au/Al_2O_3 samples was low, which is consistent with reports [56,57] that have demonstrated a limited capacity of Au to chemisorb hydrogen. This can be linked to the high activation energy barrier required for the dissociative adsorption of hydrogen on Au [45,58]. The incorporation (chemically or as a physical mixture) of Pd resulted in an increase in H_2 uptake for the DP samples (see **Table 4.1**), which was proportional to the Pd content. The higher uptake on Pd/Au-DP (Au/Pd = 20) compared with the corresponding physical mixture suggests a surface Pd-Au synergy that serves to increase the chemisorption capacity. In the case of the IMP system, the inclusion of Pd did not result in an increase in H_2 uptake. This response may be due to the higher Cl content that acts to suppress H_2 chemisorption allied to the larger particle size observed by TEM (see **Table 4.1**).

Indeed, it has been shown [47,59] that Cl and Br can act to inhibit CO uptake on Au where CO also adsorbs on low coordination surface sites. The monometallic Pd reference catalysts (DP or IMP) did not generate any signal during TPR and did not exhibit any measurable H_2 chemisorption, which we attribute to the very low Pd content resulting in experimental measurements that fell below instrumental detector limits.

4.3.1.2 DRIFTS Analysis

DRIFTS analysis using CO as a probe molecule was performed and the resultant spectra are given in **Figure 4.4**.

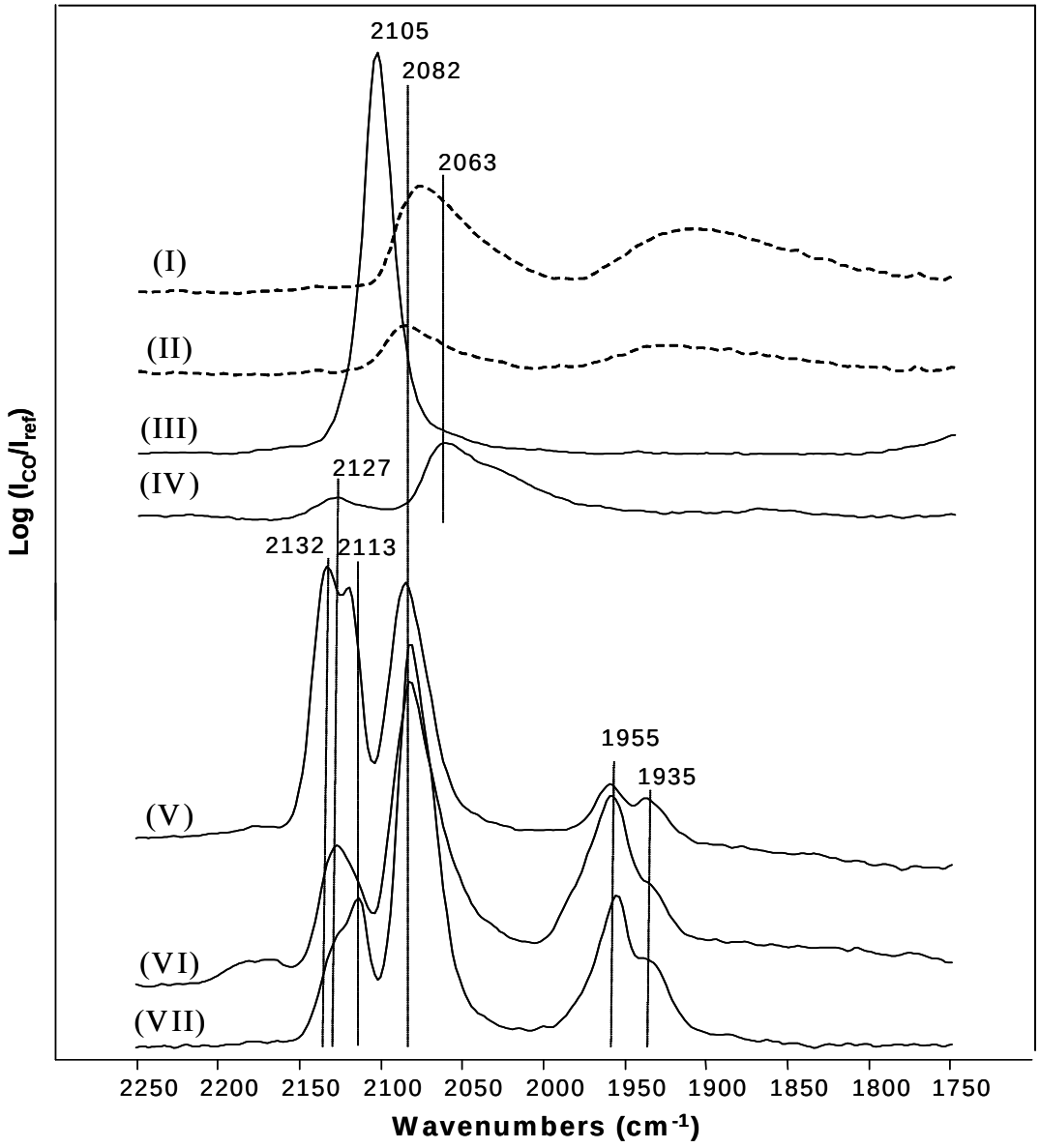

Figure 4.4: DRIFTS spectra (under 1% v/v CO/He at 298 K) of (I) Pd-DP, (II) Pd-IMP, (III) Au-DP, (IV) Au-IMP, (V) Pd/Au-IMP (Au/Pd = 20), (VI) Pd/Au-DP (Au/Pd = 8) and (VII) Pd/Au-DP (Au/Pd = 20).

The spectra of the carbonyl region for Pd-DP (profile I) and Pd-IMP (profile II) are similar and can be divided into two regions, *i.e.* high (2200-2000 cm^{-1}) and low (2000-1800 cm^{-1}) wave numbers. The bands at high wave numbers have been assigned in the literature [60] to linearly adsorbed carbonyl species on different Pd crystal planes (2105-2070 cm^{-1}). Those at low wave numbers have been related to bridged (two-fold bound, 2000-1895 cm^{-1}) and three-fold bound carbonyl species (1920-1830 cm^{-1}) on metallic Pd [60,61]. The Au-DP sample (profile III) shows an intense single band at 2105 cm^{-1}, which has been previously associated with CO linearly adsorbed on low coordination sites of metallic Au nanoparticles [62-64]. The spectrum of Au-IMP (profile IV) is characterised by a broad band with a maximum at 2063 cm^{-1} and a weak broad band at 2127 cm^{-1}. The presence of bands at wave numbers lower than those for CO linearly adsorbed on metallic Au (around 2100 cm^{-1}) has been reported previously [65-69]. The formation of bridged CO species can be discounted as they give rise to bands around 2000-1950 cm^{-1} [65,66]. Bands observed in the region 2050-2080 cm^{-1} can be ascribed either to CO adsorbed on metallic sites at the support/particle interface [67,68] or to CO adsorbed on negatively charged $Au^{\delta-}$ sites [65,69]. The presence of $Au^{\delta-}$ in Au-IMP can result as a consequence of the high chloride content (**Table 4.1**). The residual chloride may be located either on the alumina support in close proximity to the Au particles or associated directly with the Au particles as reported in recent papers [47,70,71]. Computer modelling of Cl^- interactions with Au (111) has revealed that Cl^- adsorption on Au^0 should result in a 0.05 positive electric charge associated with the Cl atom while the conjoined Au atom should develop a 0.190 negative electric charge where the other surface Au atoms adopt a negative charge from 0.05 to 0.08 [72]. The weak band at 2127 cm^{-1} has been previously assigned either to CO adsorbed on metallic Au at low CO coverage [20,60,73] or to CO-$Au^{\delta+}$ species [74-77]. At this juncture, we can not propose a definitive interpretation for this band but it is important to note that the IR spectra of Au-IMP and Au-DP are quite distinct. We associate these differences with the higher chloride content and the slightly larger Au particle size exhibited by Au-IMP.

In the case of the three spectra (profiles V-VII) for the bimetallic catalysts, we also observed carbonyl bands at high (2150-2050 cm^{-1}) and low (2000-1900 cm^{-1}) wave numbers but the spectra deviate significantly from that expected on the basis of the sum of the monometallic Au and Pd contributions (combination of profiles I and III and profiles II and IV). The bands at low wave numbers can again be assigned to CO

bridged species on Pd crystal planes. However, the broad and poorly resolved feature that characterised the monometallic Pd samples (profiles I and II) is transformed into two resolved peaks at 1955 and 1935 cm^{-1} for the bimetallic Pd-Au catalysts, *i.e.* at a higher wave number than that which characterises three-fold bound carbonyl species on Pd. These observations suggest the absence of three-fold CO bridges and the presence of only two-fold bridged species. At higher frequencies, a band at ~2082 cm^{-1} is observed for all the Pd-Au catalysts at a similar frequency to that of linear adsorbed CO on Pd but with a greater intensity. It should be noted that the band at 2105 cm^{-1}, associated with CO linearly adsorbed on gold, exhibits an appreciable decrease in intensity. By analogy with observations reported for Au-Pd films [78] and Au-Pd clusters on silica films [79], the disappearance of the three-fold bridge band and concomitant increases in intensity of the band due to linear CO on Pd^0 (with the decrease in intensity of the band due to linear CO on Au^0) represent evidence for the formation of bimetallic particles. The dilution of Pd in Au limits the extent of multi-bonded CO on Pd, especially three-fold bridge CO formation and thus favours linear interaction between CO and any isolated Pd^0 sites. The spectra of our Au-Pd samples also show bands at higher wave numbers (2110-2135 cm^{-1}), which were not systematically observed on Au-Pd films [78,80] or Au-Pd clusters [79]. However, in the latter case, a frequency shift of the band for CO linearly adsorbed on Au clusters (from 2109 to 2129 cm^{-1}) was noted with a decrease in CO coverage. Accordingly, we tentatively assign the bands at 2110-2135 cm^{-1} to CO linearly adsorbed on Au^0 sites in monometallic or bimetallic particles. Our DRIFTS results indicate that, in the case of the Pd-Au samples, the contribution of multi-bonded CO on Pd is reduced with respect to the linearly bonded CO on Pd. A geometric effect, due to the formation of bimetallic Pd-Au nanoparticles and resulting in a decrease in the size and/or the number of Pd ensembles required for multiple bonding (three-fold), can account for this response [81]. This suggests that there is a larger proportion of isolated singleton Pd sites in the Pd-Au/Al_2O_3 catalysts prepared by both DP and IMP. It should be noted that the slight shift of the band due to CO linearly adsorbed on Pd^0 in the Au-Pd samples has also been also observed by Goodman *et al.* [78] and attributed to changes in dipole-dipole coupling due to variations in CO intermolecular distances rather than to chemical interaction mediated by the substrate, *i.e*. an electronic effect.

4.3.2 Catalytic Response

Hydrogenation of *p*-chloronitrobenzene over Au-DP and Au-IMP generated exclusively the target product, *p*-chloroaniline, with no evidence of any hydrodenitrogenation, hydrodechlorination or ring reduction, in agreement with our earlier work [3,4]. The time-on-stream profiles for the conversion of *p*-chloronitrobenzene over both Au/Al_2O_3 catalysts are shown in **Figure 4.5** where it can be seen that Au-DP delivered a consistently higher fractional conversion ($x_{p\text{-}CNB}$) than Au-IMP.

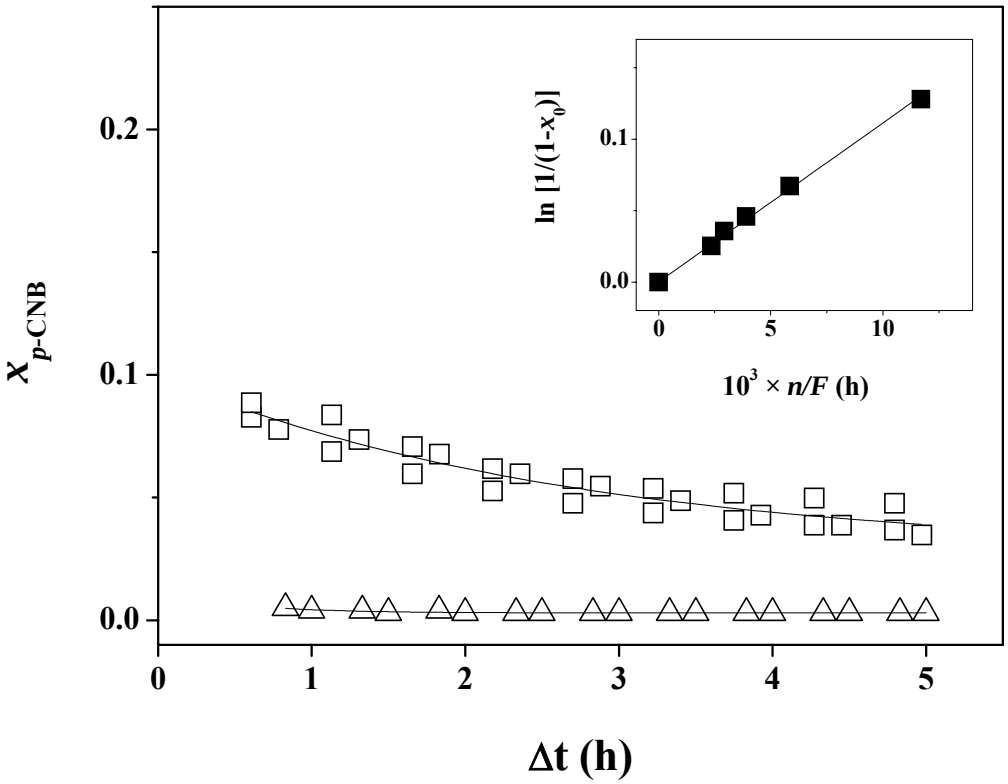

Figure 4.5: Variation of *p*-chloronitrobenzene fractional conversion ($x_{p\text{-}CNB}$) with time-on-stream over (Δ) Au-IMP (*p*-chloronitrobenzene/Au = 74 $mol_{p\text{-}CNB}$ mol_{Au}^{-1} h^{-1}) and (□) Au-DP (*p*-chloronitrobenzene/Au = 284 $mol_{p\text{-}CNB}$ mol_{Au}^{-1} h^{-1}). Inset: Pseudo-first order kinetic plot for the hydrogenation of *p*-chloronitrobenzene over Au-DP.

The temporal variation of activity can be represented by [82]

$$\frac{(x_{p\text{-}CNB} - x_0)}{(x_{5h} - x_0)} = \frac{\Delta t}{(\beta + \Delta t)} \qquad (4.1)$$

where x_{5h} represents fractional conversion after 5 h on-stream and β is a time scale fitting parameter. Fit convergence yields values for x_0, the initial fractional conversion, which is a measure of initial activity. The applicability of pseudo-first order kinetics can be tested using the following kinetic expression

$$\ln(1-x_0)^{-1} = k\left(\frac{n}{F}\right) \qquad \textbf{(4.2)}$$

and is demonstrated in the inset to **Figure 4.5** for Au-DP. The extracted pseudo-first order rate constants are given in **Table 4.2**.

Table 4.2: Pseudo-first order initial rate constants (k) for the hydrogenation of *p*-chloronitrobenzene over mono- and bimetallic catalysts and monometallic physical mixtures with product selectivities at the same initial fractional conversion (x_0 ~ 0.12).

Catalyst	Au/Pd	Rate constant (k, h^{-1})	Product(s) (% selectivity)
Au-DP	-	12	*p*-chloroaniline (100)
Pd/Au-DP	88	24	*p*-chloroaniline (100)
Pd/Au-DP	20	39	*p*-chloroaniline (100)
Pd/Au-DP	8	92	*p*-chloroaniline (80) nitrobenzene (20)
Au-IMP	-	1	*p*-chloroaniline (100)
Pd/Au-IMP	20	22	*p*-chloroaniline (100)
Pd-IMP + Au-IMP	20	130	nitrobenzene (80) aniline (20)
Pd-DP + Au-DP	20	77	nitrobenzene (45) aniline (55)

Converting the raw (experimental) rate constants to specific rates (per Au surface area, based on the mean Au particle size obtained from TEM), Au-DP delivered a rate (418 μmol m_{Au}^{-2} h^{-1}) that was over an order of magnitude higher than that recorded for Au-IMP (29 μmol m_{Au}^{-2} h^{-1}). This suggests that smaller Au particles are intrinsically more active. Taking an overview of the available literature, the role of Au particle size in hydrogenation reactions appears to be dependent on the nature of the reaction [83], the support [84] and even the catalyst preparation method [85]. Although under optimum reaction conditions, Au particles as large as 20 nm can exhibit significant activity [86], the general trend suggests increasing hydrogenation efficiency over smaller Au particles (≤ 10 nm) [56]. Mohr *et al.* [21] have considered the hydrogenation of acrolein to allyl alcohol over Au/TiO_2 and Au/ZrO_2 catalysts which exhibited similar Au particle sizes. The Au/TiO_2 catalyst was approximately twice as active and more selective in terms of allyl alcohol production, a response that was attributed to a greater preponderance of uncoordinated Au atoms associated with the titania support. Jia *et al.* [87] have recorded a maximum acetylene hydrogenation over Au/Al_2O_3 bearing Au particles of 3 nm diameter while Zanella *et al.* [24] have reported a significant increase in crotonaldehyde hydrogenation turnover frequency (TOF) over Au/TiO_2 with a decrease in Au particle size from 8.7 to 1.7 nm. The higher TOF exhibited by smaller Au particles may be associated with an increased capacity to activate/dissociate hydrogen [23,24]. Stobiński *et al.* [88] proposed that the chemisorption of H_2 is facilitated on Au surface atoms with low coordination number to form a AuH_2 complex. The lower activity associated with Au-IMP may also be related to the higher residual Cl content (**Table 4.1**). Indeed, we have demonstrated elsewhere [46] that the presence of chloride in Au/Al_2O_3 samples served to lower butadiene hydrogenation activity regardless of Au particle size. DRIFTS analysis has indicated that the presence of surface Cl species can induce strong modifications to the electronic state of the Au particles, which may affect reactant adsorption/activation and impact on hydrogenation performance. Indeed, there is evidence in the literature [47,49,70] that halides can adsorb on metallic gold with a resultant suppression of reactant adsorption. In short, the observed catalytic response for the monometallic samples where Au-DP outperformed Au-IMP can be attributed to a composite effect due to higher intrinsic activity for smaller Au particles (Au-DP) and the deleterious effects of surface Cl (Au-IMP).

In earlier work [3], we reported that the incorporation of Au with Pd *via* reductive deposition to generate $Au\text{-}Pd/Al_2O_3$ (where Pd/Au =10) did not influence *p*-

chloronitrobenzene hydrogenation activity or selectivity, which were equivalent to that delivered by Pd/Al_2O_3, where aniline was the predominant product. In this study, the inclusion of a low Pd content to Au/Al_2O_3 by DP and IMP (Au/Pd >8) was considered and the results are presented in **Figure 4.6** and **Table 4.2**.

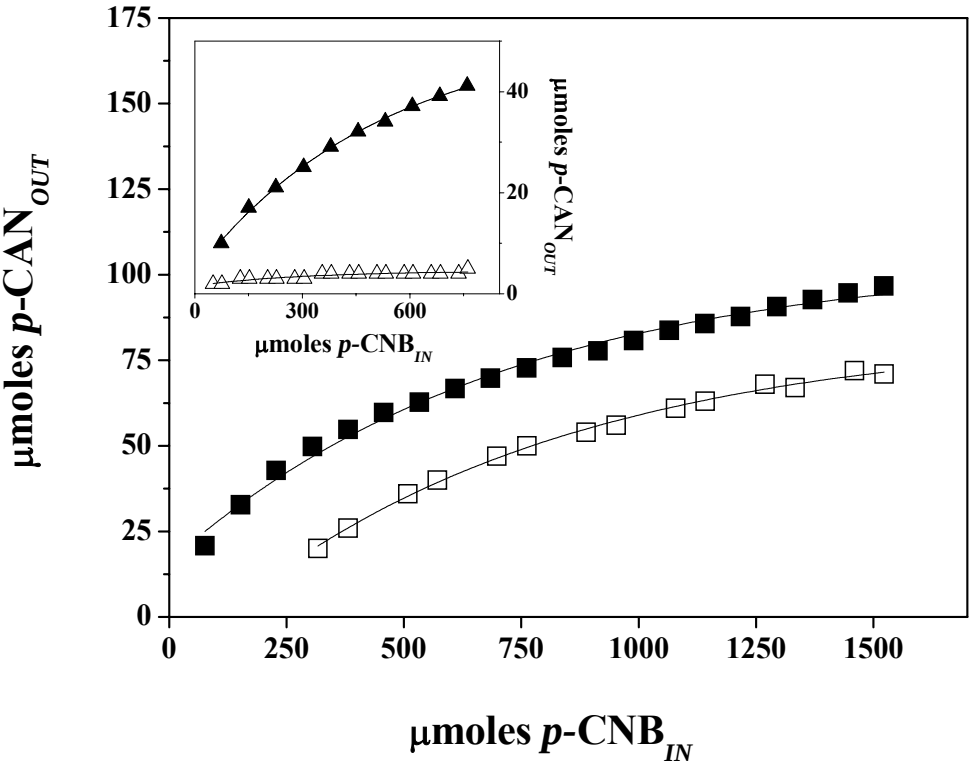

Figure 4.6: *p*-Chloroaniline output (μmoles *p*-CAN_{OUT}) as a function of the number of moles of *p*-chloronitrobenzene that had been processed (μmoles *p*-CNB_{IN}) over Au-DP (□) and Pd/Au-DP (■, Au/Pd = 20). Inset: Au-IMP (Δ) and Pd/Au-IMP (▲, Au/Pd = 20); inlet Au/*p*-chloronitrobenzene = 1×10^{-2} mol_{metal} h $mol_{p\text{-}CNB}^{-1}$.

The presence of Pd served to significantly raise the hydrogenation rate constant, which increased with increasing Pd content (**Table 4.2**). Where Au/Pd ≥ 20, the reaction was 100 % selective in terms of *p*-chloroaniline production with no detectable by-products. At a lower Au/Pd ratio, reaction over Pd-Au/Al_2O_3–DP (Au/Pd = 8) generated *p*-chloroaniline and nitrobenzene, the latter resulting from a hydrodechlorination step (see **Figure 4.1**), which is a characteristic of catalysis by Pd. The combination of both Au/Al_2O_3 and Pd/Al_2O_3 (DP and IMP samples) as physical mixtures (Au/Pd = 20) resulted in the formation of nitrobenzene and aniline (composite hydrodechlorination/hydrogenation product). Such a response demonstrates that, under these reaction conditions, Au/Al_2O_3 had little effect on reaction selectivity, which was governed by the Pd/Al_2O_3 component. This result is consistent with catalytic action due

to segregated Pd and Au particles where the catalytic properties of Pd dominate. At Au/Pd = 20, the rate constants delivered by the physical mixtures were appreciably higher than that delivered by Pd-Au/Al_2O_3 (both DP and IMP). Allied to the quite distinct product composition (at an equivalent *p*-chloronitrobenzene conversion, see **Table 4.2**), these results demonstrate that the contribution of Pd and Au to the catalytic action of Pd-Au/Al_2O_3 is not merely an additive effect and is the result of a surface Pd/Au synergism. The *p*-chloroaniline produced (μmoles *p*-CAN_{OUT}) as a function of the number of moles of *p*-chloronitrobenzene that had been processed (μmoles *p*-CNB_{IN}) is illustrated in **Figure 4.6** where it can be seen that the inclusion of Pd ensured an appreciably higher output of the target product for both DP and IMP bimetallics. These results establish the viability of Pd promoted selective -NO_2 reduction over supported Au.

4.3.3 General Discussion

The catalytic results demonstrate the bimetallic character of active sites in the Au/Pd-DP and Au/Pd-IMP samples (which promote exclusive formation of *p*-chloroaniline) as opposed to the segregation of both metals in the physical mixtures (leading to the formation of nitrobenzene and aniline). There is, however, an upper limit to the amount of Pd that can be incorporated in the Au system (Au/Pd ≤ 8), above which the selectivity of Au is diminished by the catalytic action of Pd, resulting in hydrodechlorination with the formation of nitrobenzene. The presence of bimetallic Au-Pd particles is consistent with our TPR and DRIFTS measurements. A feature of the IMP synthesis has been the incorporation of a significant residual Cl content which impacts on the reducibility of gold and induces metal particle sintering with an overall decrease in hydrogenation activity. Our results demonstrate that Pd-Au synthesis by DP with urea is an effective route for the production of efficient supported bimetallic particles. More detailed characterisation at the scale of individual metal nanoparticles is, however, necessary to explicitly establish the bimetallic character of the supported particles. Advanced electron microscopy techniques, such as High Angle Annular Dark Field (HAADF) or Energy Filtered Transmission Electron Microscopy (EFTEM) could provide this level of analysis. This is far from straightforward as the low proportion of Pd present renders detection very difficult. Nevertheless, the results presented here demonstrate that the use of Pd as a promoter in Au systems prepared by either co-deposition-precipitation and/or co-impregnation results in the formation of bimetallic

Au-Pd particles that promote the exclusive hydrogenation of *p*-chloronitrobenzene to *p*-chloroaniline. The promotional effect of Pd has resulted in a significant increase in hydrogenation rate while still retaining the selectivity due to Au. Future work will examine the applicability of these bimetallic Au-Pd systems to other industrially relevant substituted aromatic hydrogenation processes with a consideration of alternative promoters.

4.4 Conclusions

The catalytic results presented in this study establish Pd promotion of selective hydrogenation over supported Au, which can be exploited as a cleaner sustainable route for the production of *p*-chloroaniline. Both Au–DP and Au-IMP catalyse the exclusive hydrogenation of *p*-chloronitrobenzene to *p*-chloroaniline where Au–DP delivered a (greater than) order of magnitude higher specific hydrogenation rate, which we can link to smaller Au particle size and a lesser residual Cl content. The inclusion of Pd (at Au/Pd $\geq$ 20, IMP and DP) resulted in increased activity while retaining exclusivity to *p*-chloroaniline. At higher Pd contents, a further increase in reaction rate was accompanied by the formation of nitrobenzene as a result of a Pd promoted hydrodechlorination. DRIFTS analysis using CO as a probe molecule has demonstrated a decrease in the contribution due to multi-bonded CO on Pd relative to linearly bonded CO in the bimetallic samples, an effect that we take to be diagnostic of Pd-Au surface interaction.

4.5 References

[4.1] A. Boehnecke, J. Kielhorn, G. Konnecker, C. Pohlenz-Michel, I. Mangelsdorf, CICADS Report 48, W.H.O., Geneva, 2003, p. 78.

[4.2] X. D. Wang, M. H. Liang, J. L. Zhang, Y. Wang, Curr. Org. Chem., 11, 299 (2007)

[4.3] F. Cárdenas-Lizana, S. Gómez-Quero, M. A. Keane, Catal. Commun., 9, 475 (2008)

[4.4] F. Cárdenas-Lizana, S. Gómez-Quero, M. A. Keane, ChemSusChem, 1, 215 (2008)

[4.5] F. Cárdenas-Lizana, S. Gómez-Quero, M. A. Keane, Appl. Catal. A: Gen., 334, 199 (2008)

[4.6] C. Xi, H. Cheng, J. Hao, S. Cai, F. Zhao, J. Mol. Catal. A: Chem., 282, 80 (2008)
[4.7] Y.-Z. Chen, Y.-C. Chen, Appl. Catal. A: Gen., 115, 45 (1994)
[4.8] Y.-C. Liu, C.-Y. Huang, Y.-W. Chen, Ind. Eng. Chem. Res., 45, 62 (2006)
[4.9] Y.-C. Liu, Y.-W. Chen, Ind. Eng. Chem. Res., 45, 2973 (2006)
[4.10] Z. Yu, S. Liao, Y. Xu, B. Yang, D. Yu, J. Mol. Catal. A: Chem., 120, 247 (1997)
[4.11] V. Kratky, M. Kralik, M. Mecarova, M. Stolcova, L. Zalibera, M. Hronec, Appl. Catal. A: Gen., 235, 225 (2002)
[4.12] B. Coq, A. Tijani, F. Figuéras, J. Mol. Catal., 68, 331 (1991)
[4.13] V. L. Khilnani, S. B. Chandalia, Org. Proc. Res. Dev., 5, 257 (2001)
[4.14] M. L. Kantam, T. Bandyopadhyay, A. Rahman, N. M. Reddy, B. M. Choudary, J. Mol. Catal. A: Chem., 133, 293 (1998)
[4.15] B. Coq, A. Tijani, R. Dutartre, F. Figuéras, J. Mol. Catal., 79, 253 (1993)
[4.16] A. Tijani, B. Coq, F. Figuéras, Appl. Catal., 76, 255 (1991)
[4.17] X.-X. Han, R.-X. Zhou, G.-H. Lai, B.-H. Yue, X.-M. Zheng, J. Mol. Catal. A: Chem., 209, 83 (2004)
[4.18] B. Coq, A. Tijani, F. Figuéras, J. Mol. Catal., 71, 317 (1992)
[4.19] Q. Xu, X.-M. Liu, J.-R. Chen, R.-X. Li, X.-J. Li, J. Mol. Catal. A: Chem., 260, 299 (2006)
[4.20] G. C. Bond, D. T. Thompson, Catal. Rev.-Sci. Eng., 41, 319 (1999)
[4.21] C. Mohr, H. Hofmeister, P. Claus, J. Catal., 213, 86 (2003)
[4.22] C. Milone, C. Crisafulli, R. Ingoglia, L. Schipilliti, S. Galvagno, Catal. Today, 122, 341 (2007)
[4.23] E. Bus, J. T. Miller, J. A. van Bokhoven, J. Phys. Chem. B, 109, 14581 (2005)
[4.24] R. Zanella, C. Louis, S. Giorgio, R. Touroude, J. Catal., 223, 328 (2004)
[4.25] P. Claus, A. Brückner, C. Mohr, H. Hofmeister, J. Am. Chem. Soc., 122, 11430 (2000)
[4.26] F. Cárdenas-Lizana, S. Gómez-Quero, N. Perret, M. A. Keane, Gold Bulletin, in press (2009)
[4.27] M. Okumura, T. Akita, M. Haruta, Catal. Today, 74, 265 (2002)
[4.28] R. J. H. Grisel, P. J. Kooyman, B. E. Nieuwenhuys, J. Catal., 191, 430 (2000)
[4.29] J. K. Nørskov, Rep. Prog. Phys., 53, 1253 (1990)
[4.30] A. C. Gluhoi, S. D. Lin, B. E. Nieuwenhuys, Catal. Today, 90, 175 (2004)
[4.31] A. C. Gluhoi, M. A. P. Dekkers, B. E. Nieuwenhuys, J. Catal., 219, 197 (2003)
[4.32] M. O. Nutt, J. B. Hughes, M. S. Wong, Environ. Sci. Technol., 39, 1346 (2005)

[4.33] M. O. Nutt, K. N. Heck, P. Alvarez, M. S. Wong, Appl. Catal. B: Environ., 69, 115 (2006)

[4.34] P. Sangeetha, P. Seetharamulu, K. Shanthi, S. Narayanan, K.S. Rama Raob, J. Mol. Catal. A: Chem., 273, 244 (2007)

[4.35] L. M. Sikhwivhilu, N. J. Coville, B. M. Pulimaddi, J. Venkatreddy, V. Vishwanathan, Catal. Commun., 8, 1999 (2007)

[4.36] V. Vishwanathan, V. Jayasri, P. M. Basha, N. Mahata, L. M. Sikhwivhilu, N. J. Coville, Catal. Commun., 9, 453 (2008)

[4.37] R. Zanella, S. Giorgio, C. R. Henry, C. Louis, J. Phys. Chem. B, 106, 7634 (2002)

[4.38] G. Tavoularis, M. A. Keane, J. Chem. Technol. Biotechnol., 74, 60 (1999)

[4.39] G. Yuan, M. A. Keane, Chem. Eng. Sci., 58, 257 (2003)

[4.40] A. Sandoval, A. Gómez-Cortés, R. Zanella, G. Díaz, J. M. Saniger, J. Mol. Catal. A: Chem., 278, 200 (2007)

[4.41] C. Baatz, U. Prüße, J. Catal., 249, 34 (2007)

[4.42] Y.-J. Chen, C.-T. Yeh, J. Catal., 200, 59 (2001)

[4.43] A. C. Gluhoi, X. Tang, P. Marginean, B. E. Nieuwenhuys, Top. Catal., 39, 101 (2006)

[4.44] C. K. Costello, J. Guzman, J. H. Yang, Y. M. Wang, M. C. Kung, B. C. Gates, H. H. Kung, J. Phys. Chem. B, 108, 12529 (2004)

[4.45] E. Bus, R. Prins, J. A. van Bokhoven, Phys. Chem. Chem. Phys., 9, 3312 (2007)

[4.46] A. Hugon, L. Delannoy, C. Louis, Gold Bulletin, 41, 127 (2008)

[4.47] S. M. Oxford, J. D. Henao, J. H. Yang, M. C. Kung, H. H. Kung, Appl. Catal. A: Gen., 339, 180 (2008)

[4.48] C.-H. Lin, S. D. Lin, J.-F. Lee, Catal. Lett., 89, 235 (2003)

[4.49] F. Arena, P. Famulari, N. Interdonato, G. Bonura, F. Frusteri, L. Spadaro, Catal. Today, 116, 384 (2006)

[4.50] G. J. Hutchings, Catal. Today, 100, 55 (2005)

[4.51] E. D. Park, J. S. Lee, J. Catal., 186, 1 (1999)

[4.52] A. P. Kozlova, A. I. Kozlov, S. Sugiyama, Y. Matsui, K. Asakura, Y. Iwasawa, J. Catal., 181, 37 (1999)

[4.53] V. Ferrer, A. Moronta, J. Sánchez, R. Solano, S. Bernal, D. Finol, Catal. Today, 107-108, 487 (2005)

[4.54] F. Pinna, F. Menegazzo, M. Signoretto, P. Canton, G. Fagherazzi, N. Pernicone, Appl. Catal. A: Gen., 219, 195 (2001)

[4.55] M. Hosseini, S. Siffert, H. L. Tidahy, R. Cousin, J.-F. Lamonier, A. Aboukais, A. Vantomme, B.-L. Su, Catal. Today, 122, 391 (2007)

[4.56] P. Claus, Appl. Catal. A: Gen., 291, 222 (2005)

[4.57] B. Hammer, J. K. Nørskov, Nature, 376, 238 (1995)

[4.58] J. Harris, Surf. Sci., 221, 335 (1989)

[4.59] H.-S. Oh, J. H. Yang, C. K. Costello, Y. M.Wang, S. R. Bare, H. H. Kung, M. C. Kung, J. Catal., 210, 375 (2002)

[4.60] K. I. Hadjiivanov, G. N. Vayssilov, Adv. Catal., 47, 307 (2002)

[4.61] E. A. Sales, J. Jove, M. de Jesus Mendes, F. Bozon-Verduraz, J. Catal., 195, 88 (2000)

[4.62] M. A. Bollinger, M. A. Vannice, Appl. Catal. B: Environ., 8, 417 (1996)

[4.63] J. D. Grunwaldt, M. Maciejewski, O. S. Becker, P. Fabrizioli, A. Baiker, J. Catal., 186, 458 (1999)

[4.64] S. Minicò, S. Scirè, C. Crisafulli, A. M. Visco, S. Galvagno, Catal. Lett., 47, 273 (1997)

[4.65] F. Boccuzzi, A. Chiorino, M. Manzoli, D. Andreeva, T. Tabakova, J. Catal., 188, 176 (1999)

[4.66] J. Y. Lee, J. Schwank, J. Catal., 102, 207 (1986)

[4.67] M. Manzoli, A. Chiorino, F. Boccuzzi, Surf. Sci., 532, 377 (2003)

[4.68] F. Boccuzzi, A. Chiorino, S. Tsubota, M. Haruta, Catal. Lett., 29, 225 (1994)

[4.69] T. Diemant, Z. Zhao, H. Rauscher, J. Bansmann, R. J. Behm, Top. Catal., 44, 83 (2007)

[4.70] T. A. Baker, C. M. Friend, E. Kaxiras, J. Am. Chem. Soc., 130, 3720 (2008)

[4.71] I. Sobczak, A. Kusior, J. Grams, M. Ziolek, J. Catal., 245, 259 (2007)

[4.72] B. Qiao, Y. Deng, Appl. Catal. B: Environ., 66, 241 (2006)

[4.73] J. France, P. J. Hollins, J. Electron Spectrosc. Relat. Pehom., 64, 251 (1993)

[4.74] J.-D. Grunwaldt, A. Baiker, J. Phys. Chem. B, 103, 1002 (1999)

[4.75] Tz. Venkov, K. Fajerwerg, L. Delannoy, Hr. Klimev, K. Hadjiivanov, C. Louis, Appl. Catal. A: Gen., 301, 106 (2006)

[4.76] F. Boccuzzi, A. Chiorino, M. Manzoli, Surf. Sci., 454-456, 942 (2000)

[4.77] Z.-X. Gao, Q. Sun, H.-Y. Chen, X. Wang, W. M.H. Sachtler, Catal. Lett., 72, 1 (2001)

[4.78] T. Wei, J. Wang, D. W. Goodman, J. Phys. Chem. C, 111, 8781 (2007)

[4.79] K. Luo, T. Wei, C.-W. Yi, S. Axnanda, D. W. Goodman, J. Phys. Chem. B, 109, 23517 (2005)

[4.80] C. W. Yi, K. Luo, T. Wei, D. W. Goodman, J. Phys. Chem. B, 109, 18535 (2005)

[4.81] A. M. Venezia, V. La Parola, G. Deganello, B. Pawelec, J. L. G. Fierro, J. Catal., 215, 317 (2003)

[4.82] S. Jujjuri, E. Ding, E. L. Hommel, S. G. Shore, M. A. Keane, J. Catal., 239, 486 (2006)

[4.83] H. Sakurai, M. Haruta, Appl. Catal. A: Gen., 127, 93 (1995)

[4.84] C. Milone, R. Ingoglia, L. Schipilliti, C. Crisafulli, G. Neri, S. Galvagno, J. Catal., 236, 80 (2005)

[4.85] S. Schimpf, M. Lucas, C. Mohr, U. Rodemerck, A. Brückner, J. Radnick, H. Hofmeister, P. Claus, Catal. Today, 72, 63 (2002)

[4.86] J. E. Bailie, H. A. Abdullah, J. A. Anderson, C. H. Rochester, N. V. Richardson, N. Hodge, J. G. Zhang, A. Burrows, C. J. Kiely, G. J. Hutchings, Phys. Chem. Chem. Phys., 3, 4113 (2001)

[4.87] J. Jia, K. Haraki, J. N. Kondo, K. Domen, K. Tamaru, J. Phys. Chem. B, 104, 11153 (2000)

[4.88] L. Stobiński, L. Zommer, R. Duś, Appl. Surf. Sci., 141, 319 (1999)

Chapter 5

Exclusive Production of Chloroaniline from Chloronitrobenzene over Au/TiO_2 and Au/Al_2O_3

Exclusive nitro-group reduction at low reaction conversion over Au has been established in previous Chapters. With a view to increasing hydrogenation rate, the possible role of the support was investigated by direct comparison of Au/Al_2O_3 and Au/TiO_2 in the selective gas phase hydrogenation of *p*-chloronitrobenzene where catalytic behaviour has been correlated to critical characterization data.

5.1 Introduction

The concept of process efficiency in the chemical industry is being progressively redefined as a response to the increasing restrictions imposed by environmental legislation, which encourage the development of alternative and cleaner routes to a target product. Green chemistry is essential for sustainability where catalysis is established as a fundamental process component [1]. In the early 1970s, Bond *et al.* [2] studying the hydrotreatment of buta-1,3-diene and but-2-yne, reported what would constitute the first study addressing the use of gold in catalytic hydrogenation. It was proposed that surface defects and smaller Au particle sizes are required for significant hydrogenation activity, a proposition that has since been demonstrated [3,4]. Although Au delivers lower hydrogenation rates when compared with "traditional" metals (Pd and Pt), the possibility of a selective partial hydrogenation over Au has untapped potential. Gold has now been employed to hydrogenate reactants ranging from CO [5], CO_2 [5], NO_x [6,7], N_2O [8], "simple" alkenes [9], alkynes [2,10,11] and alkadienes [2,12], to more "complex" systems, *i.e.* *α,β*-unsaturated aldehydes, ketones and polyaromatics [4,12-17]. Moreover, recent publications [18-20] have established selectivity in the batch liquid phase hydrogenation of nitroarenes. In this study, we compare for the first time the action of Au/TiO_2 with Au/Al_2O_3 in the selective gas phase hydrogenation of *p*-chloronitrobenzene (*p*-CNB) and consider also the reactivity of the *o*- and *m*-isomers. The target product, *p*-chloroaniline (*p*-CAN), is a high production volume chemical used in the manufacture of many fine chemicals [21]. Large scale production has

involved the Fe promoted reduction of nitro compounds in acid media, *i.e.* the Béchamp process [22]. The major drawbacks to this approach are the production of Fe/FeO sludge waste and low selectivites/product yields [23]. As an alternative, liquid phase catalytic hydrogenation employing Pd and Pt has been proposed where the catalyst must show a high resistance to Cl poisoning [24]. Despite the appreciable work that has been conducted in batch systems, liquid phase hydrogenation has fallen short in terms of selectivity as a consequence of unwanted C-Cl bond scission [22,25]. Recent gas phase studies using Pd/TiO_2 [26] and promoted Pd/Al_2O_3 [27], while promising, have failed to achieve 100% selectivity to the target halo-amine.

The lower catalytic hydrogenation activity of gold is linked to a less effective activation/ dissociation of H_2 but it is believed that activity is strongly influenced by particle size, morphology, oxidation state and support interactions [28,29]. Significant activity in hydrogen mediated reactions has been achieved using nanoscale Au particles ($\leq$ 10 nm) [4,30], with an increase in specific hydrogenation rates for smaller particle sizes [13,15]. Oxides are the most commonly used Au supports, where non-reducible oxides (*e.g.* Al_2O_3, MgO and SiO_2) have been identified as "inert" when compared with reducible supports (*e.g.* Fe_2O_3, NiO_x, CoO_x and TiO_2) [31]; Au-oxide interactions can contribute to catalyst performance [32]. Such interactions can result in metal size/morphology changes and/or electron transfer that modifies the catalytic response [9,14,33-35]. Metal/support effects have been demonstrated to impact not only on catalytic activity but also on selectivity [16]. Indeed, Galvagno *et al.* [36], using a series of iron oxide supported Au catalysts in the hydrogenation of benzalacetone and cinnamaldehyde, concluded that the nature of the support (notably reducible supports) strongly influenced activity/selectivity and proposed that the formation of electron rich Au species *via* support-metal electron transfer resulted in an enhanced C=O activation. Lopez-Sanchez and Lennon [11], in the hydrogenation of propyne, reported a different activity-selectivity response over Au/TiO_2 and Au/Fe_2O_3, which was ascribed to differences in metal-support interactions. Haruta *et al.* [12] showed that selectivity to crotyl alcohol from crotonaldehyde over oxide supported Au (3-5 nm) was sensitive to the nature of the support, observing equivalent responses for Au/SiO_2 and Au/Al_2O_3 but significantly higher selectivity over Au/TiO_2. We have recently reported an exclusive conversion of *p*-CNB to *p*-CAN for continuous gas phase reaction over Au/Al_2O_3 [37]. Given the cases cited above, which establish the role that the metal-support can play in Au catalysis, we have extended that work to consider Au/TiO_2 and report herein the

results of a comparative study. Our results provide the basis for a sustainable high throughput production of haloamines under mild conditions.

5.2 Experimental

5.2.1 Catalyst Preparation and Activation

The Al_2O_3 (Puralox, Condea Vista Co.), TiO_2 (Degussa) and fumed SiO_2 (Sigma-Aldrich) supports were used as received. A 1 mol % Au loading was obtained by standard impregnation with a $HAuCl_4$ solution (Aldrich, 25×10^{-3} g cm^{-3}, pH = 2). The slurry was heated (2 K min^{-1}) to 353 K and maintained under constant agitation (600 rpm) in a He purge. The solid residue was dried in a flow of He at 383 K for 3 h and stored under He in the dark at 277 K. Prior to use in catalysis, the samples (sieved into a batch of 75 μm average diameter) were activated in 60 cm^3 min^{-1} H_2 at 2 K min^{-1} to 603 ± 1 K, which was maintained for 2.5 h. After activation, the samples were passivated in 1% v/v O_2/He at room temperature for off-line analysis.

5.2.2 Catalysis Procedure

Reactions were carried out under atmospheric pressure, in situ after activation, in a fixed bed vertical glass reactor (l = 600 mm, i.d. = 15 mm) at T = 453 K. The catalytic reactor, and operating conditions to ensure negligible heat/mass transport limitations, have been fully described elsewhere [38] but some features, pertinent to this study, are given below. A preheating zone (layer of borosilicate glass balls) ensured that the organic reactant was vaporized and reached the reaction temperature before contacting the catalyst. Isothermal conditions (± 1 K) were maintained by thoroughly mixing the catalyst with ground glass (75 μm) [39]. The temperature was continuously monitored by a thermocouple inserted in a thermowell within the catalyst bed. The reactant was delivered, in a co-current flow of H_2, *via* a glass/teflon air-tight syringe and a teflon line, using a microprocessor controlled infusion pump (Model 100 kd Scientific) at a fixed calibrated flow rate, with an inlet CNB molar flow over the range 0.1-0.4 $mmol_{CNB}$ h^{-1}; the molar Au to inlet CNB feed rate (F) spanned the range 2×10^{-3} - 43×10^{-3} h. The H_2 content was up to 50 times in excess of the stochiometric requirement (< 1% v/v Aromatic/H_2), the flow rate of which was monitored using a Humonics (Model 520) digital flowmeter; $GHSV = 2 \times 10^4$ h^{-1}. In a series of blank tests, passage of each reactant in a stream of H_2 through the empty reactor or over the support alone, *i.e.* in the absence of Au, did not result

in any detectable conversion. The reactor effluent was frozen in a liquid N_2 trap for subsequent analysis which was made using a Perkin-Elmer Auto System XL gas chromatograph (programmed split/splitless injector and a flame ionization detector), employing a DB-1 50 m × 0.20 mm i.d., 0.33 μm film thickness capillary column (J&W Scientific), as described elsewhere [40]. *p*-CNB (Aldrich, ≥ 99.9% purity), *o*-CNB (Aldrich, > 99.0%), *m*-CNB (Aldrich, > 98.0%) and the solvents (ethanol: Aldrich, 96 %; 1-propanol: Aldrich, 99.7%; 1-butanol: Riedel-de Häen, ≥ 99.5% and 1-pentanol: Fluka, > 98.0 %) were used as supplied without further purification.

5.2.3 Catalyst Characterization

BET surface area, temperature programmed reduction (TPR) and H_2 chemisorption were determined using the commercial CHEM-BET 3000 (Quantachrome) unit. The samples were loaded into a U-shaped Pyrex glass cell (100 mm ×. 3.76 mm i.d.) and heated in 17 cm^3 min^{-1} 5% v/v H_2/N_2 (Brooks mass flow controlled) to 603 K at 2 K min^{-1}. The effluent gas passed through a liquid N_2 trap and H_2 consumption was monitored by a thermal conductivity detector, with data acquisition/manipulation using the TPR Win^{TM} software. The reduced samples were maintained at the final temperature for at least 1 h in H_2, swept with a 65 cm^3 min^{-1} N_2 for 1.5 h, cooled to room temperature and subjected to H_2 chemisorption using a pulse (10-50 μl) titration procedure. BET areas were recorded with a 30% v/v N_2/He flow; pure N_2 (99.9%) served as the internal standard. At least 2 cycles of nitrogen adsorption-desorption were employed to determine total surface area using the standard single point method. H_2 uptakes and BET surface areas were reproducible to within ± 5% and the values quoted in this paper are the mean.

Diffuse reflectance UV-vis (DR UV-vis) measurements were conducted using a Perkin Elmer Lambda 35 UV-Vis Spectrometer with $BaSO_4$ powder as reference; absorption profiles were calculated from the reflectance data using the Kubelka-Munk function. A high resolution UV-Vis spectrum of the aqueous $HAuCl_4$ solution was obtained using a Spectronic Unicam HEλIOS β UV-Visible Spectrophotometer. Powder X-ray diffractograms were recorded on a Bruker/Siemens D500 incident X-ray diffractometer using Cu Kα radiation. The samples were scanned at 0.02º $step^{-1}$ over $20º \leq 2\theta \leq 90º$ (scan time = 5 s $step^{-1}$). Diffractograms were identified using the JCPDS-

ICDD reference standards, *i.e.* anatase (21-1272), rutile (21-1276), γ-Al_2O_3 (10-0425) and Au (04-0784). Gold particle size (d_{hkl}) was estimated using the Scherrer equation:

$$d_{hkl} = \frac{K \cdot \lambda}{\beta \cdot \cos\theta} \qquad (5.1)$$

where K = 0.9, λ is the incident radiation wavelength (1.54056 Å), β is the peak width at half the maximum intensity and θ represents the diffraction angle corresponding to the (111) plane for Au metal. Au particle morphology and size was also determined by transmission electron microscopy analysis; JEOL JEM 2011 HRTEM unit with a UTW energy dispersive X-ray detector (Oxford Instruments) operated at an accelerating voltage of 200 kV and using Gatan DigitalMicrograph 3.4 for data acquisition/manipulation. The specimens were prepared by dispersion in acetone and deposited on a holey carbon/Cu grid (300 Mesh). Up to 300 individual Au particles were counted for each catalyst and the surface area-weighted metal diameter (d_{TEM}) was calculated from

$$d_{TEM} = \frac{\sum_i n_i d_i^3}{\sum_i n_i d_i^2} \qquad (5.2)$$

where n_i is the number of particles of diameter d_i.

5.3 Result and Discussion

5.3.1 Catalyst activity/selectivity

The hydrogenation of *p*-CNB over Au/TiO_2, Au/Al_2O_3 and Au/SiO_2 generated *p*-CAN as the sole product, *i.e.* 100% selectivity in promoting -NO_2 reduction with no evidence of hydrodechlorination or ring reduction. Such reaction exclusivity, notably the absence of any dechlorination, is unique when compared with the catalytic systems tested to date [22] and represents a critical advancement in the clean production of haloamines. Over the range of inlet *p*-CNB/Au considered, Au/SiO_2 delivered low conversions ($x_{p\text{-}CNB} \leq 0.02$), activity that was an order of magnitude lower than that generated by Au/TiO_2 and Au/Al_2O_3. We accordingly focused our attention on a comparison of Au/TiO_2 with Au/Al_2O_3 in order to develop an efficient *p*-CNB → *p*-

CAN process. The temporal dependence of *p*-CNB fractional conversion, shown in **Figure 5.1** (I), reveals an induction period where activity declined (slightly) to attain a steady state conversion after 3 h on-stream.

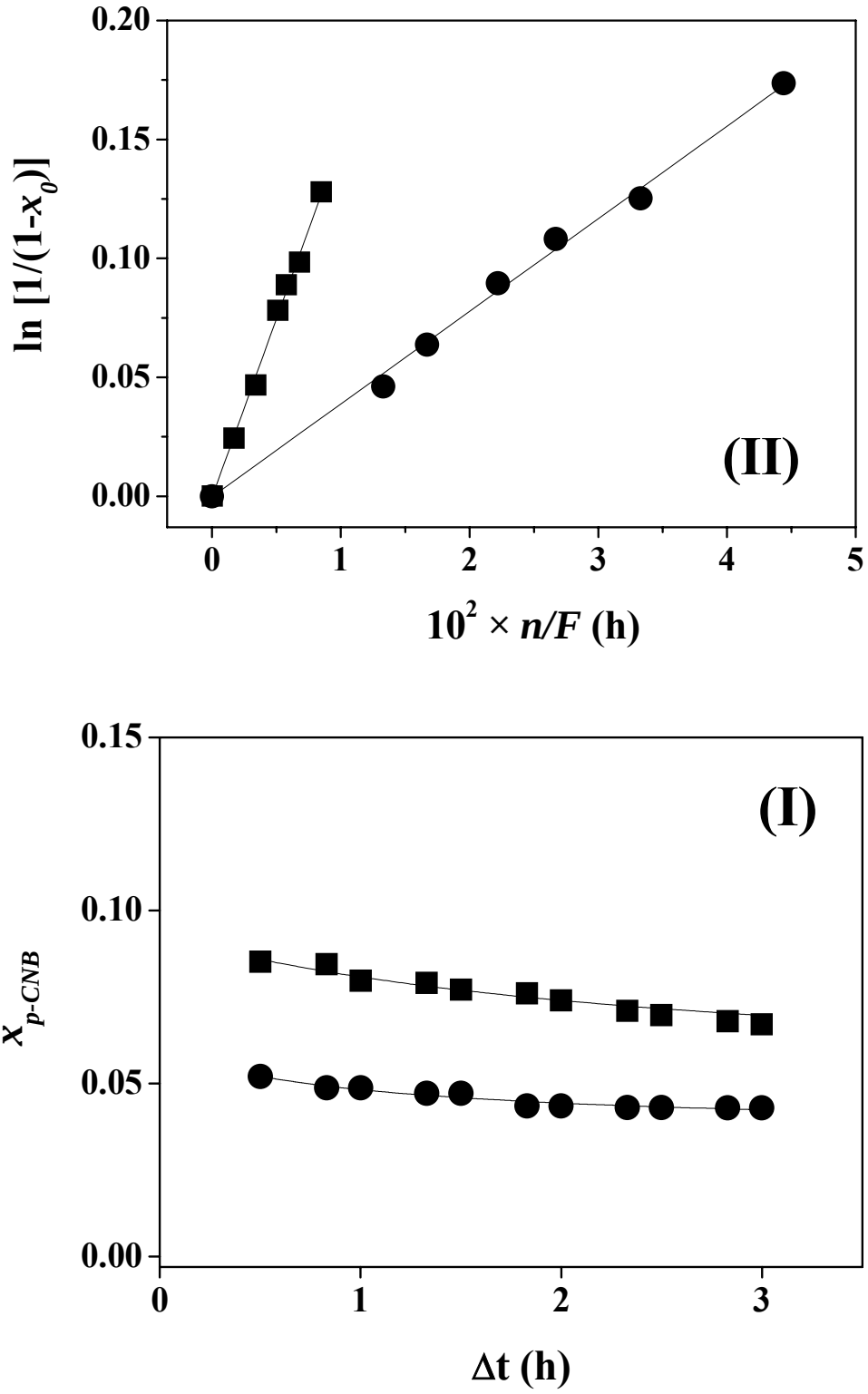

Figure 5.1: (I) Variation of *p*-CNB (in butanol) fractional conversion ($x_{p\text{-}CNB}$) to *p*-CAN with time-on-stream over Au/TiO_2 (■) and Au/Al_2O_3 (●) (Au/*p*-CNB= 10^{-2} mol_{Au} h $mol_{p\text{-}CNB}^{-1}$); lines represent fit to Equation (5.3). (II) Pseudo-first order kinetic plot for reaction over Au/TiO_2 (■) and Au/Al_2O_3 (●).

This temporal variation of activity can be represented by the empirical relationship [41]

$$\frac{\Delta t}{(\beta + \Delta t)} = \frac{(x_{p\text{-}CNB} - x_0)}{(x_{3h} - x_0)} \qquad \textbf{(5.3)}$$

where β is a time scale fitting parameter, x_{3h} is the fractional conversion after 3 h on-stream and x_0 represents the initial fractional conversion. Fit convergence allows us to extract values for x_0, which we employ as a measure of initial catalyst activity. We applied a pseudo-first order kinetic treatment in our earlier report [42] for reaction under plug-flow conditions where H_2 was maintained far in excess, which gives

$$\ln\left[\frac{1}{(1 - x_0)}\right] = k\left(\frac{n}{F}\right) \qquad \textbf{(5.4)}$$

The parameter F represents the inlet hourly molar CNB feed rate and n is the number of moles of Au in the catalyst bed; n/F has the physical significance of contact time. The linear fits shown in **Figure 5.1** (II) confirm the applicability of the kinetic treatment. The resultant pseudo-first order rate constants (k, h^{-1}) are given in **Table 5.1** where Au/TiO_2 consistently generated higher values. Converting the raw rate constants to specific rates (per Au surface area, see **Table 5.1**), Au/TiO_2 delivered values that were up to four times greater than those recorded for Au/Al_2O_3, indicative of a support effect. Indeed, our observation can supplement earlier studies that demonstrated higher activity in liquid phase hydrogenation for Au/TiO_2 when compared with other oxide supported Au systems [12,43]. Furthermore, in gas phase hydrogenation, higher rates over other transition metals supported on TiO_2 *vs.* Al_2O_3 (*e.g.* Ni [44] and Pt [45]) have also been reported. The *p*-CNB feed was introduced to the reactor as an alcohol solution and subsequently vaporised before contacting the catalyst. There was a measurable decrease in activity in going from ethanol to pentanol, notably in the case of the less active Au/Al_2O_3. In gas phase applications, rate inhibition due to the solvent has been attributed to a competitive solvent/reactant adsorption on the catalyst [38,46]. There is evidence in the literature that, in gas phase applications, alcohols can adsorb on Al_2O_3 [47-49] and TiO_2 [49,50]. Surface interaction can occur *via* the hydroxyl group oxygen and a cation vacancy (Lewis acid site) or *via* the "acidic" H of the alcohol and a surface oxygen atom (Lewis base site) [47,49,51]. Lewis acid and base sites are generated by

Table 5.1: Pseudo-first order rate constant (k) for the hydrogenation of *p*-CNB (as C_2-C_5 alcohol solutions) to *p*-CAN: Au/*p*-CNB = 10^{-2} mol_{Au} h $mol_{p\text{-}CNB}^{-1}$. Temperature programmed reduction (TPR) peaks, BET surface area, H_2 uptake, DR UV-vis spectroscopic characteristics, Au particle size mean/range and specific Au surface area (S_{Au}) associated with Au/TiO_2 and Au/Al_2O_3.

		Au/TiO_2	Au/Al_2O_3
Rate Constant (k)	Ethanol	19^a $(18\times10^{-4})^b$	7^a $(10\times10^{-4})^b$
	Propanol	17^a $(16\times10^{-4})^b$	5^a $(7\times10^{-4})^b$
	Butanol	15^a $(14\times10^{-4})^b$	4^a $(6\times10^{-4})^b$
	Pentanol	14^a $(13\times10^{-4})^b$	2^a $(<3\times10^{-4})^b$
TPR T_{max} (K)		432, 457	434
BET area (m^2 g^{-1})		47	161
$H_{2\ uptake}$ (μmol $g_{catalyst}^{-1}$)		0.4	0.4
DR UV-vis A_{max} (nm)		568	540
d_{hkl}[c] (nm)		-[d]	18
d_{TEM}[e] (nm)		6	9
Au size range[e] (nm)		1-10	1-20
S_{Au} (m^2 g_{Au}^{-1}) [e,f]		53	35

[a]units: h^{-1}
[b]units: $mol_{p\text{-}CNB}$ h^{-1} m_{Au}^{-2}
[c]based on XRD line broadening (See **Equation (5.1)**)
[d]XRD response did not permit an accurate Au size measurement
[e]based on TEM analysis (See **Equation (5.2)**)
[f]$S_{Au} = 6/(\rho_{Au} \times d_{TEM})$ where $\rho_{Au} = 18.88$ g cm^{-3}

heating Al_2O_3 and TiO_2 to temperatures in excess of 473 K [52] and 500 K [50], respectively, and can be formed during our TPR treatment. We tentatively attribute the lower hydrogenation rates obtained with the longer chain alcohols to a more facile polarization (of pentanol relative to ethanol) [53] that results in a stronger interaction with the catalyst, which serves to inhibit *p*-CNB hydrogenation to a greater degree. The hydrogenation of the *o*- and *m*-CNB isomers over both catalysts also yielded the corresponding amino-compound with 100% selectivity. The associated pseudo-first order rate constants for the three isomers are presented in **Figure 5.2** where the

following reactivity sequence applies to both catalysts: *o*- > *p*- > *m*-; Au/TiO_2 consistently delivered the higher reaction rate.

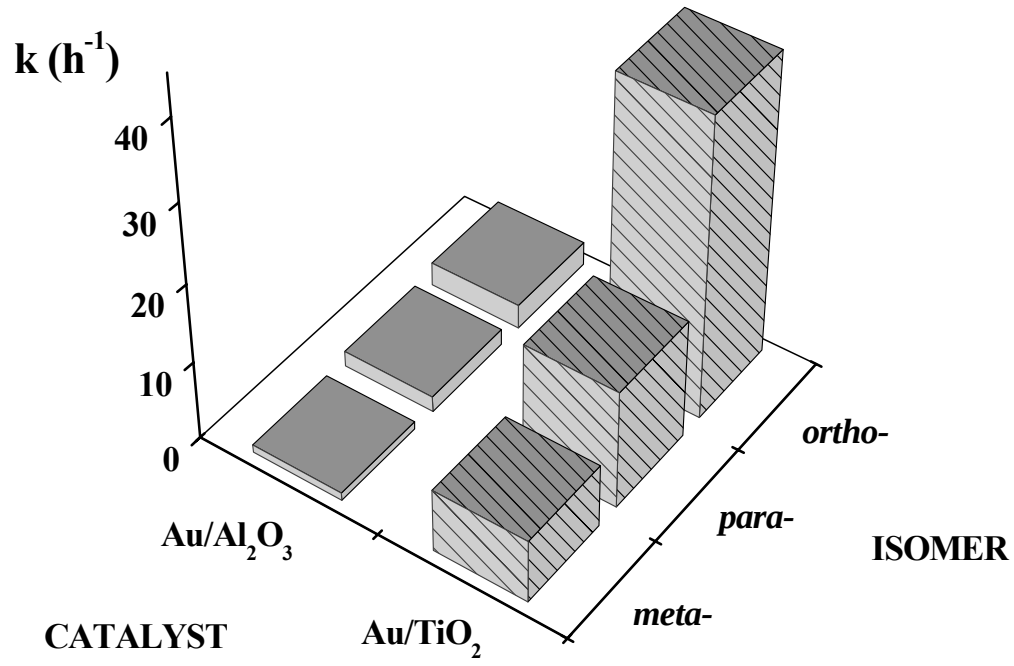

Figure 5.2: Pseudo-first order rate constants (k) for the hydrogenation of the three CNB isomers (in butanol) to the corresponding chloroaniline isomer over Au/TiO_2 (hatched bars) and Au/Al_2O_3 (solid bars): Au/CNB = 10^{-2} mol_{Au} h mol_{CNB}^{-1}.

The participation of a negatively charged intermediate has been proposed elsewhere [37], resulting from N=O attack by chemisorbed hydrogen that acts as a weak nucleophilic agent [25,54]. The higher rates generated for *o*- and *p*-isomers relative to the *m*-form suggests that resonance stabilisation rather than steric effects govern the reaction rate, *i.e.* the involvement of a greater number of resonance structures in the case of the *o*- and *p*-isomers as opposed to *m*-CNB [55]. Furthermore, the higher reaction rate achieved for the *o*-isomer can be explained on the basis of the close proximity of the $-NO_2$ and -Cl substituents on the ring which results in a more electrophilic N [56], *i.e.* the more positively charged nitrogen in the nitro group makes it more susceptible to nucleophilic attack. This is in contrast to batch liquid systems where a lower conversion of *o*-CNB has been reported and attributed to steric constraints [57].

5.3.2 Catalyst Characterization

In order to account for the differences in catalytic activity recorded for Au/TiO_2 and Au/Al_2O_3, the catalysts were subjected to a characterisation that focused on the activation step and the ultimate Au particle size/dispersion. The BET surface areas, H_2 chemisorption uptakes, range/mean Au particle sizes and specific Au surface areas are given in **Table 5.1**; the temperature programmed reduction (TPR) profiles are presented in **Figure 5.3**.

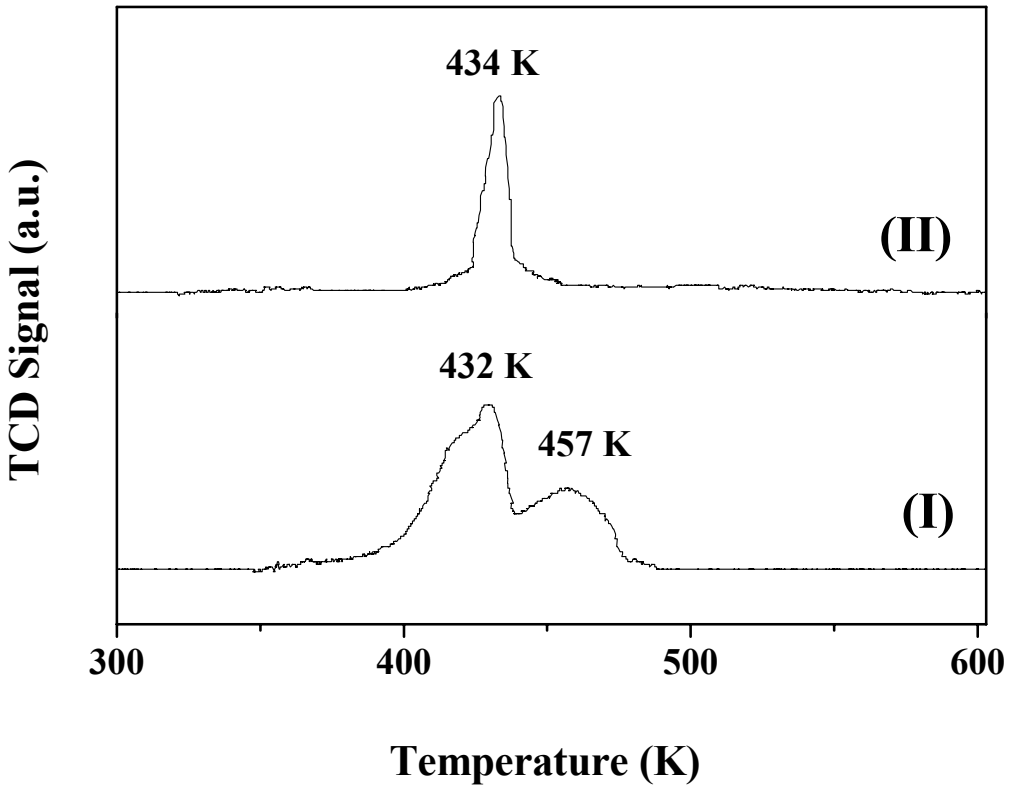

Figure 5.3: TPR profiles for (I) Au/TiO_2 and (II) Au/Al_2O_3.

The profile for Au/TiO_2 (profile I) is characterised by two positive signals, a principal peak at 432 K with a shoulder at 457 K. In contrast, the TPR of Au/Al_2O_3 (profile II) shows a single peak at T_{max} = 434 K, which can be linked to the reduction of Au^{3+} to Au^0. A single step reduction of Au/Al_2O_3 has been recorded previously at 436 K [58] and 503 K [59]. The principal reduction peak for Au/TiO_2 arose at a very similar temperature to that recorded for Au/Al_2O_3 and can also be ascribed to the reduction of

cationic gold to zero valent metal. The secondary peak suggests a stronger interaction of the gold precursor with TiO_2, necessitating higher reduction temperature. A similar effect has been reported for CrO_x supported on Al_2O_3 and TiO_2, where the TPR profiles where characterized by one (593–663 K) and two (553–593 K and 693–713 K) distinct reduction peaks, respectively, and attributed to differences in support interaction [60]. Venugopal and Scurrell [61] have reported an increase in the reduction temperature for Au_xO_y when supported on Fe_2O_3 and associated this with metal oxide-support interaction(s). The number of reported TPR analyses of supported Au is as of yet insufficient to allow any comprehensive comparisons or explicit TPR peak assignments. Indeed, the additional peak in the TPR of Au/TiO_2 may result from a partial reduction of the support that is promoted by gold. Idakiev *et al.* [62], working with deposited-precipitated Au/TiO_2, attributed a TPR peak at 373 K to a $Ti^{4+} \rightarrow Ti^{3+}$ transformation at the metal/support interface. It should be noted that TPR of the TiO_2 support (without Au inclusion) up to 973 K did not generate any response due to H_2 consumption. The H_2 uptakes recorded for both supported Au catalysts post-TPR are equivalent and close to the instrument detection limits, confirming the low capacity of Au for H_2 chemisorption, as has been noted in the literature [4].

The UV-Vis spectrum recorded for the aqueous $AuCl_4^-$ solution (profile I) is presented in **Figure 5.4** where the band at *ca.* 383 nm can be attributed to Cl-Au charge transfer [63,64]. The DR UV-vis spectra between 400-900 nm for the TiO_2 (profile IIa) and Al_2O_3 (IIIa) supports are featureless, as noted elsewhere [58,65] and any response after impregnation/reduction can be assigned to the supported Au phase. The spectra (profiles IIb and IIIb) for the activated catalysts exhibit absorption bands with maximum intensity (A_{max}) at 568 nm and 540 nm for Au/TiO_2 and Al_2O_3, respectively. It has been established in the literature that zero valent gold absorbs between 500-600 nm [58,66]. Furthermore, the absorption band appears to be sensitive to metal dispersion and the nature of the support [67] Centeno *et al.* [68] recorded a band at 534 nm for Au/Al_2O_3 (8.2 nm) that was shifted to a longer wavelength (569 nm) for smaller Au particles (3.8 nm) associated with $Au/CeO_2/Al_2O_3$. In contrast, Hu and Blackwood [69] reported a shift in wavelength to higher values with increasing Au size on TiO_2. Our UV response is consistent with a supported Au^0 phase post-TPR for both catalysts where the differences in characteristic wavelength may be the result of differences in Au particle size.

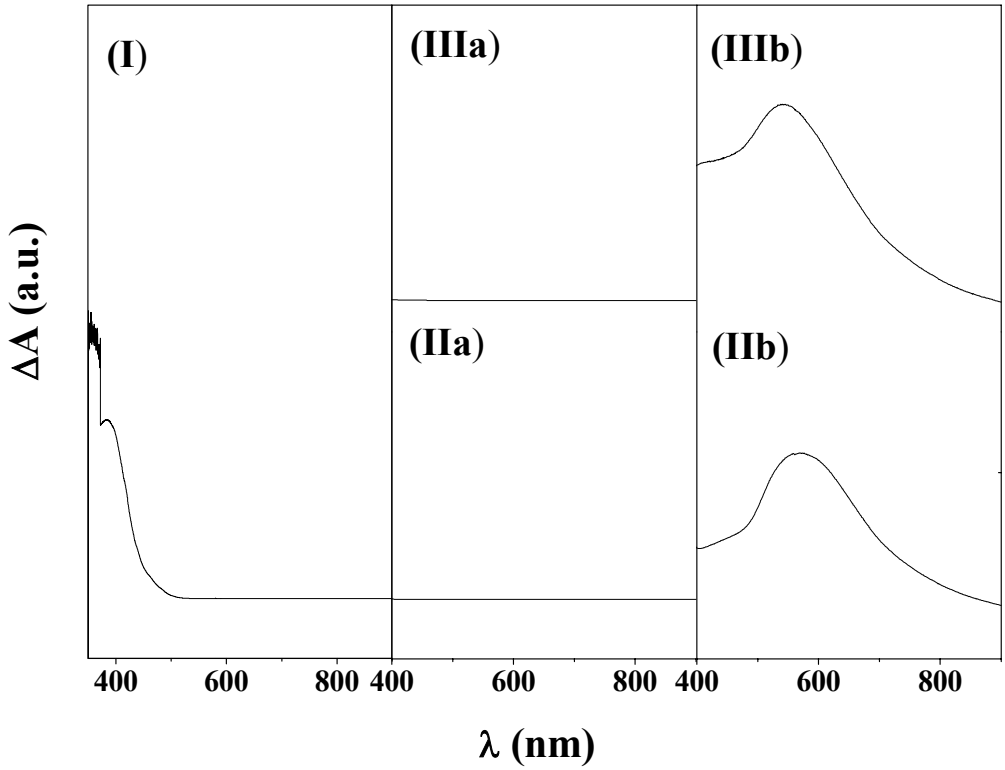

Figure 5.4: UV-Vis spectrum of (I) $HAuCl_4$ aqueous solution and DR UV-vis spectra of (IIa) TiO_2, (IIIa) Al_2O_3, and reduced/passivated (IIb) Au/TiO_2 and (IIIb) Au/Al_2O_3.

The XRD patterns of the oxide supports and the activated gold catalysts are given in **Figure 5.5**. Peak assignments for TiO_2 (profile Ia, $2\theta = 25.3°$, 37.8° and 48.1°) are consistent with the (101), (004) and (200) planes associated with tetragonal anatase (JCPDS-ICDD 21-1272). The peak at 27.4°, associated with (110) plane, suggests the presence of tetragonal rutile (JCPDS-ICDD 21-1276). The XRD response is consistent with a mixture of anatase (80% volume fraction) and rutile forms of TiO_2 which has been reported elsewhere [70] for Degussa P25. The peaks generated for Al_2O_3 (profile IIa) over the range $2\theta = 30\text{-}70°$ can be assigned to the (311), (222), (400) and (440) planes of cubic γ-Al_2O_3 (JCPDS-ICDD 10-0425). XRD diffractograms for Au/TiO_2 (Ib) and Au/Al_2O_3 (IIb) exhibit, in addition to the support peaks, a response due to Au metal (JCPDS-ICDD 04-0784), *i.e.* $2\theta = 38.1°$, 44.4°, 64.7° and 77.5° corresponding to (111), (200), (220) and (311) planes, respectively. It should be noted that the XRD signals for Au on Al_2O_3 are strong and well defined. In contrast, only the main peak for metallic Au ($2\theta = 38.1°$) is distinguishable for Au/TiO_2 and overlaps with the response for (004) anatase. The latter suggests that Au is present as very small crystallites in Au/TiO_2. Standard X-Ray line broadening analysis based on the Scherrer formula yielded a mean

metal particle size of 18 nm in the case of Au/Al_2O_3, while the XRD response in the case of Au/TiO_2 was too weak to allow a valid mean Au size estimation.

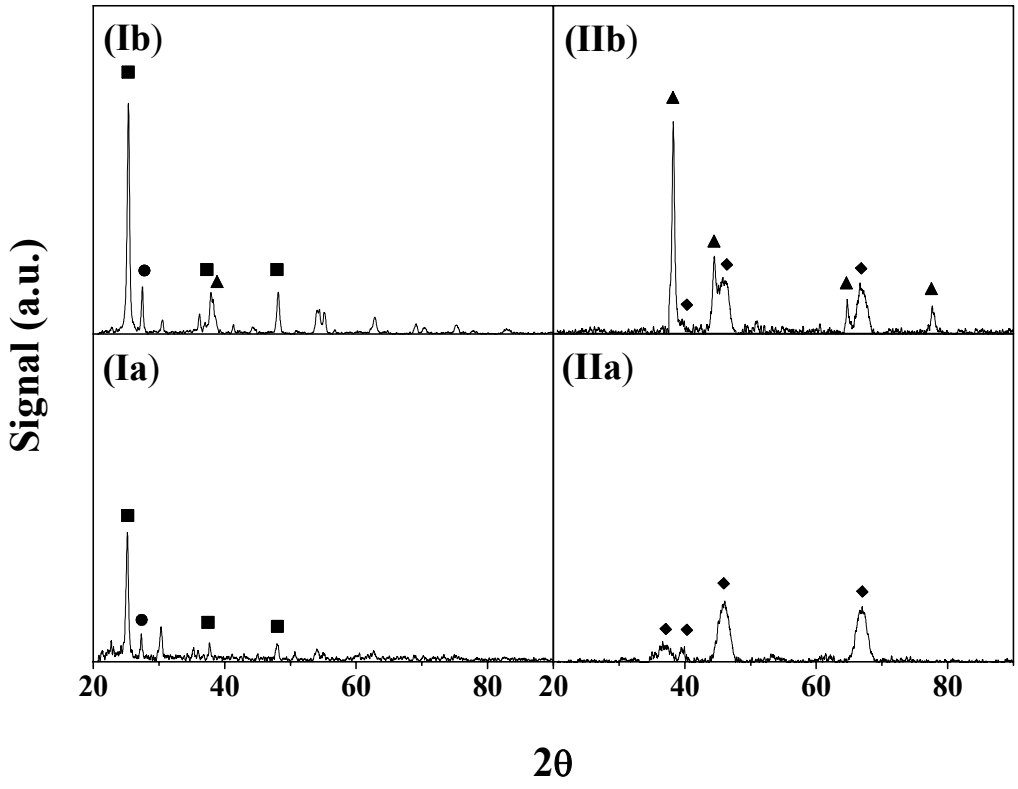

Figure 5.5: XRD patterns for (Ia) TiO_2 and (IIa) Al_2O_3 supports and the reduced/passivated (Ib) Au/TiO_2 and (IIb) Au/Al_2O_3. *Note*: peak assignments based on JCPDS-ICDD reference data: (■) anatase (21-1272); (●) rutile (21-1276); (♦) γ-Al_2O_3 (10-0425); (▲) Au (04-0784).

Particle size/morphology was further examined by TEM analysis. Representative (a) low, (b) medium and (c) high resolution TEM images of (I) Au/TiO_2 and (II) Au/Al_2O_3 are given in **Figure 5.6**. The diffractogram patterns for a single particle in (Ic) Au/TiO_2 and (IIc) Au/Al_2O_3 have been included as insets. In both cases, the spacings (0.23 and 0.20 nm) between the planes in the atomic lattice are characteristic of the (111) and (200) planes of metallic gold (JCPDS-ICDD 04-0784). The metal particles associated with Au/Al_2O_3 fall within a 1-20 nm size range with the majority of the particles in the 2-8 nm range (see **Figure 5.6**, images (IIa) and (IIb)). Nevertheless, there is a significant presence of larger particles (15-20 nm, see **Figure 5.6**, image

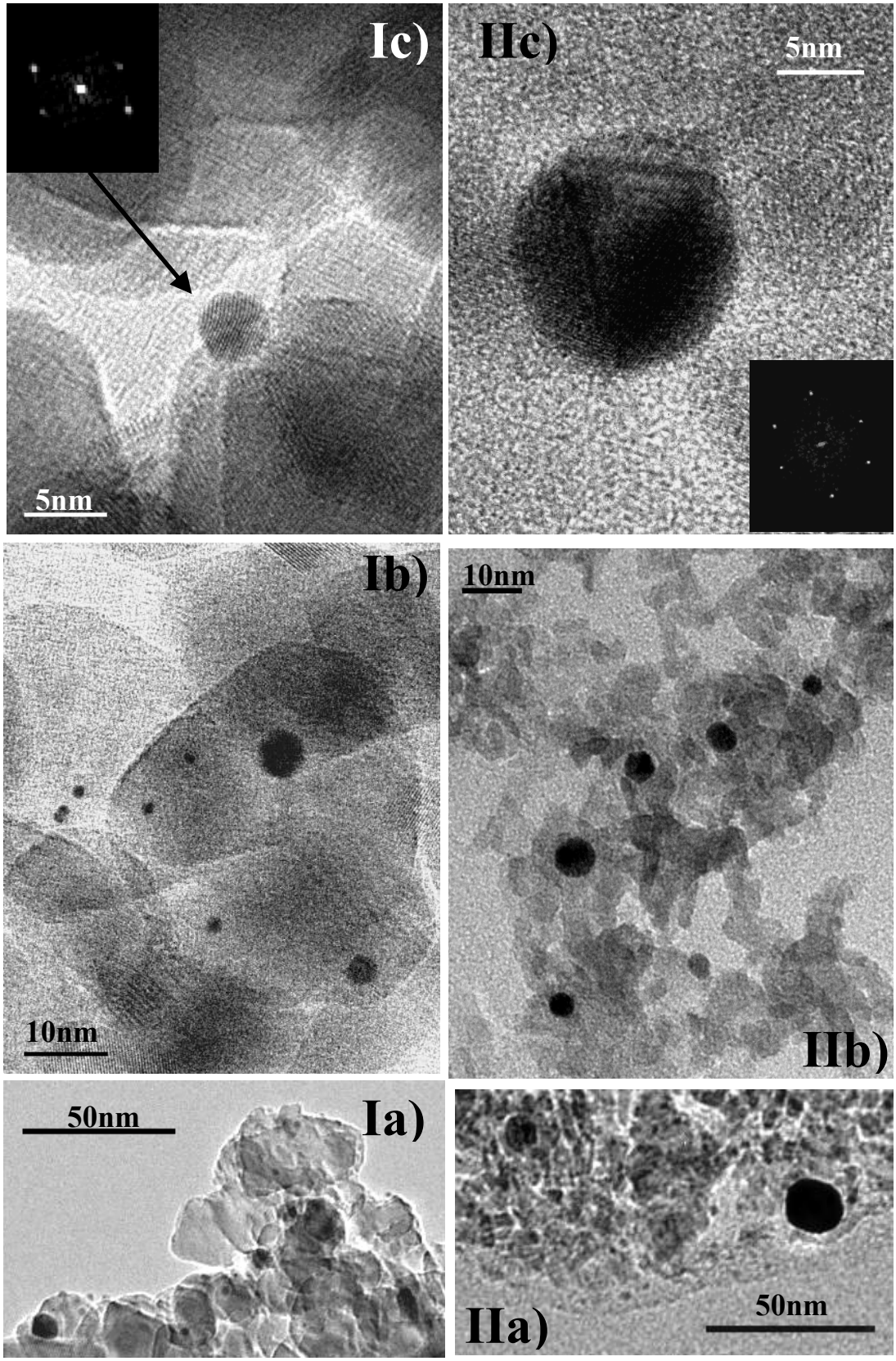

Figure 5.6: Representative TEM images of (I) Au/TiO_2 and (II) Au/Al_2O_3; (a) low, (b) medium and (c) high resolution.

(IIa)), which can account for the XRD response (**Figure 5.5** IIb). In contrast, Au/TiO_2 exhibited a narrower size distribution (1-10 nm) to give a surface area weighted mean particle size (6 nm) that is lower than that obtained for Au/Al_2O_3 (9 nm). The gold particles exhibited a near spherical morphology (see **Figure 5.6**, images (Ic) and (IIc), as noted in the literature [71]. Gold particle size (and distribution) can have a direct impact on hydrogenation activity where the presence of nanoscale Au particles ($\leq$ 10 nm) has been deemed essential for significant activity [4,30] with a decrease in efficiency for larger Au particles [12,13,72]. We should, however, flag recent work by Bus *et al.* [73], which has demonstrated that hydrogenation activity/selectivity over supported Au is dependent on the nature of the functional group that is attacked. The occurrence of defects is higher for smaller Au particles where steps, edges and corners have been proposed as hydrogen adsorption/activation sites [3]. Claus *et al.* [15] have reported higher rates over smaller particles in the hydro-treatment of acrolein over Au/ZrO_2 (4-8 nm). In the same study, they reported a higher activity (by a factor of 2) over Au/TiO_2 (~5 nm) that was attributed to differences in Au morphology and a higher relative amount of low-coordinate surface sites, *i.e.* activity was enhanced over smaller Au particles with a greater number of defects. Nevertheless, the opposite effect has also been reported in the literature and ascribed to quantum size effects that altered the electronic properties of Au particles below 2 nm [74].

While the nature of the support can impact indirectly on catalytic activity through differences in Au particle size, there is also the possibility of a direct contribution *via* reactant activation. The latter is possible *via* support surface coordinatively unsaturated sites formed during activation [52]. Haruta *et al.* [75] have considered a contribution to reactant activation involving both Au and TiO_2 where the metal/oxide interface can dictate reaction rate. Indeed, Coq *et al.* [76] concluded that strong Pt interaction with TiO_x species ($x < 2$) resulted in a tenfold increase of turnover frequency compared with Pt/Al_2O_3 in liquid phase *p*-CNB hydrogenation. Xiong *et al.* [77] studied the hydrogenation of *o*-CNB over a series of oxide (SiO_2, ZrO_2, TiO_2 and Al_2O_3) supported Ni catalysts and reported the highest conversion and selectivity to *o*-CAN over Ni/TiO_2 due to a strong polarization of the N=O bond induced by the oxygen vacancies of TiO_x. Our results suggest an Au-TiO_2 synergism that influences Au particle size (relative to Au/Al_2O_3) with possible electronic interactions that impact on Au site electron density and a surface activation of the nitro-group for hydrogen attack. The net effect is an enhanced hydrogenation activity without affecting nitro-group reduction exclusivity. In

this study, we have established the basis for an alternative "sustainable" continuous gas phase process for the production of chloroanilines. This catalytic route operates under mild conditions with no by-products and has potential applicability for the selective reduction of $-NO_2$ in a wide range of polyfunctional nitrocompounds where selectivity/clean synthesis is very much a critical issue.

5.4 Conclusions

1 mol % Au on TiO_2 and Al_2O_3 were prepared by impregnation with $HAuCl_4$ to deliver (after reduction) Au particles in the overall size range 1-20 nm with mean values of 6 and 9 nm in the case of Au/TiO_2 and Au/Al_2O_3, respectively. Temperature programmed reduction of Au/Al_2O_3 resulted in one H_2 consumption peak at 434 K while the reduction of Au/TiO_2 was characterised by a principal H_2 consumption at 432 K with a shoulder at 457 K. We attribute the lower temperature peak for both catalysts to the reduction of Au^{3+} to Au^0. The additional peak for Au/TiO_2 is possibly due to the reduction of an Au precursor component that interacts more strongly with the support or is the result of a partial TiO_2 reduction. UV-vis and XRD measurements confirm the presence of zero valent Au post-TPR. Both catalysts promoted the hydrogenation of *p*-CNB to *p*-CAN with 100% selectivity. Au/TiO_2 delivered an up to four-fold higher specific hydrogenation rate, which we attribute to the combination of smaller Au particle size with higher number of defect sites for hydrogen adsorption and a possible *p*-CNB activation *via* interaction(s) with TiO_2 surface oxygen vacancies. Reaction in longer chain alcohol solvents (pentanol *vs.* ethanol) results in diminished hydrogenation rates as a result of alcohol/surface interactions that inhibit hydrogenation. The higher activity associated with Au/TiO_2 extends to the hydrogenation of *o*- and *m*-CNB isomers where the reactivity sequence, *o*- > *p*- >*m*-, is consistent with resonance stabilization effects. Our results provide the basis for the development of a "green" high throughput route for the production of chloroanilines. This continuous process is potentially suitable for selective $-NO_2$ reduction in a range of polyfunctional aromatics to deliver a diversity of high value amin*o*-compounds; this will be the focus of future work.

5.5 References

[5.1] M. M. Kirchhoff, Resour., Conserv. Recycling, 44, 237 (2005)

[5.2] G. C. Bond, P. A. Sermon, G. Webb, D. A. Buchanan, P. B. Wells, J. C. S. Chem. Comm., 444 (1973)

[5.3] E. Bus, J. T. Miller, J. A. van Bokhoven, J. Phys. Chem. B, 109, 14581 (2005)

[5.4] P. Claus, Appl. Catal. A: Gen., 291, 222 (2005)

[5.5] H. Sakurai, M. Haruta, Appl. Catal. A: Gen., 127, 93 (1995)

[5.6] L. Ilieva, G. Pantaleo, I. Ivanov, A. M. Venezia, D. Andreeva, Appl. Catal. A: Gen., 65, 101 (2006)

[5.7] A. Ueda, M. Haruta, Gold Bulletin, 32, 3 (1999)

[5.8] A. C. Gluhoi, M. A. P. Dekkers, B. E. Nieuwenhuys, J. Catal., 219, 197 (2003)

[5.9] J. Chou, N. R. Franklin, S-H. Baeck, T. F. Jaramillo, E. W. McFarland, Catal. Lett., 95, 107 (2004)

[5.10] T. V. Choudhary, C. Sivadinarayana, A. K. Datye, D. Kumar, D. W. Goodman, Catal. Lett., 86, 1 (2003)

[5.11] J. A. Lopez-Sanchez, D. Lennon, Appl. Catal. A: Gen., 291, 230 (2005)

[5.12] M. Okumura, T. Akita, M. Haruta, Catal. Today, 74, 265 (2002)

[5.13] R. Zanella, C. Louis, S. Giorgio, R. Touroude, J. Catal., 223, 328 (2004)

[5.14] B. Campo, M. Volpe, S. Ivanova, R. Touroude, J. Catal., 242, 162 (2006)

[5.15] C. Mohr, H. Hofmeister, P. Claus, J. Catal., 213, 86 (2003)

[5.16] C. Milone, R. Ingoglia, L. Schipilliti, C. Crisafulli, G. Neri, S. Galvagno, J. Catal., 236, 80 (2005)

[5.17] P. Claus, H. Hofmeister, C. Mohr, Gold Bulletin, 37, 3 (2004)

[5.18] Y. Chen, J. Qiu, X. Wang, J. Xiu, J. Catal., 242, 227 (2006)

[5.19] A. Corma, P. Serna, Science, 313, 332 (2006)

[5.20] T. Joseph, K. V. Kumar, A. V. Ramaswamy, S. B. Halligudi, Catal. Commun., 8, 629 (2007)

[5.21] A. Boehnecke, J. Kielhorn, G. Konnecker, C. Pohlenz-Michel, I. Mangelsdorf, CICADS Report 48, W.H.O., Geneva, 2003, p. 78.

[5.22] X. D. Wang, M. H. Liang, J. L. Zhang, Y. Wang, Curr. Org. Chem., 11, 299 (2007)

[5.23] K. R. Westerterp, K. B. van Gelder, H. J. Janssen, M. H. Oyevaar, Chem. Eng. Sci., 43, 2229 (1988)

[5.24] P. Albers, J. Pietsch, S. F. Parker, J. Mol. Catal. A: Chem., 173, 275 (2001)

[5.25] B. Coq, F. Figuéras, Coord. Chem. Rev., 178-180, 1753 (2000)

[5.26] L. M. Sikhwivhilu, N. J. Coville, B. M. Pulimaddi, J. Venkatreddy, V. Vishwanathan, Catal. Commun., 8, 1999 (2007)

[5.27] V. Vishwanathan, V. Jayasri, P. M. Basha, N. Mahata, L. M. Sikhwivhilu, N. J. Coville, Catal. Commun., 9, 453 (2008)

[5.28] P. Mäki-Arvela, J. Hájek, T. Salmi, D.Yu. Murzin, Appl. Catal. A: Gen., 292, 1 (2005)

[5.29] X. Zhang, H. Shi, B. Q. Xu, Angew. Chem. Int. Ed., 44, 7132 (2005)

[5.30] A. S. K. Hashmi, G. J. Hutchings, Angew. Chem. Int. Ed., 45, 7896 (2006)

[5.31] G. Rupprechter, G. Seeber, H. Goller, K. Hayek, J. Catal., 186, 201 (1999)

[5.32] M. Haruta, Catal. Today, 36, 153 (1997)

[5.33] Jörg Radnik, C. Mohr, P. Claus, Phys. Chem. Chem. Phys., 5, 172 (2003)

[5.34] L. Ilieva, J. W. Sobczak, M. Manzoli, B. L. Su, D. Andreeva, Appl. Catal. A: Gen., 291, 85 (2005)

[5.35] B.K. Min, W.T. Wallace, D.W. Goodman, Surf. Sci. Lett., L7-L11, (2006)

[5.36] C. Milone, C. Crisafulli, R. Ingoglia, L. Schipilliti, S. Galvagno, Catal. Today, 122, 341 (2007)

[5.37] F. Cárdenas-Lizana, S. Gómez-Quero, M. A. Keane, Catal. Commun., 9, 475 (2008)

[5.38] E.-J. Shin, M. A. Keane, J. Catal., 173, 450 (1998)

[5.39] C. M. Van Den Bleek, K. Van Der Wiele, P. J. Van Der Berg, Chem. Eng. Sci., 24, 681 (1969)

[5.40] G. Yuan, M. A. Keane, Chem. Eng. Sci., 58, 257 (2003)

[5.41] G. Yuan, C. Louis, L. Delannoy, M. A. Keane, J. Catal. , 247, 256 (2007)

[5.42] F. Cárdenas-Lizana, S. Gómez-Quero, M. A. Keane, Appl. Catal. A: Gen., in press (2007)

[5.43] S. Lin, M.A. Vannice, Catal. Lett., 10, 47 (1991)

[5.44] A. C. Gluhoi, P. Mărginean, U. Stănescu, Appl. Catal. A: Gen., 294, 208 (2005)

[5.45] M. Arai, Y. Takada, T. Ebina, M. Shirai, Appl. Catal. A: Gen., 183, 365 (1999)

[5.46] A. Guevara, R. Bacaud, M. Vrinat, Appl. Catal. A: Gen., 253, 515 (2003)

[5.47] S. Cai, K. Sohlberg, J. Mol. Catal. A: Chem., 193, 157 (2003)

[5.48] M. Xu, J. H. Lunsford, D. Wayne Goodman, A. Bhattacharyya, Appl. Catal. A: Gen., 149, 289 (1997)

[5.49] M.A. Hasan, M.I. Zaki, L. Pasupulety, J. Mol. Catal. A: Chem., 178, 125 (2002)

[5.50] G. Lu, A. Linsebigler, J. T. Yates, J. Phys. Chem., 98, 11733 (1994)

[5.51] B. Shi, H. A. Dabbagh, B. H. Davis, J. Mol. Catal. A: Chem., 141, 257 (1999)

[5.52] V.M. Mastikhinn, Colloids Surfaces A: Physicochem. Eng. Aspects, 78, 143 (1993)

[5.53] B. Bogdanov, M. Peschke, D. S. Tonner, J. E. Szulejko, T. B. McMahon, Int. J. Mass Spectrom., 187, 707 (1999)

[5.54] S. Galvagno, A. Donato, G. Neri, R. Pietropaolo, J. Mol. Catal., 42, 379 (1987)

[5.55] T. M. Krygowski, M. Palusiak, A. Plonka, J. E. Zachara-Horeglad, J. Phys. Org. Chem., 20, 297 (2007)

[5.56] W. B. Knighton, R. S. Mock, D. S. McGrew, E. P. Grimsrud, J. Phys. Chem., 98, 3770 (1994)

[5.57] V. Kratky, M. Kralik, M. Mecarova, M. Stolcova, L. Zalibera, M. Hronec, Appl. Catal. A: Gen., 235, 225 (2002)

[5.58] A. C. Gluhoi, X. Tang, P. Marginean, B. E. Nieuwenhuys, Top. Catal., 39, 101 (2006)

[5.59] C. K. Costello, J. Guzman, J. H. Yang, Y. M. Wang, M. C. Kung, B. C. Gates, H. H. Kung, J. Phys. Chem. B, 108, 12529 (2004)

[5.60] S. D. Yim, I.-S. Nam, J. Catal., 221, 601 (2004)

[5.61] A. Venugopal, M. S. Scurrell, Appl. Catal. A: Gen., 258, 241 (2004)

[5.62] V. Idakiev, T. Tabakova, Z.-Y. Yuan, B.-L. Su, Appl. Catal. A: Gen., 270, 135 (2004)

[5.63] H. Wei, B. Li, Y. Du, S. Dong, E. Wang, Chem. Mater., 19, 2987 (2007)

[5.64] M. Harada, H. Einaga, Langmuir, 23, 6536 (2007)

[5.65] R. S. Sonawane, M. K. Dongare, J. Mol. Catal. A: Chem., 243, 68 (2006)

[5.66] J.L. Margitfalvi, A. Fási, M. Hegedűs, F. Lónyi, S. Gőbölös, N. Bogdanchikova, Catal. Today, 72, 157 (2002)

[5.67] S. Deki, Y. Aoi, H. Yanagimoto, K. Ishii, K. Akamatsu, M. Mizuhata, A. Kajinami, J. Mater. Chem., 6, 1879 (1996)

[5.68] M.A. Centeno, M. Paulis, M. Montes, J.A. Odriozola, Appl. Catal. A: Gen., 234, 65 (2002)

[5.69] X. Hu, D. J. Blackwood, J. Electroceram., 16, 593 (2006)

[5.70] R. I. Bickley, T. Gonzalez-Carreno, J. S. Lees, L. Palmisano, R. J. D. Tilley, J. Solid State Chem., 92, 178 (1991)

[5.71] G. C. Bond, C. Louis, D. T. Thompson, Catalysis by Gold, Imperial College Press, London, 2006.

[5.72] J. Słoczyński, R. Grabowski, A. Kozłowska, P. Olszewski, J. Stoch, J. Skrzypek, M. Lachowska, Appl. Catal. A: Gen., 278, 11 (2004)

[5.73] E. Bus, R. Prins, J. A. van Bokhoven, Catal. Commun., 8, 1397 (2007)

[5.74] P. Claus, A. Brückner, C. Mohr, H. Hofmeister, J. Am. Chem. Soc., 122, 11430 (2000)

[5.75] M. Haruta, M. Daté, Appl. Catal. A: Gen., 222, 427 (2001)

[5.76] B. Coq, A. Tijani, R. Dutartre, F. Figuéras, J. Mol. Catal., 79, 253 (1993)

[5.77] J. Xiong, J. X. Chen, J. Y. Zhang, Catal. Commun., 8, 345 (2007)

Chapter 6

Support Effects in the Selective Gas Phase Hydrogenation of *p*-Chloronitrobenzene over Gold

In the preceding Chapter, exclusive formation of *p*-chloroaniline (from *p*-chloronitrobenzene) was established over Au/TiO_2 and Au/Al_2O_3. A higher rate for Au/TiO_2 was recorded and tentatively linked to the redox properties of the support and higher associated Au dispersion. In this Chapter, both factors have been independently analyzed by considering a series of Au/Al_2O_3, Au/TiO_2, Au/CeO_2 and Au/Fe_2O_3 catalysts prepared by impregnation and deposition-precipitation.

6.1 Introduction

Hydrogenation promoted by gold has emerged as one of the most challenging topics in gold catalysis, as reflected in the reviews by Claus [1] and Hashmi [2]. The lower hydrogenation activity associated with Au when compared with traditional metals (*e.g.* Pt, Pd) [3,4] is compensated for in terms of the high selectivity that Au can deliver in hydrogenation applications [1]. In order to develop viable processes based on Au catalysis, an explicit correlation of activity/selectivity with catalyst structure is required. One issue that must be resolved is the difference in catalytic performance observed for Au supported on different oxide carriers [1,3,5-9]. The nature of the support can affect the morphology and dispersion of Au particles *via* metal-support interactions [3,10,11] and it is established that smaller ($\leq$ 10 nm) supported Au particles exhibit electronic properties that are quite distinct from bulk Au [12]. This feature is critical in that the catalytic response of Au in hydrogenation reactions may be dependent on changes in the electronic character of the supported metal [13]. Furthermore, while the carrier can impact on the properties of the Au component, the supported Au phase has been reported to induce changes in the oxide support, notably by promoting the reduction of (reducible) oxides, including Fe_2O_3 [14], CeO_2 [15] and TiO_2 [16,17]. Considering the complex nature of Au-support interactions, it is not surprising that the effect of the support on the hydrogenation response still remains largely unresolved.

The selective reduction of aromatic nitro-group substituents in the presence of other functional groups (*e.g.* carbonyl, cyano, chloro or alkenic groups) is difficult as the reduction/substitution of these groups (by H_2) can be more facile than the target $-NO_2$ group [18,19]. In the selective reduction of nitroarenes, promising results have been recently published for supported gold catalysts in batch liquid operation [20-26], although the formation of highly toxic by-products (azoxy-derivates) and the requirement of high hydrogen pressures (3-4 MPa) are drawbacks that require further consideration. *p*-Chloroaniline (the target product in this study) is a high production volume compound [27] extensively used as an intermediate in the synthesis of a broad range of fine chemicals, *e.g.* pharmaceuticals and agrochemicals [28]. The traditional production route from *p*-chloronitrobenzene involves the use of Fe in acid media (Béchamp process) but the generation of large amounts (5-20 times greater than that of the target product) of toxic waste (Fe hydroxide sludge) and low overall product yields have limited its applicability [29]. Catalytic hydrogenation in batch liquid systems over transition metal catalysts provides a cleaner alternative [30]. However, the challenge is to achieve selective hydrogenation of the nitro group and avoid scission of the C-Cl bond [30,31] and/or cleavage of $-NH_2$ [32] from the product. The hydrogenolysis of the Cl substituent can lead to the formation of aniline either (a) *via* the reduction of nitrobenzene or (b) as a result of the further transformation of *p*-chloroaniline as shown in **Figure 6.1**, with both steps reported in the literature for catalytic operation (in gas and/or liquid phase) over supported metals [32-40].

We have recently demonstrated exclusivity in the hydrogenation of a series of halonitrocompounds to the respective halogenated aromatic amine in continuous gas phase operation over supported Au [33,41]. In this study we have extended that work to probe the effect of the support in modifying the catalytic action of a well dispersed Au phase. We have considered four oxide supports (Al_2O_3, TiO_2, CeO_2 and Fe_2O_3) that present a range of acid-base and redox surface properties. In addition, we have compared the catalytic behaviour of these systems with an Au/TiO_2 reference catalyst supplied by the World Gold Council.

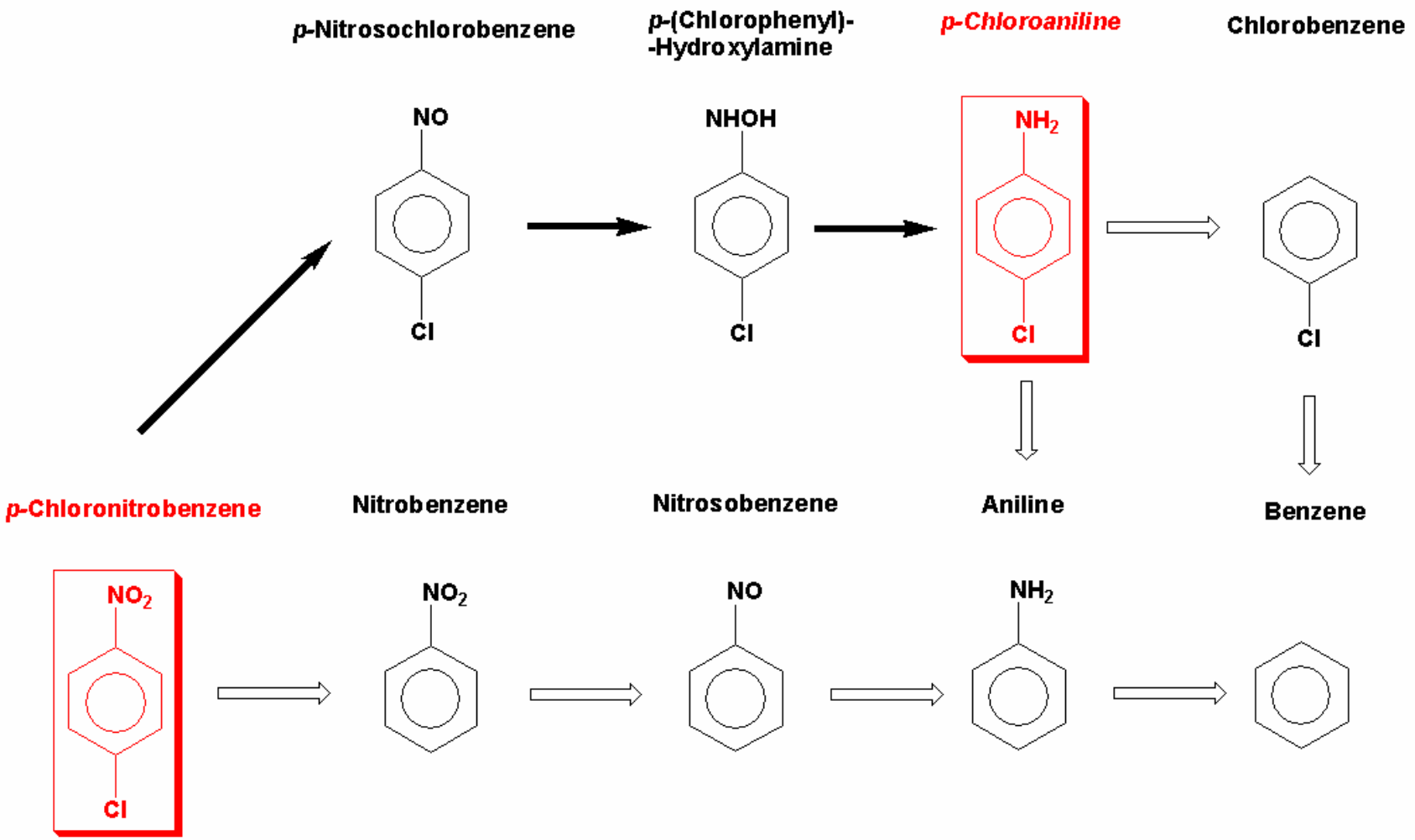

Figure 6.1: Reaction pathways associated with the hydrogen mediated conversion of *p*-chloronitrobenzene. *Note*: Targeted route to *p*-chloroaniline is represented by bold arrows. The *p*-chloronitrobenzene reactant and *p*-chloroaniline product are framed in red.

6.2 Experimental

6.2.1 Catalyst Preparation and Activation

The effect of the support on Au catalytic hydrogenation performance was investigated by selecting a group of reducible (CeO_2, TiO_2 and α-Fe_2O_3) and non-reducible (γ-Al_2O_3) oxides. The CeO_2 (HSA5, Rhodia), TiO_2 (Degussa) and γ-Al_2O_3 (Puralox, Condea Vista Co.) supports were used as received. Hematite (α-Fe_2O_3) was prepared by precipitation in basic media according to [42-44]

$$2[Fe(NO_3)_3 \cdot 9H_2O] + 3Na_2CO_3 \longrightarrow 2Fe(OH)_3 + 6NaNO_3 + 3CO_2 + 15H_2O \quad (6.1)$$

100 cm^3 aqueous Na_2CO_3 (1 M) were placed in a three-necked round-bottom flask and heated in a water bath to 358 ± 5 K under constant agitation (300 rpm) using a glass impeller. An aqueous solution of $Fe(NO_3)_3 \cdot 9H_2O$ (300 cm^3, 1 M) was then added drop wise (300 cm^3 h^{-1}) by means of a microprocessor-controlled infusion pump (100 kd Scientific). Basic conditions (pH > 7.3) were maintained during precipitation by adding Na_2CO_3 (five additions of 10 g). The solid hydroxide was subsequently aged for 2 h to enhance the BET area [44], washed with warm distilled water until the wash water approached neutral pH and dried for 3 days at 353 K (2 K min^{-1}) in ultra pure He (60 cm^3 min^{-1}) to produce hematite:

$$2Fe(OH)_3 \longrightarrow Fe_2O_3 + 3H_2O \quad (6.2)$$

A series of 1 mol % oxide supported Au was prepared by deposition-precipitation (DP) and impregnation (IMP). These synthesis routes were chosen as it has been demonstrated that catalyst synthesis can significantly influence metal dispersion where DP has been shown to generate small Au particles (< 5 nm) [45,46]. In contrast, even at low Au loading (1-2 wt. %), catalysts prepared by the less controlled IMP procedure normally exhibit larger (10-35 nm) Au diameters [5]. In the case of the DP samples, urea (used as basification agent) was added (*ca.* 100-fold urea excess) to a solution of $HAuCl_4$ (300 cm^3, 5 × 10^{-4} M). The support (γ-Al_2O_3, TiO_2, CeO_2 and α-Fe_2O_3) was added and the suspension was stirred and heated to 353 K for 16 h. The pH of the

suspension progressively increased to reach *ca.* 7 after 16 h as a result of the thermally-induced urea decomposition [47]

$$NH_2\text{-}CO\text{-}NH_2 + 3H_2O \xrightarrow{T=353K} 2NH_4^+ + 2OH^- + CO_2 \qquad (6.3)$$

The solids obtained were separated by centrifugation, washed three times with deionized water (with centrifugation between each washing) and dried under vacuum at 298 K for 12 h. In the case of the IMP synthesis, the support was dispersed in appropriate volumes of $HAuCl_4$ solution (Aldrich, 25×10^{-3} g cm^{-3}, pH = 2) and the resulting slurry was vigorously stirred (600 rpm) and slowly heated (2 K min^{-1}) to 353 K in a He purge. The solid residue was dried in a flow of He at 383 K for 3 h. After preparation, the samples were sieved to 75 μm average particle diameter (ATM fine test sieves) and stored at 298 K (in the dark). The Au loading was determined (to within ± 2 %) by inductively coupled plasma-optical emission spectrometry (ICP-OES, Vista-PRO, Varian Inc.) from the diluted extract of aqua regia. The catalytic behaviour of a 1 mol % Au/TiO2 reference catalyst supplied by the World Gold Council (type A, lot number Au-TiO_2 #02-7, sample number 110) was also investigated. The preparation and characterization details of this reference sample have been recorded elsewhere [48,49]. Prior to use in catalysis, the samples were activated in 60 cm^3 min^{-1} H_2 at 2 K min^{-1} to 423-603 ± 1 K. The requirements for the reduction of the Au precursor to metallic Au for catalysts prepared by IMP and/or DP have been demonstrated previously [33,41,50]. Samples for off-line analysis were passivated in 1% v/v O_2/He at room temperature.

6.2.2 Catalysis Characterization

H_2 chemisorption and BET surface area were determined using the commercial CHEM-BET 3000 (Quantachrome) unit. The samples were activated as above, swept with a 65 cm^3 min^{-1} flow of N_2 for 1.5 h, cooled to room temperature and subjected to H_2 chemisorption using a pulse (10 μl) titration procedure. BET areas were recorded with a 30% v/v N_2/He flow using pure N_2 (99.9%) as internal standard. At least 2 cycles of nitrogen adsorption-desorption in the flow mode were employed to determine total surface area using the standard single point method. BET surface area and H_2 uptake values were reproducible to within ± 5%; the values quoted represent the mean. Powder X-ray diffractograms were recorded on a Bruker/Siemens D500 incident X-ray diffractometer using Cu Kα radiation. The samples were scanned at 0.02º $step^{-1}$ over

$20^o \leq 2\theta \leq 90^o$ (scan time = 5 s $step^{-1}$). Diffractograms were identified using the JCPDS-ICDD reference standards, *i.e.* γ-Al_2O_3 (10-0425) and Au (04-0784). Diffuse reflectance (DRS UV-Vis) measurements were conducted using a Perkin Elmer Lambda 35 UV-Vis Spectrometer with $BaSO_4$ powder as reference; absorption profiles were calculated from the reflectance data using the Kubelka-Munk function. Au particle morphology and size were determined by transmission electron microscopy analysis; JEOL JEM 2011 HRTEM unit with a UTW energy dispersive X-ray detector (Oxford Instruments) operated at an accelerating voltage of 200 kV and using Gatan DigitalMicrograph 3.4 for data acquisition/manipulation. The specimens were prepared by dispersion in acetone and deposited on a holey carbon/Cu grid (300 Mesh). Up to 1000 individual Au particles were counted for each catalyst and the surface area-weighted metal diameter (d_{TEM}) was calculated from

$$d_{TEM} = \frac{\sum_i n_i d_i^3}{\sum_i n_i d_i^2} \qquad \textbf{(6.4)}$$

where n_i is the number of particles of diameter d_i. The size limit for the detection of Au particles is *ca.* 1 nm.

6.2.3 Catalyst Procedure

Reactions were carried out under atmospheric pressure at T = 423 K, *in situ* immediately after activation, in a fixed bed vertical continuous glass reactor (l = 600 mm; i.d. = 15 mm). The catalytic reactor and operating conditions to ensure negligible heat/mass transport limitations, have been fully described elsewhere [51] but some features, pertinent to this study, are given below. A layer of borosilicate glass beads served as preheating zone, ensuring that the *p*-chloronitrobenzene reactant was vaporized and reached reaction temperature before contacting the catalyst. Isothermal conditions (± 1 K) were ensured by diluting the catalyst bed with ground glass (75 μm) [52]; the ground glass was mixed thoroughly with catalyst before insertion into the reactor. Temperature was continuously monitored by a thermocouple inserted in a thermowell within the catalyst bed. The reactant was delivered to the reactor *via* a glass/teflon air-tight syringe and teflon line using a microprocessor controlled infusion pump (Model 100 kd Scientific) at a fixed calibrated flow rate. A co-current flow of *p*-

chloronitrobenzene and ultra pure H_2 (< 1% v/v -NO_2/H_2) was maintained at a *GHSV* = 2 × 10^4 h^{-1} with an inlet -NO_2 molar flow (F) in the range 15×10^{-2} – 38×10^{-2} $mmol_{\text{-}NO_2}$ h^{-1}, where the H_2 content was up to 350 times in excess of the stoichiometric requirement (P_{H_2} = 0.92 atm), the flow rate of which was monitored using a Humonics (Model 520) digital flowmeter. The molar metal (n_{Au}) to inlet molar -NO_2 feed rate (F) ratio spanned the range 5×10^{-4}–169×10^{-4} h. In a series of blank tests, passage of *p*-chloronitrobenzene in a stream of H_2 through the empty reactor or over the support alone, *i.e.* in the absence Au, did not result in any detectable conversion. The reactor effluent was frozen in a liquid nitrogen trap for subsequent analysis, which was made using a Perkin-Elmer Auto System XL gas chromatograph equipped with a programmed split/splitless injector and a flame ionization detector, employing a DB-1 50 m × 0.20 mm i.d., 0.33 μm film thickness capillary column (J&W Scientific), as described elsewhere [53]. Any possible HCl produced was monitored by passing the effluent gas through an aqueous NaOH trap (7.0×10^{-4} mol dm^{-3}, kept under constant agitation at 400 rpm) with continuous pH (Hanna HI Programmable Printing pH Bench-Meter) analysis. *p*-Chloronitrobenzene (Aldrich, ≥99.9% w/w purity) and the 1-butanol solvent (Riedel-de Häen, ≥ 99.5%) were used without further purification. Hydrogenation performance is quantified in terms of the degree of nitro-group reduction ($x_{\text{-}NO_2}$)

$$x_{\text{-}NO_2} = \frac{[\text{-NH}_2]_{out}}{[\text{-NO}_2]_{in}} \qquad \textbf{(6.5)}$$

The percentage selectivity with respect to *p*-chloroaniline ($S_{p\text{-}CAN}$) is given by

$$S_{p\text{-}CAN} = \frac{[p\text{-CAN}]_{out}}{[p\text{-CNB}]_{in} - [p\text{-CNB}]_{out}} \qquad \textbf{(6.6)}$$

Repeated reactions with samples from the same batch of catalyst delivered activity values that were reproducibility to within ± 6%.

6.3 Result and Discussion

6.3.1 Catalyst Characterization

Hydrogen chemisorption, BET surface areas and (surface weighted mean) Au particle size obtained by TEM (d_{TEM}) for the catalysts considered in this study are recorded in **Table 6.1**.

Table 6.1: Gold particle size obtained from TEM (d_{TEM}) analysis, H_2 uptake, BET surface area and pseudo-first order *p*-chloronitrobenzene hydrogenation rate constant (k) obtained for oxide supported Au (1 mol %) prepared by deposition-precipitation (DP) and impregnation (IMP).

Catalyst	d_{TEM} (nm)	H_2 uptake ($\mu mol\ g_{Au}^{-1}$)	BET area ($m^2\ g_{cat}^{-1}$)	k (h^{-1})
Au/Al_2O_3-DP	2.8	33	112	95
Au/CeO_2-DP	1.5	63	195	147
Au/Fe_2O_3-DP	2.6	21	57	89
Au/TiO_2-DP	2.4	28	48	80
Au/TiO_2-Ref	3.3	46	50	45
Au/Al_2O_3-IMP	9.0	22	161	1
Au/Fe_2O_3-IMP	3.5	27	56	35
Au/TiO_2-IMP	6.0	16	47	1

Hydrogen uptake post-activation for all the supported Au catalysts was considerably lower ($\leq$ 63 $\mu mol\ g_{Au}^{-1}$) than that obtained for conventional transition metals on oxide supports, *e.g.* Pd/Al_2O_3 (353 $\mu mol\ g_{Pd}^{-1}$) [33], Ni/SiO_2 (843 $\mu mol\ g_{Ni}^{-1}$) [54] and Ni/TiO_2 (702 $\mu mol\ g_{Ni}^{-1}$) [55]. Hydrogen/gold interaction is still not well understood but it appears that Au coordination number is a critical factor in determining adsorption capability [1]. While molecular hydrogen does not chemisorb on bulk Au at room temperature [56], there is evidence for dissociative chemisorption on Au films containing defect sites [57-59]. Indeed, some consensus emerges from the literature that

smaller Au particles [60-62] with a higher number of defects (steps, edges and corners) exhibit a greater facility for dissociative hydrogen uptake. X-ray diffraction analysis can provide important bulk structural characteristics.

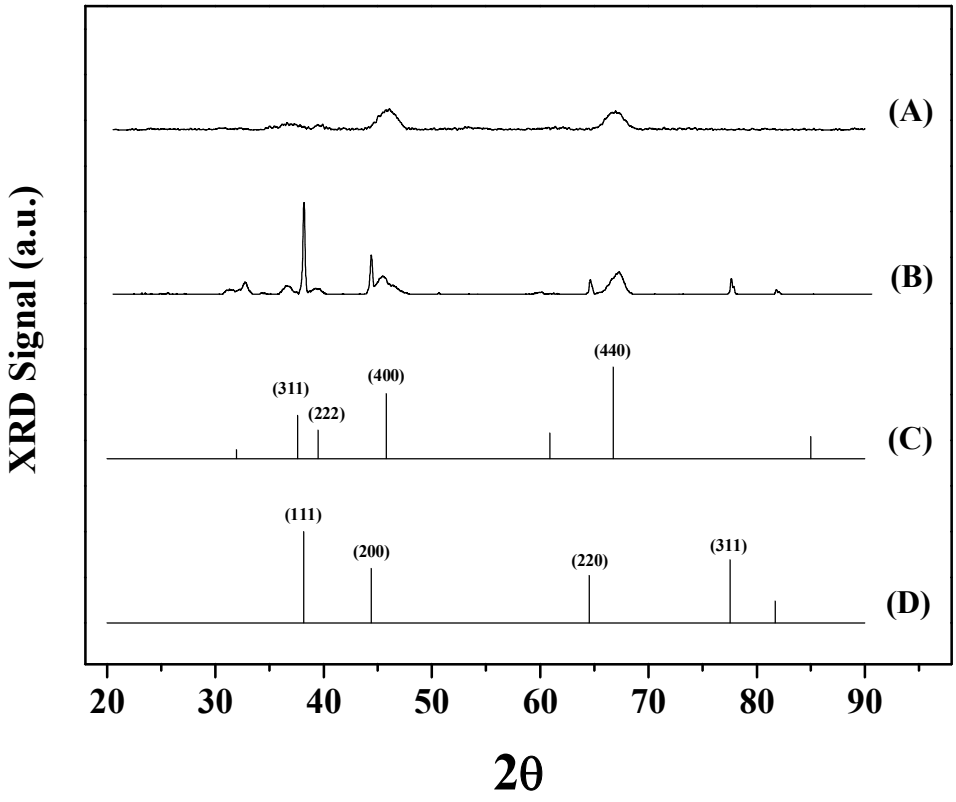

Figure 6.2: XRD patterns associated with (A) Au/Al_2O_3-DP, (B) Au/Al_2O_3-IMP and JCPDS-ICDD reference diffractograms for (C) γ-Al_2O_3 (10-0425) and (D) Au (04-0784).

Figure 6.2 shows the diffraction patterns for two representative samples, *i.e.* Au/Al_2O_3-DP (profile (A)) and Au/Al_2O_3-IMP (profile (B)). The markers included illustrate the position and relative intensity of the XRD peaks for γ-Al_2O_3 (profile (C)) and cubic Au (profile (D)) taken from the JCPDS-ICDD standards (card numbers 10-0425 and 04-0784, respectively). The XRD patterns for both catalysts exhibit signals over the range 2θ = 30-70° that can be associated with the (311), (222), (400) and (440) planes of cubic γ-Al_2O_3 (see profile (C)), where the broadness of the peaks is indicative of short range order. In addition, the XRD pattern for Au/Al_2O_3-IMP (see profile (B)) also shows strong reflections at 2θ = 38.1°, 44.4°, 64.7° and 77.5° corresponding to (111), (200), (220) and (311) planes of Au metal (see profile (D)), with an extracted

(from standard line broadening analysis [41]) mean Au particle size = 18 nm. In contrast, there are no distinguishable peaks characteristic of metallic gold in the Au/Al_2O_3-DP spectrum (see profile (A)), suggesting a highly dispersed Au phase. The DRS UV-Vis spectra of the alumina support, Au/Al_2O_3-DP and Au/Al_2O_3-IMP, in the range 400-800 nm, are presented in **Figure 6.3**.

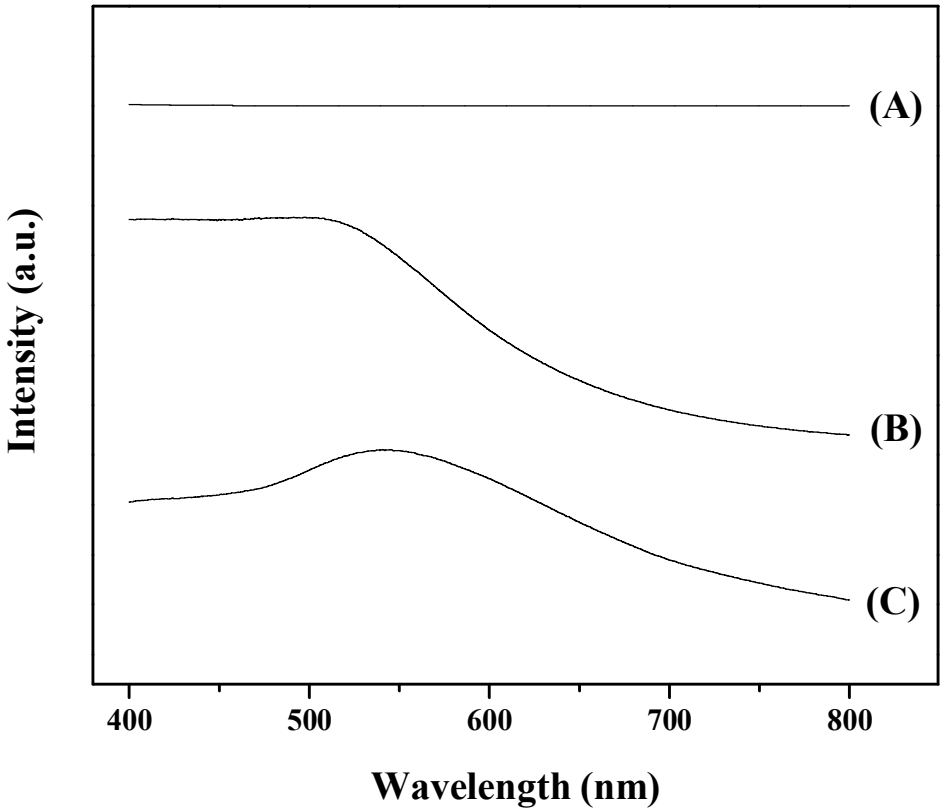

Figure 6.3: DRS UV-Vis spectra for (A) γ-Al_2O_3, (B) Au/Al_2O_3-DP and (C) Au/Al_2O_3-IMP.

The spectrum for Al_2O_3 (profile (A)) is featureless, consistent with results presented elsewhere [63]. The absorption band between 500-540 nm present in the spectrum of Au/Al_2O_3-DP (profile (B)) is characteristic of metallic gold [63,64]. The signal associated with Au/Al_2O_3-IMP (profile (C)) exhibits a greater intensity with a displacement to a higher wavelength, a response that has been ascribed in the literature [65] to the presence of larger Au particles, which is in agreement with the XRD analysis.

Representative TEM images of Au/Al_2O_3-DP (AI) and Au/Al_2O_3-IMP (BI and BII) are presented in **Figure 6.4**, which show quasi-spherical Au particles dispersed on the support.

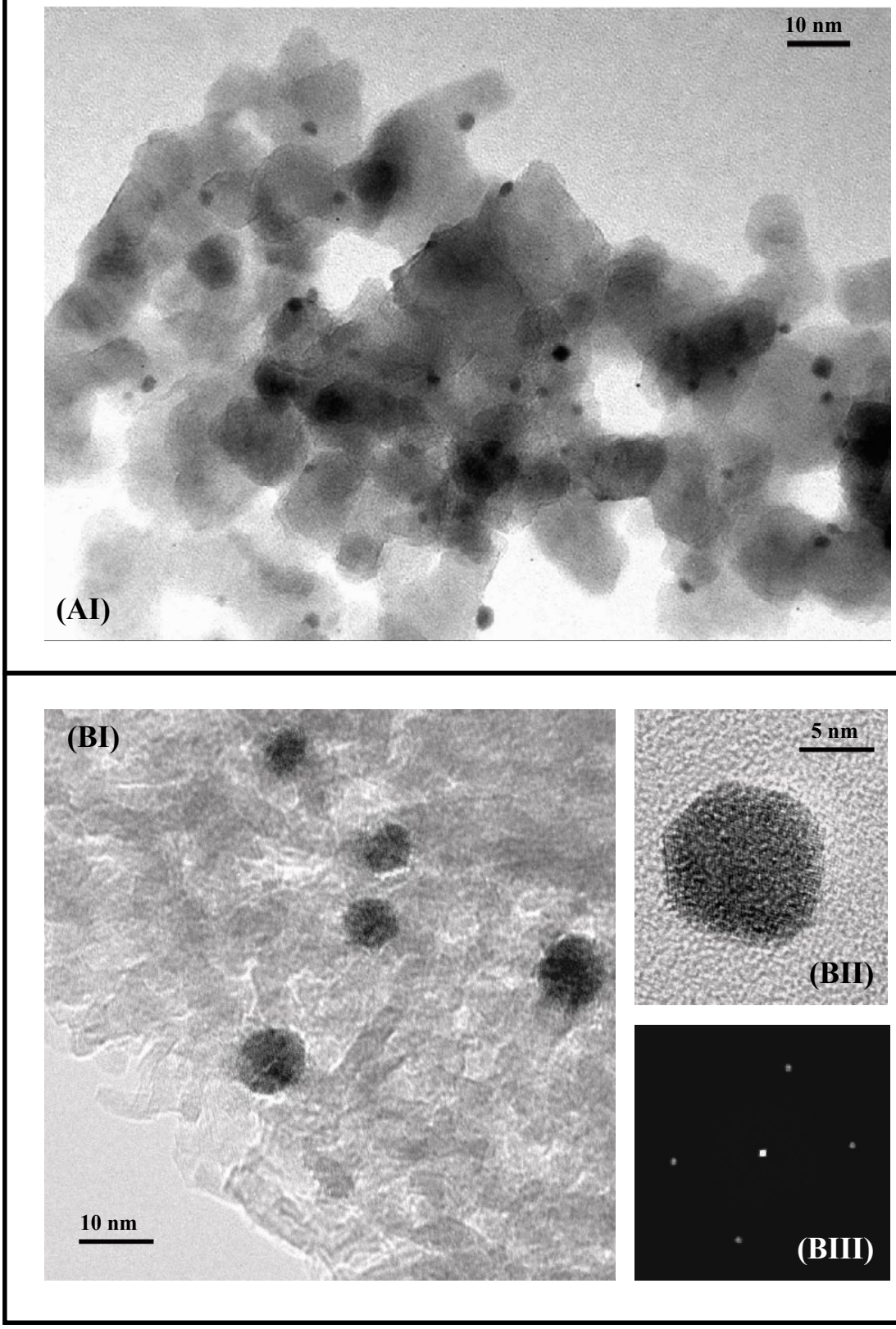

Figure 6.4: Representative TEM images of (A) Au/Al_2O_3-DP and (B) Au/Al_2O_3-IMP: (I) low magnification images; (II) high magnification image of a single Au particle (with associated diffractogram pattern (III)).

The diffractogram pattern for an isolated single gold particle in the case of Au/Al_2O_3-IMP is shown in image BIII where the *d*-spacings (0.20/0.23) are consistent with the (111) and (200) planes of metallic gold (JCPDS-ICDD 04-0784), confirming precursor reduction to Au^0 post-activation, in agreement with XRD and DRS UV-Vis data. The images indicate that Au is present as smaller particles in Au/Al_2O_3-DP when compared with Au/Al_2O_3-IMP, a trend that extends to the other samples, *i.e.* for the same support, the IMP samples exhibit larger Au particles (≥ 3.5 nm, see **Table 6.1**). The sequence of increasing mean Au particle size for the samples prepared by DP, Au/CeO_2-DP < Au/TiO_2-DP < Au/Fe_2O_3-DP < Au/Al_2O_3-DP, suggests a dependency on the reducibility of the carrier, where the largest Au particle size is associated with the least reducible support (Al_2O_3). Alumina is well established as an irreducible support and an insulator material due to its wide band gap (9 eV) [66,67] whereas CeO_2, TiO_2 and Fe_2O_3 are reducible carriers with semiconductor nature (2-3 eV) [68,69]. The same trend is also in evidence for the IMP samples where the Au particle size on Al_2O_3 is appreciably higher than that for reducible TiO_2 or Fe_2O_3 (see **Table 6.1**). Our observations find some support in the literature [10] where a partial reduction of the oxide carrier has been shown to result in metal-support interactions that impact on Au dispersion. Indeed, Min *et al.* [11], using scanning tunnelling microscopy, demonstrated that reducible oxides provide more nucleation sites, leading to the formation of Au clusters with a smaller particle size.

6.3.2 Catalyst activity/selectivity

The gas phase hydrogenation of *p*-chloronitrobenzene over each supported Au catalyst generated *p*-chloroaniline as the sole product, *i.e.* exclusive reduction of the nitro-group with no evidence of hydrodechlorination, hydrodenitrogenation or aromatic ring reduction. It is significant that the exclusive formation of *p*-chloroaniline was a feature of each catalyst, demonstrating that the support did not influence reaction selectivity, which was governed by the Au phase. In contrast, in the hydrogenation of chloronitrobenzene over conventional transition metals, support effects have been deemed responsible for differences in selectivity. Xiong and co-workers [70] studied the reaction of *o*-chloronitrobenzene over a series of oxide (SiO_2, ZrO_2, TiO_2 and Al_2O_3) supported Ni catalysts and attributed the highest selectivity to *o*-chloroaniline over Ni/TiO_2 to strong polarization of the N=O band induced by the oxygen vacancies of TiO_x. Han *et al.* [71] investigated the hydrogenation of *p*-chloronitrobenzene over Pt on

TiO_2, γ-Al_2O_3 and ZrO_2 and associated the highest *p*-chloroaniline yield, obtained using Pt/TiO_2, with strong metal/support interactions. While Hugon *et al.* [72] have recently reported that the selectivity response in the hydrogenation of 1,3-butadiene over Au supported on TiO_2, Al_2O_3, CeO_2 and ZrO_2 was independent of the nature of the support, there is evidence in the literature [6,7] of support effects in terms of hydrogenation selectivity for supported Au systems. Campo and co-workers [3] have reported that Au/CeO_2 is highly selective in the gas phase hydrogenation of crotonaldehyde to crotyl alcohol whereas Au/Nb_2O_5 is non-selective and proposed that niobia promoted the formation of non-selective Au particles with a distinct morphology. Milone *et al.* [8] reported a strong support effect with respect to C=O hydrogenation in the case of benzalacetone where electron-enriched Au particles generated *via* electron transfer from a reducible support (iron oxide) resulted in higher selectivities to the corresponding α,β-unsaturated alcohol. The level of reaction exclusivity reported in our study, notably the avoidance of C-Cl bond scission, is unique when compared with the catalytic batch liquid systems tested to date [30] and represents a critical advancement in the development of a sustainable continuous production of aromatic haloamines.

The activity of these catalysts was assessed by fitting the temporal $x_{\text{-}NO_2}$ (see **Figure 6.5**) response to an empirical relationship described in detail elsewhere [33] in order to obtain a measure of initial activity. As a general observation, smaller Au particles (≤ 3.5 nm) generated higher initial activities but exhibited a temporal decline, whereas catalysts with a lower Au dispersion did not show any significant time-on-stream variation in conversion. This is demonstrated by the two representative cases presented in **Figure 6.5**: Au/Al_2O_3-IMP (d_{TEM} = 9.0 nm) delivered an invariant conversion with time-on-stream (up to 5 h), while a decline in conversion is observed for Au/Fe_2O_3-DP, which bears smaller Au particles (d_{TEM} = 2.6 nm). These results suggest a higher activity but a susceptibility to deactivation for smaller Au clusters. Metal catalyst deactivation is a feature of gas phase -NO_2 group reduction as a result of H_2O formation [73] and/or coke deposition [31,74-76]. The latter has been suggested as responsible for the loss of activity during hydrogenation over supported Au [77,78]. We have previously established the applicability of a pseudo-first order kinetic treatment [41,79],

$$\ln\left[\frac{1}{\left(1-(x_{-NO_2})_0\right)}\right] = k\left(\frac{n_{Au}}{F}\right) \qquad (6.7)$$

where n_{Au}/F has the physical meaning of contact time.

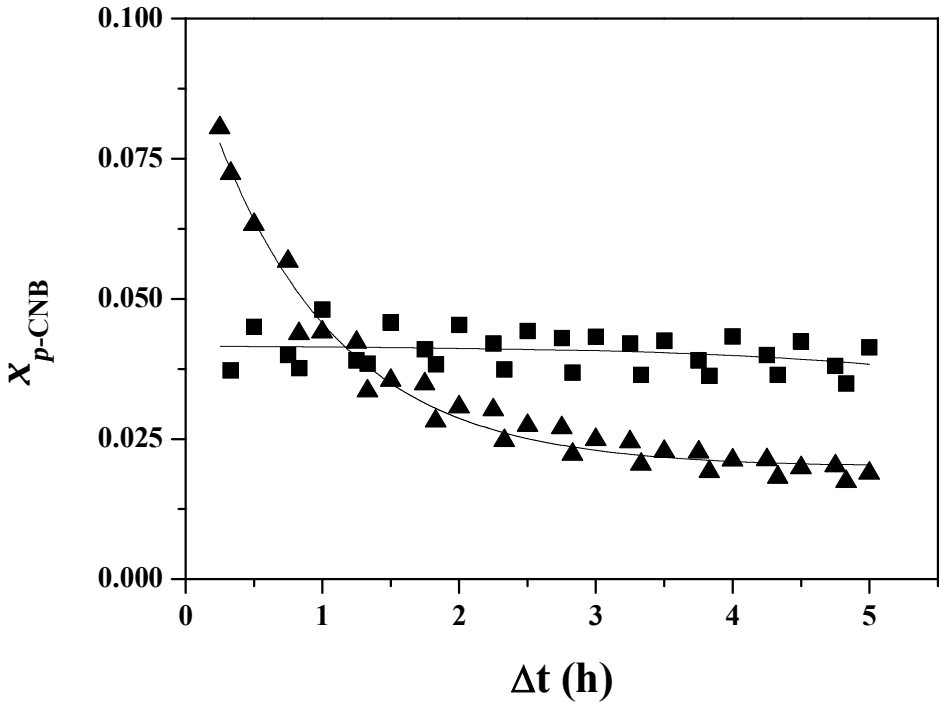

Figure 6.5: Variation of *p*-chloronitrobenzene fractional conversion ($x_{p\text{-}CNB}$) with time-on-stream over (▲) Au/Fe_2O_3-DP (*p*-CNB/Au = 463 $mol_{p\text{-}CNB}$ mol_{Au}^{-1} h^{-1}) and (■) Au/Al_2O_3-IMP (*p*-CNB/Au = 75 $mol_{p\text{-}CNB}$ mol_{Au}^{-1} h^{-1}).

The linear relationship between $\ln(1-(x_{-NO_2})_0)^{-1}$ and n_{Au}/F (forced through the origin) is shown in **Figure 6.6,** taking Au/Fe_2O_3-DP as a representative case. The resultant raw pseudo-first order rate constants (k) are given in **Table 6.1**. In order to explicitly demonstrate structure sensitivity in terms of Au particle size, it is necessary to determine the relationship between Au size and the specific rate constant (k') in terms of the exposed Au surface area (as estimated from mean TEM particle size, see **Table 6.1**). The results are shown in **Figure 6.7**, which reveals that the catalysts prepared by DP with smaller Au particles (1.5-3.3 nm) delivered higher specific activities when compared with the IMP samples that bear larger Au particles (3.5-9.0).

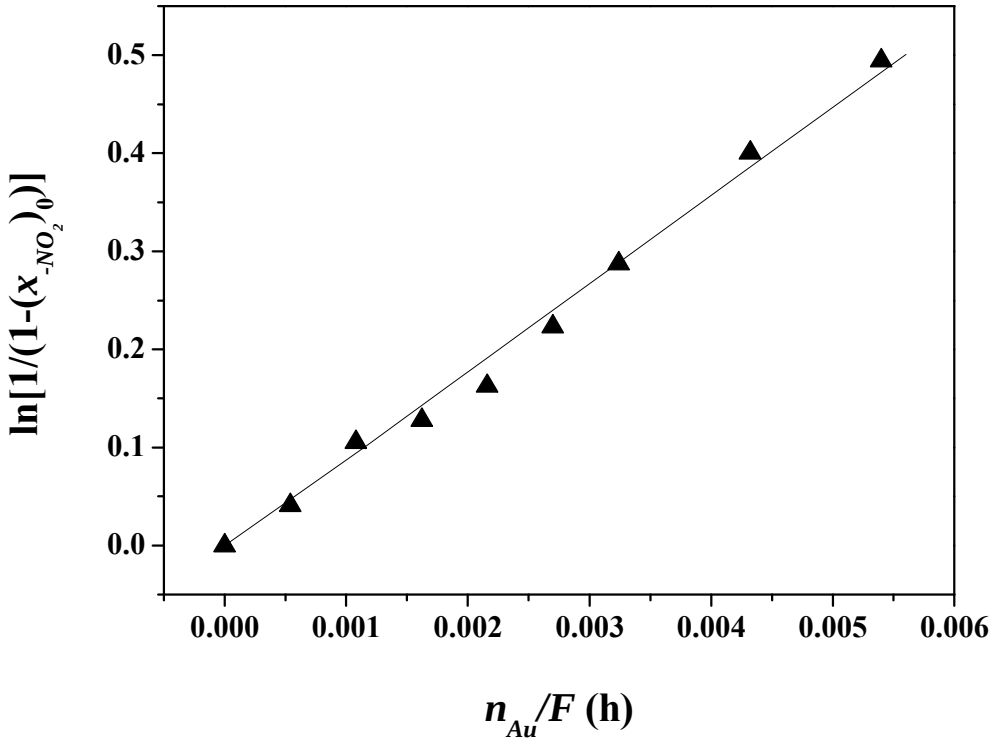

Figure 6.6: Pseudo-first order kinetic plot for the hydrogenation of *p*-chloronitrobenzene over Au/Fe_2O_3-DP.

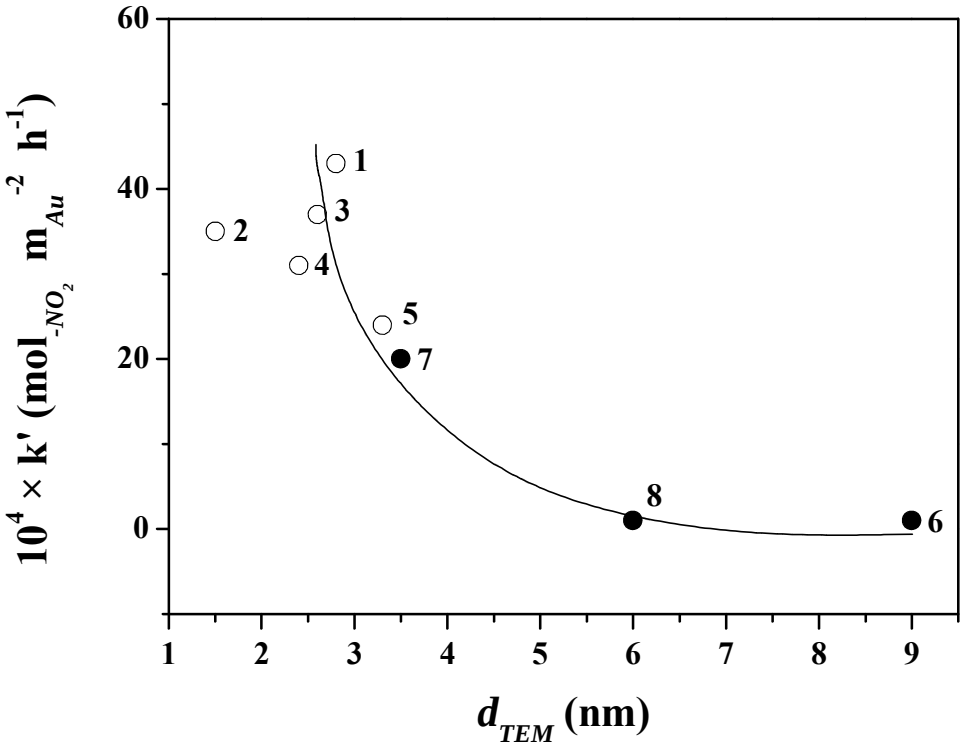

Figure 6.7: Relationship between specific rate constant (k′) and Au particle size (d_{TEM}) for reaction over Au/Al_2O_3-DP (1), Au/CeO_2-DP (2), Au/Fe_2O_3-DP (3), Au/TiO_2-DP (4), Au/TiO_2-Ref (5), $AuAl_2O_3$-IMP (6), Au/Fe_2O_3-IMP (7) and Au/TiO_2-IMP (8): DP catalysts represented by open circles; IMP catalysts represented by solid circles.

The observed decrease in k' with increasing Au particle size is consistent with structure sensitivity where Au particles < 4 nm are intrinsically more active for nitro-group reduction. The particle size/specific rate response for seven catalyst systems (laboratory synthesised and the World Gold Council Reference sample) fall on a common trend line. This suggests that the nature of the support does not impact significantly on hydrogenation rate, which is controlled by the Au particle size. Indeed, taking a common support (Al_2O_3, see points 1 and 6 in **Figure 6.7**) Au/Al_2O_3-DP (d_{TEM} = 2.8 nm) delivered a specific rate that was over 40 times greater than that obtained for Au/Al_2O_3-IMP (d_{TEM} = 9.0 nm), representing the upper and lower rate values recorded in this study. Moreover, systems with similar Au dispersion on different oxides present similar activity, as illustrated by points 3 (Au/Fe_2O_3-DP, d_{TEM} = 2.6 nm) and 4 (Au/TiO_2-DP, d_{TEM} = 2.4 nm) in **Figure 6.7**. It should be noted that Au/CeO_2-DP which presented the smallest Au particle size (1.5 nm) deviates somewhat from the general trend. We tentatively attribute this response to the small Au particle size which falls into the region (< 2 nm) where catalytic activity is severely modified by electronic and quantum size effects [80]. Indeed, the electronic character of Au can affect the catalytic response in hydrogenation reactions [13] and for particles sufficiently small (< 2 nm) a transition in the electronic state of gold from metal to non-metal has been suggested [81,82]. Moreover, Claus and co-workers [83], studying the gas phase hydrogenation of acrolein over nanosized Au/TiO_2 catalysts, associated the decrease in activity (400 → 41 mmol g_{Au}^{-1} s^{-1}) with decreasing Au particle size (2.0 → 1.4 nm) to the loss of metallic character for the smaller Au particles. In this study, we have established a significant Au particle size effect for the gas phase selective hydrogenation of *p*-chloronitrobenzene with an optimum mean Au particle size of *ca.* 3 nm that is independent of the nature of the oxide support. Future work will focus on alternative polyfunctional nitroarenes with the goal of achieving the product selectivity that we report in this study.

6.4 Conclusions

The results presented in this study support the following conclusions:

i) The continuous gas phase hydrogenation of *p*-chloronitrobenzene over Au supported on Al_2O_3, TiO_2, Fe_2O_3 and CeO_2 under mild reaction conditions (P = 1 atm; T = 423 K) results in the exclusive formation of *p*-chloroaniline.

ii) At a common Au loading (1 mol %), catalyst preparation by DP generates smaller (surface area weighted) mean Au particle sizes (≤ 3.3 nm) when compared with IMP (≥ 3.5 nm)**.** Moreover, Au particle size was greater on the non-reducible (Al_2O_3) carrier for both preparation methods.

iii) The nature of the support does not impact directly on the rate of nitro-group reduction, which is governed by Au particle size. An increase in specific hydrogenation rate is observed with a decrease in mean Au size from 9 to 3 nm. A lower specific rate recorded for smaller particles (< 2 nm) can be attributed to a quantum size effect. A temporal loss of activity was observed for reaction over smaller Au particles whereas those catalysts with a mean particle size > 4 nm displayed a time invariant conversion.

iv) Our results can serve as a proof concept, demonstrating the feasibility of gold catalysis as a viable sustainable route for the production of aromatic amines.

6.5 References

[6.1] P. Claus, Appl. Catal. A: Gen., 291, 222 (2005)

[6.2] A. S. K. Hashmi, Chem. Rev., 107, 3180 (2007)

[6.3] B. C. Campo, S. Ivanova, C. Gigola, C. Petit, M. A. Volpe, Catal. Today, 133-135, 661 (2008)

[6.4] T. Osaki, T. Hamada, Y. Tai, React. Kinet. Catal. Lett., 78, 217 (2003)

[6.5] G. C. Bond, C. Louis, D. T. Thompson, Catalysis by Gold, Imperial College Press, London, 2006.

[6.6] J. A. Lopez-Sanchez, D. Lennon, Appl. Catal. A: Gen., 291, 230 (2005)

[6.7] H. Sakurai, M. Haruta, Appl. Catal. A: Gen., 127, 93 (1995)

[6.8] C. Milone, R. Ingoglia, L. Schipilliti, C. Crisafulli, G. Neri, S. Galvagno, J. Catal., 236, 80 (2005)

[6.9] C. Milone, R. Ingoglia, A. Pistone, G. Neri, S. Galvagno, J. Catal., 222, 348 (2004)

[6.10] J. Radnik, C. Mohr, P. Claus, Phys. Chem. Chem. Phys., 5, 172 (2003)

[6.11] B. K. Min, W. T. Wallace, D. W. Goodman, Surf. Sci., 600, L7-L11 (2006)

[6.12] C. Binns, Surf. Sci. Rep., 44, 1 (2001)

[6.13] C. Mohr, H. Hofmeister, P. Claus, J. Catal., 213, 86 (2003)

[6.14] B. A. A. Silberova, G. Mul, M. Makkee, J. A. Moulijn, J. Catal., 243, 171 (2006)

[6.15] D. Andreeva, V. Idakiev, T. Tabakova, L. Ilieva, P. Falaras, A. Bourlinos, A. Travlos, Catal. Today, 72, 51 (2002)

[6.16] A. Sandoval, A. Gómez-Cortés, R. Zanella, G. Díaz, J. M. Saniger, J. Mol. Catal. A: Chem., 278, 200 (2007)

[6.17] V. Idakiev, T. Tabakova, Z.-Y. Yuan, B.-L. Su, Appl. Catal. A: Gen., 270, 135 (2004)

[6.18] P. N. Rylander, Catalytic Hydrogenation in Organic Synthesis. "Catalytic Dehydrohaloganation" Academic Press, Inc., New York, 1979.

[6.19] B. Chen, U. Dingerdissen, J. G. E. Krauter, H. G. J. L. Rotgerink, K. Möbus, D. J. Ostgard, P. Panster, T. H. Riermeier, S. Seebald, T. Tacke, H. Trauthwein, Appl. Catal. A: Gen., 280, 17 (2005)

[6.20] D. He, H. Shi, Y. Wu, B.-Q. Xu, Green Chem., 9, 849 (2007)

[6.21] A. Corma, P. Serna, H. García, J. Am. Chem. Soc. , 129, 6358 (2007)

[6.22] A. Corma, P. Concepción, P. Serna, Angew. Chem. Int. Ed., 46, 7266 (2007)

[6.23] M. Boronat, P. Concepción, A. Corma, S. González, F. Illas, P. Serna, J. Am. Chem. Soc., 129, 16230 (2007)

[6.24] A. Corma, P. Serna, Science, 313, 332 (2006)

[6.25] L. Liu, B. Qiao, Y. Ma, J. Zhang, Y. Deng, Dalton Trans., 2008, p. 2542.

[6.26] Y. Chen, J. Qiu, X. Wang, J. Xiu, J. Catal., 242, 227 (2006)

[6.27] G. Konnecker, A. Boehncke, S. Schmidt, Fresenius Environ. Bull., 12, 589 (2003)

[6.28] A. Boehnecke, J. Kielhorn, G. Konnecker, C. Pohlenz-Michel, I. Mangelsdorf, CICADS Report 48, W.H.O., Geneva, 2003, p. 78.

[6.29] K. R. Westerterp, E. J. Molga, K. B. van Gelder, Chem. Eng. Process., 36, 17 (1997)

[6.30] X. D. Wang, M. H. Liang, J. L. Zhang, Y. Wang, Curr. Org. Chem., 11, 299 (2007)

[6.31] V. Vishwanathan, V. Jayasri, P. M. Basha, N. Mahata, L. M. Sikhwivhilu, N. J. Coville, Catal. Commun., 9, 453 (2008)

[6.32] V. Kratky, M. Kralik, M. Mecarova, M. Stolcova, L. Zalibera, M. Hronec, Appl. Catal. A: Gen., 235, 225 (2002)

[6.33] F. Cárdenas-Lizana, S. Gómez-Quero, M. A. Keane, Catal. Commun., 9, 475 (2008)

[6.34] C. Xi, H. Cheng, J. Hao, S. Cai, F. Zhao, J. Mol. Catal. A: Chem., 282, 80 (2008)

[6.35] Y.-Z. Chen, Y.-C. Chen, Appl. Catal. A: Gen., 115, 45 (1994)

[6.36] Y.-C. Liu, C.-Y. Huang, Y.-W. Chen, Ind. Eng. Chem. Res., 45, 62 (2006)

[6.37] Y.-C. Liu, Y.-W. Chen, Ind. Eng. Chem. Res., 45, 2973 (2006)

[6.38] Z. Yu, S. Liao, Y. Xu, B. Yang, D. Yu, J. Mol. Catal. A: Chem., 120, 247 (1997)

[6.39] B. Coq, A. Tijani, F. Figuéras, J. Mol. Catal., 68, 331 (1991)

[6.40] V. L. Khilnani, S. B. Chandalia, Org. Proc. Res. Dev., 5, 257 (2001)

[6.41] F. Cárdenas-Lizana, S. Gómez-Quero, M. A. Keane, ChemSusChem, 1, 215 (2008)

[6.42] G. Neri, A. M. Visco, S. Galvagno, A. Donato, M. Panzalorto, Thermochim. Acta, 329, 39 (1999)

[6.43] F. E. Wagner, S. Galvagno, C. Milone, A. M. Visco, L. Stievano, S. Calogero, J. Chem. Soc., Faraday Trans., 93, 3403 (1997)

[6.44] D. Andreeva, V. Idakiev, T. Tabakova, A. Andreev, R. Giovanoli, Appl. Catal. A: Gen., 134, 275 (1996)

[6.45] G. C. Bond, D. T. Thompson, Catal. Rev.-Sci. Eng., 41, 319 (1999)

[6.46] M. Haruta, Catal. Today, 36, 153 (1997)

[6.47] M. Khoudiakov, M. C. Gupta, S. Deevi, Appl. Catal. A: Gen., 291, 151 (2005)

[6.48] M. Haruta, S. Tsubota, T. Kobayashi, H. Kageyama, M. J. Genet, B. Delmon, J. Catal., 144, 175 (1993)

[6.49] S. Tsubota, A. Yamaguchi, M. Daté, M. Haruta, "Characterization of Reference Gold Catalysts" in *GOLD2003, 3rd International Conference on Gold Science, Technology and its Applications*, September-October, 2003, Vancouver, Canada,

[6.50] L. Delannoy, N. Weiher, N. Tsapatsaris, A. M. Beesley, L. Nchari, S. L.M. Schroeder, C. Louis, Top. Catal., 44, 263 (2007)

[6.51] G. Tavoularis, M. A. Keane, J. Chem. Technol. Biotechnol., 74, 60 (1999)

[6.52] C. M. Van Den Bleek, K. Van Der Wiele, P. J. Van Der Berg, Chem. Eng. Sci., 24, 681 (1969)

[6.53] G. Yuan, M. A. Keane, Chem. Eng. Sci., 58, 257 (2003)

[6.54] G. Yuan, J. L. Lopez, C. Louis, L. Delannoy, M. A Keane, Catal. Commun., 6, 555 (2005)

[6.55] G. Yuan, C. Louis, L. Delannoy, M. A. Keane, J. Catal. , 247, 256 (2007)

[6.56] A. G. Sault, R. J. Madix, C. T. Campbell, Surf. Sci., 169, 347 (1986)

[6.57] L. Stobiński, L. Zommer, R. Duś, Appl. Surf. Sci., 141, 319 (1999)

[6.58] M. Okada, M. Nakamura, K. Moritani, T. Kasai, Surf. Sci., 523, 218 (2003)

[6.59] M. Okada, S. Ogura, W. A. Diño, M. Wilde, K. Fukutani, T. Kasai, Appl. Catal. A: Gen., 291, 55 (2005)

[6.60] M. Okumura, T. Akita, M. Haruta, Catal. Today, 74, 265 (2002)

[6.61] R. Zanella, C. Louis, S. Giorgio, R. Touroude, J. Catal., 223, 328 (2004)

[6.62] J. Słoczyński, R. Grabowski, A. Kozłowska, P. Olszewski, J. Stoch, J. Skrzypek, M. Lachowska, Appl. Catal. A: Gen., 278, 11 (2004)

[6.63] A. C. Gluhoi, X. Tang, P. Marginean, B. E. Nieuwenhuys, Top. Catal., 39, 101 (2006)

[6.64] T.-H. Kim, D.-W. Kim, J.-M. Lee, Y.-G. Lee, S.-G. Oh, Mater. Res. Bull., 43, 1126 (2008)

[6.65] X. Hu, D. J. Blackwood, J. Electroceram., 16, 593 (2006)

[6.66] C. Karunakaran, P. Anilkumar, J. Mol. Catal. A: Chem., 265, 153 (2007)

[6.67] C. Karunakaran, P. Anilkumar, Sol. Energy Mater. Sol. Cells, 92, 490 (2008)

[6.68] C. Karunakaran, R. Dhanalakshmi, S. Karuthapandian, J. Photochem. Photobiol., A 170, 233 (2005)

[6.69] C. Sol, R. J. D. Tilley, J. Mater. Chem., 11, 815 (2001)

[6.70] J. Xiong, J. X. Chen, J. Y. Zhang, Catal. Commun., 8, 345 (2007)

[6.71] X.-X. Han, R.-X. Zhou, G.-H. Lai, X.-M. Zheng, Catal. Today, 93-95, 433 (2004)

[6.72] A. Hugon, L. Delannoy, C. Louis, Gold Bulletin, 41, 127 (2008)

[6.73] P. Sangeetha, P. Seetharamulu, K. Shanthi, S. Narayanan, K.S. Rama Raob, J. Mol. Catal. A: Chem., 273, 244 (2007)

[6.74] S. Diao, W. Qian, G. Luo, F. Wei, Y. Wang, Appl. Catal. A: Gen., 286, 30 (2005)

[6.75] L. Petrov, K. Kumbilieva, N. Kirkov, Appl. Catal., 59, 31 (1990)

[6.76] E. Klemm, B. Amon, H. Redlingshöfer, E. Dieterich, G. Emig, Chem. Eng. Sci., 56, 1347 (2001)

[6.77] Y. Azizi, C. Petit, V. Pitchon, J. Catal., 256, 338 (2008)

[6.78] B. Pawelec, A. M. Venezia, V. La Parola, S. Thomas, J. L. G. Fierro, Appl. Catal. A: Gen., 283, 165 (2005)

[6.79] F. Cárdenas-Lizana, S. Gómez-Quero, M. A. Keane, Catal. Lett., 127, 25 (2009)

[6.80] M. Valden, X. Lai, D. W. Goodman, Science, 281, 1647 (1998)

[6.81] K. Okazaki, S. Ichikawa, Y. Maeda, M. Haruta, M. Kohyama, Appl. Catal. A: Gen., 291, 45 (2005)

[6.82] C. P. Vinod, G. U. Kulkarni, C. N. R. Rao, Chem. Phys. Lett., 289, 329 (1998)

[6.83] P. Claus, A. Brückner, C. Mohr, H. Hofmeister, J. Am. Chem. Soc., 122, 11430 (2000)

Chapter 7

Controlled Nitro-group Reduction in the Conversion of *m*-Dinitrobenzene over Oxide Supported Gold: Role of the Support

In the hydrogenation of *p*-chloronitrobenzene over Au, exclusive nitro-group reduction has been established where the nature of the support does not impact directly on the catalytic response, which is mainly controlled by the particle size. In this Chapter, the influence of the support chemistry on activity and selectivity behaviour is considered in the hydrogenation of *m*-dinitrobenzene.

7.1 Introduction

Aromatic amines are important intermediates in the manufacture of a range of fine chemicals, including herbicides, pesticides, dyes and pigments [1]. The conventional route for the production of aminoarenes is the batch hydrogenation of the corresponding nitro-compound either in dilute acid media using Fe (Béchamp process) [2] or over Ni [3], Pt [4] and Pd [5] catalysts. Both approaches suffer major drawbacks in terms of low product yields and costly waste treatment/disposal due to the formation of highly toxic compounds [6], *i.e.* iron oxide sludges and azo/azoxy-derivates. Reaction selectivity is particularly challenging in the hydrogenation of *m*-dinitrobenzene (*m*-DNB), where the exclusive formation of either *m*-nitroaniline (*m*-NAN), *i.e.* partial -NO_2 reduction, or *m*-phenylenediamine (*m*-PDM), *i.e.* complete -NO_2 reduction, has yet to be achieved [7,8]. The catalytic activity of Au in hydrogen mediated reactions is significantly lower than that of Group VIII metals [9-11]. The higher rates delivered by Ni-, Pd-, or Pt-based catalysts has been associated with the greater facility of these metals (relative to Au) to dissociatively adsorb H_2 [12]. However, when highly dispersed (≤10 nm) on a support [13,14], Au is known to exhibit high selectivity in a number of hydrogenation reactions [15,16]. To date, the hydrogenation of aromatic nitro compounds over Au catalysts has focused on batch reaction in the liquid phase [10,17-22] involving high H_2 pressures (3-4 MPa) [20-22].

The catalytic response in hydrogenation reactions over supported Au systems can be governed by contributions due to the morphology, dispersion and electronic properties of the Au phase which, in turn, can be influenced by interactions with the support [23,24]. Oxides have been the most widely used Au carriers where the support redox and/or acid-base properties can impact on catalytic performance [25]. The redox character has a direct role to play where a partial reduction of the support generates Au-oxide interactions that affect Au morphology [26,27], resulting in a preponderance of a particular crystallographic plane with distinct catalytic properties [28]. Support acid-base properties [29,30] can result in electron transfer [26,31] from/to the metal phase giving rise to positively (electron-deficient) or negatively charged Au particles [28]. The available literature that addresses support effects in hydrogenation reactions over Au is limited but Milone and co-workers [32] have shown that the use of a reducible support (notably Fe_2O_3) strongly influenced activity/selectivity in benzalacetone and cinnamaldehyde hydrogenation where the formation of electron rich Au species, *via* support-metal electron transfer, enhanced C=O activation. Lopez-Sanchez and Lennon [24], using Au/TiO_2 and Au/Fe_2O_3 to promote the hydrogenation of propyne, reported differences in activity-selectivity which they ascribed to differences in metal-support interactions in both systems. Campo *et al.* [33], in the gas phase hydrogenation of crotonaldehyde over Au/CeO_2 and Au/Nb_2O_5, recorded a distinct catalytic response in that Au/CeO_2 was highly selective to crotyl alcohol but Au/Nb_2O_5 was non-selective and they attributed this to the formation of unselective Au particles on Nb_2O_5 with a different morphology. Bailie and Hutchings [34] obtained differences in selectivity for the hydrogenation of crotonaldehyde over Au supported on ZnO and ZrO_2 and they established that treatment with thiophene affected selectivity, proposing that sites at the Au-support interface were responsible for carbonyl activation.

We have recently demonstrated [35-37] that oxide supported Au is 100% selective in the gas phase continuous hydrogenation of halonitroarenes to the respective halogenated aromatic amine. This study represents an extension to that work with the objective of probing the effect(s) of varying the nature of the oxide support (Al_2O_3, TiO_2, CeO_2 and Fe_2O_3) on the activity, selectivity and stability of Au in the hydrogenation of *m*-DNB. We demonstrate that product composition can be adjusted (or tuned) through the choice of support.

7.2 Experimental

7.2.1 Catalyst Preparation and Activation

The effect of the support on catalytic performance was investigated by selecting a group of reducible (CeO_2, TiO_2 and α-Fe_2O_3) and non-reducible (γ-Al_2O_3) oxides with distinct acid-base properties. The CeO_2 (HSA5, Rhodia,), TiO_2 (Degussa, P-25) and γ-Al_2O_3 (Puralox, Condea Vista Co.) supports were used as received. Hematite (α-Fe_2O_3) was prepared by precipitation in basic media according to [38,39]

$$2[Fe(NO_3)_3 \cdot 9H_2O] + 3Na_2CO_3 \longrightarrow 2Fe(OH)_3 + 6NaNO_3 + 3CO_2 + 15H_2O \quad (7.1)$$

100 cm^3 aqueous Na_2CO_3 (1 M) were placed in a three-necked round-bottom flask and heated in a water bath to 358 ± 5 K under constant agitation (300 rpm) provided by a glass impeller. An aqueous solution of $Fe(NO_3)_3 \cdot 9H_2O$ (300 cm^3, 1 M) was then added dropwise (300 cm^3 h^{-1}) by means of a microprocessor-controlled infusion pump (100 kd Scientific). Basic conditions (pH > 7.3) were maintained during precipitation by adding Na_2CO_3 (five additions of 10 g). The solid hydroxide was subsequently aged for 2 h to enhance the BET area [40], washed with warm distilled water until the washwater reached neutrality and dried for 3 days at 353 K (2 K min^{-1}) in an atmosphere of ultra pure He (60 cm^3 min^{-1}) to produce hematite:

$$2Fe(OH)_3 \longrightarrow Fe_2O_3 + 3H_2O \quad (7.2)$$

A series of 1 mol % oxide supported Au were prepared by deposition-precipitation (DP) and impregnation (IMP). These synthesis routes were chosen as it has been shown that catalysts prepared by DP generate smaller metal particles when compared with the less controlled IMP procedure [41]. In the case of the DP samples, urea (used as basification agent) was added (*ca.* 100-fold urea excess) to a solution of $HAuCl_4$ (5×10^{-4} M). The support (3-5 g, γ-Al_2O_3, TiO_2, CeO_2 and α-Fe_2O_3) was added and the suspension was stirred and heated to 353 K for 16 h. The pH of the suspension progressively increased to reach *ca.* 7 after 16 h as a result of the thermally-induced urea decomposition

$$NH_2\text{-}CO\text{-}NH_2 + 3H_2O \xrightarrow{T=353K} 2NH_4^+ + 2OH^- + CO_2 \quad (7.3)$$

The solids obtained were separated by centrifugation, washed three times with deionized water (with centrifugation between each washing) and dried under vacuum at 298 K for 12 h. In the case of the IMP synthesis, the support was dispersed in appropriate volumes of $HAuCl_4$ solution (Aldrich, 25 × 10^{-3} g cm^{-3}, pH = 2) and the resulting slurry was vigorously stirred (600 rpm) and slowly heated (2 K min^{-1}) to 353 K in a He flow. The solid residue was dried in He at 383 K for 3 h. For comparison purposes, a 10 mol % Au on Fe_2O_3 was synthesized by IMP. The samples prepared by impregnation or deposition-precipitation are denoted in this paper by the suffix "-IMP" and "-DP", respectively, with the associated Au content (1 or 10 mol %) specified in parentheses. After preparation, the samples were sieved to 75 μm average particle diameter (ATM fine test sieves) and stored at 277 K (in the dark). The Au loading was determined (to within ± 2%) by inductively coupled plasma-optical emission spectrometry (ICP-OES, Vista-PRO, Varian Inc.) from the diluted extract of aqua regia. The catalytic behaviour of a 1 mol % Au/TiO_2 reference catalyst supplied by the World Gold Council (type A, lot number $Au\text{-}TiO_2$ #02-7, sample number 110) was also considered. The preparation and characterization details of this reference sample have been fully described elsewhere [42,43]. Prior to use in catalysis, the samples were activated in 60 cm^3 min^{-1} H_2 at 2 K min^{-1} to 423-603 ± 1 K. Samples for off-line analysis were passivated in 1% v/v O_2/He at room temperature.

7.2.2 Catalysis Characterization

Temperature programmed reduction (TPR), H_2 chemisorption, temperature programmed desorption (TPD) and BET surface area were determined using the commercial CHEM-BET 3000 (Quantachrome) unit. The samples were loaded into a U-shaped Quartz cell (10 cm ×. 3.76 mm i.d.) and heated in 17 cm^3 min^{-1} (Brooks mass flow controlled) 5% v/v H_2/N_2 at 2 K min^{-1} to 423-603 ± 1 K. The effluent gas passed through a liquid N_2 trap and changes in H_2 consumption were monitored by TCD with data acquisition/manipulation using the TPR Win™ software. The reduced samples were maintained at the final temperature in a flow of H_2 until the signal returned to baseline, swept with a 65 cm^3 min^{-1} flow of N_2 for 1.5 h, cooled to room temperature and subjected to H_2 chemisorption using a pulse (10 μl) titration procedure. H_2 TPD was conducted in a N_2 flow (65 cm^3 min^{-1}) at 50 K min^{-1} to 873 K with an isothermal hold until the signal returned to the baseline. BET areas were recorded with a 30% v/v N_2/He flow using pure N_2 (99.9%) as internal standard. At least 2 cycles of N_2 adsorption-

desorption in the flow mode were employed to determine total surface area using the standard single point method. BET surface area and H_2 uptake values were reproducible to within ± 5%; the values quoted represent the mean.

Powder X-ray diffractograms were recorded on a Bruker/Siemens D500 incident X-ray diffractometer using Cu Kα radiation. The samples were scanned at a rate of 0.02º $step^{-1}$ over the range $20º \leq 2\theta \leq 90º$ (scan time = 5 s $step^{-1}$). Diffractograms were identified using the JCPDS-ICDD reference standards, *i.e.* α-Fe_2O_3 (33-0664), Fe_3O_4 (19-0629) and Au (04-0784). Au particle morphology and size were determined by transmission electron microscopy analysis; JEOL JEM 2011 HRTEM unit with a UTW energy dispersive X-ray detector (Oxford Instruments) operated at an accelerating voltage of 200 kV using Gatan DigitalMicrograph 3.4 for data acquisition/manipulation. The specimens were prepared by dispersion in acetone and deposited on a holey carbon/Cu grid (300 Mesh). Up to 1000 individual Au particles were counted for each catalyst and the surface area-weighted metal diameter (d_{TEM}) was calculated from

$$d_{TEM} = \frac{\sum_i n_i d_i^3}{\sum_i n_i d_i^2} \qquad (7.4)$$

where n_i is the number of particles of diameter d_i. The size limit for the detection of Au particles is *ca.* 1 nm.

7.2.3 Catalyst Procedure

Reactions were carried out under atmospheric pressure at T = 423 K, in situ immediately after activation, in a fixed bed vertical continuous glass reactor (l = 600 mm; i.d. = 15 mm). The catalytic reactor and operating conditions to ensure negligible heat/mass transport limitations, have been fully described elsewhere [44] but some features, pertinent to this study, are given below. A layer of borosilicate glass beads served as preheating zone, ensuring that the *m*-DNB was vaporized and reached reaction temperature before contacting the catalyst. Isothermal conditions (± 1 K) were ensured by diluting the catalyst bed with ground glass (75 μm); the ground glass was mixed thoroughly with catalyst before insertion into the reactor. Temperature was continuously monitored by a thermocouple inserted in a thermowell within the catalyst bed. *m*-DNB

was delivered at a fixed calibrated flow rate to the reactor *via* a glass/teflon air-tight syringe and teflon line using a microprocessor controlled infusion pump (Model 100 kd Scientific). A co-current flow of *m*-DNB and ultra pure H_2 (< 1% v/v -NO_2/H_2) was maintained at a $GHSV = 2 \times 10^4$ h^{-1} with an inlet -NO_2 molar flow (F_{-NO_2}) over the range $6\times10^{-2} - 20\times10^{-2}$ $mmol_{-NO_2}$ h^{-1} . The H_2 inlet was two orders of magnitude in excess of the stoichiometric requirement (P_{H_2} = 0.92 atm), the flow rate of which was monitored using a Humonics (Model 520) digital flowmeter. The molar metal (n_{Au}) to F_{-NO_2} ratio spanned the range 29×10^{-4}–111×10^{-4} h. In a series of blank tests, passage of *m*-DNB in a stream of H_2 through the empty reactor or over the support alone, *i.e.* in the absence Au, did not result in any detectable conversion. The reactor effluent was frozen in a liquid nitrogen trap for subsequent analysis, which was made using a Perkin-Elmer Auto System XL gas chromatograph equipped with a programmed split/splitless injector and a flame ionization detector, employing a DB-1 50 m × 0.20 mm i.d., 0.33 μm film thickness capillary column (J&W Scientific), as described elsewhere [45]. *m*-DNB (Aldrich, ≥98% w/w purity) and the 1-butanol solvent (Riedel-de Häen, ≥ 99.5%) were used without further purification. The degree of nitro-group reduction (x_{-NO_2}), as a measure of hydrogenation activity, is given by

$$x_{-NO_2} = \frac{[\text{-NH}_2]_{out}}{[\text{-NO}_2]_{in}} = \frac{2\times[m\text{-PDM}]_{out} + [m\text{-NAN}]_{out}}{2\times[m\text{-DNB}]_{in}} \qquad \textbf{(7.5)}$$

where [*m*-DNB], [*m*-NAN] and [*m*-PDM] are, respectively, the concentrations of *m*-DNB, *m*-NAN and *m*-PDM; the subscripts *in* and *out* refer to the inlet and outlet streams. Selectivity in terms of (for example) *m*-NAN ($S_{m\text{-}NAN}$) is given by

$$S_{m\text{-}NAN} = \frac{[m-\text{NAN}]_{out}}{[m\text{-DNB}]_{in} - [m\text{-DNB}]_{out}} \qquad \textbf{(7.6)}$$

Repeated reactions with the same batch of catalyst delivered conversion/selectivity values that were reproducibility to within ± 6%.

7.3 Result and Discussion

7.3.1 Catalyst Characterization

7.3.1.1 BET/TPR/XRD

BET surface areas of the activated 1 mol % Au catalysts considered in this study are recorded in **Table 7.1**. The TPR activation profiles associated with the supports (γ-Al_2O_3 (A), TiO_2 (B) and CeO_2 (C)) are given in **Figure 7.1** (profiles I) and those generated for supported Au prepared by DP and IMP appear as profiles II and III, respectively. The temperatures associated with maximum H_2 consumption (T_{max}) during TPR of the Au catalysts are provided in **Table 7.1**. The profile obtained for the non-reducible γ-Al_2O_3 support is featureless, with no evidence of H_2 uptake or release, a response that is expected and is consistent with the literature [46]. In contrast, over the same temperature range (up to 1073 K), the reducible supports exhibited a positive signal (H_2 consumption) during TPR. TiO_2 presented a broad peak with an associated T_{max} at *ca.* 850 K, which can be linked to a H_2 consumption at $T \geq 773$ K reported previously [47] for TiO_2 reduction. The CeO_2 support also exhibited a broad positive signal (T_{max} at *ca.* 710 K) which can be attributed to the surface reduction of ceria [48]. TPR profiles generated for the catalysts prepared by DP (profiles II) are characterised by a H_2 consumption peak over the range 371-450 K. A single TPR peak (373-633 K) has been reported in the literature and ascribed to the reduction of Au^{3+} species to Au^0 [49,50]. We tentatively associate the different T_{max} values registered for the DP samples to differences in metal-support interactions for these Au-oxide systems. Indeed, Liu and Yang [51] have recently reported the reduction of gold species at 378 K and 450 K for Au/TiO_2 and Au/Al_2O_3, respectively. Delannoy and co-workers [52] have considered the role of the support in modifying Au reducibility for DP systems and reported a decrease in Au(III) reducibility in the sequence $TiO_2 > CeO_2 > Al_2O_3$. The profiles for the IMP samples present a principal peak at 434 K that agrees well with the literature [53,54], with a secondary peak at 457 K in the case of Au/TiO_2. Yim and Nam [55] reported a similar response for CrO_x supported on Al_2O_3 and TiO_2, where the TPR profiles where characterized by one (593–663 K) and two (553–593 K and 693–713 K) reduction peaks, respectively. Idakiev *et al.* [56], associated a TPR peak at 373 K to a $Ti^{4+} \rightarrow Ti^{3+}$ transformation at the metal/support interface for Au/TiO_2. The H_2 consumption values recorded for all the Au catalysts presented in **Figure 7.1** (DP and IMP) are close to that required for the reduction of the supported precursors

Table 7.1: Gold particle size obtained by TEM (d_{TEM}) analysis, hydrogen consumed during TPR (to 423 or 673 K) with associated T_{max}, H_2 chemisorption values and BET surface area for a series of oxide-supported Au catalysts prepared by deposition-precipitation (DP) and impregnation (IMP).

Catalyst	d_{TEM} (nm)	TPR T_{max} (K)	H_2 TPR *theoretical*[a] (μmol g_{cat}^{-1})	H_2 TPR *experimental* (μmol g_{cat}^{-1})	H_2 *uptake* (μmol g_{Au}^{-1})	BET area (m^2 g^{-1})
Au/Al_2O_3-DP(1)	2.8	450	67	62	33	142
Au/CeO_2-DP(1)	1.5	423	69	63	63	195
Au/Fe_2O_3-DP(1)	2.6	366[b,c], 512[b]	62	2093[b] 750[c]	21	57
Au/TiO_2-DP(1)	2.4	371	78	71	28	48
Au/TiO_2-Ref	3.3	[d]	79	[d]	46	50
Au/Al_2O_3-IMP(1)	9.0	434	152	140	22	161
Au/Fe_2O_3-IMP(1)	3.5	370 [b,c], 508[b]	62	2050[b] 700[c]	27	56
Au/TiO_2-IMP(1)	6.0	432,457	193	177	16	47

[a]theoretical amount of H_2 necessary to reduce the Au precursor
[b]TPR to 673 K (see **Figure 7.2**, solid line in profiles II and III)
[c]TPR to 423 K (see **Figure 7.2**, dashed line in profiles II and III)
[d]no hydrogen consumption detected during TPR

(see **Table 7.1**), indicating that the positive peak(s) recorded during TPR are due to the reduction of cationic Au to metallic Au.

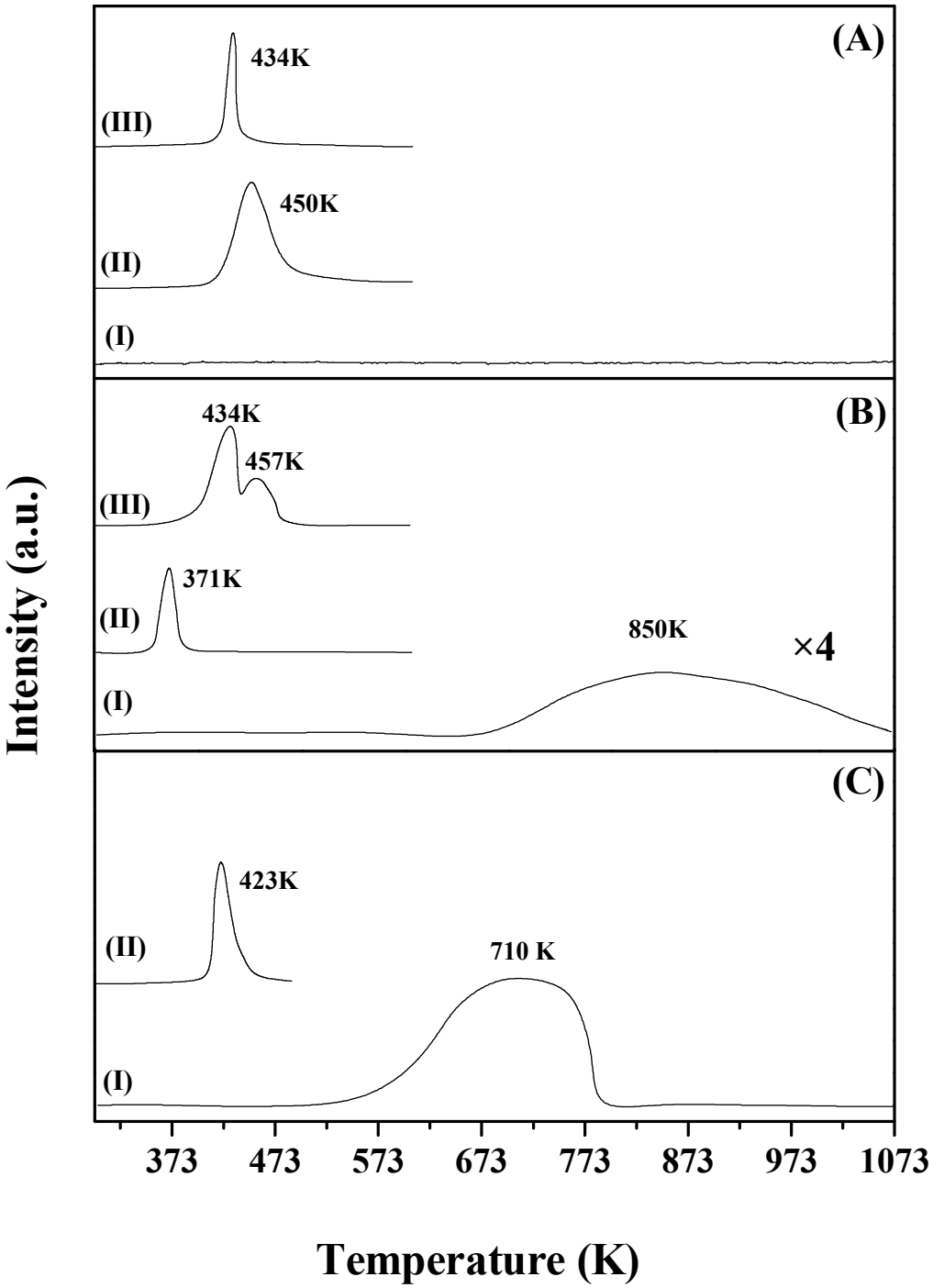

Figure 7.1: TPR profiles generated for: (A) Al_2O_3 support (I), Au/Al_2O_3-DP(1) (II) and Au/Al_2O_3-IMP(1) (III); (B) TiO_2 support (I), Au/TiO_2-DP(1) (II) and Au/TiO_2-IMP(1) (III); (C) CeO_2 support (I) and Au/CeO_2-DP(1) (II).

The X-ray diffractogram patterns for the as prepared Fe_2O_3, Au/Fe_2O_3-DP(1) and Au/Fe_2O_3-IMP(1) are identical and the common profile is presented as an inset (A) in **Figure 7.2**).

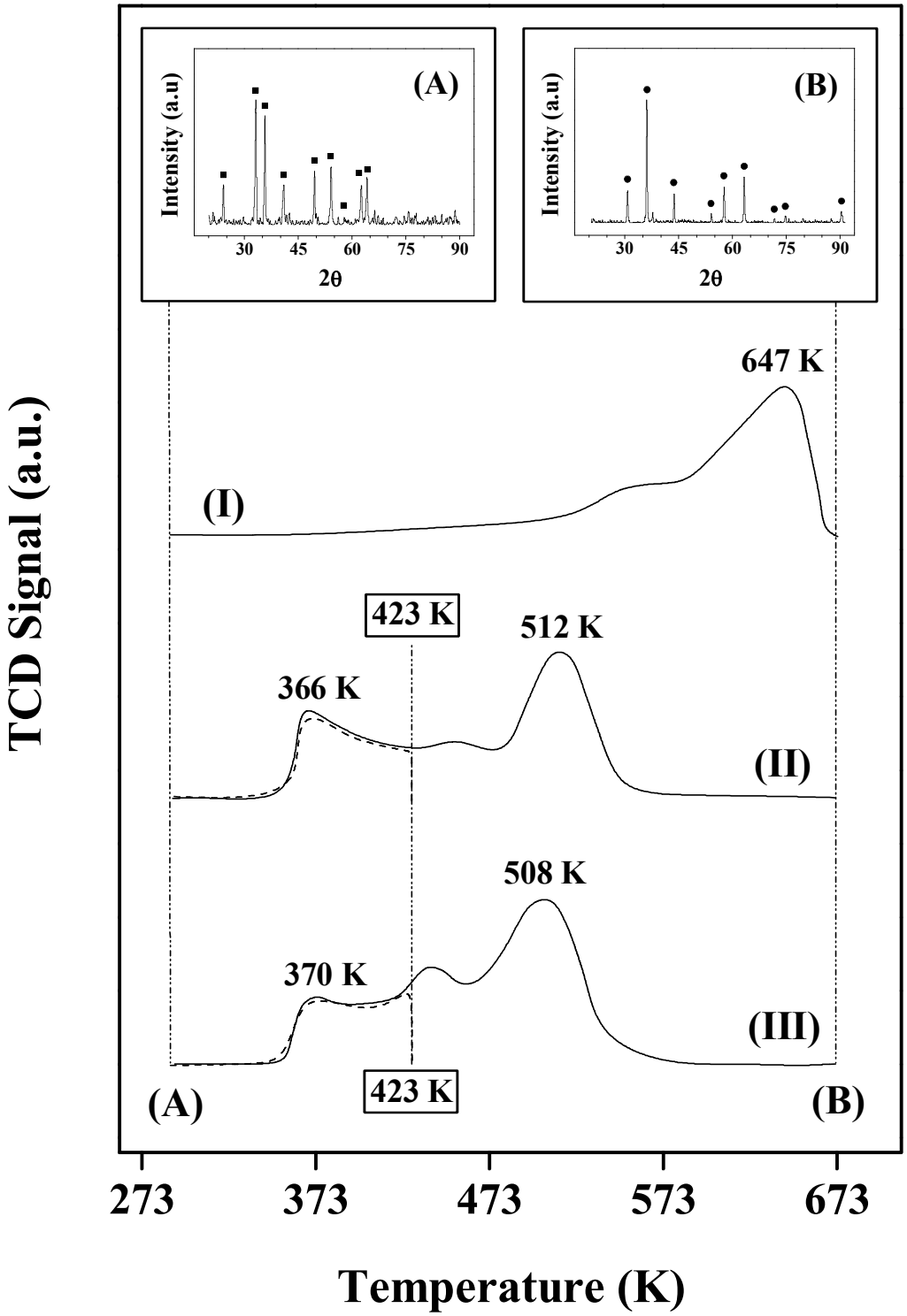

Figure 7.2: TPR profiles for (I) α-Fe_2O_3, (II) Au/Fe_2O_3-DP(1) and (III) Au/Fe_2O_3-IMP(1) activated to 423 K (dashed line) or 673 K (solid line). Common XRD patterns for Fe_2O_3, Au/Fe_2O_3-DP(1) and Au/Fe_2O_3-IMP(1): (A) starting (unreduced) samples and (B) samples activated at 673 K. *Note*: peak assignments based on JCPDS-ICDD reference data: (■) α-Fe_2O_3 (33-0664); (●) Fe_3O_4 (19-0629).

The three systems present signals at 2θ = 24.1°, 33.2°, 35.6°, 40.9°, 49.5°, 54.1°, 57.6°, 62.4° and 64.0° corresponding to the (012), (104), (110), (113), (024), (116), (018), (214) and (300) planes of α-phase Fe_2O_3 (hematite) (JCPDS-ICDD card number 33-0664). The XRD patterns of the three samples post-TPR (to 673 K) (see inset (B), **Figure 7.2**) were also identical with reflections at 2θ = 30.1°, 35.4°, 43.1°, 53.4°, 56.9°, 62.5°, 70.9°, 73.9° and 89.6° associated with the (220), (311), (400), (422), (511), (440), (620), (533) and (731) planes of Fe_3O_4 (magnetite) (JCPDS-ICDD card number 10-0629). The TPR profile for the starting hematite support (see **Figure 7.2**, profile I) is characterized by the appearance of one main hydrogen consumption peak at 647 K that can be associated with the formation of Fe_3O_4 [57]. Two main peaks at 368±2 K and 510±2 K characterize the TPR profiles obtained for Au/Fe_2O_3-DP(1) and Au/Fe_2O_3-IMP(1) (**Figure 7.2**, solid lines in profiles II and III, respectively). The hydrogen consumption during TPR matched (to within ± 5%) that required for the reduction of $Fe_2O_3 \rightarrow Fe_3O_4$ in the three systems and far exceeded the requirements for Au precursor reduction in the case of Au/Fe_2O_3-DP(1) and Au/Fe_2O_3-IMP(1) (see **Table 7.1**). Li *et al.* [58] reported a reduction peak at *ca.* 373 K for Au/Fe_2O_3 prepared by DP and associated this with a partial reduction of Fe_2O_3 to Fe_3O_4. A comparison of the TPR response of Au/Fe_2O_3 with that of Fe_2O_3 suggests that Au served to lower the temperature requirements for the reduction of hematite to magnetite. Indeed, a decrease (by up to 200 K) in the reduction temperature of Fe_2O_3 to Fe_3O_4 has been reported post-Au incorporation [59,60]. The TPR profiles generated for sample activation up to 423 K (reaction temperature) are identified in **Figure 7.2** by dashed lines. This activation temperature was chosen based on the results presented in **Figure 7.1** which show that the $Au^{3+} \rightarrow Au^0$ reduction step occurred at $T \leq 457$ K. The quantity of hydrogen associated with the single peak (368±2 K) recorded in **Table 7.1** exceeded (by up to a factor of 12) the amount required to reduce the Au precursor to the metallic form but was still lower (by a factor of 3) than that required to fully transform Fe_2O_3 to Fe_3O_4.

These findings suggest that the presence of Au results in a "partial" reduction of the iron oxide support at 423 K. This response was probed further by XRD analysis and the results are presented in **Figure 7.3**. The XRD patterns of Au/Fe_2O_3-DP(1) (profile I) and Au/Fe_2O_3-IMP(1) (profile II) reduced at 423 K show XRD reflections that are characteristic of α-Fe_2O_3 (hematite) (see profile V). Nevertheless, it should be noted that the relative intensity of the two main peaks at 2θ = 33.2° and 35.6° ((104)/(110))

differs from that which characterises the reference hematite (see dashed square "a" in **Figure 7.3**): α-Fe_2O_3 = 4/3; Au/Fe_2O_3-DP(1) = 3/4; Au/Fe_2O_3-IMP(1) = 1/1. As the XRD peak for the (110) plane of hematite coincides with the main characteristic peak for magnetite (2θ = 35.4°, plane (311)), the variation in relative intensities suggests a partial transformation of hematite to magnetite during the reduction of Au/Fe_2O_3. Moreover, this step appears to be promoted to a greater extent for Au/Fe_2O_3-DP(1) when compared with Au/Fe_2O_3-IMP(1).

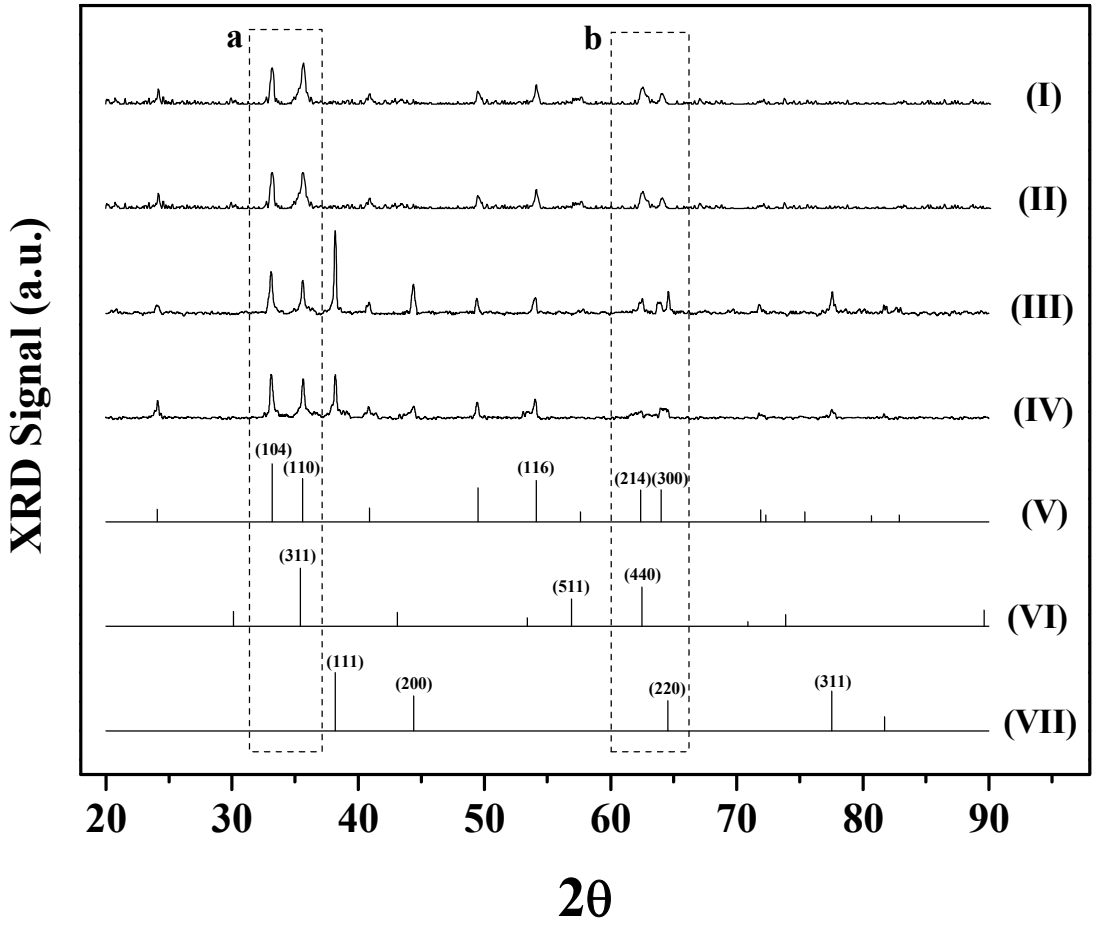

Figure 7.3: XRD patterns associated with passivated/reduced (at 423 K) (I) Au/Fe_2O_3-DP(1), (II) Au/Fe_2O_3-IMP(1), (III) Au/Fe_2O_3-IMP(10) and (IV) as prepared Au/Fe_2O_3-IMP(10); JCPDS-ICDD reference diffractograms for (V) α-Fe_2O_3 (33-0664), (VI) Fe_3O_4 (19-0629) and (VII) Au (04-0784).

Wang *et al.* [61] suggested that the presence of $Au^{\delta+}$ modifies the polarity of the Fe-O bond, resulting in a more facile reduction of Fe_2O_3 to Fe_3O_4. A similar trend is observed for the XRD signals at 2θ = 62.4° and 64.0° (planes (214) and (300) of α-Fe_2O_3) and the (440) plane (at 2θ = 62.5°) of Fe_3O_4 (see dashed square "b" in **Figure 7.3**), *i.e.* modified relative intensities for the characteristic signals of hematite with simultaneous appearance of one of the main peaks of magnetite, a result that is consistent with a

partial reduction of the support. Moreover, the formation of magnetite post-activation (at 423 K) is confirmed by the presence of a new peak at $2\theta = 56.9°$, associated with the (511) plane of Fe_3O_4. Thus, the "overconsumption" of H_2 during TPR to 423 K (see **Table 7.1**) can be attributed to Au induced partial reduction of α-Fe_2O_3. It is important to note that there were no detectable signals for metallic Au in the XRD profiles for Au/Fe_2O_3-DP(1) or Au/Fe_2O_3-IMP(1), which suggests a highly dispersed Au phase. It has been established [62,63] that one of the main factors determining Au particle size is Au loading in that a higher Au content favours agglomeration and the formation of larger Au particles. In order to confirm Au precursor reduction to Au^0 post-TPR, a higher Au loading (10 mol %) on Fe_2O_3 was prepared and activated under the same conditions, where the expected formation of larger Au particles as a result of the higher metal content should result in the appearance of XRD signals due to metallic Au. The XRD diffractograms for the activated and as prepared Au/Fe_2O_3-IMP(10) (profiles III and IV, respectively in **Figure 7.3**) exhibit, in addition to the reflections due to the support, peaks for Au metal (JCPDS-ICDD 04-0784), *i.e.* $2\theta = 38.1°$, 44.4°, 64.7° and 77.5° corresponding to (111), (200), (220) and (311) planes, respectively. The activated sample presents stronger Au metal XRD reflections, a response consistent with an increase in Au particle size upon thermal treatment [63,64], *i.e.* from 7 nm to 12 nm (based on standard line broadening analysis [36]), in the as prepared and reduced samples, respectively. The relative intensity of the (104)/(110) hematite peaks in the activated Au/Fe_2O_3-IMP(10) (4/3) is close to that recorded for the support, indicating that there is no evidence of any significant reduction of α-Fe_2O_3 in the higher Au loaded sample. Moreover, the appearance of an Au XRD peak in the as prepared Au/Fe_2O_3-IMP(10) suggests that a reduction of the Au precursor can occur pre-TPR, *i.e.* a decomposition of the Au precursor into metallic Au during the drying step (at 383 K). In previous work [65], we have demonstrated that a supported gold ethanediamine precursor can undergo decomposition to metallic Au during drying (at 373 K) in the preparation of Au/TiO_2 and Au/SiO_2. Hodge *et al.* [66] have employed Mössbauer spectroscopy to demonstrate the presence of a mainly metallic Au (up to 86 % content) component after subjecting Au/Fe_2O_3, prepared by co-precipitation, to a drying step (up to 393 K). Milone and co-workers [32] reported a single reduction peak in the TPR of Au/Fe_2O_3–DP that is common to the Fe_2O_3 support and which they took as proof of Au reduction pre-TPR. There is also evidence in the literature suggesting the presence of unreduced gold species pre-TPR with H_2 consumption peaks reported at 468 K [67], 489 K [38] and 425 K [68] for Au/Fe_2O_3 prepared by DP, IMP and co-precipitation. Our

TPR and XRD measurements are consistent with the presence of Au^0 pre-activation where the presence of small Au particles promotes the transformation (during TPR) of Fe_2O_3 to Fe_3O_4.

7.3.1.2 TEM

TEM images of three representative samples, Au/Fe_2O_3-DP(1) (A), Au/Fe_2O_3-IMP(1) (B) and Au/Fe_2O_3-IMP(10) (C), are given in **Figure 7.4**. It is immediately evident that Au is present as discrete particles with a quasi-spherical morphology. The diffractogram patterns for a single gold particle in Au/Fe_2O_3-DPU(1) (AII) and Au/Fe_2O_3-IMP(1) (BII) are shown in images AIII and BIII, respectively. The *d*-spacings (0.20/023) are consistent with the (111) and (200) planes of metallic gold (JCPDS-ICDD 04-0784). EDX analysis confirmed the presence of Au^0 in all the areas mapped. The absence of a signal due to metallic Au in the XRD diffractograms of Au/Fe_2O_3-DP(1) and Au/Fe_2O_3-IMP(1) (see **Figure 7.3**) is then due to the presence of small Au crystallites ($\leq$ 4 nm) in both catalysts. Au/Fe_2O_3-IMP(1) exhibited larger particles than Au/Fe_2O_3-DP(1) with surface area weighted mean particle sizes of 3.5 and 2.6 nm, respectively. This response extends to Au supported on Al_2O_3 and TiO_2 (see **Table 7.1**) and agrees with the general consensus which emerges from the literature that catalysts prepared by DP consistently generate small Au particles (< 5 nm) [62,69]. Catalyst preparation by IMP, even at low Au loadings (1-2 % w/w), typically delivers low Au dispersions (10-35 nm) [25]. Okumura and co-workers [70], taking Au/Al_2O_3 (1 % w/w) prepared by DP and IMP, quoted mean Au particle sizes of 2.5 nm and 37 nm, respectively. Bailie and Hutchings [34] reported that Au/ZnO (5 % w/w) prepared by DP and IMP exhibited Au particles of 2-4 nm and > 150 nm, respectively. It should be noted that, regardless of the method of preparation (DP or IMP), larger Au particles are associated with the non-reducible carrier (Al_2O_3). This suggests a correlation between the reducibility of the support and Au dispersion, an observation that it is in line with the work of Min *et al.* [27] who demonstrated the formation of smaller Au clusters on reducible oxides due to the greater number of nucleation sites. The sequence of decreasing Au particle size obtained from TEM analysis for the Fe_2O_3 supported samples (Au/Fe_2O_3-IMP(10) (4.6 nm) > Au/Fe_2O_3-IMP(1) (3.5 nm) > Au/Fe_2O_3-DPU(1) (2.6 nm)) matches the increasing deviation in the relative intensity of the two principal hematite XRD peaks ((104)/(110)) when compared with the as prepared support, *i.e.* α-Fe_2O_3 (4/3) $\approx$ Au/Fe_2O_3-IMP(10) (4/3) > Au/Fe_2O_3-IMP(1) (1/1) > Au/Fe_2O_3-DPU(1) (3/4). This result suggests an increase in the partial reduction of

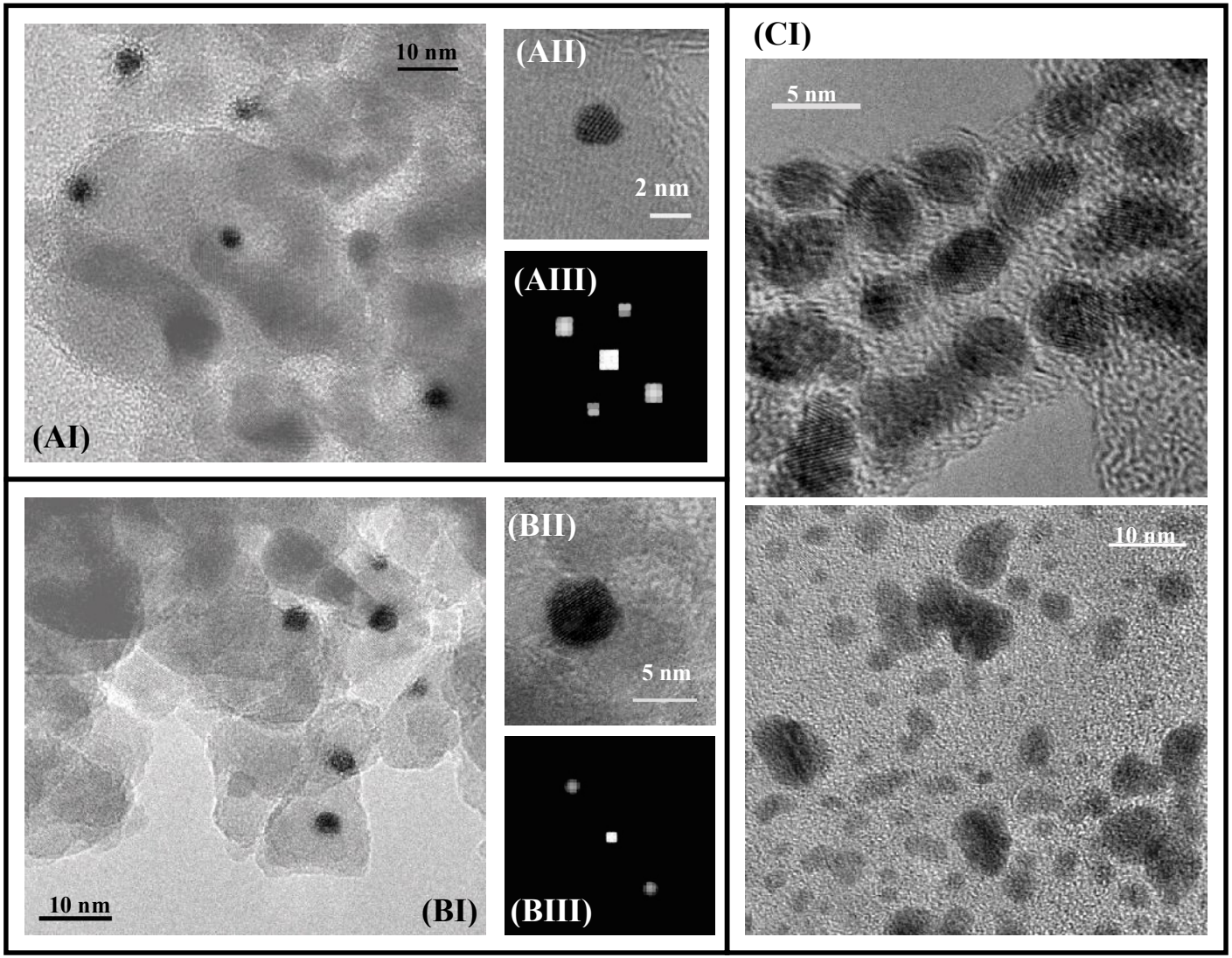

Figure 7.4: Representative TEM images of reduced/passivated (at 423 K) (A) Au/ Fe_2O_3-DP(1), (B) Au/Fe_2O_3-IMP(1) and (C) Au/Fe_2O_3-IMP(10): (I) medium/high magnification images; (II) images of a single Au particle (with associated diffractogram pattern (III)).

hematite with a decrease in Au particle size (< 5 nm), which can be explained on the basis of the extended Au-support interface associated with higher Au dispersion that must facilitate reduction of the support during TPR.

7.3.1.3 H_2 Chemisorption/TPD

Hydrogen uptake (see **Table 7.1**) on all the supported Au catalysts was low (≤ 63 μmol g_{Au}^{-1}). We could not find any other report in the literature that provides a measure of room temperature H_2 chemisorption on comparable supported Au systems. Our recorded H_2 uptake values are significantly lower than those obtained for conventional supported transition metal catalysts with a similar metal content, *e.g.* Pd/Al_2O_3 (1870 μmol g_{Pd}^{-1}) [71] and Pt/SiO_2 (1461 μmol g_{Pt}^{-1}) [14]. The dynamics of H_2 adsorption on Au are still far from being resolved but recent studies suggest that the chemisorption temperature [72] and Au coordination number [15] are key factors. Bus *et al.* [14] demonstrated an increase in the amount of chemisorbed H_2 (by up to a factor of 3) with an increase in the temperature (298 K → 373 K) used during their titration measurements. In terms of Au particle size dependence, there is some consensus that there is an increase in H_2 uptake on small clusters [11,70] (with higher number of defects) when compared with bulk Au [73]. Hydrogen temperature programmed desorption (TPD) is a practical approach that can serve to indicate differences in metal/support interactions and electronic properties of the supported metal [74]. The TPD profiles (up to 873 K), following H_2 chemisorption, generated for Au/Fe_2O_3-DP(1) (profile I), Au/Fe_2O_3-IMP(1) (profile II) and Au/Fe_2O_3-IMP(10) (profile III) are shown in **Figure 7.5**. Each profile exhibits a region of desorption over the *T* range 500-873 K with a maximum at *ca.* T = 700 K in the case of the lower Au loading: TPD from Au/Fe_2O_3-IMP(10) generated a broad ill-defined profile. In each case, the total specific (per m_{Au}^2) volume of H_2 desorbed was appreciably greater (by two orders of magnitude) than that taken up in the chemisorption step. This response is a strong indication that the hydrogen released from each sample is predominantly spillover species [75]. This assertion is in line with recent studies that have demonstrated (by FTIR) hydrogen spillover formation associated with Au supported on TiO_2 [76] and CeO_2-ZrO_2 [77]. In terms of energy requirements, the desorption of spillover hydrogen has been shown to require temperatures in excess of 503 K [78,79] while desorption directly from the metal occurs at lower temperatures (T < 473 K) [80]. Taking the three catalysts presented in **Figure 7.5**, the specific volume of H_2 desorbed decreased in the following

order: Au/Fe_2O_3-DP(1) (42 μmol m^2_{Au}) > Au/Fe_2O_3-IMP(1) (14 μmol m^2_{Au}) > Au/Fe_2O_3-IMP(10) (4 μmol m^2_{Au}). This sequence matches that of increasing Au particle size and there is evidence in the literature that the H_2 spillover phenomenon is structure sensitive [74,78]. The higher level of surface hydrogen associated with Au/Fe_2O_3-DP(1) can explain the greater degree of support reduction, *i.e.* transformation of hematite to magnetite, observed for this sample. Indeed, Boccuzzi *et al.* [81] have suggested that spillover hydrogen on Au/Fe_2O_3 can participate in a superficial reduction of the support.

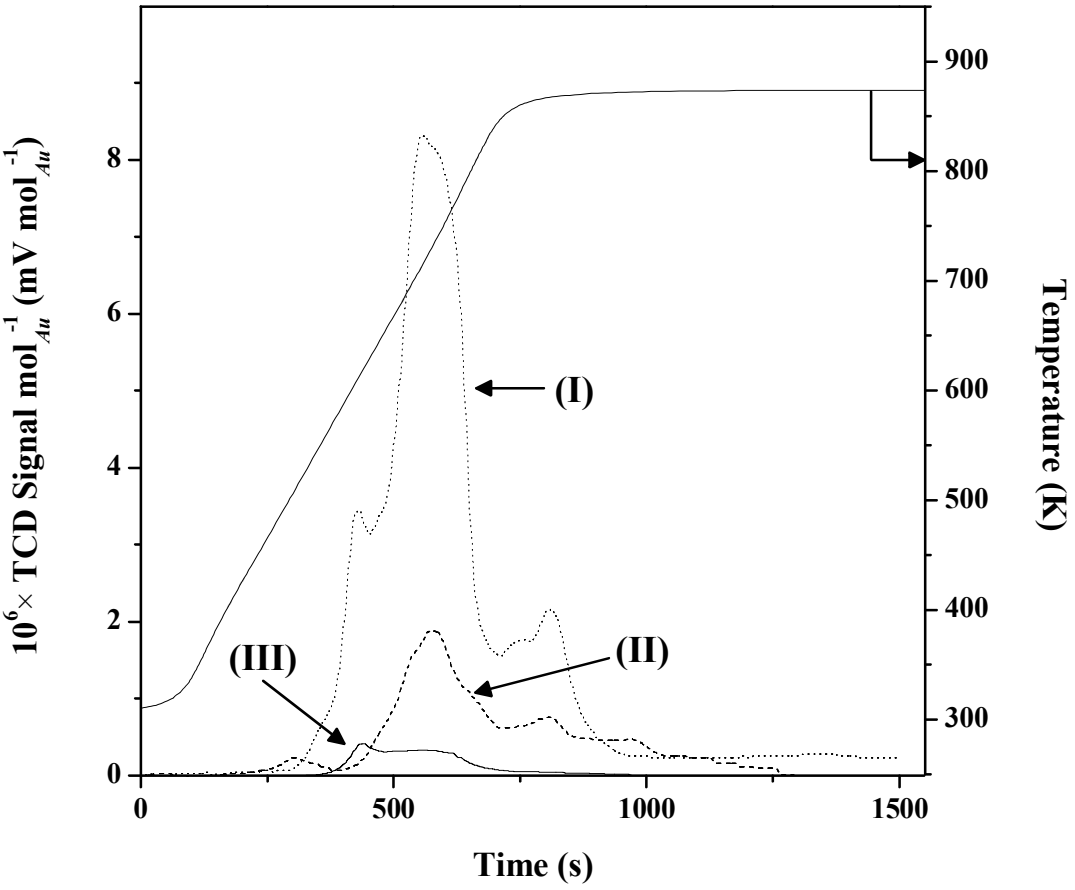

Figure 7.5: H_2 TPD (to 873 K) for: (I) Au/Fe_2O_3-DP(1) (dotted line); (II) Au/Fe_2O_3-IMP(1) (dashed line); (III) Au/Fe_2O_3-IMP(10) (solid line).

7.3.2 Catalyst activity/selectivity

The gas phase hydrogenation of *m*-DNB over all the Au catalysts delivered a time-invariant conversion (for up to 5 h on-stream, not shown) and 100 % selectivity in terms of -NO_2 group reduction, *i.e.* no evidence of hydrodenitrogenation and/or aromatic ring reduction. This combination of stability and selectivity represents a significant development in terms of the application of Au to promote -NO_2 group

hydrogenation. A temporal loss of hydrogenation activity has been observed for reaction over Au supported on Al_2O_3 [82,83], CeO_2 [30], Fe_2O_3 [84], SiO_2 [82], TiO_2 [85,86] and ZrO_2 [83] and linked to metal sintering [83,85] but has mainly been attributed to coke formation [30,82,85,86]. Moreover, catalyst deactivation in the gas phase hydrogenation of nitroarenes over Pd/Al_2O_3 [87-89], Pd/Hydrotalcite [90], Cu/SiO_2 [91] and Cu/Kieselghur [92] has been reported and ascribed to the deleterious effect of H_2O as by-product [90], metal leaching [89] and coking [87,88,91,92]. Catalytic activity in terms of nitro group reduction efficiency can be assessed by applying pseudo-first order kinetics [35,36,93]

$$\ln\left[\frac{1}{\left(1-(x_{-NO_2})_0\right)}\right] = k\left(\frac{n_{Au}}{F_{-NO_2}}\right) \qquad (7.7)$$

where F_{-NO_2} is the total inlet molar $-NO_2$, n_{Au} the number of moles of Au in the catalyst bed; $\left(n_{Au}/F_{-NO_2}\right)$ has the physical meaning of contact time. The extracted pseudo-first order rate constants (k) are shown in **Table 7.2**. A direct comparison of rate constants for catalysts bearing different Au particle sizes is only meaningful in terms of specific activities, *i.e.* per m^2 of exposed metal. The Au metal surface area was estimated from

$$S_{Au}\ (m^2_{Au}\ g^{-1}_{Au}) = \frac{6}{\rho_{Au} \times d_{TEM}} \qquad (7.8)$$

where ρ_{Au} = 18.88 g cm^{-3} and d_{TEM} is the surface area weighted mean Au particle size, as measured by TEM (see **Table 7.1**). The specific pseudo-first order rate constant (k') was then calculated from

$$k'(mol_{-NO_2}\ m^{-2}_{Au}\ h^{-1}) = \frac{k\ (mol_{-NO_2}\ g^{-1}_{Au}\ h^{-1})}{S_{Au}\ (m^2_{Au}\ g^{-1}_{Au})} \qquad (7.9)$$

The relationship between the specific activity and mean Au particle size (with the corresponding specific exposed Au surface area) for all the systems considered in this study is presented in **Figure 7.6**.

Table 7.2: Pseudo-first order rate constants for nitro-group reduction with product selectivities at a common fractional *m*-DNB conversion ($x_0 \approx 0.1$) over a series of oxide supported Au prepared by DP and IMP.

Catalyst	Rate Constant k (h^{-1})	Product(s) (Selectivity %)
Au/Al_2O_3-DP(1)	20	*m*-NAN (30) / *m*-PDM (70)
Au/CeO_2-DP(1)	24	*m*-PDM (100)
Au/Fe_2O_3-DP(1)	18	*m*-NAN (100)
Au/TiO_2-DP(1)	13	*m*-NAN (100)
Au/TiO_2-Ref	7	*m*-NAN (100)
$AuAl_2O_3$-IMP(1)	< 1	[a]
Au/Fe_2O_3-IMP(1)	9	*m*-NAN (100)
Au/TiO_2-IMP(1)	< 1	[a]
Au/Fe_2O_3-IMP(10)	1	*m*-NAN (100)

[a]not possible to achieve $x_0 = 0.1$ due to low catalyst activity

The tendency of increasing activity (k') with decreasing Au size (and higher S_{Au}) is consistent with a structure sensitive reaction where an enhanced intrinsic -NO_2 hydrogenation efficiency is associated with smaller Au particles (9→3 nm). The results indicate that the nature of the support does not impact significantly on hydrogenation rate, which is governed by the Au particle size. Indeed, a similar specific -NO_2 group reduction activity was obtained over systems with similar Au particle size on different carriers, as illustrated by points 5 (Au/TiO_2-Ref, d_{TEM} = 3.3 nm) and 7 (Au/Fe_2O_3-IMP(1), d_{TEM} = 3.5 nm). Taking a common support (Al_2O_3, see points 1 and 6 in **Figure 7.6**), the catalyst with the smaller mean Au diameter (Au/Al_2O_3-DP(1), d_{TEM} = 2.8 nm) delivered a specific rate that was three orders of magnitude greater than that obtained over the catalyst bearing larger Au particles (Au/Al_2O_3-IMP(1), d_{TEM} = 9.0 nm), representing the upper and lower rates recorded in this study. Our findings are in agreement with published studies suggesting that the presence of nanoscale Au particles

(≤ 10 nm) is essential for significant activity [15,94]. It should be noted that Au/CeO_2-DP(1) with the smallest mean Au size (d_{TEM} = 1.5 nm) deviates somewhat from the general trend, a response that we can attribute to quantum size effects. Differences in the catalytic behaviour of Au particles ≤ 2 nm have been associated with variations in the electronic character of the active site [95]. For Au particles in the 1-3 nm size range, it has been reported that the electronic properties vary considerably with a switch from metal to semiconductor characteristics [96-98]. Claus and co-workers [99], studying the gas phase hydrogenation of acrolein over Au/TiO_2, linked an order of magnitude decrease in activity (400 → 41 mmol g_{Au}^{-1} s^{-1}) with decreasing Au particle size (down to 1.4 nm) to a transition from metallic to non-metallic character for small Au particles.

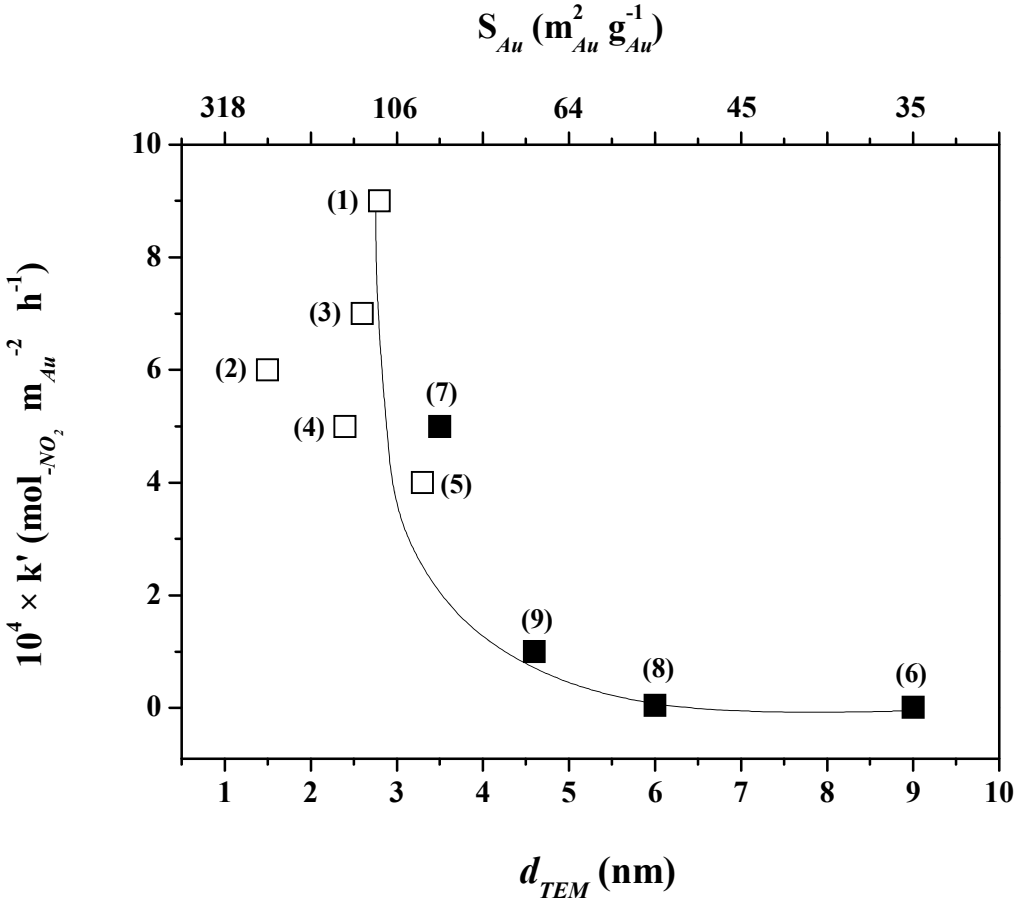

Figure 7.6: Relationship between specific rate constant (k') and Au particle size (and specific Au surface area) for (1) Au/Al_2O_3-DP(1), (2) Au/CeO_2-DP(1), (3) Au/Fe_2O_3-DP(1), (4) Au/TiO_2-DP(1), (5) Au/TiO_2-Ref, (6) AuAl_2O_3-IMP(1), (7) Au/Fe_2O_3-IMP(1), (8) Au/TiO_2-IMP(1) and (9) Au/Fe_2O_3-IMP(10): DP catalysts represented by open squares; IMP catalysts represented by solid squares.

A series of experiments were conducted to study the effect(s) of the nature of the support on reaction selectivity at the same degree of initial conversion. The results are presented in **Table 7.2** where clear differences in the selectivity response are in

evidence. Exclusive formation of *m*-NAN (partial -NO_2 group reduction) was recorded over Fe_2O_3 and TiO_2 supported Au catalysts. In complete contrast, *m*-PDM (full -NO_2 reduction) was the only product generated over Au/CeO_2-DP(1) while a mixture of both products was obtained over Au/Al_2O_3-DP(1). The sole formation of either *m*-NAN or *m*-PDM in continuous operation under mild reaction conditions represents an important advancement in the selective hydrogenation of *m*-DNB as the exclusive formation of either product has been identified as a critical processing issue. Zhao *et al.* [100] working in the gas phase (T = 323 K and P = 16 MPa) quoted up to 97 % selectivity to *m*-NAN over 5 % w/w Pt/C. In liquid phase operation, conditions of high temperatures and/or pressures have been deemed essential to achieve high selectivities to *m*-NAN or *m*-PDM. Khilnani and Chandalia [101] recorded up to 84 % selectivity to *m*-NAN over 5 % w/w Pd/C (T = 304 K and P = 34 atm) whereas Liu *et al.* [102] obtained up to 98 % selectivity to *m*-PDM over 20 % w/w Ni/SiO_2 (T = 373 K and P = 2.6 MPa). We can link the distinct selectivity response that we observe to the differences in acid-base Lewis character of the supports, which can influence the electronic nature of the Au particles and ultimately *m*-DNB adsorption/activation. The presence of Lewis basic sites in CeO_2 [103] is known to induce support→metal electron transfer [28] that can give rise to $Au^{\delta-}$ particles. It follows that the Lewis acid sites (cation vacancies) in Fe_2O_3 and TiO_2 [103] can promote the formation of $Au^{\delta+}$ particles as a result of a Au→support electron transfer. The formation of both $Au^{\delta+}$ and $Au^{\delta-}$ species is possible in the case of Au/Al_2O_3 due to the presence of both basic and acid Lewis sites on Al_2O_3 [46]. *m*-DNB adsorption on Au^{δ} (in Au/CeO_2) *via* the aromatic ring results in repulsion between the π-delocalized electrons and the partially (negatively) charged gold resulting in the formation of a resonance structure with two positive localized charges on the ring where both -NO_2 groups are activated, ultimately resulting in the formation of *m*-PDM *via* nucleophilic attack. Adsorption on $Au^{\delta+}$ sites (in Au/Fe_2O_3 and Au/TiO_2) results in the formation of a resonance form with a single delocalized positive charge on the ring where only one of the -NO_2 groups is activated, giving rise to the formation of *m*-NAN. The presence of negatively and electron-deficient Au particles in Au/Al_2O_3 can account for the formation of both *m*-NAN and *m*-PDM. Our results demonstrate that smaller supported Au particles exhibit a higher intrinsic hydrogenation where selectivity can be tuned or controlled as a function of the support acidity. Moreover, continuous operation under the mild reaction conditions employed represents a significant and novel advance in the selective hydrogenation of *m*-DNB.

7.4 Conclusions

We have demonstrated that 1 mol % Au on TiO_2, Fe_2O_3, CeO_2 and Al_2O_3 prepared by DP generated smaller (surface area weighted) mean Au particle sizes (≤ 3.3 nm) when compared with synthesis by IMP (≥ 3.5 nm). Moreover, regardless of the preparation method, larger Au particles were formed on the non-reducible (Al_2O_3) oxide. TPR of Au/TiO_2, Au/CeO_2 and Au/Al_2O_3 generated H_2 consumption peaks with T_{max} in the range 371-457 K that we attribute to the reduction of Au^{3+} to Au^0. XRD analysis has established the presence of metallic gold in Au/Fe_2O_3 pre-TPR and the activation of Au/Fe_2O_3 to 423 or 673 K resulted in a partial or full reduction of the support from hematite to magnetite. This effect was more pronounced for Au particle size < 5 nm and H_2 TPD analysis suggests the involvement of spillover hydrogen in the reduction step. The nature of the oxide support does not have a direct effect on the rate of nitro-group reduction, which is controlled by Au particle size. A decrease in Au size (from 9 to 3 nm) was accompanied by an increase in specific hydrogenation rate. A lower specific rate recorded for Au particles < 2 nm can be attributed to a quantum size effect. Hydrogenation activity was invariant with time on-stream for all the supported Au systems. Au/TiO_2 and Au/Fe_2O_3 promoted the exclusive hydrogenation of *m*-DNB to *m*-NAN (partial -NO_2 group reduction), Au/CeO_2 delivered *m*-PDM (full -NO_2 group reduction) as the sole product and Au/Al_2O_3 generated a mixture of *m*-NAN and *m*-PDM. We can account for this response on the basis of a modification to the electronic character of the Au particles induced by the Lewis acid-base properties of the support that impacts on the adsorption/activation of *m*-DNB.

7.5 References

[7.1] P. F. Vogt, J. J. Gerulis, Ullmann's Encyclopedia of Industrial Chemistry. "Aromatic Amines", Wiley-VCH Verlag GmbH & Co. KGaA, Weinheim, 2005.

[7.2] B. Kammermeier, Ullmann's Encyclopedia of Industrial Chemistry. "Reduction", Wiley-VCH Verlag GmbH & Co. KGaA, Weinheim, 2005.

[7.3] N. Yao, J. Chen, J. Zhang, J. Zhang, Catal. Commun., 9, 1510 (2008)

[7.4] X. D. Wang, M. H. Liang, J. L. Zhang, Y. Wang, Curr. Org. Chem., 11, 299 (2007)

[7.5] M. Takasaki, Y. Motoyama, K. Higashi, S.-H. Yoon, I. Mochida, H. Nagashima, Org. Lett., 10, 1601 (2008)

[7.6] R. A. Sheldon, H. van Bekkum, Fine Chemicals through Heterogeneous Catalysis."Aromatic Nitro Compounds", Wiley-VCH, Weinheim (Germany), 2001.

[7.7] S. Zhao, H. Liang, Y. Zhou, Catal. Commun., 8, 1305 (2007)

[7.8] M. M. Telkar, J. M. Nadgeri, C. V. Rode, R. V. Chaudhari, Appl. Catal. A: Gen., 295, 23 (2005)

[7.9] E. P. Maris, W. C. Ketchie, M. Murayama, R. J. Davis, J. Catal., 251, 281 (2007)

[7.10] A. Corma, P. Serna, H. García, J. Am. Chem. Soc. , 129, 6358 (2007)

[7.11] R. Zanella, C. Louis, S. Giorgio, R. Touroude, J. Catal., 223, 328 (2004)

[7.12] B. Hammer, J. K. Nørskov, Nature, 376, 238 (1995)

[7.13] A. Corma, M. Boronat, S. González, F. Illas, Chem. Commun., 2007, p. 3371.

[7.14] E. Bus, J. T. Miller, J. A. van Bokhoven, J. Phys. Chem. B, 109, 14581 (2005)

[7.15] P. Claus, Appl. Catal. A: Gen., 291, 222 (2005)

[7.16] A. S. K. Hashmi, Chem. Rev., 107, 3180 (2007)

[7.17] D. He, H. Shi, Y. Wu, B.-Q. Xu, Green Chem., 9, 849 (2007)

[7.18] A. Corma, P. Concepción, P. Serna, Angew. Chem. Int. Ed., 46, 7266 (2007)

[7.19] M. Boronat, P. Concepción, A. Corma, S. González, F. Illas, P. Serna, J. Am. Chem. Soc., 129, 16230 (2007)

[7.20] A. Corma, P. Serna, Science, 313, 332 (2006)

[7.21] L. Liu, B. Qiao, Y. Ma, J. Zhang, Y. Deng, Dalton Trans., 2008, p. 2542.

[7.22] Y. Chen, J. Qiu, X. Wang, J. Xiu, J. Catal., 242, 227 (2006)

[7.23] H. Sakurai, M. Haruta, Appl. Catal. A: Gen., 127, 93 (1995)

[7.24] J. A. Lopez-Sanchez, D. Lennon, Appl. Catal. A: Gen., 291, 230 (2005)

[7.25] G. C. Bond, C. Louis, D. T. Thompson, Catalysis by Gold, Imperial College Press, London, 2006.

[7.26] J. Radnik, C. Mohr, P. Claus, Phys. Chem. Chem. Phys., 5, 172 (2003)

[7.27] B. K. Min, W. T. Wallace, D. W. Goodman, Surf. Sci., 600, L7-L11 (2006)

[7.28] A. Y. Stakheev, L. M. Kustov, Appl. Catal. A: Gen., 188, 3 (1999)

[7.29] M. A. Centeno, I. Carrizosa, J. A. Odriozola, Appl. Catal. A: Gen., 246, 365 (2003)

[7.30] B. Campo, C. Petit, M. A. Volpe, J. Catal., 254, 71 (2008)

[7.31] C. Milone, R. Ingoglia, L. Schipilliti, C. Crisafulli, G. Neri, S. Galvagno, J. Catal., 236, 80 (2005)

[7.32] C. Milone, C. Crisafulli, R. Ingoglia, L. Schipilliti, S. Galvagno, Catal. Today, 122, 341 (2007)

[7.33] B. C. Campo, S. Ivanova, C. Gigola, C. Petit, M. A. Volpe, Catal. Today, 133-135, 661 (2008)

[7.34] J. E. Bailie, G. J. Hutchings, Chem. Commun., 1999, p. 2151.

[7.35] F. Cárdenas-Lizana, S. Gómez-Quero, M. A. Keane, Catal. Commun., 9, 475 (2008)

[7.36] F. Cárdenas-Lizana, S. Gómez-Quero, M. A. Keane, ChemSusChem, 1, 215 (2008)

[7.37] F. Cárdenas-Lizana, S. Gómez-Quero, N. Perret, M. A. Keane, Gold Bulletin, in press (2009)

[7.38] G. Neri, A. M. Visco, S. Galvagno, A. Donato, M. Panzalorto, Thermochim. Acta, 329, 39 (1999)

[7.39] F. E. Wagner, S. Galvagno, C. Milone, A. M. Visco, L. Stievano, S. Calogero, J. Chem. Soc., Faraday Trans., 93, 3403 (1997)

[7.40] D. Andreeva, V. Idakiev, T. Tabakova, A. Andreev, R. Giovanoli, Appl. Catal. A: Gen., 134, 275 (1996)

[7.41] G. Pina, C. Louis, M. A. Keane, Phys. Chem. Chem. Phys., 5, 1924 (2003)

[7.42] M. Haruta, S. Tsubota, T. Kobayashi, H. Kageyama, M. J. Genet, B. Delmon, J. Catal., 144, 175 (1993)

[7.43] S. Tsubota, A. Yamaguchi, M. Daté, M. Haruta, "Characterization of Reference Gold Catalysts" in *GOLD2003, 3rd International Conference on Gold Science, Technology and its Applications*, September-October, 2003, Vancouver, Canada,

[7.44] G. Tavoularis, M. A. Keane, J. Chem. Technol. Biotechnol., 74, 60 (1999)

[7.45] G. Yuan, M. A. Keane, Chem. Eng. Sci., 58, 257 (2003)

[7.46] M. Trueba, S. P. Trasatti, Eur. J. Inorg. Chem., 2005, p. 3393.

[7.47] L. Ilieva, J. W. Sobczak, M. Manzoli, B. L. Su, D. Andreeva, Appl. Catal. A: Gen., 291, 85 (2005)

[7.48] L. Ilieva, G. Pantaleo, I. Ivanov, A. M. Venezia, D. Andreeva, Appl. Catal. A: Gen., 65, 101 (2006)

[7.49] M. M. Mohamed, T. M. Salama, R. Ohnishi, M. Ichikawa, Langmuir, 17, 5678 (2001)

[7.50] E. Bus, R. Prins, J. A. van Bokhoven, Phys. Chem. Chem. Phys., 9, 3312 (2007)

[7.51] S. Y. Liu, S. M. Yang, Appl. Catal. A: Gen., 334, 92 (2008)

[7.52] L. Delannoy, N. Weiher, N. Tsapatsaris, A. M. Beesley, L. Nchari, S. L.M. Schroeder, C. Louis, Top. Catal., 44, 263 (2007)

[7.53] C. Baatz, U. Prüße, J. Catal., 249, 34 (2007)

[7.54] A. C. Gluhoi, X. Tang, P. Marginean, B. E. Nieuwenhuys, Top. Catal., 39, 101 (2006)

[7.55] S. D. Yim, I.-S. Nam, J. Catal., 221, 601 (2004)

[7.56] V. Idakiev, T. Tabakova, Z.-Y. Yuan, B.-L. Su, Appl. Catal. A: Gen., 270, 135 (2004)

[7.57] A. Pineau, N. Kanari, I. Gaballah, Thermochim. Acta, 447, 89 (2006)

[7.58] J. Li, Y. Zhan, X. Lin, Q. Zheng, Acta Phys. Chim. Sin., 24, 932 (2008)

[7.59] M. Khoudiakov, M. C. Gupta, S. Deevi, Appl. Catal. A: Gen., 291, 151 (2005)

[7.60] B. A. A. Silberova, G. Mul, M. Makkee, J. A. Moulijn, J. Catal., 243, 171 (2006)

[7.61] G. Y. Wang, H. L. Lian, W. X. Zhang, D. Z. Jiang, T. H. Wu, Kinet. Catal., 43, 433 (2002)

[7.62] G. C. Bond, D. T. Thompson, Catal. Rev.-Sci. Eng., 41, 319 (1999)

[7.63] S. H. Overbury, V. Schwartz, D. R. Mullins, W. Yan, S. Dai, J. Catal., 241, 56 (2006)

[7.64] J. Huang, W.-L. Dai, H. Li, K. Fan, J. Catal., 252, 69 (2007)

[7.65] G. Yuan, C. Louis, L. Delannoy, M. A. Keane, J. Catal. , 247, 256 (2007)

[7.66] N. A. Hodge, C. J. Kiely, R. Whyman, M. R. H. Siddiqui, G. J. Hutchings, Q. A. Pankhurst, F. E. Wagner, R. R. Rajaram, S. E. Golunski, Catal. Today, 72, 133 (2002)

[7.67] A. Venugopal, M. S. Scurrell, Appl. Catal. A: Gen., 258, 241 (2004)

[7.68] Z. Hao, L. An, H. Wang, T. Hu, React. Kinet. Catal. Lett., 70, 153 (2000)

[7.69] M. Haruta, Catal. Today, 36, 153 (1997)

[7.70] M. Okumura, T. Akita, M. Haruta, Catal. Today, 74, 265 (2002)

[7.71] S. Gómez-Quero, F. Cárdenas-Lizana, M. A. Keane, Ind. Eng. Chem. Res., 47, 6841 (2008)

[7.72] H. Berndt, I. Pitsch, S. Evert, K. Struve, M.-M. Pohl, J. Radnik, A. Martin, Appl. Catal. A: Gen., 244, 169 (2003)

[7.73] A. G. Sault, R. J. Madix, C. T. Campbell, Surf. Sci., 169, 347 (1986)

[7.74] C. Amorim, M. A. Keane, J. Colloid Interface Sci., 322, 196 (2008)

[7.75] W. C. Conner, J. L. Falconer, Chem. Rev., 95, 759 (1995)

[7.76] D. A. Panayotov, J. T. Yates, J. Phys. Chem. C, 111, 2959 (2007)

[7.77] S. E. Collins, J. M. Cíes, E. del Río, M. López-Haro, S. Trasobares, J. J. Calvino, J. M. Pintado, S. Bernal, J. Phys. Chem. C, 111, 14371 (2007)

[7.78] M. Snåre, I. Kubičková, P. Mäki-Arvela, K. Eränen, D. Y. Murzin, Ind. Eng. Chem. Res., 45, 5708 (2006)

[7.79] F. Benseradj, F. Sadi, M. Chater, Appl. Catal. A: Gen., 228, 135 (2002)

[7.80] S. Velu, S. K. Gangwal, Solid State Ionics, 177, 803 (2006)

[7.81] F. Boccuzzi, A. Chiorino, M. Manzoli, D. Andreeva, T. Tabakova, J. Catal., 188, 176 (1999)

[7.82] B. Pawelec, A. M. Venezia, V. La Parola, S. Thomas, J. L. G. Fierro, Appl. Catal. A: Gen., 283, 165 (2005)

[7.83] X. Zhang, H. Shi, B.-Q. Xu, Catal. Today, 122, 330 (2007)

[7.84] C. Milone, M. L. Tropeano, G. Gulino, G. Neri, R. Ingoglia, S. Galvagno, Chem. Commun., 2002, p. 868.

[7.85] T. V. Choudhary, C. Sivadinarayana, A. K. Datye, D. Kumar, D. W. Goodman, Catal. Lett., 86, 1 (2003)

[7.86] Y. Azizi, C. Petit, V. Pitchon, J. Catal., 256, 338 (2008)

[7.87] E. Klemm, B. Amon, H. Redlingshöfer, E. Dieterich, G. Emig, Chem. Eng. Sci., 56, 1347 (2001)

[7.88] V. Vishwanathan, V. Jayasri, P. M. Basha, N. Mahata, L. M. Sikhwivhilu, N. J. Coville, Catal. Commun., 9, 453 (2008)

[7.89] K. K. Yeong, A. Gavriilidis, R. Zapf, V. Hessel, Catal. Today, 81, 641 (2003)

[7.90] P. Sangeetha, P. Seetharamulu, K. Shanthi, S. Narayanan, K.S. Rama Raob, J. Mol. Catal. A: Chem., 273, 244 (2007)

[7.91] S. Diao, W. Qian, G. Luo, F. Wei, Y. Wang, Appl. Catal. A: Gen., 286, 30 (2005)

[7.92] L. Petrov, K. Kumbilieva, N. Kirkov, Appl. Catal., 59, 31 (1990)

[7.93] F. Cárdenas-Lizana, S. Gómez-Quero, M. A. Keane, Catal. Lett., 127, 25 (2009)

[7.94] A. S. K. Hashmi, G. J. Hutchings, Angew. Chem. Int. Ed., 45, 7896 (2006)

[7.95] C. Mohr, H. Hofmeister, P. Claus, J. Catal., 213, 86 (2003)

[7.96] L. Stievano, S. Santucci, L. Lozzi, S. Calogero, F. E. Wagner, J. Non-Cryst. Solids 232-234, 644 (1998)

[7.97] Q. Guo, K. Luo, K. A. Davis, D. W. Goodman, Surf. Interface Anal., 32, 161 (2001)

[7.98] H.-G. Boyen, Th. Herzog, G. Kästle, F. Weigl, P. Ziemann, Phys. Rev. B, 65, 075412 (2002)

[7.99] P. Claus, A. Brückner, C. Mohr, H. Hofmeister, J. Am. Chem. Soc., 122, 11430 (2000)

[7.100] F. Zhao, S.-I. Fujita, J. Suna, Y. Ikushima, M. Arai, Catal. Today, 98, 523 (2004)

[7.101] V. L. Khilnani, S. B. Chandalia, Org. Proc. Res. Dev., 5, 263 (2001)

[7.102] Y. X. Liu, J. X. Chen, J. Y. Zhang, Chin. J. Chem. Eng., 15, 63 (2007)

[7.103] G. Busca, Phys. Chem. Chem. Phys., 1, 723 (1999)

Chapter 8

Gold Particle Size Effects in the Gas Phase Hydrogenation of Dinitrobenzene over Au/TiO_2

The results obtained in the previous Chapter suggest a modification of the Au site electronic character by the acid-base Lewis nature of the support, which impacts on the selectivity response in the gas phase hydrogenation of *m*-dinitrobenzene. In this Chapter, the influence of particle size is considered in the absence of other factors that can mask Au dispersion effects. A series of Au/TiO_2 catalysts with different Au content and activated under controlled thermal treatment have been examined in the hydrogenation of *m*-dinitrobenzene.

8.1 Introduction

Supported metal nano-particles have found widespread use as catalysts in a range of industrial applications [1]. The term "structure sensitive" was first introduced in 1969 by Boudart [2], who proposed a dependence of the catalytic response on surface structure associated with variations in the exposed crystal plane(s) or changes in the metal crystallite size, typically over the range 1-10 nm. This is now a well established effect in the hydrogenation of aromatic compounds over conventional transition metals (*e.g.* Pt [3] or Pd [4]). The development of gold catalysts is an emerging area of research that is attracting increasing attention [5] but has of yet limited applications in hydrogenation. This can be related to a lesser capacity of Au for hydrogen chemisorption due to the filled *d*-band and high associated ionization potential [6]. Nevertheless, when finely divided as small particles ($\leq$ 10 nm), gold is catalytically active in hydrogen mediated reactions with some evidence of unique selectivities [7,8]. The reason for the selectivity response is still not well understood and there is no consensus regarding the Au size required to achieve an optimal specific hydrogenation rate. The results reported to date suggest that Au particles smaller than 5 nm (and especially those below 3 nm) are intrinsically more effective [9-11]. This effect has been linked to enhanced H_2 dissociation on corner and edge positions of smaller Au particles [11,12]. Bus *et al.* [13], studying the liquid-phase hydrogenation of cinnamaldehyde to cinnamyl alcohol over Au/Al_2O_3, attributed the highest activity recorded to a more effective C=O activation. Mohr and co-workers [14] have identified

the edge sites of gold nanoparticles (in Au/TiO_2 and Au/ZrO_2) as the preferred sites for C=O activation in the hydrogenation of acrolein to allyl alcohol. It should, however, be noted that the opposite response has also been observed for hydrogenation reactions and attributed to electronic effects, *i.e.* lower catalytic activity for particles < 2 nm [9,15]. There is some limited evidence that hydrogenation selectivity (in the treatment of but-2-enal) can also be influenced by variations in Au dispersion [16] but such an effect has yet to be irrefutably established. The ultimate Au particle size is determined by the Au precursor [17,18], preparation method [19,20], activation conditions [21-23] and the nature of the support [24,25], which in turn can influence hydrogenation performance to varying degrees. It is difficult to establish an explicit link between catalytic performance and Au particle size from the available literature.

Aromatic amino-compounds are extensively used as intermediates in the production of a diversity of fine chemicals [1]. The traditional manufacture route, from the corresponding nitro-derivate using stoichiometric amounts of iron as reducing agent in acid media (Béchamp process), is no longer viewed as sustainable due to the production of large amounts of toxic iron oxides [26]. An alternative batch liquid phase operation over supported Pt [27] or Pd [28] also has an associated negative environmental impact due to the formation of secondary harmful products, *i.e.* azo- [29] and/or azoxy-derivates [30]. Recently, there have been studies [31-34] that have shown the potential of Au for chemoselective $-NO_2$ group reduction in batch liquid phase operation. We have demonstrated exclusivity in the gas phase continuous hydrogenation of a range of nitroarenes over supported gold-based catalysts [9,20,24,35,36]. In this report, we extend that work and provide for the first time a direct correlation between catalytic response and Au particle size in the hydrogenation of *m*-dinitrobenzene (*m*-DNB) over Au/TiO_2. Moreover, we demonstrate that product composition can be altered (or tuned) by varying Au particle size.

8.2 Experimental

8.2.1 Materials and Catalyst Preparation

The TiO_2 (Degussa, P25) support was used as received. Two (0.1 and 1 mol %) supported Au catalysts were prepared by standard impregnation of the TiO_2 support (5 g) with $HAuCl_4$ (Aldrich, 25×10^{-3} g cm^{-3}, pH = 2) solutions. The slurry was heated (2 K min^{-1}) to 353 K and maintained under constant agitation (600 rpm) in a He purge. The

solid residue was dried in a flow of He at 383 K for 3 h, sieved into a batch of 75 μm average diameter and stored under He in the dark at 277 K. Prior to use in catalysis, the samples were activated in 60 cm^3 min^{-1} H_2 at 2 K min^{-1} to a final temperature in the range 603-873 K, which was maintained for at least 1 h. For comparison purposes, a series of rutile supported Au catalysts were prepared using two approaches: (i) activation of 0.1 mol % and 1 mol % Au/TiO_2 in H_2 to 1273 K; (ii) formation of rutile (confirmed by XRD analysis) by thermal treatment of TiO_2 to 1273 K and subsequent impregnation with $HAuCl_4$ (0.1 mol % Au), post-treatment as above. After activation, the samples were passivated in 1% v/v O_2/He at room temperature for off-line analysis.

8.2.2 Characterization Analyses

BET area and H_2 chemisorption were recorded using the commercial CHEMBET 3000 (Quantachrome Instrument) unit. The samples were loaded into a U-shaped Quartz cell (100 mm × 3.76 mm i.d.) and heated in 17 cm^3 min^{-1} (Brooks mass flow controlled) 5% v/v H_2/N_2 to the final reduction temperature (603 K $\leq T \leq$ 1273 K) at 2 K min^{-1}. The effluent gas passed through a liquid N_2 trap and changes in H_2 consumption were monitored by TCD with data acquisition/manipulation using the TPR Win™ software. The reduced samples were swept with 65 cm^3 min^{-1} N_2 for 1.5 h, cooled to room temperature and subjected to H_2 chemisorption using a pulse (10-50 μl) titration procedure. Hydrogen pulse introduction was repeated until the signal area was constant, indicating surface saturation. BET areas were recorded with a 30% v/v N_2/He flow; pure N_2 (99.9%) served as the internal standard. At least two cycles of N_2 adsorption-desorption in the flow mode were used to determine total surface area using the standard single point method. BET surface area and H_2 uptake values were reproducible to within ± 5 %; the values quoted in this paper are the mean.

Powder x-ray diffractograms were recorded on a Bruker/Siemens D500 incident x-ray diffractometer using Cu Kα radiation. The samples were scanned at a rate of 0.02º $step^{-1}$ over the range 20º ≤ 2θ ≤ 90º (scan time = 5 s $step^{-1}$). Diffractograms were identified using the JCPDS-ICDD reference standards, *i.e.* anatase (21-1272), rutile (21-1276) and Au (04-0784). The rutile:anatase ratios were determined by XRD according to the method described by Fu *et al.* [37], *i.e.*

$$\% \text{ Rutile} = \frac{1}{[(A/R) \times 0.884 + 1]} \times 100 \quad \textbf{(8.1)}$$

where A and R represent the peak areas associated with the main reflections for anatase (2θ = 25.3°) and rutile (2θ = 27.4°), respectively. Diffuse reflectance UV-vis (DRS UV-vis) measurements were conducted using a Perkin Elmer Lambda 35 UV-vis spectrometer with $BaSO_4$ powder as reference; absorption profiles were calculated from the reflectance data using the Kubelka-Munk function. Transmission electron microscopy analysis employed a JEOL JEM 2011 HRTEM unit with a UTW energy dispersive X-ray detector (EDX) detector (Oxford Instruments) operated at an accelerating voltage of 200 kV and using Gatan DigitalMicrograph 3.4 for data acquisition/manipulation. Samples for analysis were prepared by dispersion in acetone and deposited on a holey carbon/Cu grid (300 Mesh). Up to 400 individual metal particles were counted for each catalyst and the surface area-weighted mean Au diameter (d_p) was calculated from

$$d_p = \frac{\sum_i n_i d_i^3}{\sum_i n_i d_i^2} \quad \textbf{(8.2)}$$

where n_i is the number of particles of diameter d_i. The size limit for the detection of gold particles on TiO_2 is *ca.* 1 nm.

8.2.3 Catalytic Procedure

Reactions were carried out under atmospheric pressure, *in situ* immediately after activation, in a fixed bed vertical continuous flow glass reactor (l = 600 mm, i.d. = 15 mm) at T = 473 K. The catalytic reactor, and operating conditions to ensure negligible heat/mass transport limitations, have been fully described elsewhere [38] but some features, pertinent to this study, are given below. A preheating zone (layer of borosilicate glass beads) ensured that the organic reactant was vaporized and reached the reaction temperature before contacting the catalyst. Isothermal conditions (± 1 K) were maintained by thoroughly mixing the catalyst with ground glass (75 μm). The temperature was continuously monitored by a thermocouple inserted in a thermowell within the catalyst bed. A butanolic solution of *m*-DNB reactant was delivered, in a co-

current flow of H_2, *via* a glass/teflon air-tight syringe and a teflon line, using a microprocessor controlled infusion pump (Model 100 kd Scientific) at a fixed calibrated flow rate. The inlet -NO_2 molar flow ($F_{\text{-}NO_2}$) was in the range 0.08-0.20 $\text{mmol}_{\text{-}NO_2}\ \text{h}^{-1}$ where the molar metal to inlet molar -NO_2 feed rate ratio spanned a 6×10^{-4} – 629×10^{-4} h interval. Hydrogen content in the feed was at least 100 times in excess of the stoichiometric requirement, the flow rate of which was monitored using a Humonics (Model 520) digital flowmeter; $GHSV = 2 \times 10^4\ \text{h}^{-1}$. In a series of blank tests, passage of *m*-DNB reactant in a stream of H_2 through the empty reactor or over the support alone, *i.e.* in the absence of Au, did not result in any detectable conversion. The reactor effluent was frozen in a liquid nitrogen trap for subsequent analysis, which was made using a Perkin-Elmer Auto System XL gas chromatograph equipped with a programmed split/splitless injector and a flame ionization detector, employing a DB-1 50 m × 0.20 mm i.d., 0.33 μm film thickness capillary column (J&W Scientific), as described elsewhere [39]. *m*-DNB (Aldrich, ≥ 98%) and 1-butanol (Riedel-de Haën) were used as supplied without further purification. Hydrogenation activity is expressed in terms of the degree of nitro-group reduction ($x_{\text{-}NO_2}$)

$$x_{\text{-}NO_2} = \frac{[\text{-NH}_2]_{out}}{[\text{-NO}_2]_{in}} = \frac{2\times[m\text{-PDM}]_{out} + [m\text{-NAN}]_{out}}{2\times[m\text{-DNB}]_{in}} \qquad \textbf{(8.3)}$$

where [*m*-NAN] and [*m*-PDM] are, respectively, the concentrations of *m*-nitroaniline and *m*-phenylenediamine and the subscripts *in* and *out* refer to the inlet and outlet streams. Catalyst activity is also quantified in terms of the fractional conversion of *m*-DNB ($x_{m\text{-}DNB}$)

$$x_{m\text{-}DNB} = \frac{[m\text{-DNB}]_{in} - [m\text{-DNB}]_{out}}{[m\text{-DNB}]_{in}} \qquad \textbf{(8.4)}$$

while selectivity in terms of (say) *m*-NAN ($S_{m\text{-}NAN}$) is given by

$$S_{m\text{-}NAN} = \frac{[m\text{-NAN}]_{out}}{[m\text{-DNB}]_{in} - [m\text{-DNB}]_{out}} \qquad \textbf{(8.5)}$$

Table 8.1: Gold loading and activation temperature with associated H_2 chemisorption values, DRS UV-vis characteristics, TEM derived mean Au particle size (d_p), specific surface area (S_{Au}) (and size range), % fraction of rutile, BET surface area and pseudo-first order rate constants for nitro-group reduction in the hydrogenation of *m*-DNB over Au/anatase.

Catalyst	Au content (mol %)	Activation Temperature (K)	$H_{2\ uptake}$ (μmol g_{Au}^{-1})	DRS UV-vis A_{max} (nm)	d_p (nm)	Au size range[a] (nm)	S_{Au}[a] ($m^2\ g_{Au}^{-1}$)	% rutile[b]	BET ($m^2\ g^{-1}$)	10 × k (h^{-1})
Au/TiO_2-1	0.1	603	162	550	3.4	1-8	93	16	49	920
Au/TiO_2-2	0.1	873	109	560	4.7	1-10	68	67	28	300
Au/TiO_2-3	1	603	15	568	6.1	1-10	52	20	47	60
Au/TiO_2-4	1	873	4	600	9.4	1-15	34	94	20	2

[a] $S_{Au} = 6/(\rho_{Au} \times d_p)$ where $\rho_{Au} = 18.88\ g\ cm^{-3}$
[b] based on XRD analysis (see **Equation 8.1**)

8.3 Results and Discussion

The sample notation for the Au/TiO_2 catalysts, Au loading and activation conditions, H_2 chemisorption, DRS UV-vis results, rutile content and BET surface area are given in **Table 8.1**, along with the mean Au particle sizes (and range of values) obtained from TEM analysis. Titanium dioxide crystallizes primarily in three different forms, *i.e.* anatase, rutile and brookite. Anatase and rutile have found widespread use in catalytic applications [40]. In both structures, the basic building block consists of a titanium atom surrounded by six oxygens in an octahedral configuration, where structural difference arises from the packing of these octahedra [40]. Anatase is the thermodynamically unstable crystal form [41] and anatase→rutile phase conversion is possible at $T > 973$ K [42,43]. The requisite temperature for this transformation can be affected by the incorporation of a range of additives (*e.g.* Co, Ni, Cu and Zn) [44,45] that catalyze or inhibit the transformation. Heat treatment in the presence of H_2 induces (i) condensation of surface hydroxyl groups [42] and (ii) removal of the bridging oxygen shared by the Ti atoms [43] with subsequent water desorption and the formation of surface defects that quickly expand to the bulk [46,47] leading to rutile formation.

8.3.1 Catalyst Characterization

8.3.1.1 H_2 Chemisorption/DRS UV-Vis

We have reported previously [24] the TPR profile for Au/TiO_2 prepared by impregnation and established that the precursor was reduced to zero valent Au at 603 K, as has also been demonstrated elsewhere [48]. The aim of this study is to address the possible effects of Au size in determining activity and selectivity in the hydrogenation of *m*-DNB. In order to modify Au dispersion, two approaches have been taken, *i.e.* variation of (a) Au loading (0.1 and 1 mol %) and (b) activation temperatures (603 - 1273 K). Both factors have been shown [22,49] to impact on Au particle size. Hydrogen uptake (at ambient temperature) on all the Au/TiO_2 samples ($\leq$ 162 $\mu mol\, g_{Au}^{-1}$) was significantly lower than that quoted in the literature for conventional supported transition metal catalysts with a similar metal content, *e.g.* Pd/Al_2O_3 (1870 $\mu mol\, g_{Pd}^{-1}$) [50] and Pt/SiO_2 (1461 $\mu mol\, g_{Pt}^{-1}$) [12]. This is consistent with a low capacity of Au for H_2 chemisorption due to the high energy barrier for H_2 dissociation on group IB metals [51]. Nevertheless, the specific uptake was measurably lower on samples with a higher Au content (*e.g.* Au/TiO_2-3 *vs.* Au/TiO_2-1).

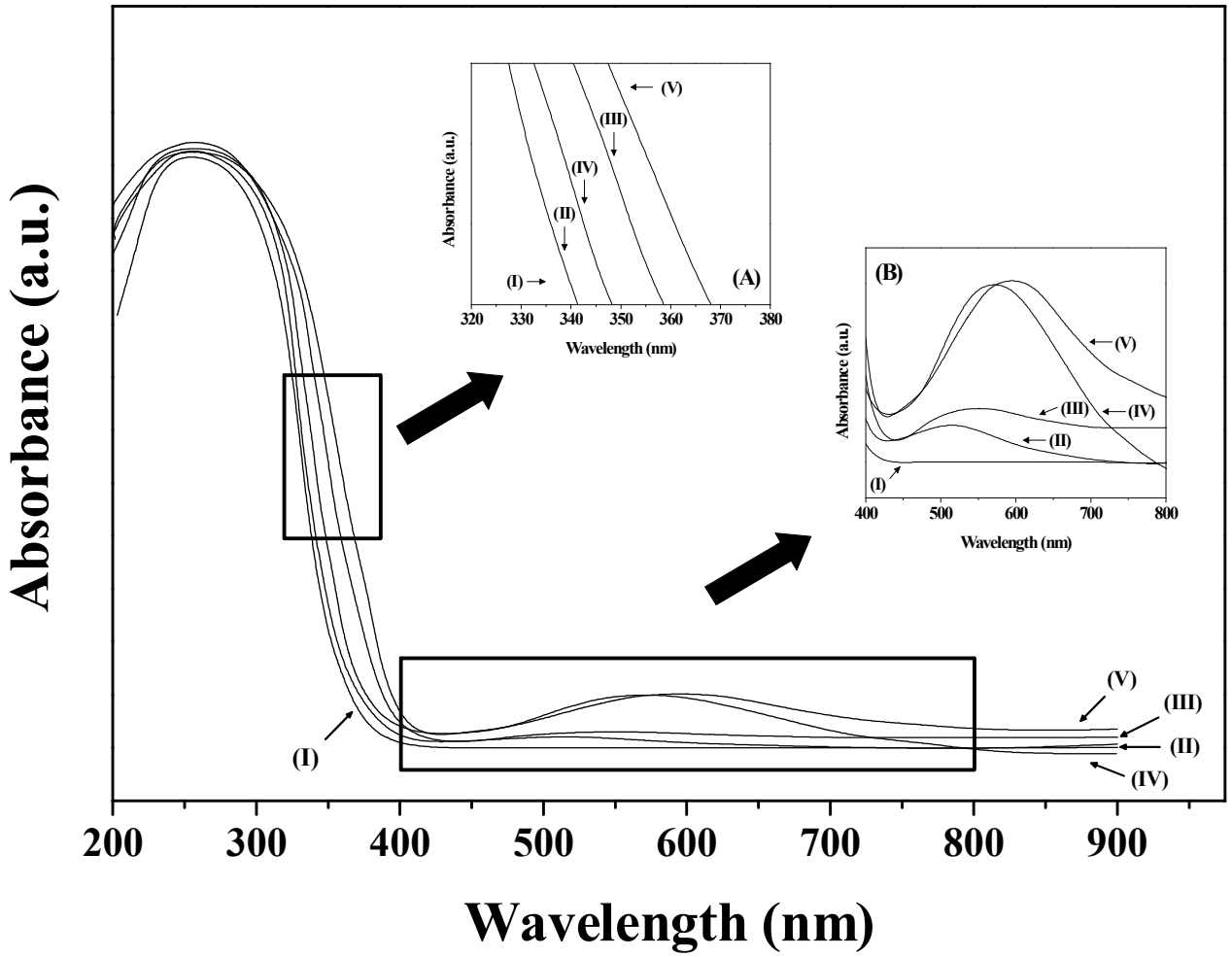

Figure 8.1: DRS UV-vis spectra of (I) starting TiO_2 support and passivated/reduced (II) Au/TiO_2-1, (III) Au/TiO_2-2, (IV) Au/TiO_2-3 and (V) Au/TiO_2-4. Inset: DRS spectra magnifications in the (A) UV and (B) visible regions.

It has been reported [21,52] that an increase in Au content facilitates agglomeration and the formation of larger Au particles. Moreover, a consensus has emerged from the literature [12] that H_2 uptake is greater on smaller Au particles with a greater preponderance of defects. Our observed variations in H_2 uptake suggest differences in Au dispersion with varying Au content and activation temperature.

The DRS UV-vis spectra recorded for the support and the Au/TiO_2 catalysts are presented in **Figure 8.1**, where selected areas in the UV (320-380 nm) and visible (400-800 nm) regions have been magnified and are shown as insets (A) and (B), respectively. In the UV range, an absorption band that is characteristic of Degussa P25 TiO_2 [53] is observed for all the samples and can be associated with charge transfer from the valence band of the oxide anions to the conduction band of Ti^{4+} cations [54]. Taking the spectrum for the starting TiO_2 support (profile I), the Au/TiO_2 samples (profiles II-V) exhibit a displacement of the UV band to higher wavelengths. This response has been associated elsewhere [55] with the formation of rutile. In the visible region (B), the spectrum for the starting TiO_2 support is featureless, as observed previously [24,56]. In contrast, the profiles for the activated catalysts exhibit a band with a peak maximum in the range 550-600 nm (see **Table 8.1**) that is consistent with the presence of Au nano-particles supported on titania [57]. There is a distinct shift in peak maximum to longer wavelengths with increasing Au loading and/or activation temperature. Similar shifts have been reported in the literature and attributed to a decrease in Au dispersion [58,59]. The DRS UV-vis results recorded are consistent with a supported Au^0 phase post-activation, where the differences in characteristic wavelengths suggest variations in Au particle size and support composition (*i.e.* anatase:rutile ratio).

8.3.1.2 TEM/Particle Size Distribution

Representative TEM images (A) and Au particle size distributions (B) associated with Au/TiO_2-1 (I), Au/TiO_2-2 (II), Au/TiO_2-3 (III)) and Au/TiO_2-4 (IV) are given in **Figure 8.2**. The TEM images reveal a pseudo-spherical morphology for the Au particles in all the samples, suggesting a relatively weak interaction and a small area of contact at the interface between the metal crystallites and the TiO_2 support. This is in agreement with published literature [60] where Au/TiO_2 prepared by impregnation is characterised by a metal-support contact angle >90°.

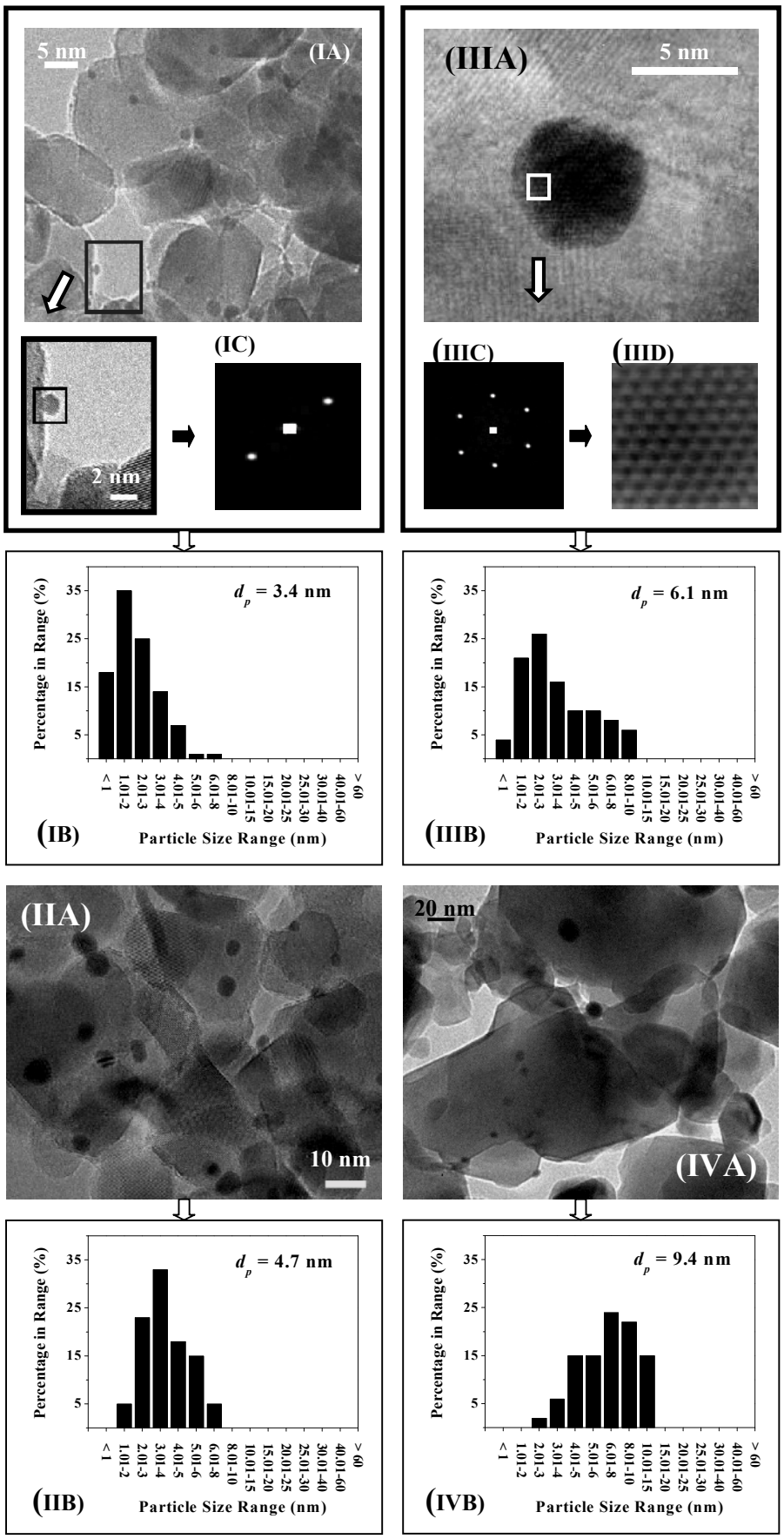

Figure 8.2: Representative (A) TEM images, (B) Au particle size distributions and (C) diffractogram patterns associated with selected areas of passivated/reduced (I) Au/TiO_2-1, (II) Au/TiO_2-2, (III) Au/TiO_2-3 and (IV) Au/TiO_2-4. *Note*: Inverse fast Fourier transform (IFFT) for framed section in IIIA (Au/TiO_2-3) is shown in image (IIID).

The *d*-spacings (0.23/0.20) between the planes in the atomic lattice obtained from the diffractogram patterns (C) of individual Au particles associated with Au/TiO_2-1 (I) and Au/TiO_2-3 (III) are consistent with the (111) and (200) planes of metallic gold (JCPDS-ICDD 04-0784) and further corroborate the reduction of the precursor to zero valent Au post-activation at 603 K. Furthermore, EDX analysis confirmed the presence of metallic Au in all the areas mapped. In order to analyze the distribution of Au atoms in more detail, an IFFT (inverse fast Fourier transform) was applied. The transformed image (IIID) corresponding to the selected region in IIIA shows the arrangement of Au atoms in the crystal structure.

An increase in Au particle size with increasing metal content and/or activation temperature is demonstrated by the TEM-generated size histograms given in **Figure 8.2**. The catalysts which bear larger mean particle sizes (Au/TiO_2-3 and Au/TiO_2-4 shown in IIIB and IVB, respectively) present a wider size distribution when compared with Au/TiO_2-1 and Au/TiO_2-2. The surface area weighted mean Au sizes fell within 3.4 nm (Au/TiO_2-1) to 9.4 nm (Au/TiO_2-4). A gold particle size $\leq$ 5 nm has been suggested as critical for catalytic activity in hydrogen mediated processes [7,11]; % of particles $\leq$ 5 nm decreases in the sequence Au/TiO_2-1 (95%) > Au/TiO_2-2 and Au/TiO_2-3 (75%) > Au/TiO_2-4 (25%). It should, however, be noted that the majority (85%) of the Au particles in Au/TiO_2-4, with higher Au content and activated at an elevated temperature (873 K), exhibited particle diameters $\leq$ 10 nm. It should be noted that the samples exhibited a colour change from the starting white powder to purple and ultimately to black during the thermal treatment. Colour changes have been associated with a partial reduction of TiO_2 [61] and variations in coloration correlate with the number of bulk defects. One consequence of this change in appearance is an increase in rutile content [62], which is suggested by our DRS UV-vis measurements.

8.3.1.3 XRD/BET

Power XRD patterns of the TiO_2 support post-thermal treatment up to 603 K (I) and 873 K (II) along with those for Au/TiO_2-1 (IV), Au/TiO_2-2 (V), Au/TiO_2-3 (VII) and Au/TiO_2-4 (VIII) are presented in **Figure 8.3**. In order to confirm the bulk composition for each sample, the XRD patterns were compared with the JCPDS-ICDD standards for anatase (21-1272), rutile (21-1276) and Au (04-0784).

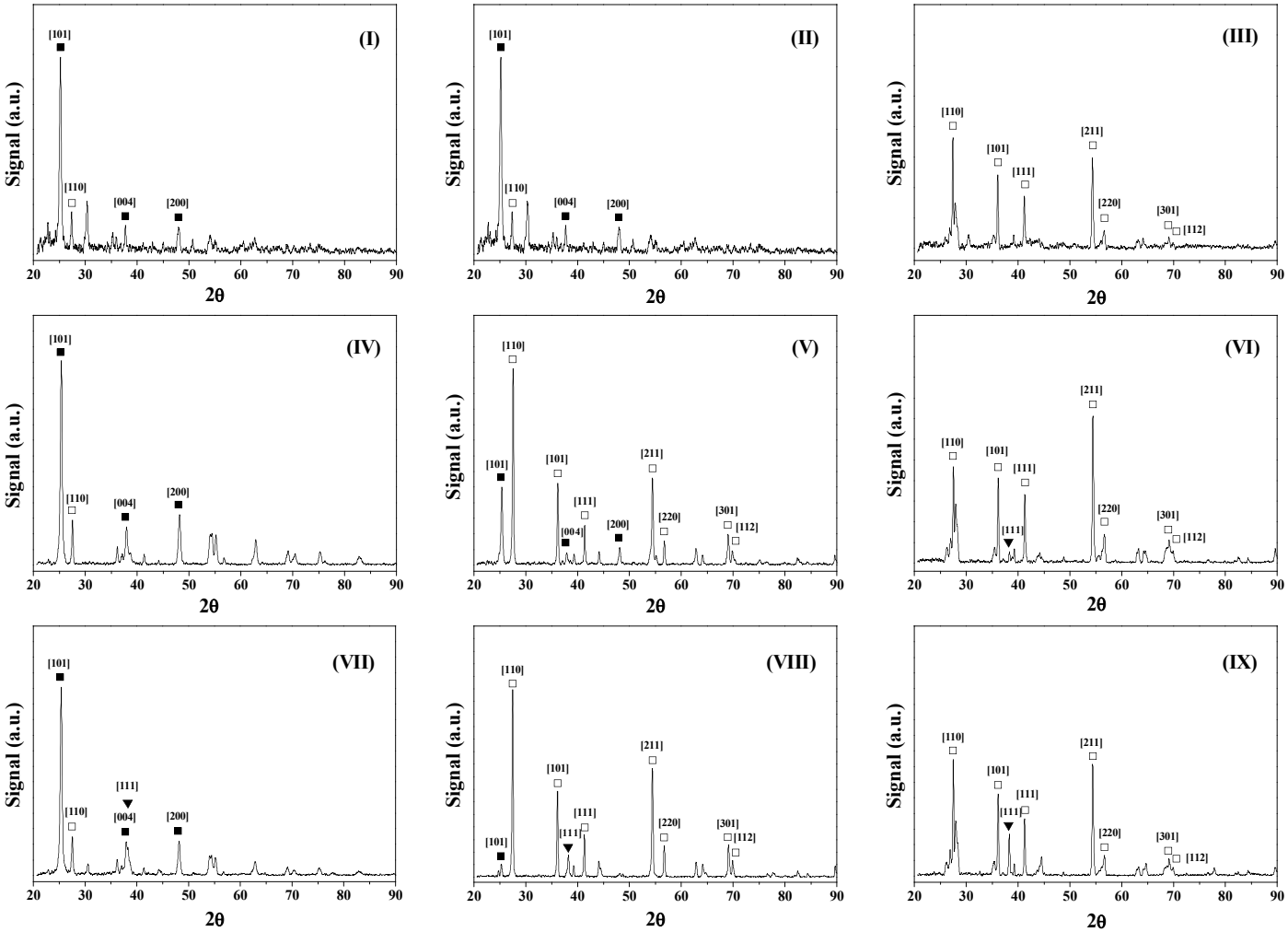

Figure 8.3: XRD patterns for the TiO_2 support post-thermal treatment up to (I) 603 K, (II) 873 K and (III) 1273 K and passivated/reduced (IV) Au/TiO_2-1, (V) Au/TiO_2-2, (VI) Au/TiO_2-5, (VII) Au/TiO_2-3, (VIII) Au/TiO_2-4 and (IX) Au/TiO_2-6. *Note*: peak assignments based on JCPDS-ICDD reference data: (■) anatase (21-1272); (□) rutile (21-1276); (▼) Au (04-0784).

The diffractograms for TiO_2 activated at 603 K and 873 K are essentially equivalent, exhibiting peaks at 25.3°, 37.8° and 48.1° that are consistent with the (101), (004) and (200) planes associated with tetragonal anatase. In addition, a signal at 27.4° is observed corresponding to the (110) main plane of tetragonal rutile. This XRD response is consistent with a mixture of anatase and rutile forms of TiO_2 where anatase:rutile ≈ 5:1, which is characteristic of Degussa P25 [63] for thermal treatment up to 923 K [43]. The diffractograms for Au/TiO_2-1 (IV) and Au/TiO_2-2 (V) do not present any detectable peak associated with Au, *i.e.* the metal particles are below the detection limits (< 3-5 nm [64,65]), which is supported by the TEM analysis. In contrast, the catalysts with higher Au content exhibited a peak at 2θ = 38.1° that corresponds to the (111) Au plane. A stronger XRD reflection is in evidence at the higher activation temperature (Au/TiO_2-4, profile VIII), indicative of Au sintering as demonstrated by TEM analysis (**Figure 8.2**).

The XRD diffractograms for Au/TiO_2-1 (IV) and Au/TiO_2-3 (VII) (reduced at 603 K) exhibit the same XRD signals due to the support, as observed for the starting TiO_2. In contrast, the XRD pattern for Au/TiO_2-2 (V) (reduced at 873 K) shows, in addition, new signals at 36.1°, 41.2°, 54.3°, 56.6°, 69.0° and 69.8° corresponding to the (101), (111), (211), (220), (301) and (112) planes of rutile. Furthermore, it should be noted that the relative intensity of the two main peaks for anatase and rutile at 2θ = 25.3° (101) and 27.4° (110), respectively, (*ca.* 1:3) differs from that which characterises the starting TiO_2 support (*ca.* 5:1, in profile II). This result suggests that the presence of Au facilitated the transition of anatase to rutile during the reduction of Au/TiO_2-2. This response also applies to Au/TiO_2-4 (VIII), *i.e.* same activation temperature but increased Au loading, where stronger rutile XRD reflections and a decrease in the anatase:rutile ratio (*ca.* 1:20) is in evidence. Indeed, only the main peak for anatase (at 2θ = 25.3°) is distinguishable and an increase in Au loading favours anatase→rutile transformation. Vargas *et al.* [45] reported that the incorporation of alkali metal, alkaline earth metal, and group 3 and 13 elements modified the requirements for the TiO_2 phase transformation (by more than 330 K) where a linear relationship between the anatase-rutile transition temperature and the ionic radius of the additive was established. Our findings suggest that the presence of Au lowers the temperature requirements for rutile formation, where Au content is a critical factor. This is illustrated in **Figure 8.4** where the rutile content, obtained from XRD analysis (see **Equation (8.1)**), is plotted as a function of activation temperature (A) and BET surface area (B).

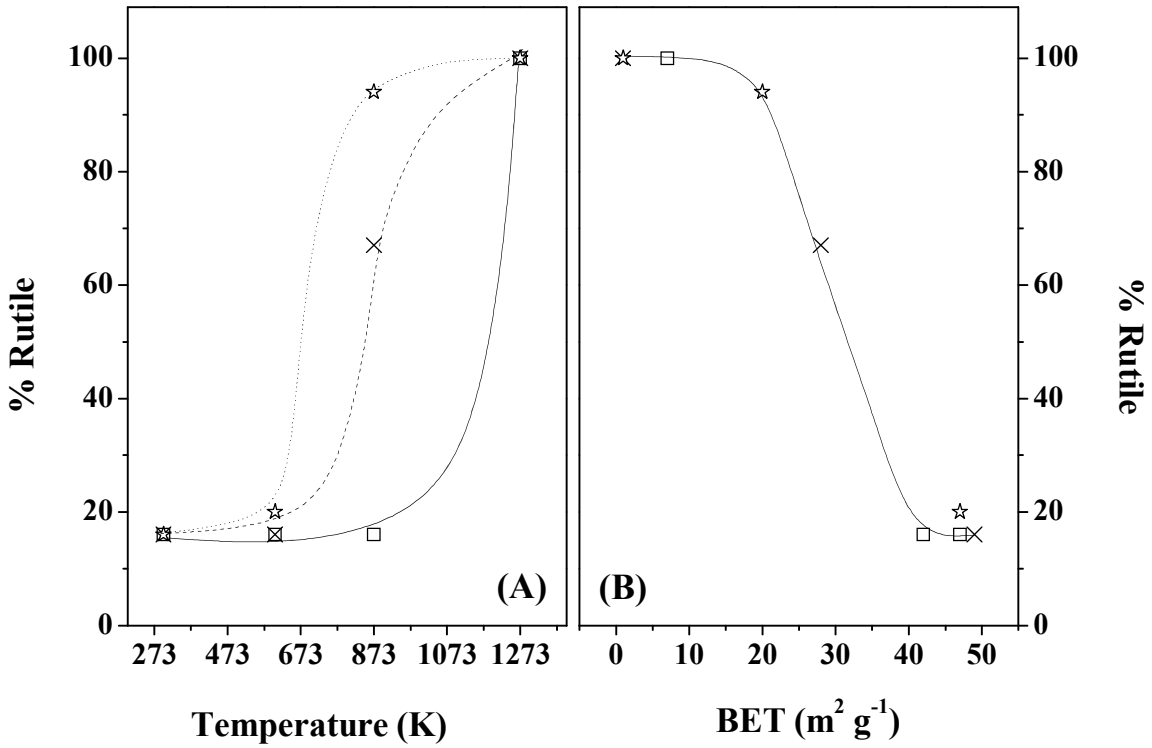

Figure 8.4: Variations in rutile content with (A) activation temperature and (B) BET surface area for (□) TiO_2 and Au/TiO_2 with (×) 0.1 and (☆) 1 mol % Au loading.

It can be seen that the rutile content in the starting TiO_2 and Au loaded TiO_2 essentially coincides for thermal treatment at $T \leq 603$ K whereas at $T > 603$ K phase transformation is dramatically promoted by incorporation of Au. A switch from anatase to rutile is accompanied by a decrease in surface area, as noted elsewhere [66] and demonstrated in **Figure 8.4**B. A complete transformation to the rutile phase upon treatment at 1273 K was a feature of TiO_2 with and without Au inclusion. This is in line with the literature [43] where, for pure (undoped) TiO_2, the transition of the thermodynamically unstable anatase (to rutile) at $T > 973$ K has been established.

Two kinds of sites, interstitial and substitutional, have been identified in the defect structure of the TiO_2 lattice [40]. Post-thermal treatment, cation dopants with a charge ≤ +4 can either replace Ti ions (increasing the number of oxygen vacancies and promoting phase transition) or locate in interstitial positions (decreasing oxygen vacancies and inhibiting phase transition) [66]. While the incorporation of Cu [67], Th [67] and Fe [67,68] has been reported to favour the TiO_2 allotropic transformation, the opposite effect has been shown in the case of Au [69,70]. Our results clearly demonstrate that the anatase→rutile step is more facile in the presence of Au,

suggesting that Au atoms are substitutionally incorporated in the TiO_2 lattice, promoting an increase of oxygen vacancies. It should, however, be noted that this transition is also favoured by the presence of Cl^- ions [71] and a contribution due to residual chloride, resulting from the decomposition of the $HAuCl_4$ precursor, may contribute to the response that we have observed. The number of oxygen vacancies, *i.e.* reduced state of TiO_2, has been found to markedly affect the size, shape and electronic character of supported Au nano-particles [72,73]. Changes to such structural features can influence the catalytic properties of Au in hydrogenation reactions [9,15,24]. The possible effect on the catalytic response due to the differences in the anatase:rutile ratio and/or Au-support interactions was investigated by preparing a series of rutile supported Au catalysts. In order to generate a range of Au particle sizes, two approaches were taken (see Experimental section) (i) activation in H_2 of 0.1 mol % (Au/TiO_2-5) and 1 mol % (Au/TiO_2-6) loadings at 1273 K and (ii) preparation of rutile by thermal treatment to 1273 K (see **Figure 8.3**, profile III) and subsequent impregnation with $HAuCl_4$ followed by activation at 603 K (Au/TiO_2-7) or 873 K (Au/TiO_2-8). The critical characterization results for these samples are compiled in **Table 8.2**. The XRD diffractogram patterns for Au/TiO_2-5 (VI) and Au/TiO_2-6 (IX), shown in **Figure 8.3**, demonstrate the presence of rutile and metallic Au with no evidence of the anatase phase. Representative TEM images (A) and Au particle size distributions (B) of Au/TiO_2-5 (I), Au/TiO_2-6 (II), Au/TiO_2-7 (III)) and Au/TiO_2-8 (IV) are given in **Figure 8.5**. The diffractogram pattern for an isolated Au particle and the support are shown in images IIIC/IVC and IIID, respectively. The *d*-spacings (0.20 and 0.33) confirm the presence of metallic gold and rutile. In addition to anatase→rutile conversion, activation at 1273 K resulted in Au sintering. At a common reduction temperature, Au/rutile catalyst exhibited a broader Au size distribution (and larger mean values) than that observed for Au/anatase, *i.e.* Au/TiO_2-1 *vs.* Au/TiO_2-7 and Au/TiO_2-2 *vs.* Au/TiO_2-8 (see **Tables 8.1** and **8.2**). This response suggests a Au size dependency on the allotropic form of the TiO_2 support and is in line with related studies where a weaker interaction (leading to metal agglomeration) with rutile relative to anatase has been proposed for Pd [74] and Ni [75].

Table 8.2: Gold loading with activation temperature and associated H_2 chemisorption values, TEM derived mean Au particle size (d_p), specific surface area (S_{Au}) (and size range), BET surface area and pseudo-first order rate constants for nitro-group reduction in the hydrogenation of *m*-DNB over Au/rutile.

Catalyst	Au content (mol %)	Activation Temperature (K)	$H_{2\ uptake}$ ($\mu mol\ g_{Au}^{-1}$)	d_p (nm)	Au size range (nm)	S_{Au}[a] ($m^2\ g_{Au}^{-1}$)	BET ($m^2\ g^{-1}$)	$10^3 \times k$ (h^{-1})
Au/TiO_2-5	0.1	1273	12	7.0	1-20	45	1	11
Au/TiO_2-6	1	1273	4	10.0	1-25	32	1	1
Au/TiO_2-7	0.1	603	66	6.4	1-15	50	1	37
Au/TiO_2-8	0.1	873	23	8.8	1-25	36	1	20

[a] $S_{Au} = 6/(\rho_{Au} \times d_p)$ where $\rho_{Au} = 18.88\ g\ cm^{-3}$

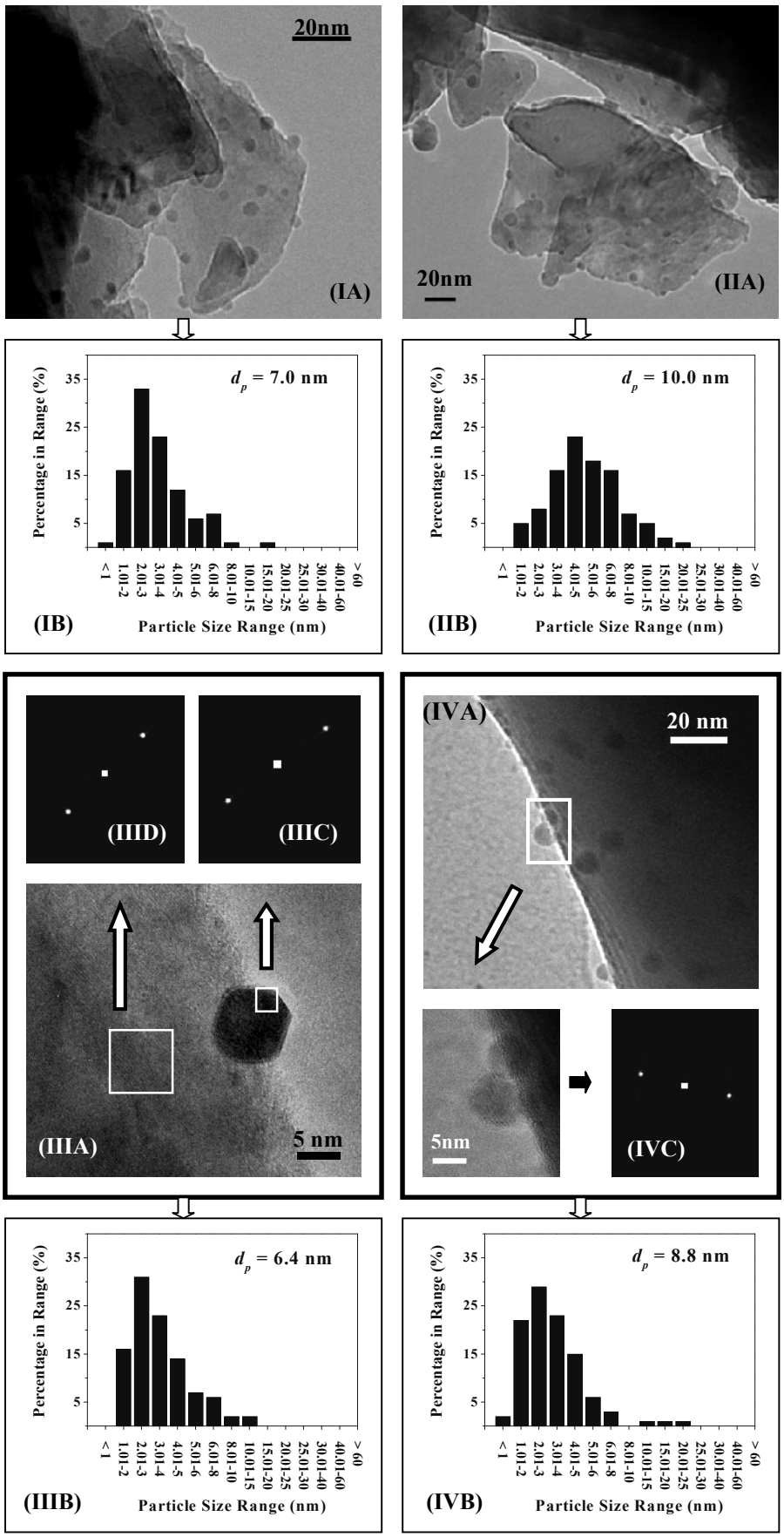

Figure 8.5: Representative (A) TEM images, (B) Au particle size distributions and diffractogram patterns associated with (C) isolated Au particles and (D) support for passivated/reduced (I) Au/TiO_2-5, (II) Au/TiO_2-6, (III) Au/TiO_2-7 and (IV) Au/TiO_2-8.

8.3.2 Catalytic activity/selectivity

8.3.2.1 Activity Dependence on Au Particle Size

Based on the characterisation results, we have generated a range of Au/anatase and Au/rutile samples with mean Au particle sizes in the range 3.4-10.0 nm. The consequence of variations in Au size and the nature of the support (anatase *vs*. rutile) on the selective hydrogenation of *m*-DNB has been considered. All the Au systems exhibited an essentially time invariant activity and 100% selectivity in terms of $-NO_2$ group reduction with no evidence of hydrodenitrogenation and/or aromatic ring reduction. This is demonstrated by the two representative cases (Au/TiO_2-1 and Au/TiO_2-3) shown in **Figure 8.6**.

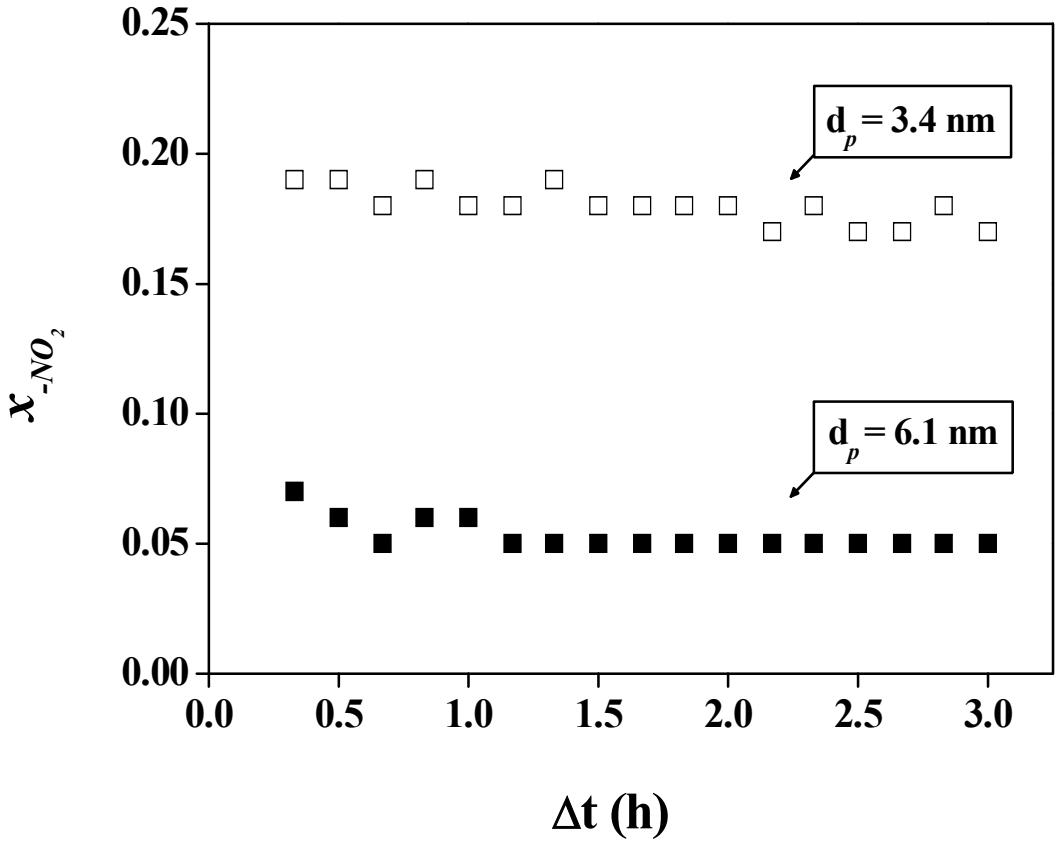

Figure 8.6: Variation of $-NO_2$ fractional conversion (x_{-NO_2}) with time-on-stream over (□) Au/TiO_2-1 ($Au/-NO_2 = 2 \times 10^{-3}$ mol_{Au} h $mol_{-NO_2}^{-1}$) and (■) Au/TiO_2-3 ($Au/-NO_2 = 1 \times 10^{-2}$ mol_{Au} h $mol_{-NO_2}^{-1}$) at 473 K.

The combination of stability and ultra-selectivity achieved in this study represents a significant development in the application of Au to promote $-NO_2$ group hydrogenation. A decrease in hydrogenation activity with time-on-stream has been

reported for reaction over Au/TiO_2 [11,76-78] and linked to saturation of active centres as a result of strong reactant chemisorption [11,78], metal sintering [76] and coke formation [77]. Deleterious effects due to the generation of water as reaction by-product [79,80], metal leaching [81] and coke formation [82-85] have been suggested as potential causes for the temporal loss of activity in the gas phase hydrogenation of nitroarenes over supported Pd [79-81,83,85] and Cu [82,84]. Catalytic activity was assessed in terms of nitro group reduction efficiency by applying pseudo-first order kinetics [24,35,36]

$$\ln\left[\frac{1}{(1-x_{\text{-}NO_2})}\right] = \mathrm{k}\left(\frac{n_{Au}}{F_{\text{-}NO_2}}\right) \qquad \textbf{(8.6)}$$

where $F_{\text{-}NO_2}$ is the total inlet molar -NO_2 and n_{Au} represents the number of moles of Au in the catalyst bed; $\left(n_{Au}/F_{\text{-}NO_2}\right)$ has the physical meaning of contact time. The linear correlation between $\ln(1-(x_{\text{-}NO_2}))^{-1}$ and $\left(n_{Au}/F_{\text{-}NO_2}\right)$ is shown in **Figure 8.7**(A), taking Au/TiO_2-1 and Au/TiO_2-3 as representative catalysts. The raw pseudo-first order rate constants (k) for Au/anatase and Au/rutile are given in **Table 8.1** and **Table 8.2**, respectively. A direct comparison of rate constants for catalysts bearing variable Au dispersion is only meaningful in terms of specific activities, *i.e.* per m^2 of exposed metal. The Au metal surface area was estimated from

$$S_{Au}\,(\mathrm{m}^2_{Au}\,\mathrm{g}^{-1}_{Au}) = \frac{6}{\rho_{Au}\times d_p} \qquad \textbf{(8.7)}$$

where ρ_{Au} = 18.88 g cm^{-3} and d_p is the surface area weighted mean Au particle size, as measured by TEM (see **Table 8.1** and **Table 8.2**). The specific pseudo-first order rate constant (k') was then calculated from

$$\mathrm{k'}\,(\mathrm{mol}_{\text{-}NO_2}\,\mathrm{m}^{-2}_{Au}\,\mathrm{h}^{-1}) = \frac{\mathrm{k}\,(\mathrm{mol}_{\text{-}NO_2}\,\mathrm{g}^{-1}_{Au}\,\mathrm{h}^{-1})}{S_{Au}\,(\mathrm{m}^2_{Au}\,\mathrm{g}^{-1}_{Au})} \qquad \textbf{(8.8)}$$

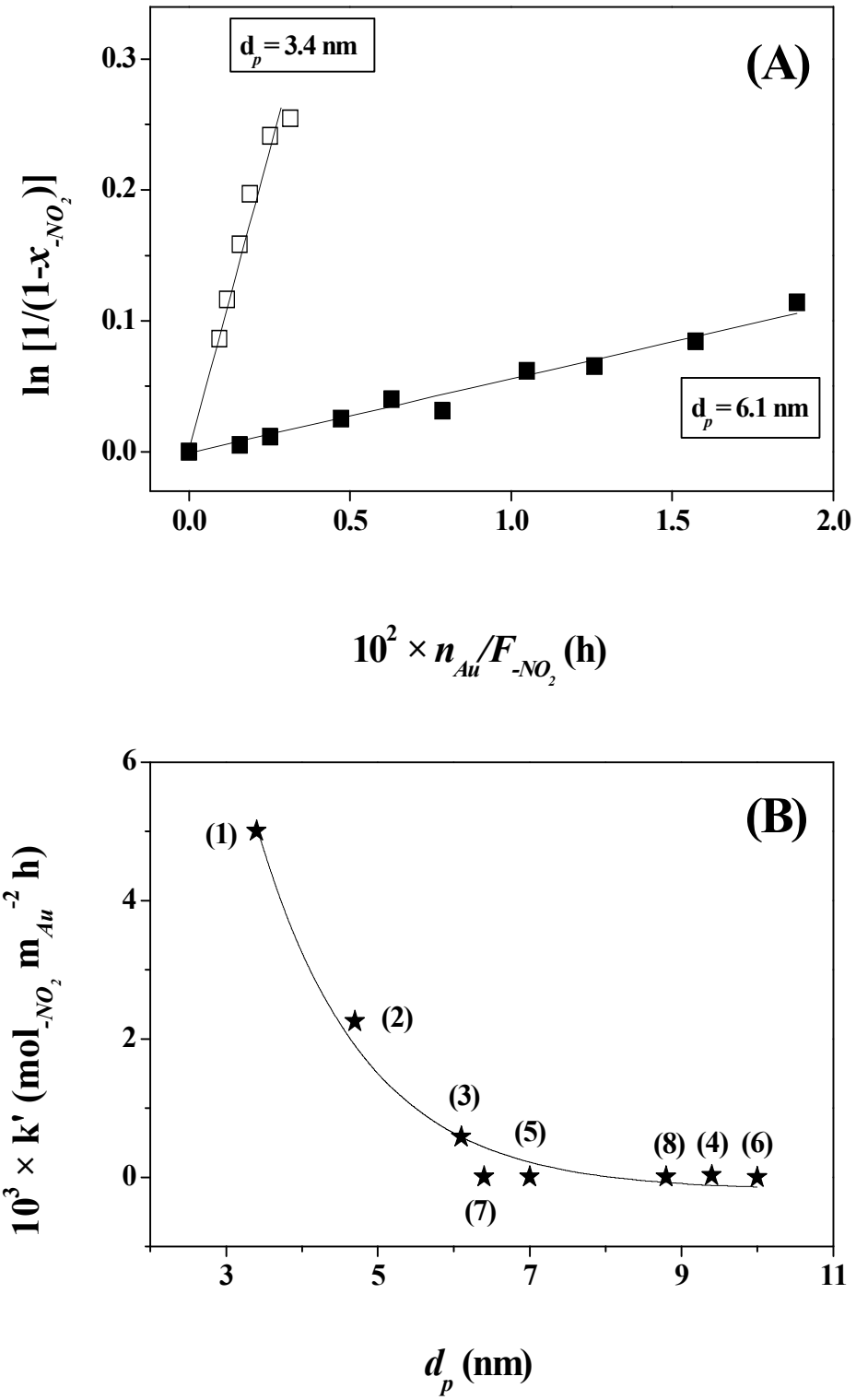

Figure 8.7: (A) Pseudo-first-order kinetic plots for reaction over (□) Au/TiO_2-1 and (■) Au/TiO_2-3 at 473 K. (B) Relationship between specific rate constant (k') and Au particle size (d_p) for reaction over Au/TiO_2-1 (1), Au/TiO_2-2 (2), Au/TiO_2-3 (3), Au/TiO_2-4 (4), Au/TiO_2-5 (5), Au/TiO_2-6 (6), Au/TiO_2-7 (7) and Au/TiO_2-8 (8).

The relationship between specific activity and mean Au particle size for all the catalysts considered in this study is presented in **Figure 8.7**(B). The tendency of increasing k' with decreasing d_p is diagnostic of structure sensitivity where smaller Au particles (10.0→3.4 nm) exhibited an enhanced intrinsic -NO_2 hydrogenation efficiency. Furthermore, the results demonstrate that the nature of the support (anatase:rutile ratio) does not impact significantly on hydrogenation rate, which is governed by the Au particle size. A dependence of hydrogenation rate on support for Au on reducible carriers has been reported [78] and ascribed to the formation of electron rich Au *via* support-metal electron transfer [86], the formation of unselective Au particles with different morphology [87] and/or reactant activation at the Au-support interface [88]. Moreover, Jongsomjit *et al.* [89] found, for Co/TiO_2, a distinct activity response in the hydrogenation of CO associated with differences in the rutile:anatase ratio. Our results show an equivalent specific -NO_2 reduction rate over systems with similar Au particle size but quite different support composition, as illustrated by data points 3 (Au/TiO_2-3, d_p = 6.1 nm and 20 % rutile) and 7 (Au/TiO_2-7, d_p = 6.4 nm and 100 % rutile). Moreover, taking an equivalent support composition (18 ± 2 % rutile, see data points 1 and 3 in **Figure 8.7**(B)), the catalyst bearing the smaller Au particles (Au/TiO_2-1, d_p = 3.4 nm) delivered an order of magnitude higher specific rate (when compared with Au/TiO_2-3, d_p = 6.1 nm). Our results find agreement with published studies suggesting that the presence of nanoscale Au particles (< 10 nm) is essential for significant activity [7,8]. Variations in hydrogenation rate for Au particles in the range 3-10 nm have been reported [9,11,90] and linked (in the case of acrolein hydrogenation over Au/TiO_2) to modifications in the electronic character of small Au particles [15]. It is instructive to note that the specific activities that we have recorded converge for Au particles > 5 nm and 5 nm represents a critical mean diameter below which there is a marked rate dependence. In a recent study [9], we examined the hydrogenation of *p*-chloronitrobenzene over oxide (Al_2O_3, TiO_2, CeO_2 and Fe_2O_3) supported Au prepared by impregnation and deposition-precipitation and demonstrated an increase in specific hydrogenation rate with decreasing Au particle size (from 9 to 3 nm) regardless of the nature of the support. The results generated in this study provide further corroboration of Au particle size effects in -NO_2 reduction over supported Au.

8.3.2.2 Selectivity Dependence on Au Particle Size

The relationship between initial selectivity (S_0) and fractional *m*-DNB conversion ($x_{m\text{-}DNB}$) resulting from reaction over all eight Au/TiO_2 catalysts is presented in **Figure 8.8**.

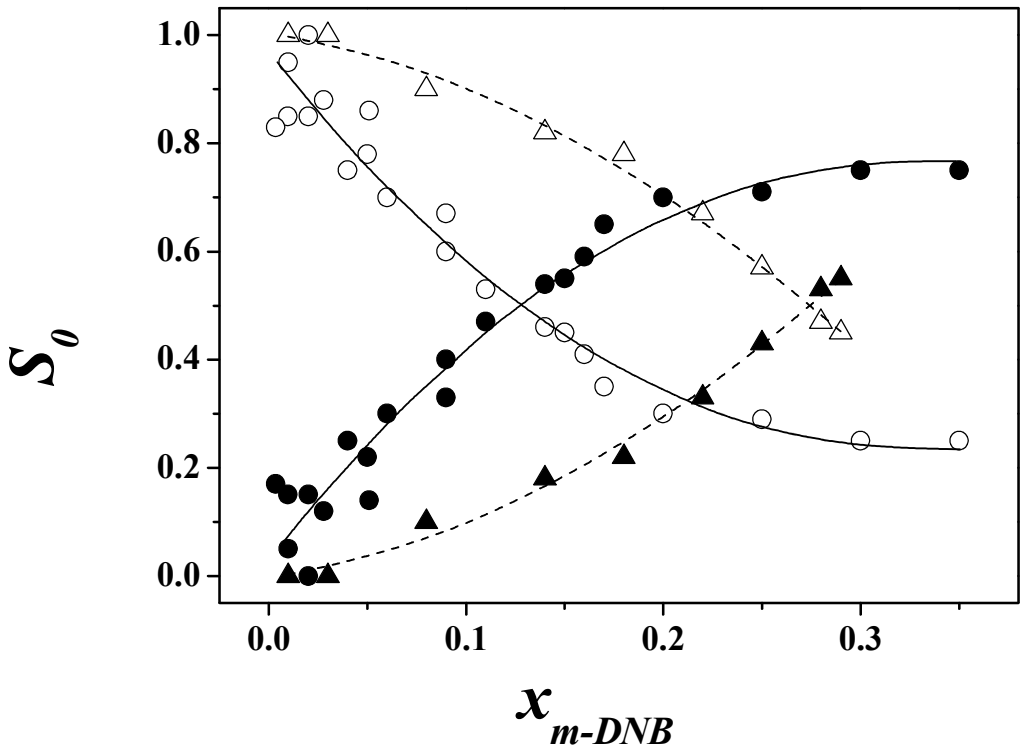

Figure 8.8: Variation of *m*-PDM (solid symbols) and *m*-NAN (open symbols) initial selectivity (S_0) with *m*-DNB fractional conversion ($x_{m\text{-}DNB}$) for reaction over catalysts with d_p < 5 nm (▲,△) and d_p ≥ 5 nm (●,○).

Two distinct trends in terms of product distribution are in evidence for systems where d_p < 5 nm and ≥ 5 nm. Reaction over Au/TiO_2 bearing Au particles < 5 nm generated *m*-NAN as the preferred product, *i.e.* $S_{m\text{-}NAN} \geq 0.5$ at $x_{m\text{-}DNB} \leq 0.3$. In contrast, for those catalysts characterised by a mean Au size ≥ 5 nm, the formation of *m*-PDM was favoured at $x_{m\text{-}DNB} > 0.10$. This response was independent of support anatase:rutile ratio and hydrogenation selectivity (in common with activity) was governed by Au particle size. Nitro group reduction in *m*-DNB can proceed *via* a consecutive and/or parallel mechanism. The two possible paths are identified in the reaction network depicted in **Figure 8.9**.

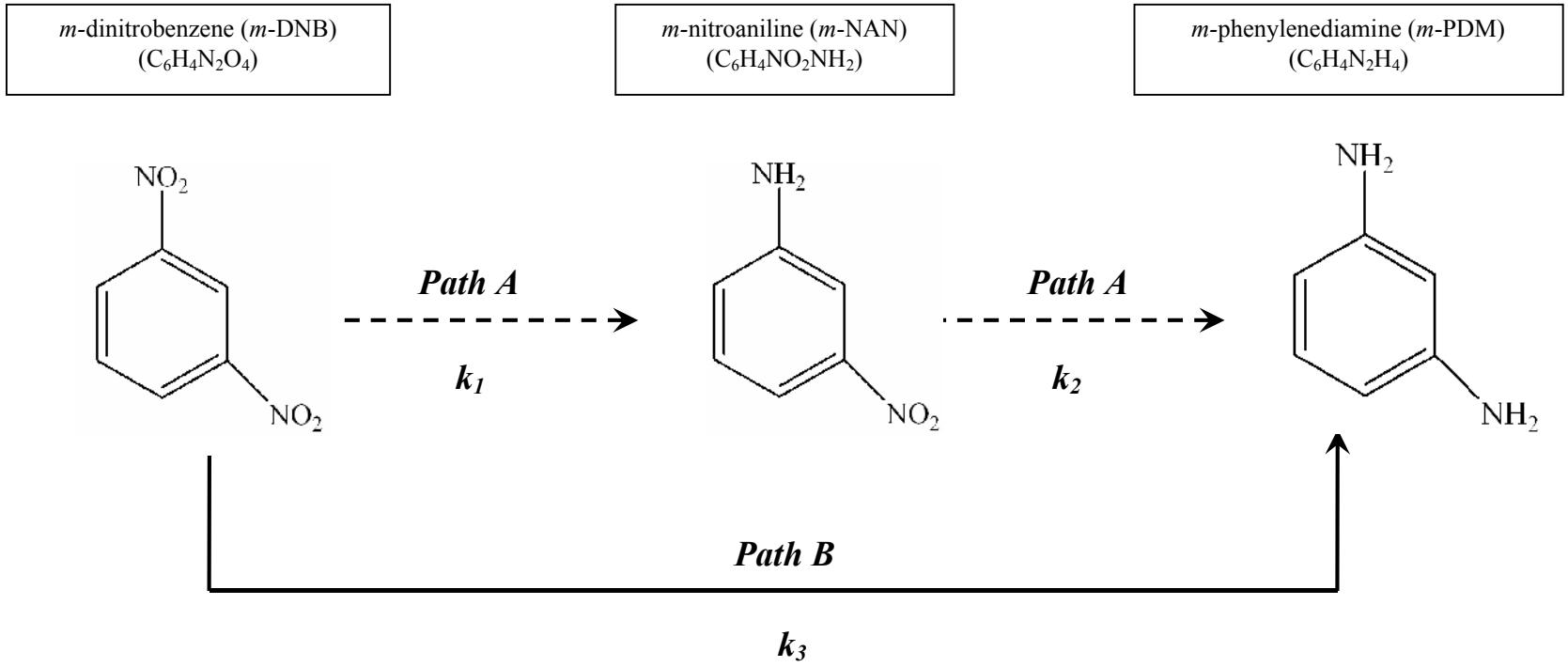

Figure 8.9: Reaction pathways associated with the hydrogenation of *m*-dinitrobenzene (*m*-DNB) to *m*-nitroaniline (*m*-NAN) and *m*-phenylenediamine (*m*-PDM).

The formation *m*-PDM can take place *via* a consecutive (Path A, with *m*-NAN as reaction intermediate) and/or a parallel (Path B) concerted mechanism according to:

$$m\text{-}DNB + 3H_2 \xrightarrow{k_1} m\text{-}NAN + 2H_2O \qquad \textbf{(8.9)}$$

$$m\text{-}NAN + 3H_2 \xrightarrow{k_2} m\text{-}PDM + 2H_2O \qquad \textbf{(8.10)}$$

$$m\text{-}DNB + 6H_2 \xrightarrow{k_3} m\text{-}PDM + 4H_2O \qquad \textbf{(8.11)}$$

and

$$\frac{dN_{m\text{-}DNB}}{d\left(n/F_{m\text{-}DNB}\right)} = -\left(k_1 + k_3\right) \times N_{m\text{-}DNB} \qquad \textbf{(8.12)}$$

$$\frac{dN_{m\text{-}NAN}}{d\left(n/F_{m\text{-}DNB}\right)} = k_1 \times N_{m\text{-}DNB} - k_2 \times N_{m\text{-}NAN} \qquad \textbf{(8.13)}$$

$$\frac{dN_{m\text{-}PDM}}{d\left(n/F_{m\text{-}DNB}\right)} = k_2 \times N_{m\text{-}NAN} + k_3 \times N_{m\text{-}DNB} \qquad \textbf{(8.14)}$$

where N_i represents the molar fraction of the i^{th} compound and k_j is the pseudo-first order rate constant of step j. Combination of **Equations (8.12)** and **(8.13)** gives

$$\frac{dN_{m\text{-}NAN}}{dN_{m\text{-}DNB}} = -L + M \times \left(\frac{N_{m\text{-}NAN}}{N_{m\text{-}DNB}}\right) \qquad \textbf{(8.15)}$$

with

$$L = \frac{k_1}{k_1 + k_3} \quad \therefore \quad M = \frac{k_2}{k_1 + k_3} \qquad \textbf{(8.16)}$$

which, by formal integration, results in

$$N_{m\text{-}NAN} = \frac{L}{1-M} \times \left({N_{m\text{-}DBN}}^{M} - N_{m\text{-}DBN} \right) \qquad \textbf{(8.17)}$$

and the values of L and M can be determined by non-linear mathematical fitting. The applicability of this parallel/consecutive mechanism can be assessed from **Figure 8.10**, which reveals a more than adequate representation of the selectivity trends.

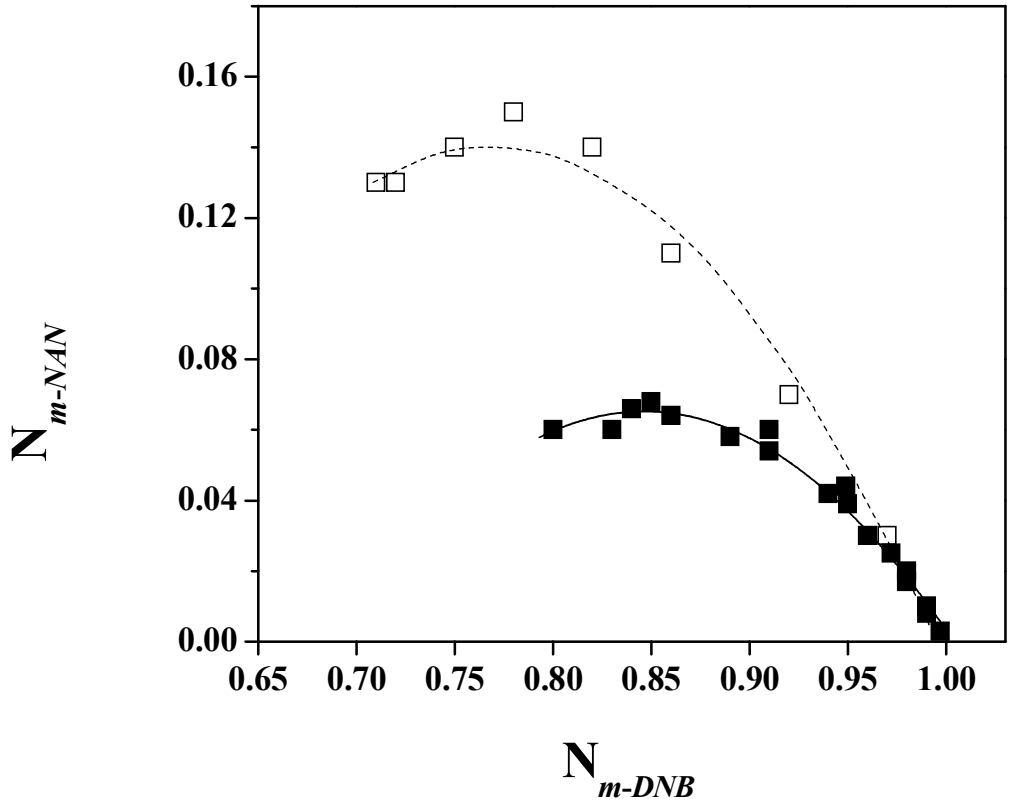

Figure 8.10: Dependence of *m*-NAN mole fraction ($N_{m\text{-}NAN}$) on *m*-DNB conversion ($N_{m\text{-}NAN}$) for reaction over catalysts with d_p < 5 nm (□) and d_p ≥ 5 nm (■). *Note*: lines represents fit to the parallel/consecutive model, see Equation 8.17.

A predominantly stepwise -NO_2 group reduction mechanism should result in a value for L close to unity, *i.e.* k_3~0. The extracted values of L = 0.99 (for d_p < 5 nm) and L = 0.81 (for $d_p \geq 5$ nm) confirms that smaller Au particles promote a predominantly consecutive hydrogenation, resulting in a higher maximum $N_{m\text{-}NAN}$ (see **Figure 8.10**).

We were unable to find any published report that has considered the effect of TiO_2 anatase and/or rutile content on the catalytic action of supported Au. However, we can flag related studies where selectivity in the hydrogenation of acetylene [91] and

alkadienes [74] over Pd/TiO_2 showed a dependence on TiO_2 composition, *i.e.* variations in the amount and/or mobility of Ti^{3+} on anatase and rutile. Claus *et al.* [92] investigated the hydrogenation of crotonaldehyde over Pt/TiO_2 and found a similar selectivity response (to crotyl alcohol) for conversions ≤ 50% but proposed an optimum (65% anatase) composition for higher conversions, attributing this to product adsorption/readsorption effects that were dependent on the TiO_2 phase composition. We can tentatively associate our observed selectivity response in terms of Au size to critical differences in the active site electronic structure, which can influence *m*-DNB adsorption/activation. Indeed, Au nanoparticle size is known to influence reactant adsorption and impact on selectivity in hydrogenation reactions [16,93]. The formation of $Au^{\delta+}$ and $Au^{\delta-}$ associated with large (9 nm) and small (3 nm) Au clusters, respectively, on TiO_2 has been demonstrated by EXAFS [94]. Indeed, Zhang *et al.* [95], studying the hydrogenation of 1,3-butadiene over Au/ZrO_2, ascribed the distinct selectivity response (with respect to butene or butane) to differences in the Au charge. Our results establish for the first time a significant Au particle size effect on product distribution for the gas phase hydrogenation of *m*-DNB.

8.4 Conclusions

The results presented in this study support the following conclusions:

i. Temperature programmed reduction of 0.1 and 1 mol % Au loaded TiO_2 over the temperature range 603-1273 K generated supported Au metal particles with mean diameters in the range 3.4-10.0 nm as confirmed by HRTEM-EDX, DRS UV-vis and XRD measurements.

ii. The complete allotropic transition (from anatase to rutile) of the starting TiO_2 support is attained at T = 1273 K where the incorporation of Au lowers the temperature requirements for this phase transformation by up to 400 K; anatase transformation is promoted to a greater extent at the higher Au loading.

iii. In the gas phase hydrogenation of *m*-DNB, all Au/TiO_2 catalysts delivered time invariant conversions. The support composition (or anatase:rutile ratio) did not influence nitro-group reduction rate, which was controlled by Au particle size

with increasing specific rates for particles < 5 nm: specific rate was insensitive to particle sizes > 5 nm.

iv. *m*-DNB hydrogenation generated *m*-NAN (partial reduction) and/or *m*-PDM (complete reduction) where the reaction proceeded *via* a predominantly stepwise reaction mechanism. *m*-NAN formation was favoured for reaction over Au particles < 5 nm. We associate this response to a modification of the electronic character of the Au nanoparticles that impacts on *m*-DNB adsorption/activation mechanism.

8.5 References

[8.1] P. F. Vogt, J. J. Gerulis, Ullmann's Encyclopedia of Industrial Chemistry. "Aromatic Amines", Wiley-VCH Verlag GmbH & Co. KGaA, Weinheim, 2005.

[8.2] M. Boudart, Adv. Catal., 20, 153 (1969)

[8.3] S. Chytil, W. R. Glomm, E. Vollebekk, H. Bergem, J. Walmsley, J. Sjöblom, E. A. Blekkan, Microporous Mesoporous Mater., 86, 198 (2005)

[8.4] K. V. R. Chary, D. Naresh, V. Vishwanathan, M. Sadakane, W. Ueda, Catal. Commun., 8, 471 (2007)

[8.5] A. Arcadi, Chem. Rev., 108, 3266 (2008)

[8.6] J. A. van Bokhoven, J. T. Miller, J. Phys. Chem. C, 111, 9245 (2007)

[8.7] P. Claus, Appl. Catal. A: Gen., 291, 222 (2005)

[8.8] A. S. K. Hashmi, G. J. Hutchings, Angew. Chem. Int. Ed., 45, 7896 (2006)

[8.9] F. Cárdenas-Lizana, S. Gómez-Quero, N. Perret, M. A. Keane, Gold Bulletin, in press (2009)

[8.10] J. Jia, K. Haraki, J. N. Kondo, K. Domen, K. Tamaru, J. Phys. Chem. B, 104, 11153 (2000)

[8.11] R. Zanella, C. Louis, S. Giorgio, R. Touroude, J. Catal., 223, 328 (2004)

[8.12] E. Bus, J. T. Miller, J. A. van Bokhoven, J. Phys. Chem. B, 109, 14581 (2005)

[8.13] E. Bus, R. Prins, J. A. van Bokhoven, Catal. Commun., 8, 1397 (2007)

[8.14] C. Mohr, H. Hofmeister, J. Radnik, P. Claus, J. Am. Chem. Soc., 125, 1905 (2003)

[8.15] P. Claus, A. Brückner, C. Mohr, H. Hofmeister, J. Am. Chem. Soc., 122, 11430 (2000)

[8.16] J. E. Bailie, H. A. Abdullah, J. A. Anderson, C. H. Rochester, N. V. Richardson, N. Hodge, J. G. Zhang, A. Burrows, C. J. Kiely, G. J. Hutchings, Phys. Chem. Chem. Phys., 3, 4113 (2001)

[8.17] I. Dobrosz, K. Jiratova, V. Pitchon, J. M. Rynkowski, J. Mol. Catal. A: Chem., 234, 187 (2005)

[8.18] F. Moreau, G. C. Bond, A. O. Taylor, J. Catal., 231, 105 (2005)

[8.19] M. Haruta, Catal. Today, 36, 153 (1997)

[8.20] F. Cárdenas-Lizana, S. Gómez-Quero, A. Hugon, L. Delannoy, C. Louis, M. A. Keane, J. Catal., 262, 235 (2009)

[8.21] S. H. Overbury, V. Schwartz, D. R. Mullins, W. Yan, S. Dai, J. Catal., 241, 56 (2006)

[8.22] J. Huang, W.-L. Dai, H. Li, K. Fan, J. Catal., 252, 69 (2007)

[8.23] T. Akita, P. Lu, S. Ichikawa, K. Tanaka, M. Haruta, Surf. Interface Anal., 31, 73 (2001)

[8.24] F. Cárdenas-Lizana, S. Gómez-Quero, M. A. Keane, ChemSusChem, 1, 215 (2008)

[8.25] B. K. Min, W. T. Wallace, D. W. Goodman, Surf. Sci., 600, L7-L11 (2006)

[8.26] K. R. Westerterp, E. J. Molga, K. B. van Gelder, Chem. Eng. Process., 36, 17 (1997)

[8.27] B. Coq, F. Figuéras, Coord. Chem. Rev., 178-180, 1753 (1998)

[8.28] G. Zhang, L. Wang, K. Shen, D. Zhao, H. S. Freeman, Chem. Eng. J., 141, 368 (2008)

[8.29] A. Corma, P. Serna, Science, 313, 332 (2006)

[8.30] N. S. Chaubal, M. R. Sawant, J. Mol. Catal. A: Chem., 261, 232 (2007)

[8.31] L. Liu, B. Qiao, Y. Ma, J. Zhang, Y. Deng, Dalton Trans., 2008, p. 2542.

[8.32] M. Boronat, P. Concepción, A. Corma, S. González, F. Illas, P. Serna, J. Am. Chem. Soc., 129, 16230 (2007)

[8.33] D. He, H. Shi, Y. Wu, B.-Q. Xu, Green Chem., 9, 849 (2007)

[8.34] Y. Chen, J. Qiu, X. Wang, J. Xiu, J. Catal., 242, 227 (2006)

[8.35] F. Cárdenas-Lizana, S. Gómez-Quero, M. A. Keane, Catal. Commun., 9, 475 (2008)

[8.36] F. Cárdenas-Lizana, S. Gómez-Quero, M. A. Keane, Catal. Lett., 127, 25 (2009)

[8.37] X . Fu, L. A. Clark, Q. Yang, M. A. Anderson, Environ. Sci. Technol., 30, 647 (1996)

[8.38] G. Tavoularis, M. A. Keane, J. Chem. Technol. Biotechnol., 74, 60 (1999)

[8.39] G. Yuan, M. A. Keane, Chem. Eng. Sci., 58, 257 (2003)

[8.40] U. Diebold, Surf. Sci. Rep., 48, 53 (2003)

[8.41] D.J. Reidy, J.D. Holmes, M.A. Morris, J. Eur. Ceram. Soc. , 26, 1527 (2006)

[8.42] R. I. Bickley, T. Gonzalez-Carreno, J. S. Lees, L. Palmisano, R. J. D. Tilley, J. Solid State Chem., 92, 178 (1991)

[8.43] T. Sekiya, T. Yagisawa, S. Kurita, J. Ceram. Soc. Jpn., 109, 672 (2001)

[8.44] R. Rodríguez-Talavera, S. Vargas, R. Arroyo-Murillo, R. Montiel-Campos, E. Haro-Poniatowski, J. Mater. Res., 12, 439 (1996)

[8.45] S. Vargas, R. Arroyo, E. Haro, R. Rodríguez, J. Mater. Res., 14, 3932 (1999)

[8.46] M. G. Blanchin, L. A. Bursill, D. J. Smith, Proc. Roy. Soc. Lond. A, 391, 351 (1984)

[8.47] L. A. Bursill, M. G. Blanchin, D. J. Smith, Proc. Roy. Soc. Lond. A, 391, 373 (1984)

[8.48] J. Guzman, S. Kuba, J. C. Fierro-Gonzalez, B. C. Gates, Catal. Lett., 95, 77 (2004)

[8.49] J. Słoczyński, R. Grabowski, A. Kozłowska, P. Olszewski, J. Stoch, J. Skrzypek, M. Lachowska, Appl. Catal. A: Gen., 278, 11 (2004)

[8.50] S. Gómez-Quero, F. Cárdenas-Lizana, M. A. Keane, Ind. Eng. Chem. Res., 47, 6841 (2008)

[8.51] B. Hammer, J. K. Nørskov, Nature, 376, 238 (1995)

[8.52] G. C. Bond, D. T. Thompson, Catal. Rev.-Sci. Eng., 41, 319 (1999)

[8.53] V. Loddo, G. Marcì, C. Martín, L. Palmisano, V. Rives, A. Sclafani, Appl. Catal. B: Environ., 20, 29 (1999)

[8.54] N. Venkatachalam, M. Palanichamy, B. Arabindoo, V. Murugesan, J. Mol. Catal. A: Chem., 266, 158 (2007)

[8.55] J.-W. Shi, J.-T. Zheng, P. Wu, J. Hazard. Mater., 161, 416 (2009)

[8.56] R. S. Sonawane, M. K. Dongare, J. Mol. Catal. A: Chem., 243, 68 (2006)

[8.57] Q. Zhao, M. Li, J. Chu, T. Jiang, H. Yin, Appl. Surf. Sci., 255, 3773 (2009)

[8.58] B. R. Panda, A. Chattopadhyay, J. Nanosci. Nanotech., 7, 1911 (2007)

[8.59] X. Hu, D. J. Blackwood, J. Electroceram., 16, 593 (2006)

[8.60] M. Haruta, CATTECH, 6, 102 (2002)

[8.61] M. Li, W. Hebenstreit, U. Diebold, A. M. Tyryshkin, M. K. Bowman, G. G. Dunham, M. A. Henderson, J. Phys. Chem. B, 104, 4944 (2000)

[8.62] S.-K. Lee, P. K. J. Robertson, A. Mills, D. McStay, N. Elliott, D. McPhail, Appl. Catal. B: Environ., 44, 173 (2003)

[8.63] G. L. Haller, D. E. Resasco, Adv. Catal., 36, 173 (1989)

[8.64] S. Díaz-Moreno, D. C. Koningsberger, a. Muñoz-Páez, Nucl. Instrum. Methods Phys. Res., Sect. B, 133, 15 (1997)

[8.65] J. Liu, Microsc. Microanal., 10, 55 (2004)

[8.66] R. Arroyo, G. Córdoba, J. Padilla, V. H. Lara, Mater. Lett., 54, 397 (2002)

[8.67] G. Sankar, K. R. Kannan, C. N. R. Rao, Catal. Lett., 8, 27 (1991)

[8.68] R. I. Bickley, T. Gonzalez-Carreño, A. R. Gonzalez-Elipé, G. Munuera, L. Palmisano, J. Chem. Soc., Faraday Trans., 90, 2257 (1994)

[8.69] A. G. Shastri, A. K. Datye, J. Schwank, J. Catal., 87, 265 (1984)

[8.70] M. A. Debeila, M. C. Raphulu, E. Mokoena, M. Avalos, V. Petranovskii, N. J. Coville, M. S. Scurrell, Mater. Sci. Eng. A, 396, 61 (2005)

[8.71] S. Kittaka, K. Matsuno, S. Takahara, J. Solid State Chem., 132, 447 (1997)

[8.72] D. Pillay, G. S. Hwang, Phys. Rev. B, 72, 205422 (2005)

[8.73] N. Lopez, J. K. Nørskov, T. V. W. Janssens, A. Carlsson, A. Puig-Molina, B. S. Clausen, J.-D. Grunwaldt, J. Catal., 225, 86 (2004)

[8.74] Y. Li, B. Xu, Y. Fan, N. Feng, A. Qiu, J. M. J. He, H. Yang, Y. Chen, J. Mol. Catal. A: Chem., 216, 107 (2004)

[8.75] N. Yao, J. Chen, J. Zhang, J. Zhang, Catal. Commun., 9, 1510 (2008)

[8.76] T. V. Choudhary, C. Sivadinarayana, A. K. Datye, D. Kumar, D. W. Goodman, Catal. Lett., 86, 1 (2003)

[8.77] Y. Azizi, C. Petit, V. Pitchon, J. Catal., 256, 338 (2008)

[8.78] J. A. Lopez-Sanchez, D. Lennon, Appl. Catal. A: Gen., 291, 230 (2005)

[8.79] P. Sangeetha, P. Seetharamulu, K. Shanthi, S. Narayanan, K.S. Rama Raob, J. Mol. Catal. A: Chem., 273, 244 (2007)

[8.80] P. Sangeetha, K. Shanthi, K. S. R. Rao, B. Viswanathan, P. Selvam, Appl. Catal. A: Gen., 353, 160 (2009)

[8.81] K. K. Yeong, A. Gavriilidis, R. Zapf, V. Hessel, Catal. Today, 81, 641 (2003)

[8.82] L. Petrov, K. Kumbilieva, N. Kirkov, Appl. Catal., 59, 31 (1990)

[8.83] E. Klemm, B. Amon, H. Redlingshöfer, E. Dieterich, G. Emig, Chem. Eng. Sci., 56, 1347 (2001)

[8.84] S. Diao, W. Qian, G. Luo, F. Wei, Y. Wang, Appl. Catal. A: Gen., 286, 30 (2005)

[8.85] V. Vishwanathan, V. Jayasri, P. M. Basha, N. Mahata, L. M. Sikhwivhilu, N. J. Coville, Catal. Commun., 9, 453 (2008)

[8.86] C. Milone, C. Crisafulli, R. Ingoglia, L. Schipilliti, S. Galvagno, Catal. Today, 122, 341 (2007)

[8.87] B. C. Campo, S. Ivanova, C. Gigola, C. Petit, M. A. Volpe, Catal. Today, 133-135, 661 (2008)

[8.88] J. E. Bailie, G. J. Hutchings, Chem. Commun., 1999, p. 2151.

[8.89] B. Jongsomjit, T. Wongsalee, P. Praserthdam, Catal. Commun., 6, 705 (2005)

[8.90] C. Mohr, H. Hofmeister, P. Claus, J. Catal., 213, 86 (2003)

[8.91] J. Panpranot, K. Kontapakdee, P. Praserthdam, J. Phys. Chem. B, 110, 8019 (2006)

[8.92] P. Claus, S. Schimpf, R. Schödel, P. Kraak, W. Mörke, D. Hönicke, Appl. Catal. A: Gen., 165, 429 (1997)

[8.93] B. Pawelec, A. M. Venezia, V. La Parola, S. Thomas, J. L. G. Fierro, Appl. Catal. A: Gen., 283, 165 (2005)

[8.94] Y. Izumi, D. M. Obaid, K. Konishi, D. Masih, M. Takagaki, Y. Terada, H. Tanida, T. Uruga, Inorg. Chim. Acta, 361, 1149 (2008)

[8.95] X. Zhang, H. Shi, B.-Q. Xu, Catal. Today, 122, 330 (2007)

Chapter 9

Tunable Gas Phase Hydrogenation of *m*-Dinitrobenzene over Alumina Supported Au and Au-Ni

The results presented in previous Chapters suggest a distinct catalytic response as a result of modifications in the Au site electronic character induced by variations in metal dispersion and/or nature of the support. In this section, we have compared the behaviour of alumina supported monometallic Au and Ni with that of bimetallic Au-Ni/Al_2O_3 (prepared by reductive deposition of Au onto Ni) in order to probe possible Au/Ni synergistic effects in selective hydrogenation.

9.1 Introduction

Catalysis by gold is a topic that is now attracting appreciable research activity, which is reflected in the range of publications recently reviewed by Hashmi [1]. Gold has been successfully used to promote oxidation [2] and hydrogenation [3] reactions with possible applications on a commercial scale [4]. Compared with "conventional metals" (*e.g.* Ni, Pd, Pt), Au is less active in hydrogenation, a response commonly associated with its low capacity to strongly adsorb/dissociate hydrogen [3,5]. Furthermore, hydrogenation over Au catalysts exhibits structure sensitivity, where smaller particles (≤ 10 nm) deliver higher activities [6,7]. It has been demonstrated, both theoretically [8] and experimentally [9], that hydrogen chemisorbs on defect sites associated with small Au particles. Despite the low activity exhibited by Au catalysts, the possibility of a selective partial hydrogenation has untapped potential. In this paper, we address this by examining selective nitroarene hydrogenation over alumina supported Au. Aromatic amino compounds are extensively used as intermediates, *e.g. p*-aminophenol and *o*-, *m*- and *p*-toluidines in pharmaceuticals [10] and haloamines in pesticides, herbicides and dyes [11]. The hydrogenation of nitroarenes over Pd or Pt can result in high conversions but 100 % selectivity to the corresponding amino compound has not been achieved [12]. We have reported previously the results of the hydrogenation of a series of halonitro-aromatics over Au [7,13] and Ni [14] catalysts in continuous flow gas phase operation. In that work, we recorded a reaction exclusivity in terms of -NO_2 reduction but low conversions over Au, a higher activity associated with

Ni but an appreciable time on-stream deactivation. We have extended that study to consider the catalytic action of Au-Ni bimetallics as a means of controlling selectivity while achieving higher conversions through a possible surface Au-Ni synergism. There is a dearth of literature dealing with the catalytic implications of Ni–Au combinations, which is the focus of this study. Nevertheless, it is worth highlighting the work of Molenbroek *et al.* [15,16] who reported an improved stability over Ni–Au/SiO_2 compared to Ni/SiO_2 in butane steam reforming, which they ascribed to the formation of a Ni–Au surface alloy that served to limit coke deposition and prolong catalytic activity. Triantafyllopoulos and Neophytides [17] and Chin *et al.* [18] have also noted that the addition of Au to Ni/YSZ and Ni/$MgAl_2O_4$, respectively, served to suppress carbon deposition during methane steam reforming.

A move from mono- to bi-metallic catalysis has proved an effective means of influencing selectivity [19-22] and catalyst stability [23,24] in the hydrogenation of aromatic nitro compounds, a response that extends to hydrogen treatment over supported bimetallic clusters containing gold. Choudhary and co-workers [25], studied the (gas phase) hydrogenation of acetylene and reported an enhanced selectivity to ethylene (by up to a factor of 5) over Au-Pd/TiO_2 relative to Pd/TiO_2. Del Angel *et al.* [26], studying the conversion of carvone over Pt/SiO_2, quoted an increase in carvomenthone selectivity upon Au incorporation. Pawelec *et al.* [27], studying the hydrotreatment of naphthalene over Pt-Pd/SiO_2-Al_2O_3 and Au-Pt-Pd/SiO_2-Al_2O_3 recorded a higher activity due to Au addition and attributed this effect to a modification of the reactant/surface interaction(s). Yuan *et al.* [28,29] have recently reported a surface synergy associated with oxide supported Au-Ni prepared by co-impregnation and co-deposition/precipitation that resulted in a significant enhancement of hydrodechlorination activity. In order to achieve an appreciable modification to catalyst performance both metals must be in close proximity (if not in direct contact) on the support and catalyst preparation is critical [30]. The synthesis of bimetallic catalysts can either involve (a) simultaneous loading of both metals precursors by, for example, co-deposition/precipitation or co-impregnation or (b) a successive introduction, typically by impregnation [31]. Catalyst activation is a crucial variable that influences metal particle mobility and bimetallic formation on the support [32]. In this study we report, for the first time, the gas phase hydrogenation of *m*-dinitrobenzene (*m*-DNB) over Au/Al_2O_3, Ni/Al_2O_3 and Au-Ni/Al_2O_3 (prepared by the reductive deposition of Au onto Ni) and demonstrate a high degree of control in terms of reaction selectivity where

product composition can be adjusted (or tuned) by switching from mono- to bi-metallic catalysts.

9.2 Experimental

9.2.1 Catalyst Preparation and Activation

The Al_2O_3 support (Puralox) was obtained from Condea Vista Co. and used as received. Ni/Al_2O_3 (10 mol %) was prepared by impregnation where a 2-butanolic $Ni(NO_3)_2$ solution (0.6 cm^3 g^{-1}) was added dropwise at 353 K to the substrate with constant agitation (600 rpm) and oven dried at 393 K for 12 h. The $Au\text{-}Ni/Al_2O_3$ precursor was prepared by first reducing Ni/Al_2O_3 in a stream of H_2 at 2 K min^{-1} to 723 ± 1 K, which was maintained for 2.5 h. The gas flow was switched to He and cooled to room temperature, at which point the sample was passivated in 1% v/v O_2/He. This treatment served to provide a protective oxide layer over the surface Ni that prevented bulk oxidation upon exposure to the atmosphere. The passivated sample was contacted with a $HAuCl_4$ solution (Aldrich, 0.0025 g cm^{-3}, pH = 2) to deliver a 1/10 Au/Ni mol ratio. The slurry was heated (*ca.* 2 K min^{-1}) to 353 K and maintained under agitation (600 rpm) with a constant He purge. The solid residue was dried in a flow of He at 383 K for 3 h and stored under He in the dark at 277 K. A 1 mol % Au/Al_2O_3 sample was prepared by impregnation with $HAuCl_4$, post-treatment as above. In addition, a supported Au-Ni alloy was generated by annealing the bimetallic at 1273 K, as reported in detail elsewhere [33]; the Au/Al_2O_3 and Ni/Al_2O_3 samples also underwent the same annealing for comparison purposes. Prior to use in catalysis, the catalyst precursors (sieved into a batch of 75 μm average particle diameter) were activated in 60 cm^3 min^{-1} H_2 at 2 K min^{-1} to 723 K (Ni/Al_2O_3) or 603 K (Au/Al_2O_3 and $Au\text{-}Ni/Al_2O_3$). The metal contents (accurate to within ± 2%) were measured by inductively coupled plasma-optical emission spectrometry (ICP-OES, Vista-PRO, Varian Inc.) from the diluted extract of aqua regia. A physical mixture of Au/Al_2O_3 + Ni/Al_2O_3 (1/10 Au/Ni mol ratio) was also examined.

9.2.2 Catalyst Characterization

BET surface area, temperature programmed reduction (TPR) and H_2 chemisorption were determined using the commercial CHEM-BET 3000 (Quantachrome) unit. The samples were loaded into a U-shaped Quartz cell (100 mm ×

3.76 mm i.d.) and heated in 17 cm^3 min^{-1} 5% v/v H_2/N_2 (Brooks mass flow controlled) at 2 K min^{-1} to a final temperature of 723 K (Ni/Al_2O_3) or 603 K (Au/Al_2O_3 and Au-Ni/Al_2O_3). The effluent gas passed through a liquid N_2 trap and changes in H_2 consumption were monitored by a thermal conductivity detector, with data acquisition/manipulation using the TPR Win™ software. The reduced samples were maintained at the final temperature until the signal returned to baseline, swept with a 65 cm^3 min^{-1} flow of N_2 for 1.5 h, cooled to room temperature and subjected to H_2 chemisorption using a pulse (10-50 μl) titration procedure. The sample was thoroughly flushed in N_2 and subjected to a temperature programmed desorption (TPD) at 50 K min^{-1} to 873 K. BET areas were recorded with a 30% v/v N_2/He flow; pure N_2 (99.9%) served as the internal standard. At least two cycles of N_2 adsorption-desorption in the flow mode were employed to determine total surface area using the standard single point BET method. Pore volume measurements were performed using the commercial Micromeritics Flowsorb II 2300 unit. Prior to analysis, the samples were outgassed at 423 K for 1 h in 20 cm^3 min^{-1} N_2. Total pore volume was obtained at a relative N_2 pressure of P/P_0 = 0.95. H_2 uptake, BET surface areas and pore volumes were reproducible to within ± 5% and the values quoted in this paper are the mean.

Diffuse reflectance UV-Vis (DRS UV-Vis) measurements were conducted using a Perkin Elmer Lambda 35 UV-Vis Spectrometer, where $BaSO_4$ powder served as reference. Absorption profiles were calculated from the reflectance data using the Kubelka-Munk function. Powder X-ray diffractograms were recorded on a Bruker/Siemens D500 incident X-ray diffractometer using Cu Kα radiation. The samples were scanned at a rate of 0.02º $step^{-1}$ over the range $20º \leq 2\theta \leq 90º$ (scan time = 5 s $step^{-1}$). Diffractograms were identified using the JCPDS-ICDD reference standards, *i.e.* γ-Al_2O_3 (10-0425), Au (04-0784) and Ni (04-0850), and Ref. [34] for the Au-Ni alloy. Metal particle size (d_{hkl}) was estimated using the Scherrer equation:

$$d_{hkl} = \frac{K \cdot \lambda}{\beta \cdot \cos\theta} \qquad \textbf{(9.1)}$$

where K = 0.9, λ is the incident radiation wavelength (1.54056 Å), β is the peak width at half the maximum intensity and θ represents the diffraction angle corresponding to the main plane associated with metallic Au (2θ = 38.1°), Ni (2θ = 44.5°) and Au-Ni

alloy (2θ = 42.8°). Transmission electron microscopy analysis was conducted using a JEOL JEM 2011 HRTEM unit with a UTW energy dispersive X-ray detector (EDX) detector (Oxford Instruments) operated at an accelerating voltage of 200 kV and using Gatan DigitalMicrograph 3.4 for data acquisition/manipulation. The specimens were prepared by dispersion in acetone and deposited on a holey carbon/Cu grid (300 Mesh). Up to 300 individual metal particles were counted for each catalyst and the surface area-weighted metal diameter (d_{TEM}) was calculated from

$$d_{TEM} = \frac{\sum_i n_i d_i^3}{\sum_i n_i d_i^2} \qquad (9.2)$$

where n_i is the number of particles of diameter d_i. X-ray photoelectron spectroscopic (XPS) analyses were conducted using a VG ESCA spectrometer equipped with monochromatized Al Kα radiation (1486 eV). Prior to analysis, a sample of activated/passivated catalyst was adhered to a conducting carbon tape, mounted in the sample holder and subjected to ultra-high vacuum conditions (*ca.* 10^{-9} Torr) overnight. Full range surveys (0–1000 eV) and high resolution spectra of Au $4f_{5/2}$ and $4f_{7/2}$ were collected. The C 1s peak, centred at 284.5 eV was used as reference to calibrate the binding energy values. Peak deconvolution was performed using Gaussian line shapes (OriginLab 7.5). The accuracy of the reported binding energies was better than ± 0.1 eV.

9.2.3 Catalysis Procedure

Reactions were carried out under atmospheric pressure, *in situ* immediately after activation, in a fixed bed vertical continuous flow glass reactor (l = 600 mm, i.d. = 15 mm) at T = 473 K. The catalytic reactor, and operating conditions to ensure negligible heat/mass transport limitations, have been fully described elsewhere [35] but some features, pertinent to this study, are given below. A preheating zone (layer of borosilicate glass balls) ensured that the organic reactant was vaporized and reached the reaction temperature before contacting the catalyst. Isothermal conditions (± 1 K) were maintained by thoroughly mixing the catalyst with ground glass (75 μm) before insertion into the reactor. The temperature was continuously monitored by a thermocouple inserted in a thermowell within the catalyst bed. A butanolic solution of

m-DNB was delivered, in a co-current flow of H_2, *via* a glass/teflon air-tight syringe and a teflon line, using a microprocessor controlled infusion pump (Model 100 kd Scientific) at a fixed calibrated flow rate, with an inlet -NO_2 molar flow ($F_{\text{-}NO_2}$) over the range 0.1-0.2 $\text{mmol}_{\text{-}NO_2}\ \text{h}^{-1}$ where the molar metal to inlet molar -NO_2 feed rate ratio spanned the range $0.5\times10^{-2} - 2.5\times10^{-2}$ h. The H_2 content was far in excess of the stoichiometric requirement, the flow rate of which was monitored using a Humonics (Model 520) digital flowmeter; $GHSV = 2 \times 10^4\ \text{h}^{-1}$. In a series of blank tests, passage of *m*-DNB in a stream of H_2 through the empty reactor or over the support alone, *i.e.* in the absence of Au and/or Ni, did not result in any detectable conversion. The reactor effluent was frozen in a liquid nitrogen trap for subsequent analysis which was made using a Perkin-Elmer Auto System XL gas chromatograph equipped with a programmed split/splitless injector and a flame ionization detector, employing a DB-1 50 m × 0.20 mm i.d., 0.33 μm film thickness capillary column (J&W Scientific), as described elsewhere [36]. *m*-DNB and *m*-nitroaniline (*m*-NAN) (Aldrich, ≥ 98%), *m*-phenylenediamine (*m*-PDM) (Fluka, ≥ 95%) and the solvent (*1*-butanol: Riedel-de Haën) were used as supplied without further purification. Hydrogenation activity is expressed in terms of the degree of nitro-group reduction ($x_{\text{-}NO_2}$)

$$x_{\text{-}NO_2} = \frac{[\text{-NH}_2]_{out}}{[\text{-NO}_2]_{in}} = \frac{2\times[m\text{-PDM}]_{out} + [m\text{-NAN}]_{out}}{2\times[m\text{-DNB}]_{in}} \qquad \textbf{(9.3)}$$

where [*m*-DNB], [*m*-NAN] and [*m*-PDM] are, respectively, the concentrations of *m*-DNB, *m*-NAN and *m*-PDM; the subscripts *in* and *out* refer to the inlet and outlet streams. Catalyst activity is also quantified in terms of fractional conversion of *m*-DNB ($x_{m\text{-}DNB}$)

$$x_{m\text{-}DNB} = \frac{[m\text{-DNB}]_{in} - [m\text{-DNB}]_{out}}{[m\text{-DNB}]_{in}} \qquad \textbf{(9.4)}$$

while selectivity in terms of (*e.g.*) *m*-PDM ($S_{m\text{-}PDM}$) is given by

$$S_{m\text{-}PDM} = \frac{[m-\text{PDM}]_{out}}{[m\text{-DNB}]_{in} - [m\text{-DNB}]_{out}} \qquad \textbf{(9.5)}$$

9.3 Result and Discussion

9.3.1 Catalyst Characterization

9.3.1.1 TPR/BET-pore volume

The TPR activation profiles are presented in **Figure 9.1** for the Au/Al_2O_3 (profile I) and Ni/Al_2O_3 (profile II) precursors; the associated maximum temperatures (T_{max}) in terms of H_2 consumption are given in **Table 9.1**.

Table 9.1: Metal loading, characteristic temperature programmed reduction (TPR) T_{max} values, BET surface areas, pore volumes, H_2 uptake/desorbed (TPD), XPS binding energies, metal particle size (range and mean), DRS UV-Vis spectroscopic characteristics and pseudo-first order rate constants (k) for the reduction of *m*-DNB (to *m*-NAN and/or *m*-PDM) associated with Au/Al_2O_3, Ni/Al_2O_3 and $Au\text{-}Ni/Al_2O_3$.

		Au/Al_2O_3	Ni/Al_2O_3	$Au\text{-}Ni/Al_2O_3$
Metal loading (mol %)		1	10	Au (1) Ni (10)
TPR T_{max} (K)		434[a]	595[a], 723[a], 490[b]	446[a], 603[a]
BET area ($m^2\ g^{-1}$)		161	141	143
Pore Volume ($10^{-3}\ cm^3\ g^{-1}$)		427	203	195
H_2 uptake ($\mu mol\ g_{catalyst}^{-1}$)		0.4	3.6	1.1
TPD	T_{max} (K)	-	873[c,d]	797[c], 873[d]
	$H_{2\ desorbed}$ ($\mu mol\ g_{catalyst}^{-1}$)	-	6[c], 83[d]	56[c],181[d]
XPS Au binding energies (eV)	$4f_{5/2}$	87.6	-	87.9
	$4f_{7/2}$	84.0	-	84.3
Metal particle size range (nm)[e]		1-20	5-50	1-50
d_{TEM} (nm)[e]		9	31	20
d_{hkl} (nm)[f]		18[g] (37)[h]	29[g] (35)[h]	23[h,i]
DR UV-Vis A_{max} (nm)		540[g] (540)[h]	485[g] (530-580)[h]	500[g] (-)[h,j]
k ($10^2\ mmol_{-NO_2}\ mol_{metal}^{-1}\ h^{-1}$)		61	221	264

[a] T_{max} associated with the TPR of the catalyst precursors
[b] T_{max} associated with TPR of the passivated/reduced Ni/Al_2O_3
[c] values associated with 1st H_2-TPD peak
[d] values associated with 2nd H_2-TPD peak
[e] based on TEM analysis (see **Equation 9.2**)
[f] based on XRD line broadening analysis (see **Equation 9.1**)
[g] post-activation at 723 K (Ni/Al_2O_3) and 603 K (Au/Al_2O_3 and $Au\text{-}Ni/Al_2O_3$)
[h] post-thermal treatment to 1273 K (see Experimental section)
[i] XRD response based on peak at $2\theta = 42.8°$
[j] DRS UV-Vis analysis did not generate any distinguishable peak(s)

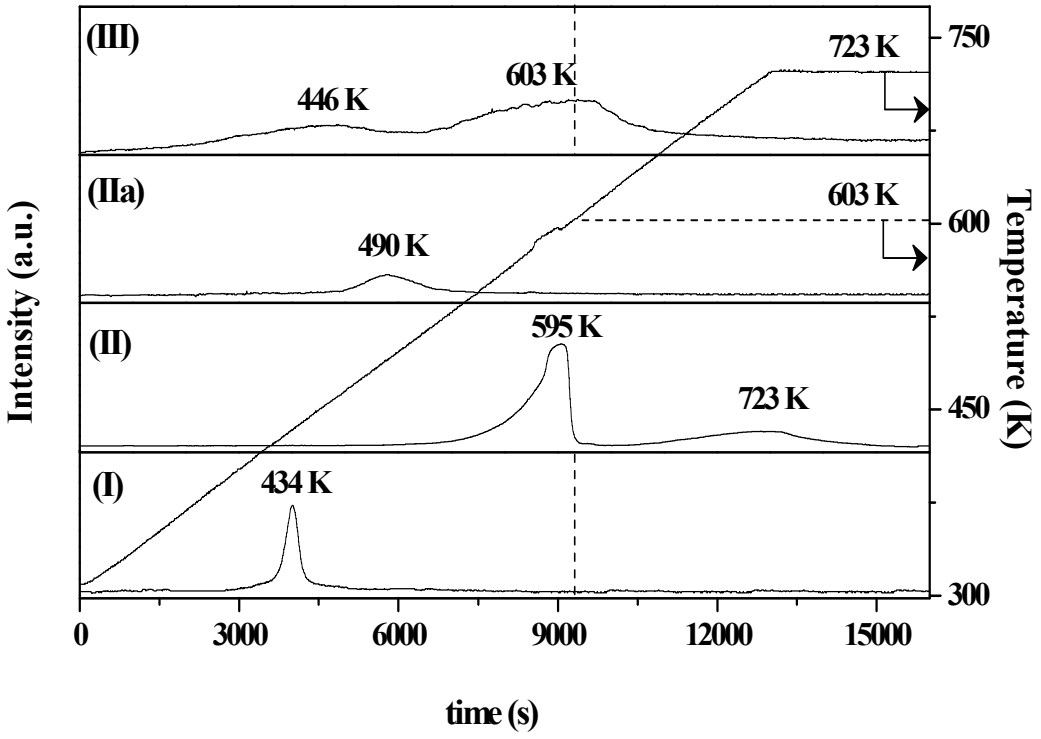

Figure 9.1: TPR profiles generated for (I) Au/Al_2O_3 and (II) Ni/Al_2O_3 precursors, II(a) passivated/reduced Ni/Al_2O_3 and (III) $Au\text{-}Ni/Al_2O_3$. Dashed lines represent final activation temperature (603 K) for the Au containing catalysts.

The reduction profile for Au/Al_2O_3 is characterised by a single positive peak at 434 K that can be attributed to the reduction of Au^{3+} to Au^0 [13,37]. The TPR profile generated for the direct reduction of Ni/Al_2O_3 delivered a H_2 consumption peak at 595 K with a secondary peak at the final reduction temperature (T = 723 K), followed by a return to baseline. This response can be ascribed to a stepwise decomposition of nickel nitrate to NiO with subsequent reduction to Ni^0 [38-40]. The Au-Ni bimetallic was prepared by introducing Au to pre-reduced and passivated Ni/Al_2O_3. The passivation step serves to provide a protective oxide overlayer on the supported Ni particles that is readily removed during a subsequent TPR at 490 K (see profile IIa in **Figure 9.1**). Such a relatively facile removal of the passivation layer as distinct from the reduction of supported NiO has been established and discussed previously [14]. For bimetallic samples prepared by a direct redox method, a metal of lower electrochemical potential (ECP) is employed to reduce the deposited metallic precursor with a higher potential [41], an effect that has been demonstrated for gold deposited on Pd [42] and Pt [43,44]. In this study, Ni (ECP = -0.27) serves to reduce the gold precursor ($HAuCl_4$, ECP = 1.00) [45]. The activation profile for $Au\text{-}Ni/Al_2O_3$ is characterised by a low intensity H_2 consumption response with two ill-defined peaks at 446 and 603 K (see profile III in

Figure 9.1). Venugopal and co-workers [46], studying Au-Ni/Fe_2O_3 (prepared by deposition co-precipitation using chloroauric acid, ferric and nickel nitrate solutions) reported the appearance of two peaks at 423 K and 483 K during TPR that they associated with the concurrent reduction of gold and nickel oxidic species and the partial reduction of the support. Chang *et al.* [47] associated a positive TPR peak at 433 K for Au-Ru/Fe_2O_3, to the coupled reduction of oxidic Au and Ru species, where the shift to higher reduction temperature in the bimetallic system (when compared with Au/Fe_2O_3 (375 and 411 K) and Ru/Fe_2O_3 (416 K)) was ascribed to interactions between Au and Ru. The BET areas of the activated catalysts (**Table 9.1**) were lower than that of the starting Al_2O_3 support (190 m^2 g^{-1}) with a reduction in pore volume that can be attributed to a partial pore blockage by the supported metal(s).

9.3.1.2 H_2 Chemisorption/TPD

Room temperature hydrogen uptake values are provided in **Table 9.1**. The value obtained for Au/Al_2O_3 was close to the instrumental detection limits, confirming the low capacity of Au to chemisorb H_2 [32]. While the nature of H_2-Au interactions in supported systems has not yet been well established, the consensus that emerges suggests a high activation energy barrier required for dissociative adsorption [48], where uptake is dependent on the nature of Au coordination to the support [3]. Any dissociative chemisorption of H_2 appears to occur on low coordination sites of the Au particles, *i.e.* at edges and corners [8,9,49]. The addition of Au to Ni/Al_2O_3 resulted in a significant reduction in H_2 uptake, a response that suggests some surface Au-Ni interaction which serves to inhibit H_2 chemisorption. An adsorption site "blocking effect" has been recently reported in the literature for bimetallic catalysts where Au was incorporated as the second metal [28,50]. Bonarowska *et al.* [42], working with Pd/SiO_2 doped with Au, associated their observed decrease in H_2 chemisorption to a lower metal dispersion. The opposite effect has also been observed, where Chimentão *et al.* [51] recorded a higher H_2 uptake on Ir-Au/γ-Al_2O_3 compared with Ir/γ-Al_2O_3 that they ascribed to (a) spillover hydrogen from Ir to adjacent Au sites or (b) an electronic modification of the Ir sites induced by Au which impacted on H_2 adsorption. In order to further probe possible modifications to H_2/surface interactions due to the incorporation of Au, H_2 temperature programmed desorption (H_2-TPD) was monitored and the results for Ni/Al_2O_3 (profile I) and Au- Ni/Al_2O_3 (profile II) are presented in **Figure 9.2**, with the corresponding T_{max} values and associated H_2 release given in **Table 9.1**.

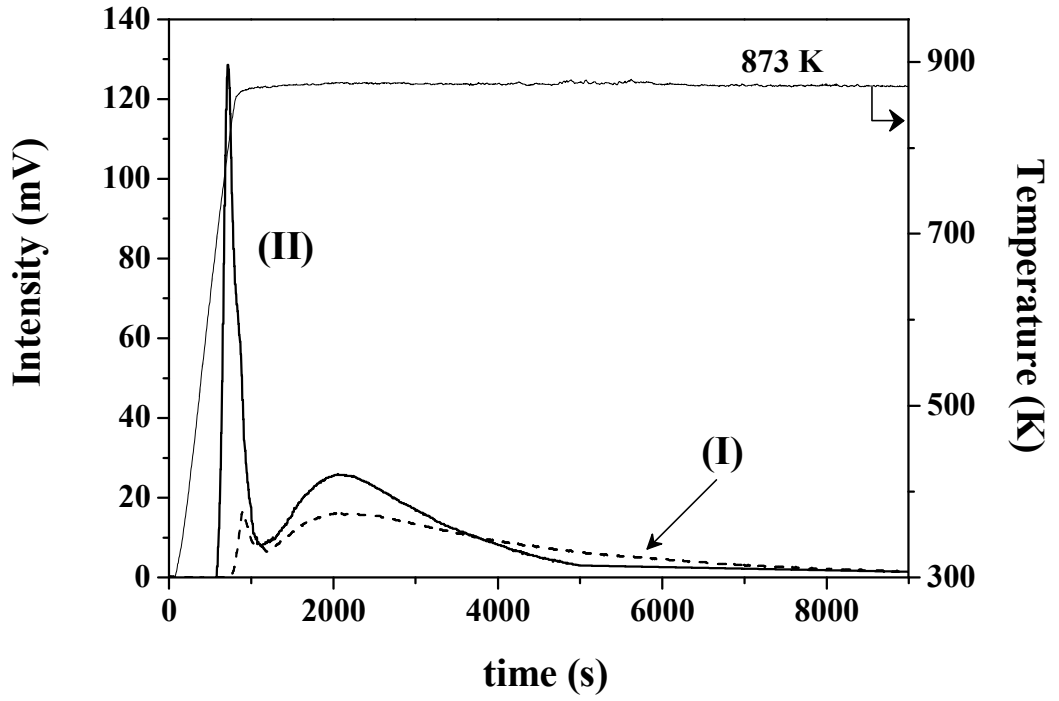

Figure 9.2: H_2 TPD profiles associated with (I, dashed line) Ni/Al_2O_3 and (II, solid line) Au-Ni/Al_2O_3.

In both profiles, two stages of desorption are in evidence, *i.e.* where $T < 873$ K and extending into the final isothermal hold (873 K). It should be noted that the total amount of H_2 desorbed was appreciably greater (by a factor of up to 200) than that taken up in the chemisorption step which preceded H_2-TPD (see **Table 9.1**). This response suggests the occurrence of hydrogen spillover during the activation step. Hydrogen spillover is the result of dissociative H_2 chemisorption to generate H atoms which migrate from the metal to the support [52] and has been linked to H_2-TPD peaks at temperatures in excess of 503 K, regardless of the metal or support [53]. In the specific case of Ni/Al_2O_3, TPD signals recorded at 550 K [54], 673 K [55], 720 K [56] and 820 K [56] have been attributed to the desorption of spillover hydrogen. It is significant that the total amount of hydrogen released from Au-Ni/Al_2O_3 is significantly greater than that recorded for Ni/Al_2O_3, which suggests some Au/Ni surface synergism that impacts on H_2 adsorption/desorption dynamics. An exhaustive search through the published work has failed to unearth any directly comparable H_2-TPD analysis for supported Au-Ni. It is, however, worth flagging the work of Espinosa *et al.* [43], who observed the opposite effect for Au-Pt/Al_2O_3, *i.e.* a decrease in the amount of H_2 released during TPD in the case of the bimetallic, which they explained on the basis of a blocking effect by Au of

the Pt surface sites. We observe a shift in the first TPD peak for Au-Ni/Al_2O_3 to a lower temperature (by *ca.* 80 K) with a marked increase in the H_2 desorbed (by up to a factor of 9) when compared with Ni/Al_2O_3, suggesting a more facile (less energetically demanding) release of a greater volume of H_2. These results find indirect support in the work of Holmblad and co-workers [57] who quoted a decrease in the desorption energy of deuterium from Au-Ni films with increasing Au coverage (0→0.7 ML). Greeley and Mavrikakis [58,59], using density functional theory calculations, demonstrated that in the case of a "near-surface alloy structure", hydrogen binds more weakly than it does on the individual metals, *i.e.* more facile H_2 desorption. Our chemisorption/TPD results demonstrate that the incorporation of Au with Ni/Al_2O_3 inhibits room temperature H_2 uptake but results in an increase in surface hydrogen generated during TPR, a response that we take to be indicative of Au-Ni interaction.

9.3.1.3 TEM/XPS

Representative (a) low, (b) medium and (c) high resolution TEM images of Au/Al_2O_3 (I), Ni/Al_2O_3 (II) and Au-Ni/Al_2O_3 (III) are given in **Figure 9.3.** Metal particle size distributions, based on TEM analysis, are presented as histograms in **Figure 9.4**. The TEM images of Au/Al_2O_3 reveal a well dispersed metal phase where the particles exhibit a near spherical morphology. There was some evidence of particle faceting in the case of Ni/Al_2O_3 (see **Figure 9.3** image IIc), an effect that is indicative of metal/support interactions [60]. The diffractogram patterns for single particles are included as insets in **Figure 9.3** Ic (Au/Al_2O_3) and **Figure 9.3** IIc (Ni/Al_2O_3). The *d*-spacings (0.23/0.20 and 0.20 nm) between the planes in the atomic lattice are consistent with the (111) and (200) planes of metallic gold (JCPDS-ICDD 04-0784) and the (111) plane of nickel (JCPDS-ICDD 04-0850). The metal particles associated with Au/Al_2O_3 present a narrower size distribution when compared with Ni/Al_2O_3 to give surface area weighted mean particle sizes of 9 and 31 nm, respectively (see **Table 9.1**). Both catalysts present a bimodal size distribution (see histograms I and II in **Figure 9.4**) with an appreciable component (50%) of metal particles in Au/Al_2O_3 ≤ 5 nm, the Au particle size range that has been proposed as critical for catalytic activity in hydrogen mediated reactions [3,61]. The Ni/Al_2O_3 catalyst exhibits a broad size distribution as has been established elsewhere for oxide supported Ni prepared by impregnation [62,63]. The Au-Ni/Al_2O_3 catalyst is characterised by a size distribution and mean value that falls between that obtained for both the monometallic catalysts. Our TEM analysis serves to rule out any significant metal sintering following Au incorporation.

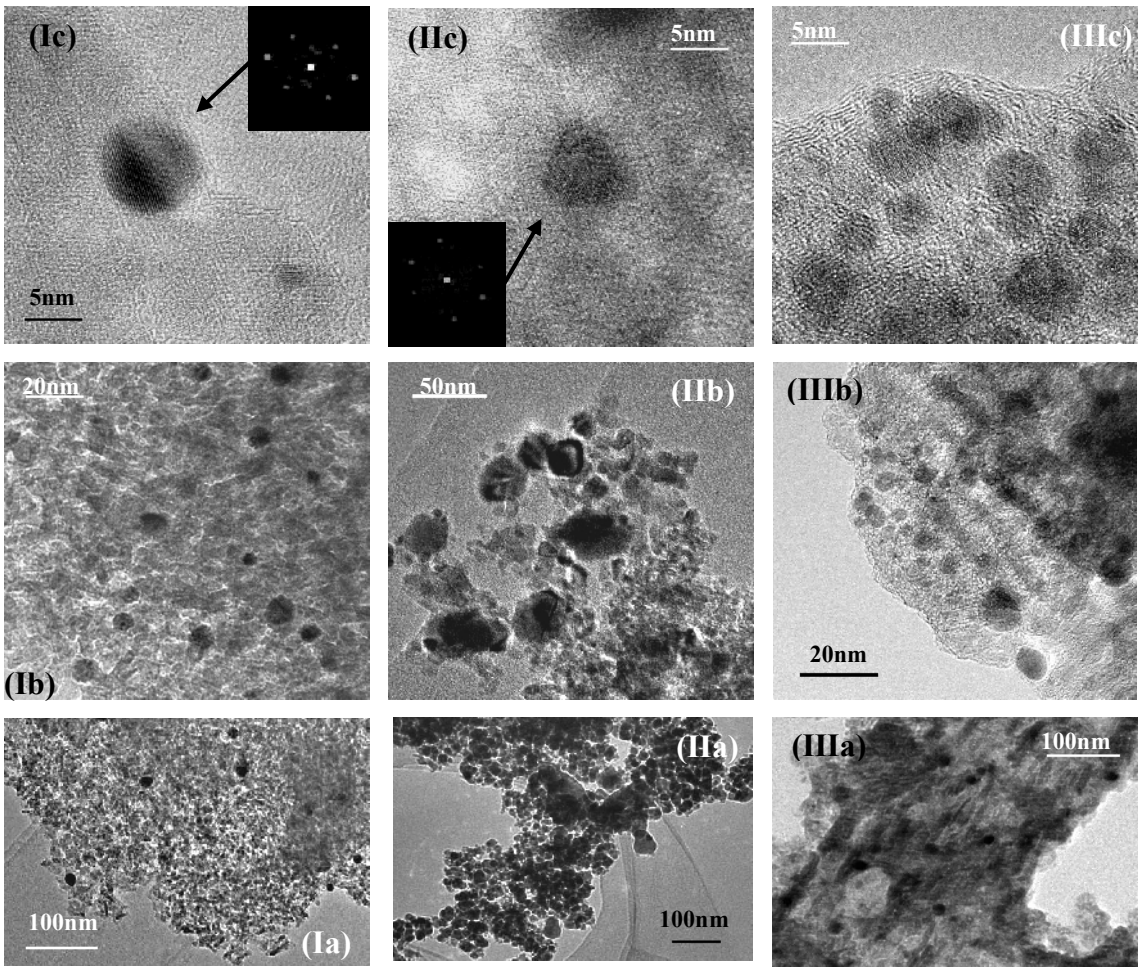

Figure 9.3: Representative TEM images of passivated/reduced (I) Au/Al_2O_3, (II) Ni/Al_2O_3 and (III) $Au\text{-}Ni/Al_2O_3$; (a) low, (b) medium and (c) high magnification.

The presence of residual surface chloride, which may result from the activation of the Cl-containing Au precursor, has been reported to induce surface migration leading to metal particle agglomeration [64,65]. This effect has been observed [66] in the case of $Pt\text{-}Au/SiO_2$ where the generation of $AuCl_4^-$ ions resulted in a sintering of Pt particles but such a response does not appear to be prevalent in our study. It is, nonetheless, possible that the addition of Au caused a re-dispersion of Ni particles, an effect previously observed for $Au\text{-}Pt\text{-}Pd/SiO_2\text{-}Al_2O_3$ [27] and $Ni\text{-}Au/SiO_2$ (Ni/Au mol ratio = 38) [15].

Menegazzo *et al.* [67] have recently reported that in the case of supported (ZrO_2 and CeO_2) Au, Pd and Au-Pd catalysts (prepared by impregnation), the incorporation of Au resulted in a decrease in particle size for the Pd-Au samples (based on HRTEM analysis) where Au clusters in close proximity induced changes in the Pd particles morphology and electron density (based on FTIR analysis).

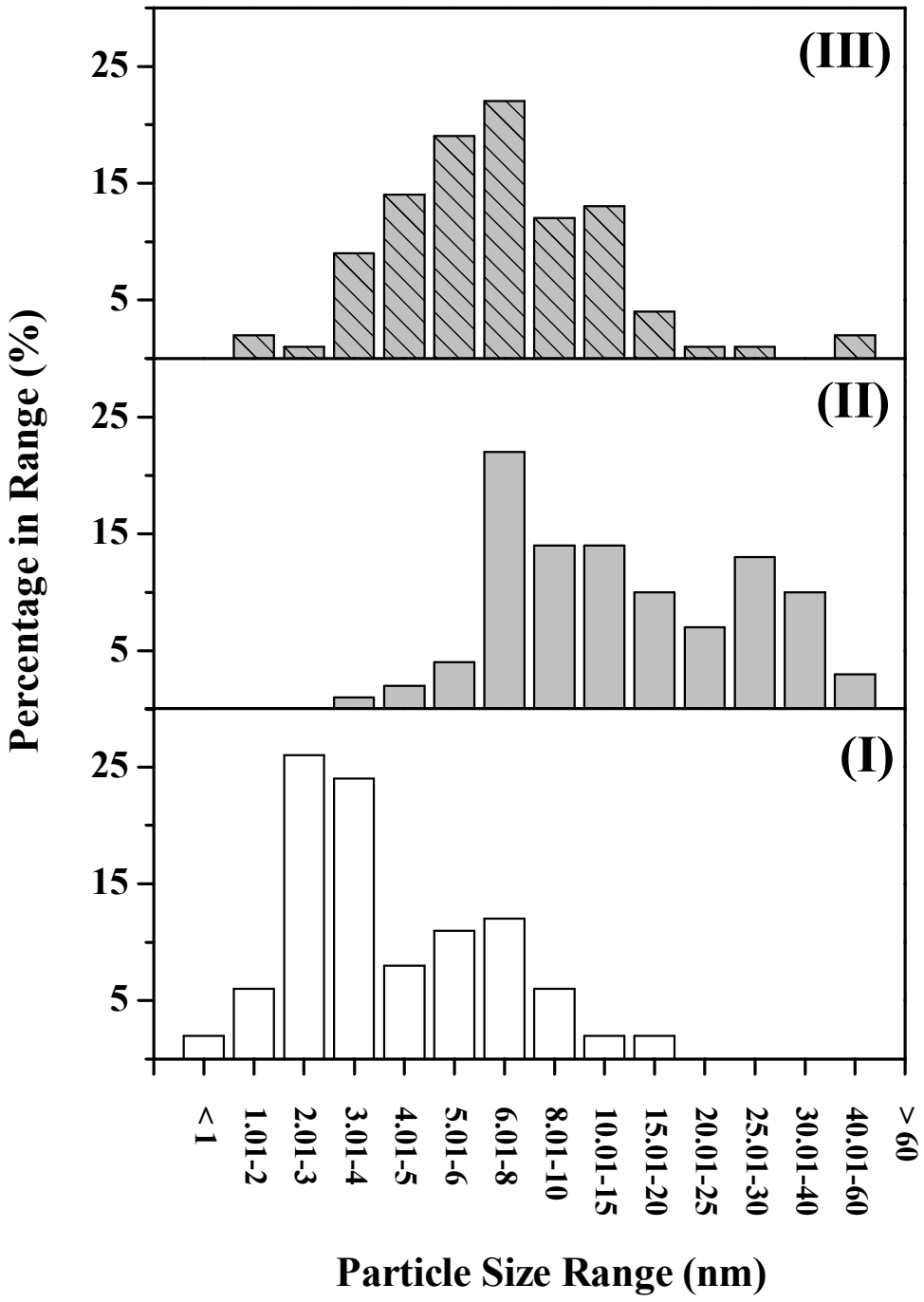

Figure 9.4: Metal particle size distributions associated with passivated/reduced (I) Au/Al_2O_3 (open bars), (II) Ni/Al_2O_3 (solid bars) and (III) Au-Ni/Al_2O_3 (hatched bars).

The surface composition of our Au-Ni/Al_2O_3 sample was probed by STEM/EDX elemental mapping. Two representative analyses are presented in **Figure 9.5**, which includes the dark field and the sample area that was mapped with the associated distribution of (a) Al, (b) O, (c) Au and (d) Ni. Repeated EDX analysis of larger sample areas (4×10^5 nm^2) delivered an average surface Ni/Au ratio = 10, which matches the bulk composition.

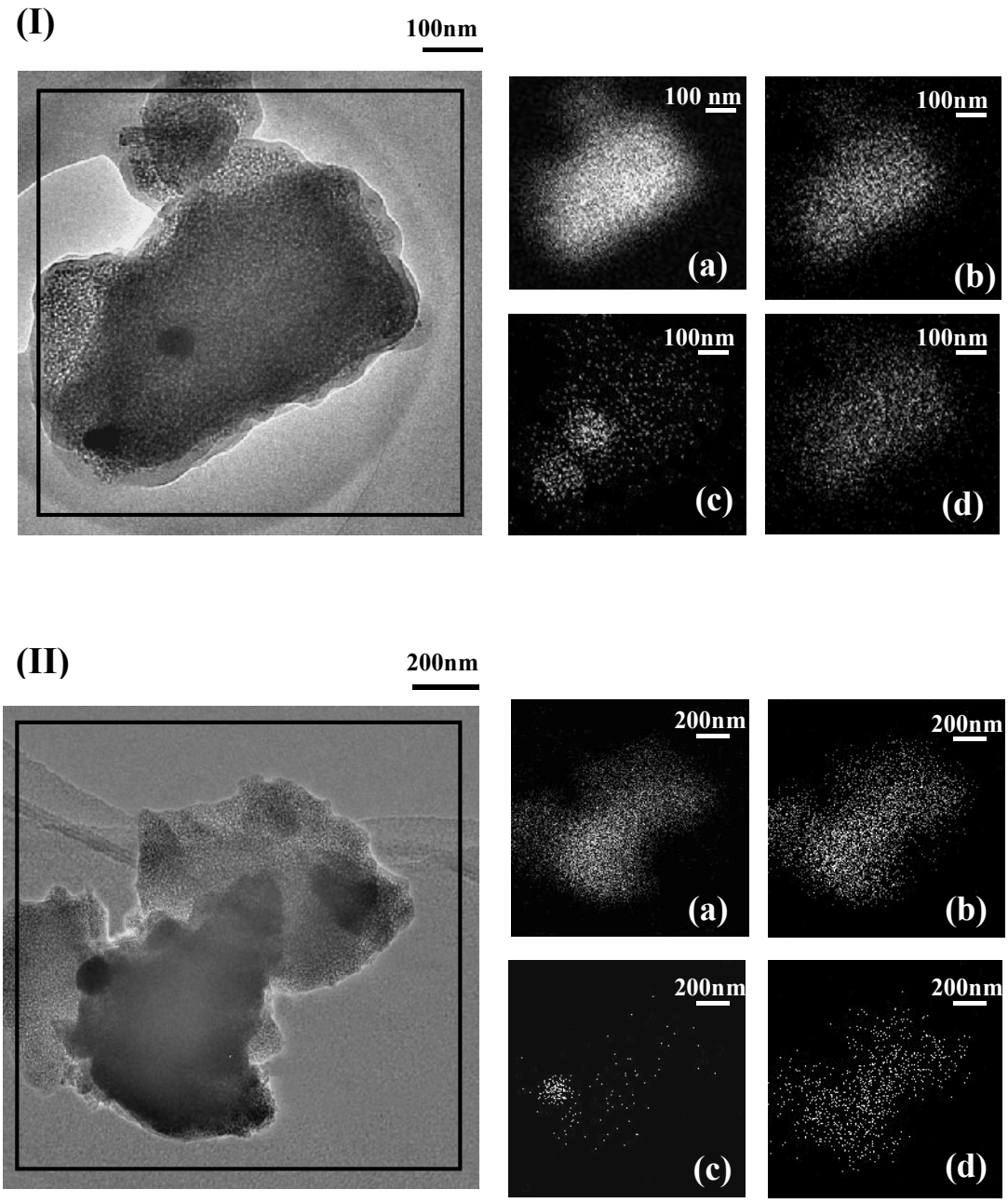

Figure 9.5: Two representative TEM/EDX analyses of passivated/reduced Au-Ni/Al_2O_3; dark field images (I) and (II) with EDX maps illustrating the distribution of (a) Al, (b) O, (c) Au and (d) Ni.

The detailed EDX mapping over smaller areas (see **Figure 9.5**) reveal a close proximity of Au and Ni on the surface. In the case of the Au-Ni system, the miscibility gap is such that bulk alloy formation is not possible at temperatures below 1083 K [68]. Nevertheless, it has been shown that a limited amount of Au can dissolve in Ni at lower temperatures [57], *i.e.* Au atoms can substitute Ni atoms in the outermost atomic layers to form a stable surface structure or "surface alloy". Indeed, Nielsen *et al.* [69] have

provided experimental evidence supporting the formation of a Ni-Au alloy on the surface of a Ni single crystal under conditions where there was no bulk alloy formation. Molenbroek and Nørskov [15] have reported the formation of a "superficial" (rather than bulk) Ni-Au alloy on silica after reduction at 823 K. Bond has proposed [70], in the case of Au-Pt, that particles sufficiently small (< 2 nm) can form "homogeneous alloy particles", suggesting that "complete solubility" is possible *via* pairing of the *s* electrons of each constituent metal atom, despite the wide miscibility gap in the bulk state. Our STEM/EDX analysis can not confirm or discount the possibility of surface Au-Ni alloy formation but does establish a close proximity of both metals on the Al_2O_3 carrier. XPS analysis was conducted to provide some insight into possible surface metal interactions and the spectra over the Au 4*f* binding energy region are shown in **Figure 9.6**; the associated binding energies are given in **Table 9.1**.

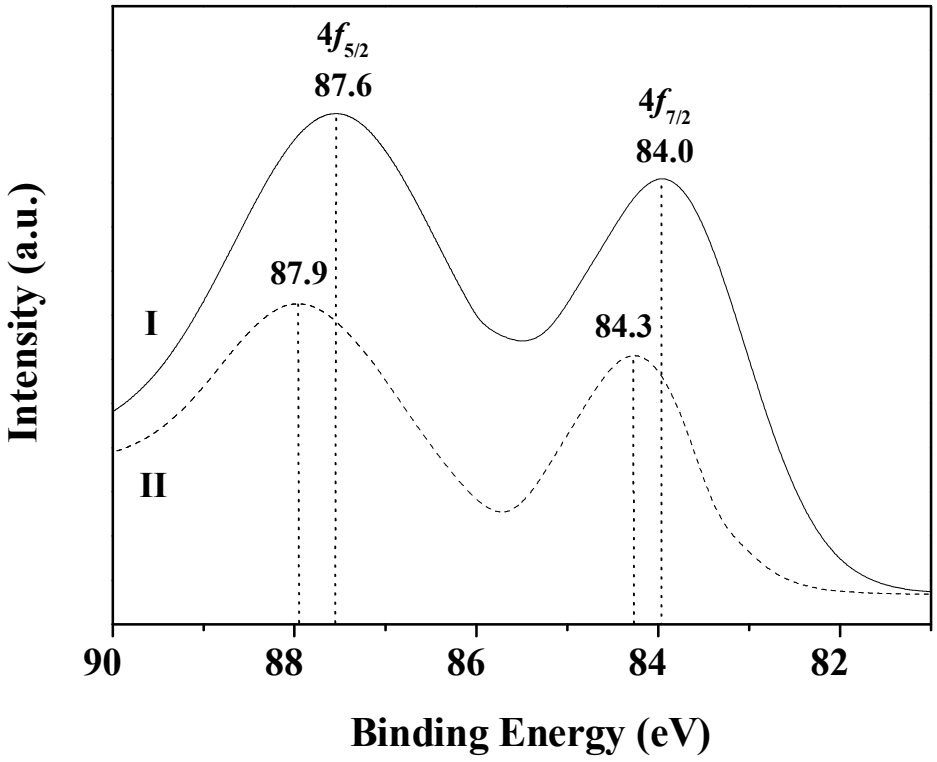

Figure 9.6: XPS spectra over the Au 4*f* region for passivated/reduced (I, solid line) Au/Al_2O_3 and (II, dashed line) $Au\text{-}Ni/Al_2O_3$. *Note:* Dotted line identifies position of the Au $4f_{5/2}$ and $4f_{7/2}$ peaks.

The XPS profile for Au/Al_2O_3 (I) exhibits two peaks with binding energies of 87.6 and 84.0 eV that can be associated, respectively, with the $4f_{5/2}$ and $4f_{7/2}$ levels of Au^0 [71,72]. The Au-Ni catalyst (profile II) also generated two peaks but at higher binding energies (by 0.3 eV). Vasil'kov *et al.* [71] ascribed a 0.3 eV shift of the Au $4f_{7/2}$ peak

for Au-Ni/SiO_2 (prepared by metal vapour deposition) to a higher binding energy to the formation of AuNiO/SiO_2, NiO/Au/SiO_2 or $AuNi_xO_y$/SiO_2 species on the surface, *i.e.* partial oxidation of Ni (to Ni^{2+}) induced by gold. Moreover, Zafeiratos and Kennou [73] and Rousset and co-workers [74], investigating Au deposition on Ni surfaces, independently proposed that positive shifts in the Au $4f_{7/2}$ binding energy are indicative of partial surface alloy formation.

9.3.1.4 XRD/DRS UV-Vis

The XRD profiles for Al_2O_3 (AI) and the passivated/reduced Au/Al_2O_3 (AII), Ni/Al_2O_3 (AIII) and Au-Ni/Al_2O_3 (AIV) are given in **Figure 9.7**.

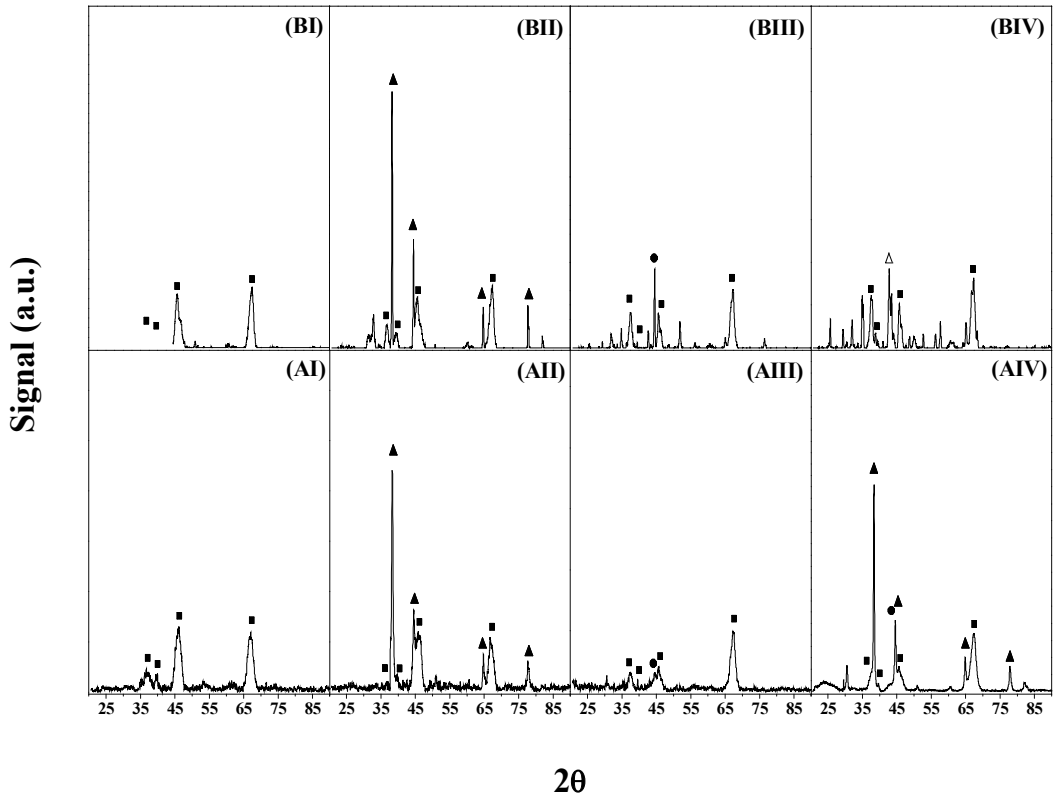

Figure 9.7: XRD patterns for the passivated/reduced samples heated to (A) catalyst activation temperature (see Experimental section) and (B) 1273 K for (I) Al_2O_3 support, (II) Au/Al_2O_3, (III) Ni/Al_2O_3 and (IV) Au-Ni/Al_2O_3. *Note*: peak assignments based on JCPDS-ICDD reference data: (■) γ-Al_2O_3 (10-0425); (▲) Au (04-0784); (●) Ni (04-0850) and [34] (Δ) Au-Ni alloy.

The diffractogram pattern for the support presents four main peaks over the 2θ range 30º-70º, corresponding to the (311), (222), (400) and (440) planes, characteristic of cubic γ-Al_2O_3 (JCPDS-ICDD 10-0425). The x-ray patterns for the monometallic catalysts exhibit, in addition to the reflections due to the support, peaks at $2\theta = 38.1°$,

44.4°, 64.7° and 77.5° (for Au/Al_2O_3) and 2θ = 44.5º (for Ni/Al_2O_3), which are consistent with the (111), (200), (220) and (311) planes of metallic Au (JCPDS-ICDD 04-0784) and the (111) plane of Ni (JCPDS-ICDD 04-0850), respectively. The XRD profile for the bimetallic $Au\text{-}Ni/Al_2O_3$ catalyst (activated at 603 K) only shows signals due to the Al_2O_3 support and metallic Au and Ni, *i.e.* there is no evidence for any Au-Ni alloy formation. In order to assess the possibility of bulk alloy formation, the passivated/reduced $Au\text{-}Ni/Al_2O_3$ catalyst was treated in flowing N_2 to 1273 K (see Experimental section), a temperature at which total bulk miscibility can be achieved [68]. Both Au/Al_2O_3 and Ni/Al_2O_3 were subjected to the same annealing treatment for comparison purposes. The resultant diffractograms for the support and both monometallic catalysts (**Figure 9.7**, BI-BIII respectively) show the characteristic signals for γ-Al_2O_3 and metallic Au and Ni, where the increase in the "sharpness" of the peaks (a lesser peak broadening) is indicative of metal particle sintering. Particle size was evaluated using the standard Scherrer line broadening analysis (**Equation (9.1)**) and the results are presented in **Table 9.1**. The annealing step resulted in an increase in metal particle size, an effect that was particularly pronounced in the case of Au/Al_2O_3. The XRD pattern for annealed $Au\text{-}Ni/Al_2O_3$ (**Figure 9.7,** BIV) did not reveal any detectable signals due to the individual metals (Au or Ni) but a new signal is observed with a characteristic $2\theta = 42.8°$ that is located between the peaks for Au^0 ($(111)_{Au}$, 2θ = 38.1°) and Ni^0 ($(111)_{Ni}$, $2\theta = 44.5°$). This new peak can be linked to the formation of a Au-Ni alloy, an assertion that finds support in the work of Togasaki *et al.* [34], who attributed an XRD peak at 2θ = 42º to amorphous Au-Ni alloy (8-51 % mol Au) prepared by addition of $KAu(CN)_2$ to a Ni-W plating bath. Alloy formation (post-annealing) is also supported by DRS UV-Vis analysis; the results are shown in **Figure 9.8**. The spectra for the activated Au/Al_2O_3 (AI) and Ni/Al_2O_3 (AII) samples are characterised by absorption bands with maximum intensity (A_{max}) at 540 nm and 485 nm, respectively, which can be assigned to zero valent Au and Ni as reported elsewhere [75,76]. The annealed monometallics generated equivalent profiles (see BI and BII). The spectrum for the activated $Au\text{-}Ni/Al_2O_3$ (AIII) is dominated by the response due to Ni but the annealed sample (BIII) did not generate any detectable peak/signal corresponding to metallic Au or Ni, which suggests alloy formation [77]. The XRD and DRS UV-Vis measurements are consistent with Au-Ni alloy formation post-annealing. While the UV-Vis response for $Au\text{-}Ni/Al_2O_3$ activated at 603 K is essentially a composite of that recorded for Au/Al_2O_3 and Ni/Al_2O_3, STEM-EDX elemental mapping

demonstrates that both metals are in close proximity while XPS and H_2-TPD measurements suggest surface Au-Ni interaction.

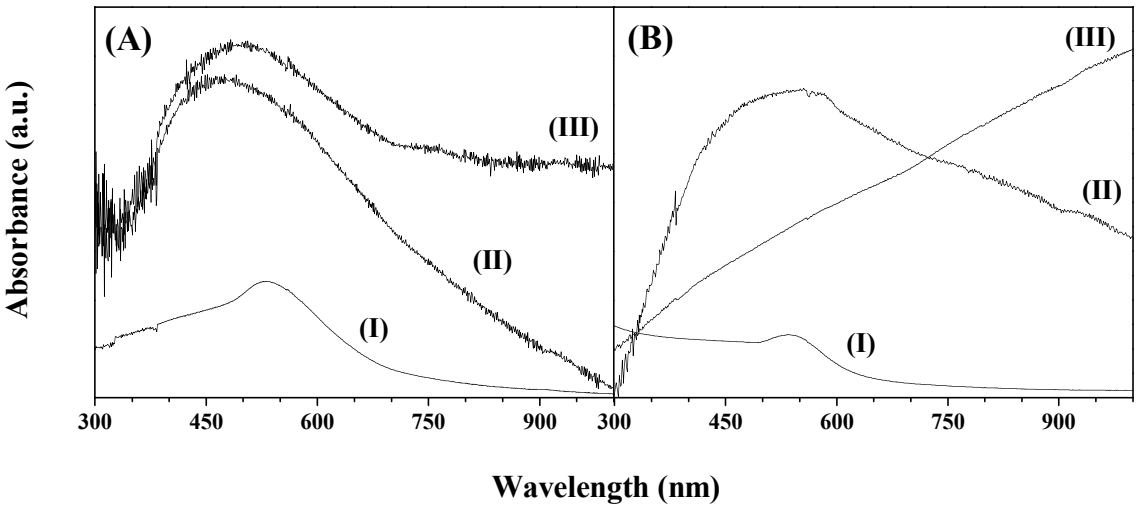

Figure 9.8: DRS UV-Vis spectra of passivated/reduced samples heated to (A) catalyst activation temperature (see Experimental section) and (B) 1273 K for (I) Au/Al_2O_3, (II) Ni/Al_2O_3 and (III) $Au-Ni/Al_2O_3$.

9.3.2 Catalytic activity/selectivity

The gas phase hydrogenation of *m*-DNB was performed over Au/Al_2O_3, Ni/Al_2O_3, $Au-Ni/Al_2O_3$ and Au/Al_2O_3+Ni/Al_2O_3 physical mixtures (Au/Ni mol ratio = 1/10). Repeated reactions with different batches of catalyst obtained from repeated sample preparations delivered conversion/selectivity data that were reproducibility to within ± 6%. This response is significant, given reports in the literature [78-80] that indicate difficulties in replicating supported Au catalyst synthesis in terms of obtaining samples with the same characteristics (notably Au particle size) and catalytic properties. The reaction pathways associated with *m*-DNB hydrogenation are shown in **Figure 9.9**. The conversion of *m*-DNB over our catalysts generated *m*-NAN (partial reduction) and/or *m*-PDM (full reduction) as the only detected products; there was no measureable hydrogenolytic activity to produce nitrobenzene, aniline or benzene. Both hydrogenation products (*m*-NAN and *m*-PDM) are important intermediates in the manufacture of polymers and dyes [81,82]. The traditional route, employing Fe in acidic media (Béchamp process), presents serious environmental problems in terms of waste (Fe/FeO sludge) production allied to low selectivites/product yields [82,83]. The alternative liquid phase batch catalytic route has been studied to a limited extent [81,83-

87] where the key challenge is the exclusive production of either *m*-NAN or *m*-PDM, *i.e.* achieving complete selectivity in terms of partial or complete -NO_2 reduction.

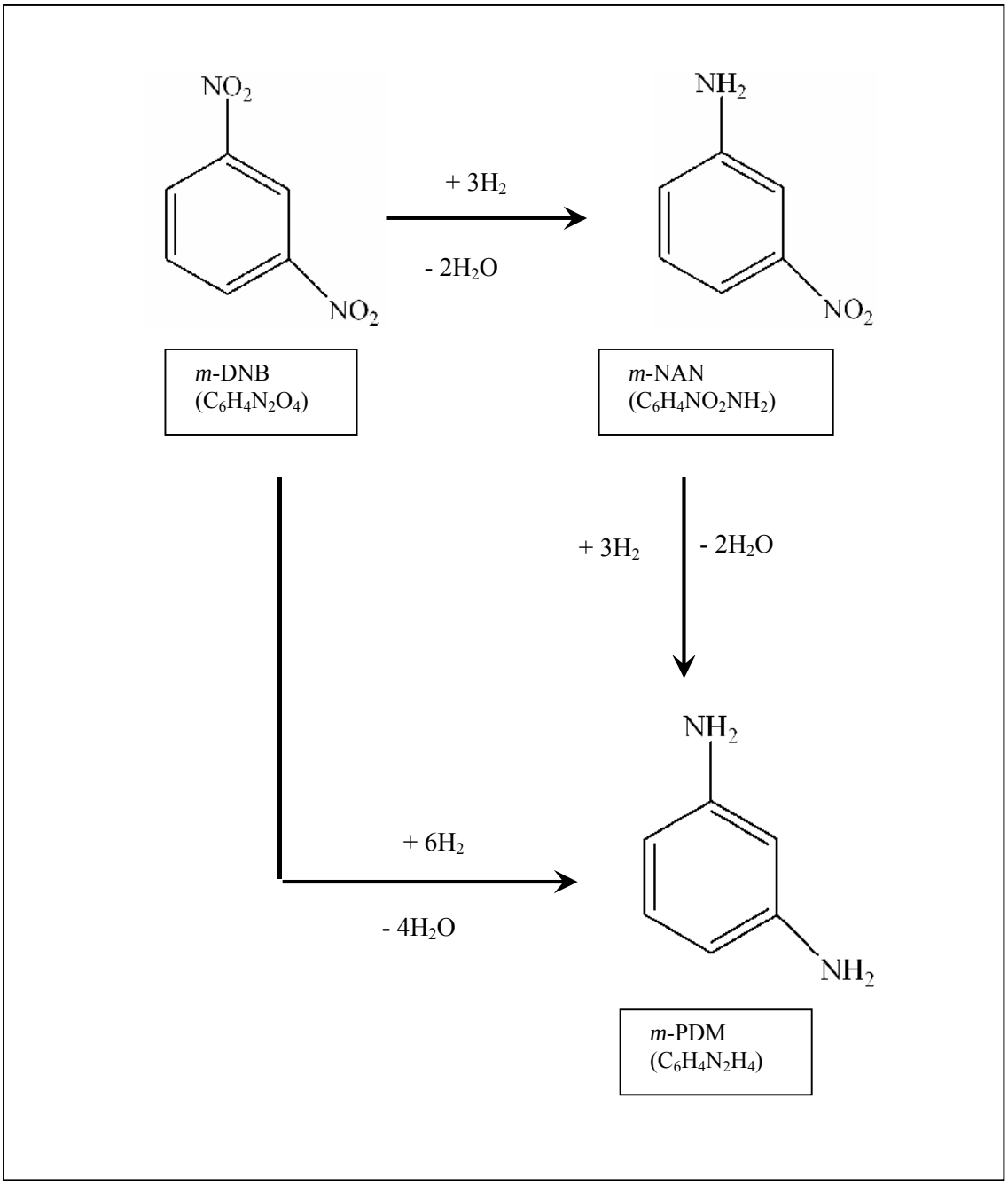

Figure 9.9: Reaction pathways associated with the hydrogenation of *m*-dinitrobenzene (*m*-DNB) to *m*-nitroaniline (*m*-NAN) and *m*-phenylenediamine (*m*-PDM).

The temporal dependence of *m*-DNB fractional conversion, shown in **Figure 9.10**, reveals that under the same reaction conditions, Au/Al_2O_3 promoted a time-invariant

(up to 5 h) conversion while both Ni/Al_2O_3 and $Au\text{-}Ni/Al_2O_3$ exhibited a decline in activity with time-on-stream.

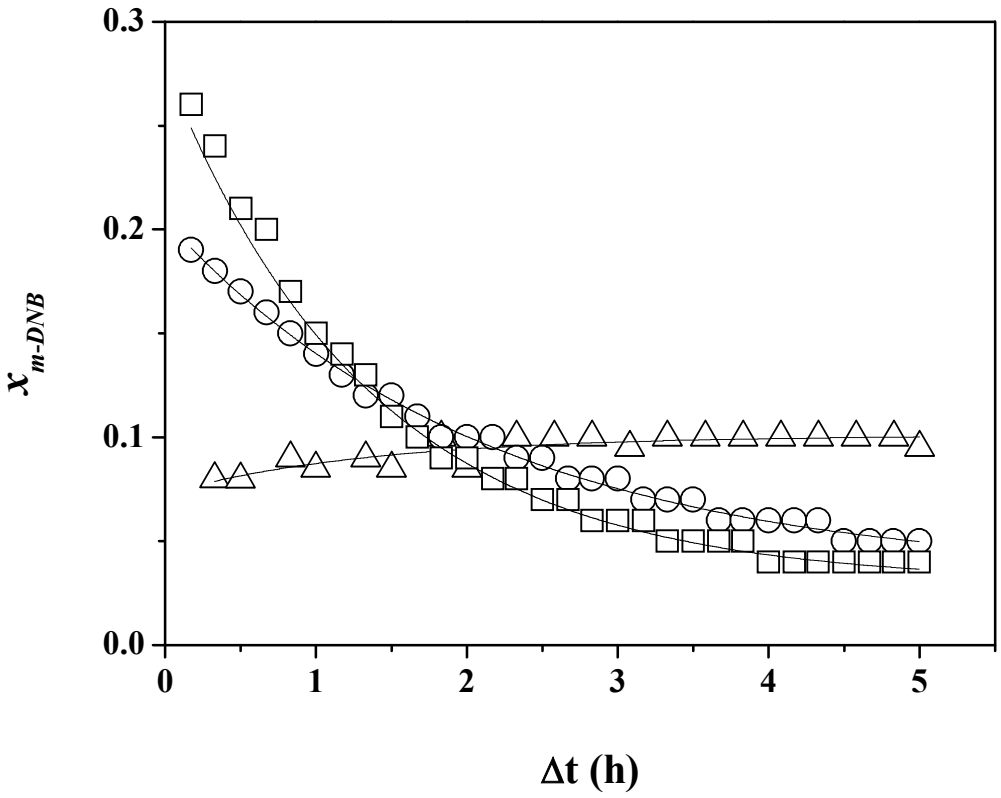

Figure 9.10: Variation of *m*-DNB fractional conversion ($x_{m\text{-}DNB}$) with time-on-stream over (Δ) Au/Al_2O_3, (○) Ni/Al_2O_3 and (□) $Au\text{-}Ni/Al_2O_3$ at 473 K (metal/-NO_2 = 10^{-2} mol_{metal} h $mol_{-NO_2}^{-1}$).

The maintenance of a constant temporal activity for Au/Al_2O_3 is significant given the number of studies of gas phase nitroarene hydrogenation where a decrease in activity with time has been shown (over supported Pd [88-91] and Cu [92,93]) and ascribed to deleterious effects of H_2O as by-product [91], metal leaching [90] and coking [88,89,92,93]. In order to assess the $-NO_2$ group reduction efficiency of the four systems, we have fitted the temporal x_{-NO_2} (see **Equation (9.3)**) response to an empirical relationship discussed previously [14] in order to obtain a measure of the initial degree of nitro-group reduction ($(x_{-NO_2})_0$). The applicability of a pseudo-first order kinetic treatment has already been established [7,14],

$$\ln\left[\frac{1}{\left(1-(x_{-NO_2})_0\right)}\right] = k\left(\frac{n}{F_{-NO_2}}\right) \qquad (9.6)$$

where F_{-NO_2} is the inlet hourly molar -NO_2 feed rate and *n* denotes moles of metal (Au and/or Ni) in the catalyst bed; n/F_{-NO_2} has the physical significance of contact time. The linear relationships between $\ln(1-(x_{-NO_2})_0)^{-1}$ and n/F_{-NO_2} presented in **Figure 9.11** confirm adherence to pseudo-first order behaviour.

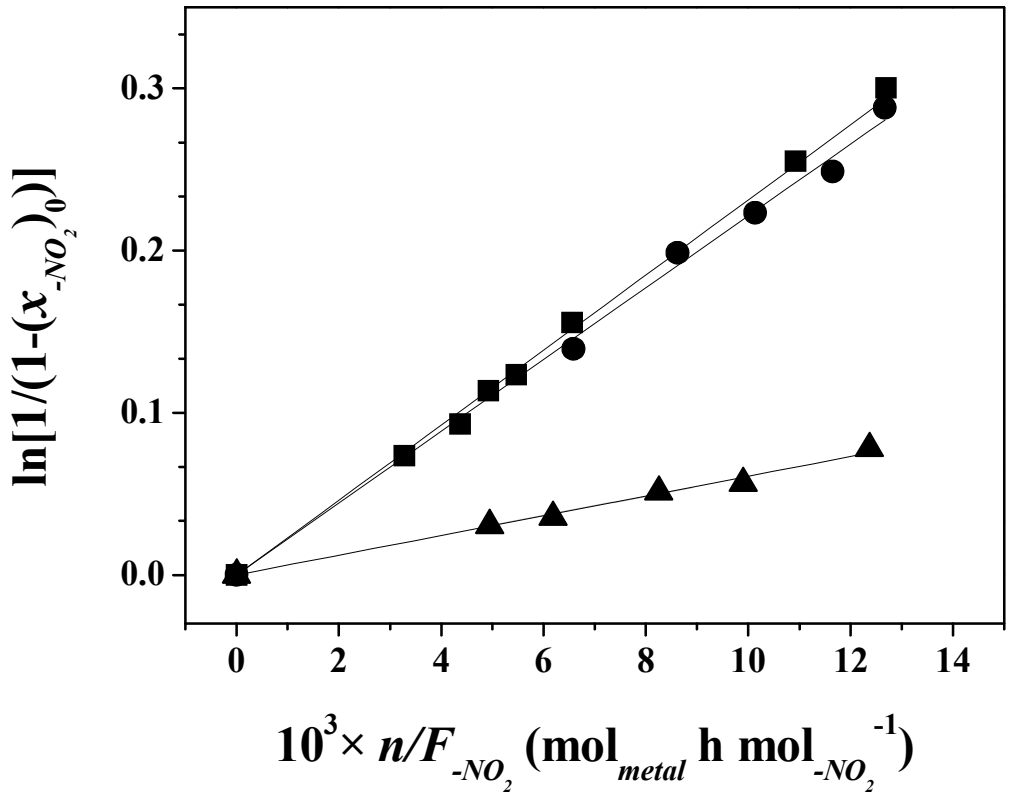

Figure 9.11: Pseudo-first-order kinetic plots for the hydrogenation of *m*-DNB over (▲) Au/Al_2O_3, (●) Ni/Al_2O_3 and (■) $Au-Ni/Al_2O_3$ at 473 K.

The monometallic Au catalyst delivered an activity that was four times lower than that of Ni/Al_2O_3 (see **Table 9.1**). This response finds agreement in the literature dealing with hydrogenation of nitroaromatics [94] in liquid phase systems but we provide here, for the first time, catalytic data obtained for gas phase continuous flow operation. The catalytic action of the Au/Al_2O_3+Ni/Al_2O_3 physical mixture was also considered with a resultant activity sequence in terms of specific rate constant (per mol of Ni): Au/Al_2O_3+Ni/Al_2O_3 (21 $mol_{-NO_2}\, mol_{Ni}^{-1}\ h^{-1}$) ≈ Ni/Al_2O_3 (22 $mol_{-NO_2}\, mol_{Ni}^{-1}\ h^{-1}$) < $Au-Ni/Al_2O_3$ (26 $mol_{-NO_2}\, mol_{Ni}^{-1}\ h^{-1}$). The activity response for the physical mixture was equivalent to that obtained with Ni/Al_2O_3, a result which demonstrates that the inclusion of Au/Al_2O_3 did not affect rate, which was governed by the Ni component. The chemical incorporation of Au in the bimetallic $Au-Ni/Al_2O_3$ resulted in a measurable

increase (greater than experimental reproducibility) in nitro-group reduction rate. This result suggests that surface interaction between Au and Ni contributes to an improved reaction rate, albeit the effect is not appreciable. We could not find any directly comparable studies of hydrogen mediated reactions promoted by bimetallic Au-Ni systems. It is, nonetheless, worth noting the work of Chin *et al.* [18] who reported a decrease in catalytic activity due to the occlusion of Ni step/edge sites by Au in CH_4 reforming over Au-Ni/$MgAl_2O_4$. In contrast, Vasil'kov and co-workers [71] and Yuan *et al.* [29] have reported an increase in catalytic activity for isomerization and hydrodechlorination reactions over Au-Ni/SiO_2, respectively, that was ascribed to surface Au-Ni interactions.

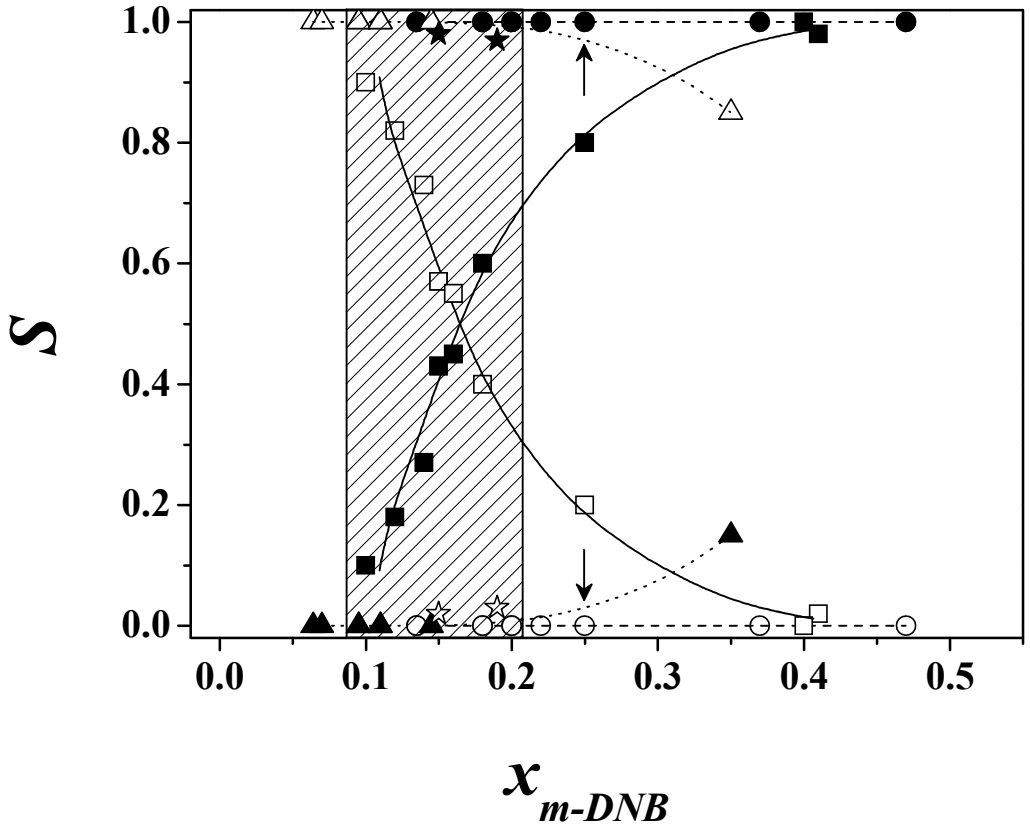

Figure 9.12: Variation of *m*-PDM (solid symbols) and *m*-NAN (open symbols) initial selectivity (*S*) with initial *m*-DNB fractional conversion ($x_{m\text{-}DNB}$) for reaction over (▲,△, dotted line) Au/Al_2O_3, (●,○, dashed line) Ni/Al_2O_3, (★,☆) Au/Al_2O_3 + Ni/Al_2O_3 and (■,□, solid line) $Au\text{-}Ni/Al_2O_3$ at T = 473 K.

The associated selectivity/activity relationships are presented in **Figure 9.12**. Au/Al_2O_3 exhibited 100% selectivity to *m*-NAN where $x_{m\text{-}DNB} < 0.25$ (see arrows in **Figure 9.12**). In marked contrast, Ni/Al_2O_3 promoted the sole formation of *m*-PDM. To the best of our knowledge, the exclusive formation of either the partial (*m*-NAN) or fully reduced product (*m*-PDM) in the hydrogenation of *m*-DNB has not been reported

to date. The catalytic systems that have been studied [81,83-87,95,96] have generated a combination of both products. In gas phase operation, Zhao *et al.* [95] working at 323 K and high pressure (16 MPa) quoted a 97 % selectivity to *m*-NAN over 5 % w/w Pt/C. In liquid phase operation, conditions of high temperatures and/or pressures have also been deemed essential to achieve high selectivities to *m*-NAN or *m*-PDM. Selectivities to *m*-NAN in excess of 80% have been reported for reaction at P_{H_2} up to 45 atm over Pd/C [82,85] and Ru/Al_2O_3 [84]. Higher selectivities to *m*-PDM (up to 99%) have been achieved for reaction over Ni/SiO_2 [86,87,97], $Ni/K_2O\text{-}La_2O_3\text{-}SiO_2$ [81] and Ni-Pt/C [96] at 373-393 K and P_{H_2} = 26-34 atm. The $Au\text{-}Ni/Al_2O_3$ catalyst exhibited a quite distinct selectivity response, generating a combination of partially (*m*-NAN) and fully (*m*-PDM) hydrogenated products where the former was favoured at $x_{m\text{-}DNB} \leq 0.15$. The selectivity/activity data generated for the $Au/Al_2O_3 + Ni/Al_2O_3$ physical coincided with the profile for Ni/Al_2O_3 (see **Figure 9.12**). This result demonstrates that Au/Al_2O_3 had a negligible contribution to hydrogenation selectivity (as it did to hydrogenation activity), which was controlled by Ni/Al_2O_3. The distinct selectivity/conversion response for the three catalytic systems is clearly illustrated by the shaded area ($x_{m\text{-}DNB}$ = 0.1-0.2) in **Figure 9.12** where Au/Al_2O_3 promotes exclusive partial hydrogenation to *m*-NAN, Ni/Al_2O_3 promotes solely the full hydrogenation to *m*-PDM and $Au\text{-}Ni/Al_2O_3$ generates both products. Such a marked deviation in reaction selectivity suggests a clear divergence in reactant/catalyst interactions. In liquid phase operation, $-NO_2$ group reduction has been viewed to occur *via* a nucleophilic mechanism with the participation of a negatively charged intermediate [98] where chemisorbed hydrogen, acting as a weak nucleophilic agent, attacks N=O [99,100]. It has been demonstrated [101,102] that substituted aromatics interact with supported Ni catalysts *via* the benzene ring. The adsorption of *m*-DNB on Ni/Al_2O_3 through the aromatic ring results in the formation of a resonance structure with two positive localized charges on the ring where both $-NO_2$ groups are activated for nucleophilic attack with the formation of *m*-PDM. The production of *m*-NAN over Au/Al_2O_3 must result from the activation of only one of the $-NO_2$ groups with the formation of a resonance structure with a single delocalized positive charge on the ring, which retains its aromaticity. The chemical incorporation of Au in the bimetallic $Au\text{-}Ni/Al_2O_3$ results in the electronic modification of the Ni active sites (Ni→Au electron transfer on the basis of XPS analysis, see section 9.3.1.3) facilitated by the close proximity of Au to Ni (as suggested by STEM-EDX analysis), which impacts on the *m*-DNB adsorption/activation mechanism in that the modified Ni sites do not activate both $-NO_2$ groups to the same extent, with the result that both

partial- and full nitro-group reduction are promoted. Our work has demonstrated that in the hydrogenation of *m*-DNB, product composition can be controlled by switching from monometallic (Ni/Al_2O_3 or Au/Al_2O_3) to bimetallic $Au\text{-}Ni/Al_2O_3$.

9.4 Conclusions

TPR of 1 mol % Au/Al_2O_3 and 10 mol % Ni/Al_2O_3 prepared by impregnation generated Ni particles with a wider size distribution (5-50 nm, mean diameter = 31 nm) when compared with Au (1-20, nm, mean = 9 nm). TPR of $Au\text{-}Ni/Al_2O_3$ (Au/Ni = 1/10) prepared by reductive deposition of Au onto Ni/Al_2O_3 produced metal particles in the range 1-50 nm (mean = 20 nm). EDX mapping of $Au\text{-}Ni/Al_2O_3$ demonstrated that Au and Ni particles are in close proximity on the surface and XPS results are consistent with electron transfer from Ni to Au. The introduction of Au to Ni/Al_2O_3 served to suppress room temperature H_2 uptake post-TPR. However, H_2-TPD analysis demonstrated a greater hydrogen release from $Au\text{-}Ni/Al_2O_3$ compared with Ni/Al_2O_3, suggesting a surface Au-Ni synergy. Au/Al_2O_3 promoted the gas phase continuous hydrogenation of *m*-DNB (P = 1 atm, T = 473 K) exclusively to *m*-NAN with no detectable catalyst deactivation. Under the same reaction conditions, Ni/Al_2O_3 delivered a higher (initial) nitro-group reduction rate, generating *m*-PDM as the sole product but with a significant temporal loss of activity. The inclusion of Au/Al_2O_3 as a physical mixture with Ni/Al_2O_3 did not affect *m*-DNB hydrogenation activity or selectivity, which was controlled by Ni/Al_2O_3. $Au\text{-}Ni/Al_2O_3$ delivered a measurably higher hydrogenation rate than Ni/Al_2O_3 and promoted both the partial and full reduction of *m*-DNB to generate *m*-NAN and *m*-PDM products. We can account for the differences in the observed selectivity/activity response in terms of differences in reactant adsorption/activation on Ni, Au and Au-Ni. Our results establish that the hydrogenation of *m*-DNB can deliver a target product composition depending on the choice of catalyst with control over exclusive partial reduction (Au/Al_2O_3), exclusive total reduction (Ni/Al_2O_3) or a combination of both ($Au\text{-}Ni/Al_2O_3$).

9.5 References

[9.1] A. S. K. Hashmi, Chem. Rev., 107, 3180 (2007)

[9.2] A. S. K. Hashmi, G. J. Hutchings, Angew. Chem. Int. Ed., 45, 7896 (2006)

[9.3] P. Claus, Appl. Catal. A: Gen., 291, 222 (2005)

[9.4] C. W. Corti, R. J. Holliday, D. T. Thompson, Top. Catal., 44, 331 (2007)

[9.5] B. Hammer, J. K. Nørskov, Nature, 376, 238 (1995)

[9.6] C. Mohr, H. Hofmeister, P. Claus, J. Catal., 213, 86 (2003)

[9.7] F. Cárdenas-Lizana, S. Gómez-Quero, M. A. Keane, ChemSusChem, 1, 215 (2008)

[9.8] A. Corma, M. Boronat, S. González, F. Illas, Chem. Commun., 3371 (2007)

[9.9] E. Bus, J. T. Miller, J. A. van Bokhoven, J. Phys. Chem. B, 109, 14581 (2005)

[9.10] S. K. Maity, N. C. Pradhan, A. V. Patwardhan, Appl. Catal. A: Gen., 301, 251 (2006)

[9.11] A. Boehnecke, J. Kielhorn, G. Konnecker, C. Pohlenz-Michel, I. Mangelsdorf, CICADS Report 48, W.H.O., Geneva, 2003, p. 78.

[9.12] L. M. Sikhwivhilu, N. J. Coville, B. M. Pulimaddi, J. Venkatreddy, V. Vishwanathan, Catal. Commun., 8, 1999 (2007)

[9.13] F. Cárdenas-Lizana, S. Gómez-Quero, M. A. Keane, Catal. Commun., 9, 475 (2008)

[9.14] F. Cárdenas-Lizana, S. Gómez-Quero, M. A. Keane, Appl. Catal. A: Gen., 334, 199 (2008)

[9.15] A. M. Molenbroek, J. K. Nørskov, J. Phys. Chem. B, 105, 5450 (2001)

[9.16] F. Besenbacher, I. Chorkendorff, B. S. Clausen, B. Hammer, A. M. Molenbroek, J. K. Nørskov, I. Stensgaard, Science, 279, 1913 (1998)

[9.17] N. C. Triantafyllopoulos, S. G. Neophytides, J. Catal., 239, 187 (2006)

[9.18] Y.-H. Chin, D. L. King, H.-S. Roh, Y. Wang, S. M. Heald, J. Catal., 244, 153 (2006)

[9.19] X.-X. Han, R.-X. Zhou, G.-H. Lai, B.-H. Yue, X.-M. Zheng, J. Mol. Catal. A: Chem., 209, 83 (2004)

[9.20] M. Liu, W. Yu, H. Liu, J. Zheng, J. Colloid Interface Sci., 214, 231 (1999)

[9.21] X. Han, R. Zhou, X. Zheng, H. Jiang, J. Mol. Catal. A: Chem., 193, 103 (2003)

[9.22] X. Yang, H. Liu, Appl. Catal. A: Gen., 164, 197 (1997)

[9.23] S. K. Ghosh, M. Mandal, S. Kundu, S. Nath, T. Pal, Appl. Catal. A: Gen., 268, 61 (2004)

[9.24] X. Yan, J. Sun, Y. Wang, J. Yang, J. Mol. Catal. A: Chem., 252, 17 (2006)

[9.25] T. V. Choudhary, C. Sivadinarayana, A. K. Datye, D. Kumar, D. W. Goodman, Catal. Lett., 86, 1 (2003)

[9.26] G. del Angel, R. Melendrez, V. Bertin, J. M. Dominguez, P. Marecot, J. Barbier, Stud. Surf. Sci. Catal., 78, 171 (1993)

[9.27] B. Pawelec, V. La Parola, S. Thomas, J. L. G. Fierro, J. Mol. Catal. A: Chem., 253, 30 (2006)

[9.28] G. Yuan, C. Louis, L. Delannoy, M. A. Keane, J. Catal. , 247, 256 (2007)

[9.29] G. Yuan, J. L. Lopez, C. Louis, L. Delannoy, M. A Keane, Catal. Commun., 6, 555 (2005)

[9.30] J. H. Sinfelt, in: Exxon (Ed.), United States Patent and Trademark Office, US, 1976.

[9.31] O. S. Alexeev, B. C. Gates, Ind. Eng. Chem. Res., 42, 1571 (2003)

[9.32] G. C. Bond, C. Louis, D. T. Thompson, Catalysis by Gold, Imperial College Press, London, 2006.

[9.33] F. Cárdenas-Lizana, S. Gómez-Quero, M. A. Keane, Catal. Lett., 127, 25 (2009)

[9.34] N. Togasaki, Y. Okinaka, T. Homma, T. Osaka, Electrochimica Acta, 51, 882 (2005)

[9.35] G. Tavoularis, M. A. Keane, J. Chem. Technol. Biotechnol., 74, 60 (1999)

[9.36] G. Yuan, M. A. Keane, Chem. Eng. Sci., 58, 257 (2003)

[9.37] E. Bus, R. Prins, J. A. van Bokhoven, Phys. Chem. Chem. Phys., 9, 3312 (2007)

[9.38] M. P. González-Marcos, J. I. Gutiérrez-Ortiz, C. González-Ortiz de Elguea, J. R. González-Velasco, J. Mol. Catal. A: Chem., 120, 185 (1997)

[9.39] J. Rynkowski, D. Rajski, I. Szyszka, J. R. Grzechowiak, Catal. Today, 90, 159 (2004)

[9.40] A. Diaz, D. R. Acosta, J. A. Odriozola, M. Montes, J. Phys. Chem. B, 101, 1782 (1997)

[9.41] J. Barbier, Handbook of Heterogeneous Catalysis. Redox Methods for Preparation of Bimetallic Catalysts, VCH Verlagsgesellschaft mbH, Weinheim (Germany), 1997.

[9.42] M. Bonarowska, J. Pielaszek, W. Juszczyk, Z. Karpiński, J. Catal., 195, 304 (2000)

[9.43] G. Espinosa, G. del Angel, J. Barbier, P. Bosch, V. Lara, D. Acosta, J. Mol. Catal. A: Chem., 164, 253 (2000)

[9.44] P. del Angel, J.M. Dominguez, G. del Angel, J.A. Montoya, J. Capilla, E. Lamy-Pitara, J. Barbier, Top. Catal., 18, 183 (2002)

[9.45] David R. Lide, Handbook of Chemistry and Physical Properties, 88th ed., Taylor Francis Group, Boca Raton (USA), 2007-2008.

[9.46] A. Venugopal, J. Aluha, M. S. Scurrell, Catal. Lett., 90, 1 (2003)

[9.47] F.-W. Chang, L. S. Roselin, T.-C. Ou, Appl. Catal. A: Gen., 334, 147 (2008)

[9.48] J. Harris, Surf. Sci., 221, 335 (1989)

[9.49] A. C. Gluhoi, H. S. Vreeburg, J. W. Bakker, B. E. Nieuwenhuys, Appl. Catal. A: Gen., 291, 145 (2005)

[9.50] E. P. Maris, W. C. Ketchie, M. Murayama, R. J. Davis, J. Catal., 251, 281 (2007)

[9.51] R. J. Chimentão, G. P. Valença, F. Medina, J. Pérez-Ramírez, Appl. Surf. Sci., 253, 5888 (2007)

[9.52] W. C. Conner, J. L. Falconer, Chem. Rev., 95, 759 (1995)

[9.53] C. Amorim, M. A. Keane, J. Colloid Interface Sci., 322, 196 (2008)

[9.54] S. Smeds, T. Salmi, L. P. Lindfors, O. Krause, Appl. Catal. A: Gen., 144, 177 (1996)

[9.55] S. Velu, S. K. Gangwal, Solid State Ionics, 177, 803 (2006)

[9.56] Y. Cesteros, P. Salagre, F. Medina, J.E. Sueiras, Appl. Catal. B: Environ., 22, 135 (1999)

[9.57] P. M. Holmblad, J. H. Larsen, I. Chorkendorff, J. Chem. Phys., 104, 7289 (1996)

[9.58] J. Greeley, M. Mavrikakis, Nature Mater., 3, 810 (2004)

[9.59] J. Greeley, M. Mavrikakis, J. Phys. Chem. B, 109, 3460 (2005)

[9.60] G. C. Bond, Chem. Soc. Rev., 20, 441 (1991)

[9.61] R. Zanella, C. Louis, S. Giorgio, R. Touroude, J. Catal., 223, 328 (2004)

[9.62] M. A. Keane, Can. J. Chem., 72, 372 (1994)

[9.63] P. Burattin, M. Che, C. Louis, J. Phys. Chem. B 101, 7060 (1997)

[9.64] H. H. Kung, M. C. Kung, C. K. Costello, J. Catal., 216, 425 (2003)

[9.65] M. V. Twigg, M. S. Spencer, Appl. Catal. A: Gen., 212, 161 (2001)

[9.66] J. Barbier, P. Marécot, G. del Angel, P. Bosch, J. P. Boitiaux, B. Didillon, J. M. Dominguez, I. Schifter, G. Espinosa, Appl. Catal. A: Gen., 116, 179 (1994)

[9.67] F. Menegazzo, P. Burti, M. Signoretto, M. Manzoli, S. Vankova, F. Boccuzzi, F. Pinna, G. Strukul, J. Catal., 257, 369 (2008)

[9.68] H. Reichert, A. Schöps, I. B. Ramsteiner, V. N. Bugaev, O. Shchyglo, A. Udyansky, H. Dosch, M. Asta, R. Drautz, V. Honkimäki, Phys. Rev. Lett., 95, 235703 (2005)

[9.69] L. P. Nielsen, F. Besenbacher, I. Stensgaard, E. Laegsgaard, C. Engdahl, P. Stoltze, K. W. Jacobsen, J. K. Nørskov, Phys. Rev. Lett., 71, 754 (1993)

[9.70] G. C. Bond, Platinum Metals Rev., 51, 63 (2007)

[9.71] A. Yu. Vasil'kov, S. A. Nikolaev, V. V. Smirnov, A. V. Naumkin, I. O. Volkov, V. L. Podshibikhin, Mendeleev Commun., 17, 268 (2007)

[9.72] A. V. Naumkin, A. Yu. Vasil'kov, I. O. Volkov, V. V. Smirnov, S. A. Nikolaev, Inorg. Mater., 43, 445 (2007)

[9.73] S. Zafeiratos, S. Kennou, Appl. Surf. Sci., 173, 69 (2001)

[9.74] J. L. Rousset, F. J. Cadete-Santos-Aires, B. R. Sekhar, P. Mélinon, B. Prevel, M. Pellarin, J. Phys. Chem. B, 104, 5430 (2001)

[9.75] A. C. Gluhoi, N. Bogdanchikova, B. E. Nieuwenhuys, J. Catal., 232, 96 (2005)

[9.76] Z. Li, Y. Deng, Y. Wu, B. Shen, W. Hu, J. Mater. Sci., 42, 9234 (2007)

[9.77] P. Mulvaney, Langmuir, 12, 788 (1996)

[9.78] R. Zanella, C. Louis, Catal. Today, 107-108, 768 (2005)

[9.79] A. Wolf, F. Schüth, Appl. Catal. A: Gen., 226, 1 (2002)

[9.80] W.-S. Lee, B.-Z. Wan, C.-N. Kuo, W.-C. Lee, S. Cheng, Catal. Commun., 8, 1604 (2007)

[9.81] L. Zhao, J. Chen, J. Zhang, J. Mol. Catal. A: Chem., 246, 140 (2006)

[9.82] V. L. Khilnani, S. B. Chandalia, Org. Process Res. Dev., 5, 263 (2001)

[9.83] Y. Liu, Z. Weib, J. Zhang, W. Yan, React. Kinet. Catal. Lett., 92, 121 (2007)

[9.84] S. Zhao, H. Liang, Y. Zhou, Catal. Commun., 8, 1305 (2007)

[9.85] V. L. Khilnani, S. B. Chandalia, Org. Proc. Res. Dev., 5, 263 (2001)

[9.86] Y. X. Liu, Z. J. Wei, J. X. Chen, J. Y. Zhang, X. X. Li, X. H. Wei, Chin. Chem. Lett., 16, 531 (2005)

[9.87] Y. X. Liu, Z. J. Wei, J. Y. Zhang, Korean J. Chem. Eng., 23, 902 (2006)

[9.88] E. Klemm, B. Amon, H. Redlingshöfer, E. Dieterich, G. Emig, Chem. Eng. Sci., 56, 1347 (2001)

[9.89] V. Vishwanathan, V. Jayasri, P. M. Basha, N. Mahata, L. M. Sikhwivhilu, N. J. Coville, Catal. Commun., 9, 453 (2008)

[9.90] K. K. Yeong, A. Gavriilidis, R. Zapf, V. Hessel, Catal. Today, 81, 641 (2003)

[9.91] P. Sangeetha, P. Seetharamulu, K. Shanthi, S. Narayanan, K.S. Rama Raob, J. Mol. Catal. A: Chem., 273, 244 (2007)

[9.92] S. Diao, W. Qian, G. Luo, F. Wei, Y. Wang, Appl. Catal. A: Gen., 286, 30 (2005)

[9.93] L. Petrov, K. Kumbilieva, N. Kirkov, Appl. Catal., 59, 31 (1990)

[9.94] A. Corma, P. Serna, P. Concepción, J. J. Calvino, J. Am. Chem. Soc., 130, 8748 (2008)

[9.95] F. Zhao, S.-I. Fujita, J. Suna, Y. Ikushima, M. Arai, Catal. Today, 98, 523 (2004)

[9.96] M. M. Telkar, J. M. Nadgeri, C. V. Rode, R. V. Chaudhari, Appl. Catal. A: Gen., 295, 23 (2005)

[9.97] Y. X. Liu, J. X. Chen, J. Y. Zhang, Chin. J. Chem. Eng., 15, 63 (2007)

[9.98] B. Coq, F. Figuéras, Coord. Chem. Rev., 178-180, 1753 (1998)

[9.99] S. Galvagno, A. Donato, G. Neri, R. Pietropaolo, J. Mol. Catal., 42, 379 (1987)

[9.100] B. Coq, F. Figuéras, Coord. Chem. Rev., 178-180, 1753 (2000)

[9.101] E.-J. Shin, M. A. Keane, J. Catal., 173, 450 (1998)

[9.102] E.-J. Shin, M. A. Keane, Ind. Eng. Chem. Res., 39, 883 (2000)

Chapter 10

Gas Phase Hydrogenation of m-Dinitrobenzene over Alumina Suppoted Au and Au-Ni Alloy

Distinct catalytic behaviour exhibited by Al_2O_3 supported monometallic (Au and Ni) and bimetallic Au-Ni catalysts in the continuous hydrogenation of *m*-dinitrobenzene presented in the previous Chapter was associated with Au-Ni surface interactions/synergy. In this Chapter the catalytic action of an Al_2O_3 supported Au-Ni alloy has been considered.

10.1 Introduction

Aromatic amino compounds are important chemicals, used as intermediates in the manufacture of a range of fine chemicals, *e.g.* pesticides, pigments and cosmetics [1]. Amino derivates are typically synthesised *via* the reduction of the corresponding nitro-compound, either by Fe promoted reduction in acid media (Béchamp process) or transition metal promoted liquid phase hydrogenation [2]. The production of toxic by-products (ferric oxide sludge), in the former case, and the low associated target product yields has shifted attention to the catalytic hydrogenation option as a cleaner alternative [3]. Conventional supported monometallic (*e.g.* Pt or Pd) catalysts can deliver high conversions but an exclusive selectivity in terms of nitro-group reduction has yet to be achieved [4]. The ineffectiveness of these systems is particularly marked in the synthesis of *m*-nitroaniline (*m*-NAN) from *m*-dinitrobenzene (*m*-DNB) where the formation of *m*-phenylenediamine (*m*-PDM) (*i.e.* reduction of both -NO_2 groups) is also promoted [5,6]. The use of Au in the selective hydrogenation of nitroarenes is now gaining increasing attention with recent reports of batch liquid phase hydrogenation over Au supported on SiO_2 [7], TiO_2 [8], Fe_2O_3 [8] and ZrO_2 [9] but the requirement of high hydrogen pressures (3-4 MPa) [7,8] and/or the formation of highly toxic compounds (azoxy-derivates) [8,9] represent decided drawbacks. Structure sensitivity has been proposed [10] while a selective activation of the nitro-group *via* interaction with Au sites may have a critical role to play [11]. We have recently reported reaction exclusivity in terms of -NO_2 group reduction for the continuous gas phase

hydrogenation of a series of nitro-haloarenes over supported Au [12,13]. We have now focused our attention on the selective hydrogenation of *m*-DNB and report here our preliminary results.

A significant recent development in catalysis by Au has been the use of Au based alloys, which have delivered distinct selectivity and activity responses [14,15]. Hutchings and co-workers [16], studying the gas phase hydrogenation of O_2 to H_2O_2, recorded higher activity (by a factor of 2) over a supported Au-Pd alloy when compared with Au and Pd. Pârvulescu *et al.* [17], using silica supported Au, Pd and Au-Pd in the hydrogenation of cinnamaldehyde, demonstrated that the alloy outperformed the monometallic catalysts in terms of activity and selectivity with respect to cinnamyl alcohol. Fierro *et al.* [18], in the gas phase hydrogenation of naphthalene over silica supported Au and Pt-Au, ascribed the higher activity observed for the bimetallic catalysts to the formation of a Pt-Au alloy. There is, however, a dearth of literature dealing with the catalytic implications of Ni–Au combinations and a comprehensive search through the literature did not unearth any study dealing with the preparation and catalytic application of (an alumina supported) Au-Ni alloy. Nevertheless, we can flag related studies involving supported Au-Ni systems: (i) Molenbroek *et al.* [19] reported improved butane steam reforming stability for reaction over Au-Ni/SiO_2 relative to Ni/SiO_2 and ascribed this response to the formation of a Au-Ni surface alloy that served to limit coke deposition and prolong catalytic activity; (ii) Triantafyllopoulos and Neophytides [20] and Chin *et al.* [21] have noted that the addition of Au to Ni/YSZ and Ni/$MgAl_2O_4$ served to suppress carbon deposition during methane steam reforming; (iii) Yuan and co-workers [22] observed an enhanced hydrodechlorination activity over Au-Ni/SiO_2 and Au-Ni/TiO_2 that they associated with a surface Au-Ni synergism.

In this paper we provide the first report of the catalytic action of Au/Al_2O_3 in the gas phase hydrogenation of *m*-DNB, comparing activity/selectivity with that obtained using an Al_2O_3 supported Au-Ni alloy. We link catalyst performance to critical structural information.

10.2 Experimental

10.2.1 Catalyst Preparation and Activation

The Al_2O_3 support (Puralox) was obtained from Condea Vista Co. and used as received. A 1 mol % Au/Al_2O_3 sample was prepared by impregnation with $HAuCl_4$ (Aldrich, 0.0025g cm^{-3}). The slurry was heated (*ca.* 2 K min^{-1}) to 353 K and maintained under agitation (600 rpm) with a constant He purge. The solid residue was dried in a flow of He at 383 K for 3 h. A Ni/Al_2O_3 (10 mol %) was prepared by impregnation where a 2-butanolic $Ni(NO_3)_2$ solution was added drop wise at 353 K to the substrate with constant agitation (600 rpm) and oven dried at 393 K for 12 h. The alumina supported Au-Ni precursor was prepared by activation of the Ni/Al_2O_3 catalyst in a stream of H_2 at 2 K min^{-1} to 723 ± 1 K, which was maintained for 2.5 h. The gas flow was switched to He and cooled to room temperature, at which point the sample was passivated in 1% v/v O_2/He. This treatment served to provide a protective oxide layer over the surface Ni that prevented bulk oxidation upon exposure to the atmosphere. The passivated sample was contacted with $HAuCl_4$, post-treatment as above. After preparation, the samples (sieved into a batch of 75 μm average diameter) were activated in 60 cm^3 min^{-1} H_2 at 2 K min^{-1} to 603 ± 1 K, cooled to room temperature in a He flow and subsequently subjected to a temperature controlled treatment in 65 cm^3 min^{-1} N_2 at 50 K min^{-1} to 1273 ± 1 K. The latter step was necessary to generate the supported alloy as the Au-Ni miscibility gap is such that bulk alloy formation is not possible at temperatures below 1083 K [23]. The Au/Al_2O_3 sample underwent the same annealing treatment to facilitate a direct comparison of the catalytic performance with that of the alloy. The samples were then cooled in N_2 and passivated in 1% v/v O_2/He at room temperature for off-line analysis. Metal loading was determined (to within ± 2%) by inductively coupled plasma-optical emission spectrometry (ICP-OES, Vista-PRO, Varian Inc.) from the diluted extract of aqua regia.

10.2.2 Catalyst Characterization

Temperature programmed reduction (TPR) and H_2 chemisorption were determined using the commercial CHEM-BET 3000 (Quantachrome) unit. The samples were loaded into a U-shaped Quartz cell (100 mm × 3.76 mm i.d.) and heated in 17 cm^3 min^{-1} 5% v/v H_2/N_2 (Brooks mass flow controlled) to 603 ± 1 K (Au/Al_2O_3 and Au-Ni/Al_2O_3) or 723 ± 1 K (Ni/Al_2O_3) at 2 K min^{-1}. The effluent gas passed through a liquid N_2 trap and H_2 consumption was monitored by a thermal conductivity detector,

with data acquisition/manipulation using the TPR Win^{TM} software. The reduced samples were maintained at the final temperature until the signal returned to the baseline. After the reduction step, the catalysts were cooled in a He flow and subjected to the annealing step described above, with subsequent H_2 chemisorption (at room temperature) using a pulse (10 μl) titration procedure, as described elsewhere [24]. BET surface area analysis and total pore volume were performed using the commercial Micromeritics Flowsorb II 2300 unit. Prior to analysis, the samples were outgassed at 423 K for 1 h in 20 cm^3 min^{-1} N_2. BET area was obtained in a 30 % v/v N_2/He flow (20 cm^3 min^{-1}) with at least three cycles of N_2 adsorption-desorption using the standard single-point BET method. Total pore volume was obtained at a relative N_2 pressure of $P/P_0 = 0.95$. The BET area and pore volume data were reproducible to within ± 5% and the values quoted in this paper are the mean. Powder X-ray diffractograms were recorded on a Bruker/Siemens D500 incident X-ray diffractometer using Cu Kα radiation. The samples were scanned at 0.02º $step^{-1}$ over $20º \leq 2\theta \leq 90º$ (scan time = 5 s $step^{-1}$). Diffractograms were identified using the JCPDS-ICDD reference standards, *i.e.* γ-Al_2O_3 (10-0425), Au (04-0784) and Ni (04-0850), and Ref. [25] for the Au-Ni alloy. Metal particle size (d_{hkl}) was estimated using the Scherrer equation:

$$d_{hkl} = \frac{K \cdot \lambda}{\beta \cdot \cos\theta} \qquad \textbf{(10.1)}$$

where $K = 0.9$, λ is the incident radiation wavelength (1.54056 Å), β is the peak width at half the maximum intensity and θ represents the diffraction angle corresponding to the main plane associated with metallic Au ($2\theta = 38.1°$) and Au-Ni alloy ($2\theta = 42.8°$). Diffuse reflectance UV-Vis (DRS UV-Vis) measurements were conducted using a Perkin Elmer Lambda 35 UV-Vis Spectrometer with $BaSO_4$ powder as reference; absorption profiles were calculated from the reflectance data using the Kubelka-Munk function. Transmission electron microscopy analysis was conducted using a JEOL JEM 2011 HRTEM unit with a UTW energy dispersive X-ray detector (Oxford Instruments) operated at an accelerating voltage of 200 kV, employing Gatan DigitalMicrograph 3.4 for data acquisition/manipulation. The specimens were prepared by dispersion in acetone and deposited on a holey carbon/Cu grid (300 Mesh).

10.2.3 Catalysis Procedure

Reactions were carried out under atmospheric pressure, *in situ* immediately after activation, in a fixed bed vertical continuous glass reactor (l = 600 mm; i.d. = 15 mm) at 573 K. The catalytic reactor and operating conditions to ensure negligible heat/mass transport limitations have been fully described elsewhere [26]. Isothermal reaction conditions (± 1 K) were ensured by diluting the catalyst bed with ground glass (75 μm). The reaction temperature was continuously monitored by a thermocouple inserted in a thermowell within the catalyst bed. A butanolic solution of *m*-DNB was delivered to the reactor *via* a glass/teflon air-tight syringe and teflon line using a microprocessor controlled infusion pump (Model 100 kd Scientific) at a fixed calibrated flow rate. A co-current flow of *m*-DNB and ultra pure H_2 (< 1% v/v *m*-DNB/H_2) was maintained at *GHSV* = 2×10^4 h^{-1} with a molar metal (*n*) to inlet molar -NO_2 feed rate (*F*) ratio that spanned the range 15×10^{-3} – 50×10^{-3} h; inlet *m*-DNB flow = 0.05-0.15 mmol h^{-1}. The H_2 content was up to 300 times in excess of the stoichiometric requirement, the flow rate of which was monitored using a Humonics (Model 520) digital flowmeter. In a series of blank tests, passage of *m*-DNB in a stream of H_2 through the empty reactor or over the support alone, *i.e.* in the absence of Au or Au-Ni alloy, did not result in any detectable conversion. The reactor effluent was frozen in a liquid N_2 trap for subsequent analysis which was made using a Perkin-Elmer Auto System XL gas chromatograph equipped with a programmed split/splitless injector and a flame ionization detector, employing a DB-1 50 m × 0.20 mm i.d., 0.33 μm film thickness capillary column (J&W Scientific). *m*-DNB (Aldrich, ≥ 98% purity) and the solvent (1-butanol: Riedel-de Haën) were used as supplied without further purification. The degree of nitro-group reduction ($x_{\text{-}NO_2}$) is given by

$$x_{\text{-}NO_2} = \frac{[\text{-}NH_2]_{out}}{[\text{-}NO_2]_{in}} = \frac{2\times[m\text{-}PDM]_{out} + [m\text{-}NAN]_{out}}{2\times[m\text{-}DNB]_{in}} \qquad \textbf{(10.2)}$$

where [*m*-NAN] and [*m*-PDM] are, respectively, the concentrations of *m*-NAN and *m*-PDM and the subscripts *in* and *out* refer to the inlet and outlet streams. Catalyst activity is also quantified in terms of the fractional conversion of *m*-DNB ($x_{m\text{-}DNB}$)

$$x_{m\text{-}DNB} = \frac{[m\text{-}DNB]_{in} - [m\text{-}DNB]_{out}}{[m\text{-}DNB]_{in}} \qquad \textbf{(10.3)}$$

while selectivity in terms of (say) *m*-NAN ($S_{m\text{-}NAN}$) is given by

$$S_{m\text{-}NAN} = \frac{[m\text{-NAN}]_{out}}{[m\text{-DNB}]_{in} - [m\text{-DNB}]_{out}} \qquad \textbf{(10.4)}$$

Repeated reactions using different samples from the same batch of catalyst delivered conversion/selectivity data that were reproducibility to within ± 6%.

10.3 Results and Discussion

Table 10.1: Temperature programmed reduction (TPR) T_{max} values, H_2 uptake, BET surface areas, total pore volumes, metal particle size and DRS UV-Vis spectroscopic characteristics for Au/Al_2O_3 and $Au\text{-}Ni/Al_2O_3$ with associated pseudo-first order rate constants (k) and reaction products (+ selectivities) obtained under conditions of equal activity ($x_{m\text{-}DNB}$ ~ 0.15) in the reduction of *m*-DNB.

	Au/Al_2O_3	$Au\text{-}Ni/Al_2O_3$
TPR T_{max} (K)[a]	**434**	446, **603**
$H_{2\ uptake}$ ($\mu mol\ g_{catalyst}^{-1}$)	0.1	0.2
BET area ($m^2\ g^{-1}$)	122	68
Pore Volume ($10^{-3}\ cm^3\ g^{-1}$)	258	212
d_{hkl} (nm)[b]	37	23[c]
DRS UV-Vis A_{max} (nm)	540	-[d]
k ($10^3\ mmol_{\text{-}NO_2}\ mol_{metal}^{-1}\ h^{-1}$)	2.0	0.3
Product(s) (% selectivity)	*m*-NAN (100)	*m*-NAN (75) *m*-PDM (25)

[a] T_{max} associated with any dominant TPR peak is given in bold
[b] based on XRD line broadening analysis (see **Equation (10.1)**)
[c] based on XRD response at $2\theta = 42.8°$
[d] no distinguishable peak(s)

Characterisation measurements are presented in **Table 10.1**, which include the T_{max} values associated with the TPR of the catalyst precursors and critical values (H_2 uptake, BET surface area, pore volume, average metal particle size and characteristic DRS UV-Vis absorbance peaks) associated with the activated catalysts. The catalytic properties of the two systems were evaluated using the gas phase hydrogenation of *m*-DNB as a model reaction. Conversion of *m*-DNB generated *m*-NAN (partial nitro-group reduction) and *m*-PDM (complete nitro-group reduction) as the sole products with no evidence of hydrodenitrogenation or aromatic ring reduction.

10.3.1 Au/Al_2O_3

10.3.1.1 Catalyst Characterization

The result of the TPR analysis for Au/Al_2O_3 is presented in **Figure 10.1** (profile I) where the appearance of a single positive peak (T = 434 K) can be attributed to the reduction of Au^{3+} to Au^0, as proposed elsewhere [27]. Bus *et al.* [28], using time-resolved *in situ* XAS, have established the presence of Al_2O_3-supported oxidic or hydroxidic Au^{3+} species in the precursor that were reduced in H_2 at 440 K to yield metallic Au. Hydrogen uptake (**Table 10.1**) on the activated sample was low, consistent with the limited H_2 chemisorptive capacity of supported gold reported in the literature [10]. The X-ray diffraction pattern for Au/Al_2O_3 is given in **Figure 10.2** (profile Ia) with four broad peaks between 30º-70º, corresponding to the (311), (222), (400) and (440) planes associated with cubic γ-Al_2O_3 (JCPDS-ICDD 10-0425). In addition, the peaks at 2θ = 38.1°, 44.4°, 64.7° and 77.5° correspond, respectively, to (111), (200), (220) and (311) planes of metallic Au (JCPDS-ICDD 04-0784). The DRS UV-Vis spectrum for Au/Al_2O_3 (**Figure 10.2**, profile IIa) presents a maximum at 540 nm corresponding to metallic Au, where the weak signal intensity is due to the low Au loading in the sample. Gluhoi *et al.* [29] have ascribed a DRS UV-Vis band between 500-600 nm, for Au/Al_2O_3 prepared by deposition-precipitation, to the presence of Au^0. Representative TEM images are presented in **Figure 10.3**. In common with reported TEM analyses of impregnated Au/Al_2O_3 [12,13,30], the Au is present as discrete particles with a pseudo-spherical morphology. The Au particles present a wide size distribution (<5-200 nm). Selected area electron diffraction analysis confirmed that Au was present in the metallic form.

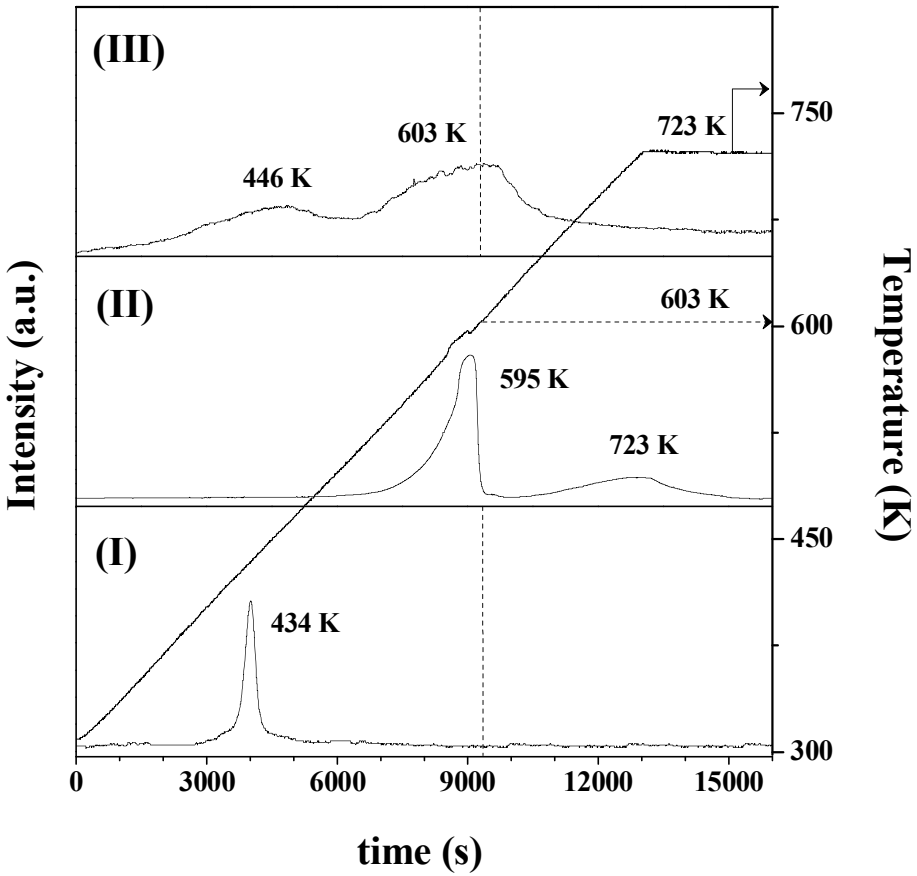

Figure 10.1:
TPR profiles for (I) Au/Al_2O_3, (II) Ni/Al_2O_3 and (III) $Au\text{-}Ni/Al_2O_3$. Dashed line represents final isothermal hold for Au/Al_2O_3 and $Au\text{-}Ni/Al_2O_3$.

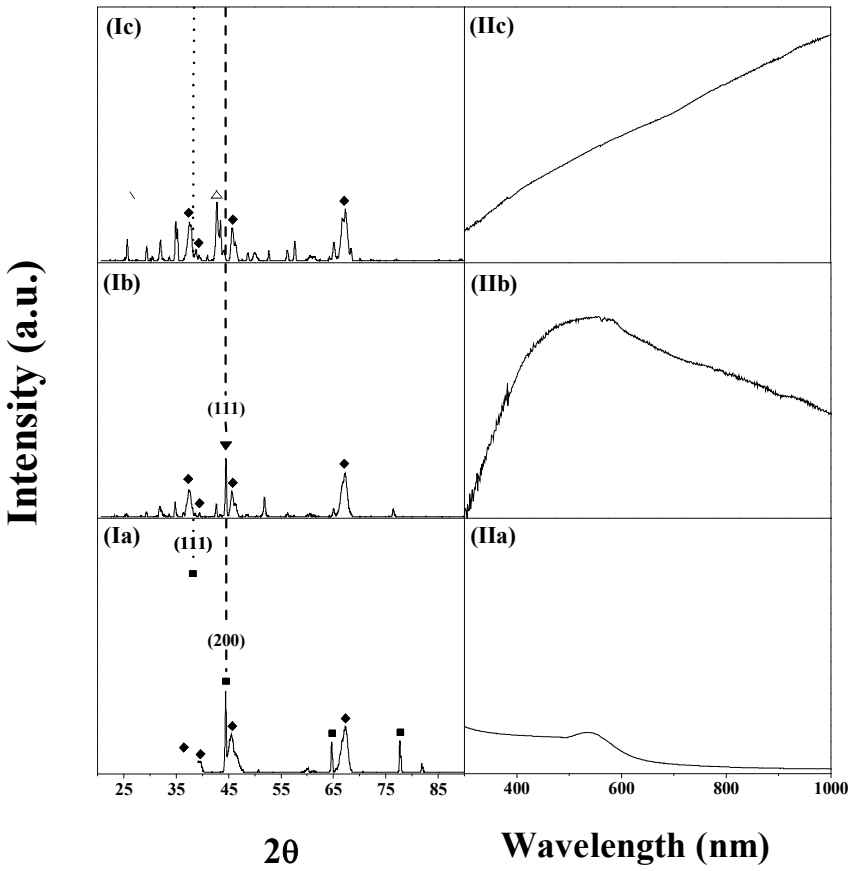

Figure 10.2:
(I) XRD patterns and (II) DRS UV-Vis spectra for (a) Au/Al_2O_3, (b) Ni/Al_2O_3 and (c) $Au\text{-}Ni/Al_2O_3$. *Note*: Dotted line identifies position of the $(111)_{Au}$ peak and dashed line the position of the $(200)_{Au}$ and $(111)_{Ni}$ peaks. JCPDS-ICDD reference data: (♦) γ-Al_2O_3 (10-0425); (■) Au (04-0784), (▼) Ni (04-0850) and (Δ) Au-Ni alloy.

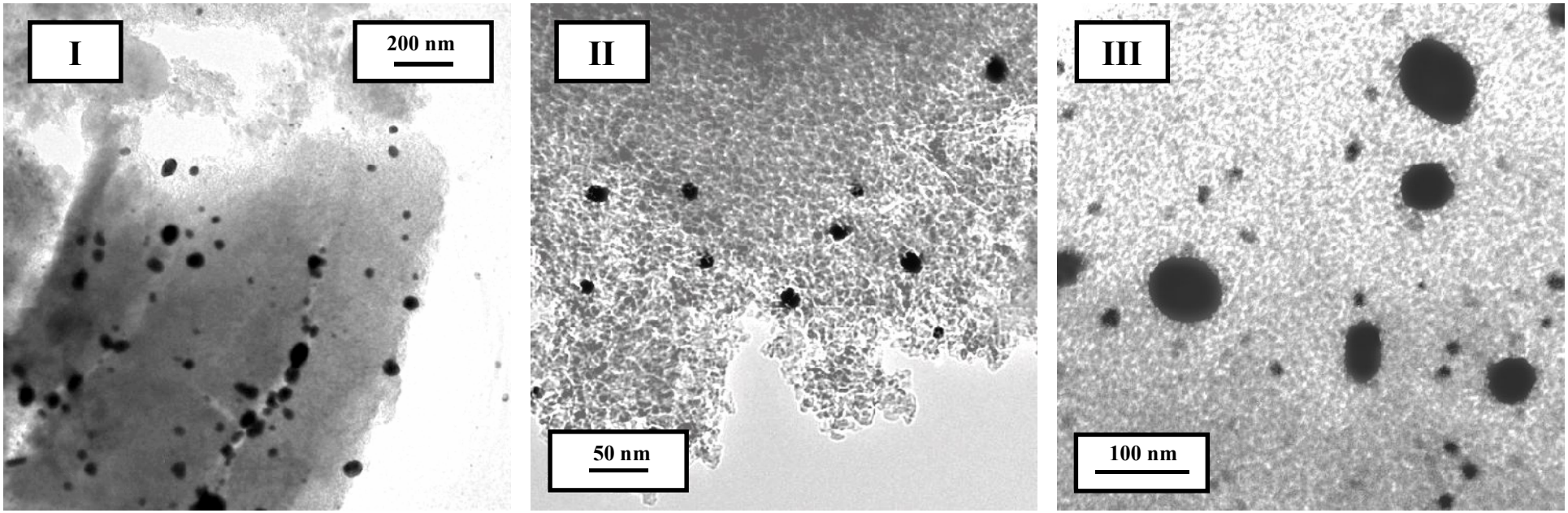

Figure 10.3: Representative TEM images of Au/Al_2O_3; (I) low, (II) and (III) medium resolution.

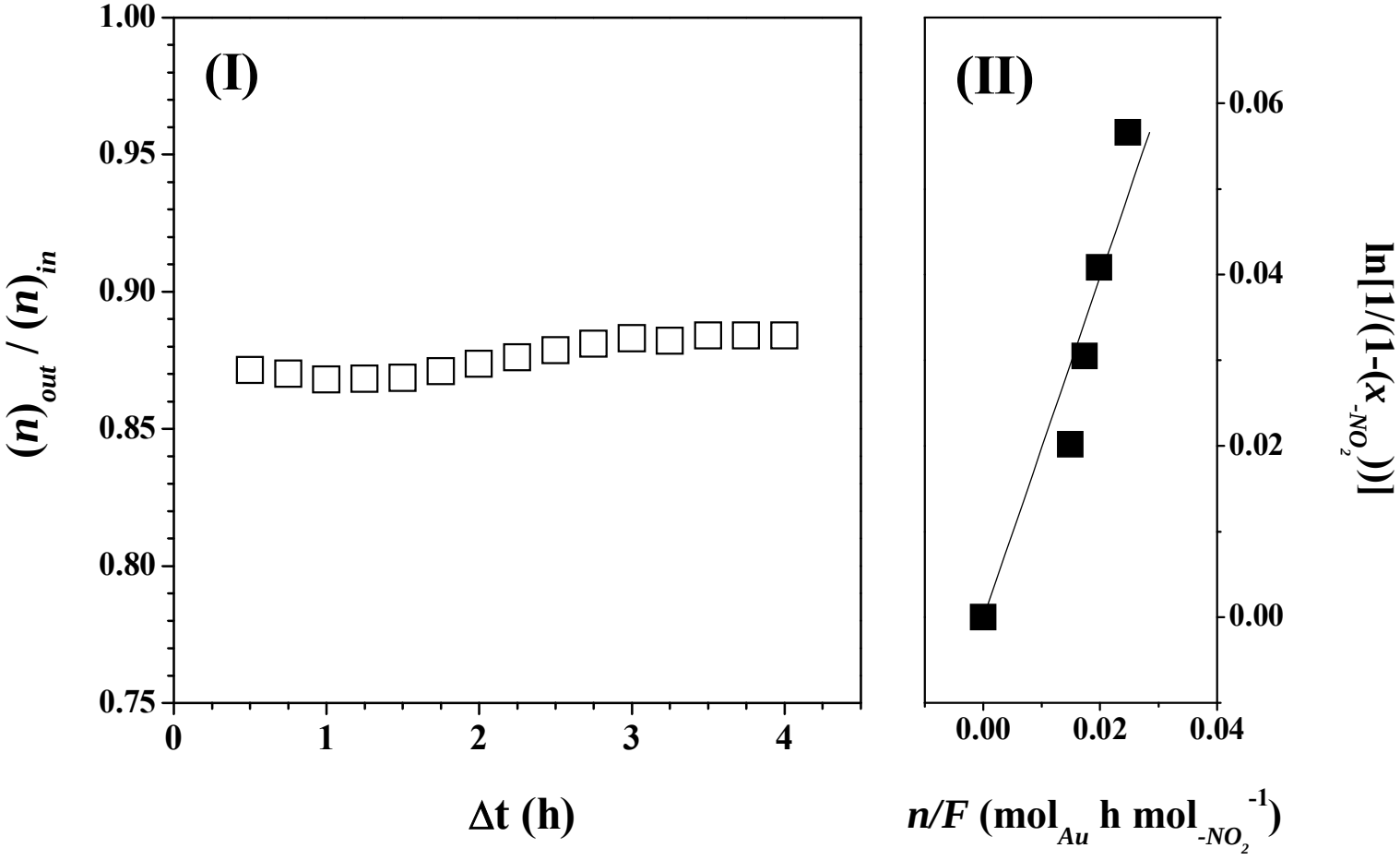

Figure 10.4: (I) Ratio of *m*-DNB in the exit stream ($(n)_{out}$) relative to that in the inlet stream ($(n)_{in}$) for reaction ($-NO_2$ /Au = 40 $mol_{-NO_2}\ mol_{Au}^{-1}\ h^{-1}$) over Au/Al_2O_3; (II) Pseudo-first-order kinetic plot for the reduction of *m*-DNB.

10.3.1.2 Catalyst activity/selectivity

In the conversion of *m*-DNB, Au/Al_2O_3 delivered 100% selectivity to the partially reduced *m*-NAN. This product is a valuable raw material employed in the manufacture of several fine chemicals [1]. Reactant conversion, presented in **Figure 10.4**(I) as the ratio of *m*-DNB in the exit ($(n)_{out}$) relative to that in the inlet ($(n)_{in}$) stream, essentially exhibited a temporal invariance. We have already established [12,13] the applicability of a pseudo-first order kinetic treatment for nitoarene reduction over supported Au where

$$\ln\left[\frac{1}{\left(1-(x_{-NO_2})\right)}\right] = k\left(\frac{n}{F}\right) \qquad \textbf{(10.5)}$$

The parameter (x_{-NO_2}) represents hydrogenation activity and (n/F) has the physical meaning of contact time. The linear relationship between $\ln(1-(x_{-NO_2}))^{-1}$ and n/F is shown in **Figure 10.4**(II) and the resultant pseudo-first order rate constant (k) is given in **Table 10.1**. The available published data dealing with the selective hydrogenation of *m*-DNB is very limited and we could not find any report that has demonstrated the exclusive formation of *m*-NAN. It is, nevertheless, worth flagging work conducted at high hydrogen pressures (10-45 atm) in the gas phase over Pt/C under supercritical CO_2 ($P_{CO_2} = 150$ atm) [31] and in the liquid phase using Pd/C [32] and polylvinylpyrrolidone stablilized Ru/Al_2O_3 [33] where *m*-NAN selectivities in excess of 80 % have been recorded.

10.3.2 Au-Ni/Al_2O_3

10.3.2.1 Catalyst Characterization

The TPR response (**Figure 10.1**, profile II) for the Ni/Al_2O_3 precursor is characterised by two stages of reduction during the temperature ramp with peak maxima at 595 K and 723 K, corresponding to the sequential $Ni(NO_3)_2 \rightarrow NiO \rightarrow Ni^0$ steps [24]. TPR of $Au\text{-}Ni/Al_2O_3$ (see profile III), prepared by the reductive deposition of Au onto passivated Ni, was accompanied by a low intensity H_2 consumption response with two ill-defined peaks at 446 and 603 K. In this preparative route (direct redox method), Ni with a lower electrochemical potential serves to reduce the deposited Au precursor ($HAuCl_4$) and, consequently, undergoes oxidation [34]. The $Au\text{-}Ni/Al_2O_3$ samples

exhibited H_2 uptake (< 1 μmol g^{-1}) close to the instrumental detection limits (see **Table 10.1**). BET area of both supported catalysts was significantly lower than that of the starting Al_2O_3 support (190 m^2 g^{-1}). This decrease in area was accompanied by a reduction in pore volume (**Table 10.1**), which can be attributed to a partial pore filling by the metal particles.

XRD analysis was undertaken to demonstrate Au-Ni alloy formation (see **Figure 10.2**). The diffractogram generated for Ni/Al_2O_3 (profile Ib) is characterised by a peak at 2θ = 44.5º due to the (111) plane of metallic Ni (JCPDS-ICDD 04-0850). XRD analysis of the bimetallic sample (profile Ic) did not reveal any peaks due to the individual metals (Au or Ni) but a new metallic phase is in evidence, with a characteristic 2θ = 42.8°, that is located between the peaks for $(111)_{Au}$ (2θ = 38.1°) and $(111)_{Ni}$ (2θ = 44.5°), the positions of which are illustrated in **Figure 10.2** by dotted and dashed vertical lines, respectively. This new phase can be attributed to the formation of a Au-Ni alloy. Indeed, this assertion is supported by the work of Togasaki and co-workers [25] who attributed an XRD peak at 2θ = 42º to amorphous Au-Ni alloy (8-51 % mol Au) prepared by the addition of $KAu(CN)_2$ to a Ni-W plating bath. Metal particle size was evaluated by the standard Scherrer line broadening approach (**Table 10.1**) where the metal particle size was smaller in the alloy compared with the monometallic sample. Au-Ni alloy formation is also supported by DRS UV-Vis analysis. The DRS UV-Vis response for Ni/Al_2O_3 shows a maximum (530-580 nm) that corresponds to metallic Ni [35]. In marked contrast, the spectrum recorded for $Au\text{-}Ni/Al_2O_3$ (profile IIc) did not generate any detectable peak/signal corresponding to metallic Au or Ni. Indeed, Mulvaney [36] established the formation of a Au-Ag alloy on the basis that the DRS UV-Vis spectrum did not exhibit the absorption bands for the component metals. Representative low (I), medium (II and III) and high (IV) resolution TEM images of $Au\text{-}Ni/Al_2O_3$ are presented in **Figure 10.5**. The particles exhibit a predominantly pseudo-spherical morphology, with a wide size distribution (<5-200 nm), similar to that observed for Au/Al_2O_3. The diffractogram pattern for an isolated particle is shown in **Figure 10.5** (IV) where the characteristic *d*-spacing obtained is consistent with that obtained by XRD, confirming alloy formation.

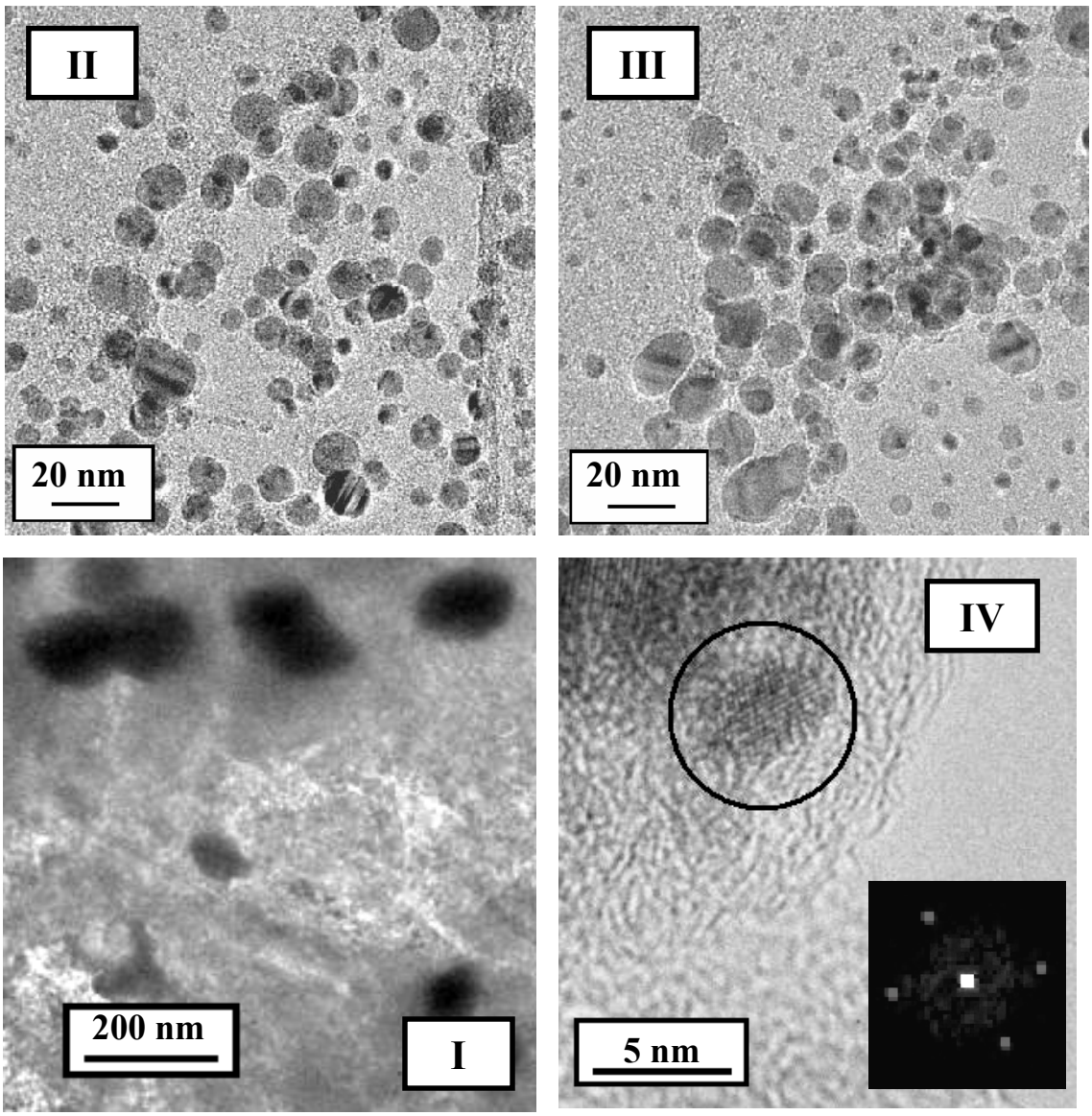

Figure 10.5: Representative TEM images of Au-Ni/Al_2O_3; (I) low, (II) and (III) medium and (IV) high resolution.

10.3.2.2 Catalyst activity/selectivity

A pseudo-first order kinetic treatment of the data generated for Au-Ni/Al_2O_3 is presented in **Figure 10.6**(I) and the associated rate constant value (k) is given in **Table 10.1**. The studies to date that have considered Au based alloy catalysts (Au-Pd [17,37], Au-Pt [18]) have resulted in an increased hydrogenation activity relative to the mono-metallic Au catalyst. In this study Au-Ni/Al_2O_3 delivered a significantly lower (by a factor of 7) rate compared with Au/Al_2O_3. We could not find any directly related study that has compared the hydrogenation performance of a supported Au-Ni alloy with that of the constituent metals. Chin *et al.* [21] employed $MgAl_2O_4$-supported Au-Ni alloy to promote CH_4 reforming and observed a decrease in catalytic activity that was ascribed

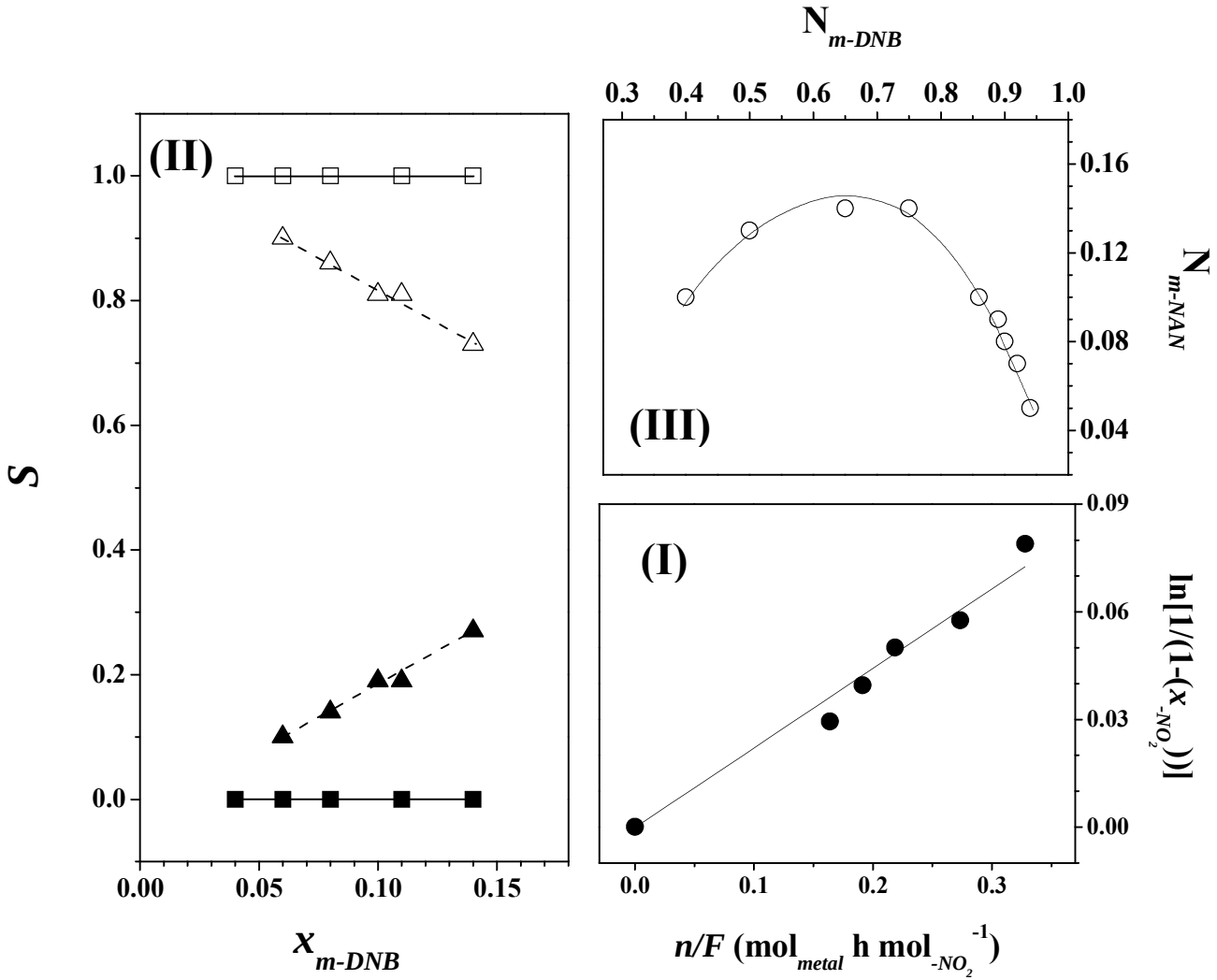

Figure 10.6: Pseudo-first-order kinetic plot for the reduction of *m*-DNB over Au-Ni/Al_2O_3; (II) Variation of *m*-PDM (solid symbols) and *m*-NAN (open symbols) selectivity (*S*) with *m*-DNB fractional conversion ($x_{m\text{-}DNB}$) for reaction over Au/Al_2O_3 (■/□, solid line) and Au-Ni/Al_2O_3 (▲/Δ, dashed line); (III) Dependence of *m*-NAN mole fraction ($N_{m\text{-}NAN}$) on *m*-DNB conversion for reaction over Au-Ni/Al_2O_3. *Note*: line represents fit to the parallel/consecutive model, see Equation (10.14).

to an occlusion of the Ni step and edge sites by Au. Vasil'kov and co-workers [38] have recently quoted an increased catalytic activity (up to two orders of magnitude) for the isomerization of allylbenzene over Au-Ni/SiO_2 as a consequence of a surface Au-Ni synergism (demonstrated by XPS). A series of experiments were conducted to probe the effect(s) of alloy formation on reaction selectivity. The results are presented in **Figure 10.6**(II) where quite distinct selectivity responses are in evidence. While Au/Al_2O_3 delivered 100% selectivity to the partially reduced *m*-NAN, Au-Ni/Al_2O_3 generated a mixture of partially and fully (*m*-PDM) reduced products with a shift in favour of the latter with increasing *m*-DNB conversion. We tentatively link the differences in the activity/selectivity responses presented in **Figure 10.6**(II) for the two systems under study to differences in the reactant adsorption/activation mechanism. Indeed, a distinct mechanism in the adsorption of nitroarenes over Au and Au-M (M = Pb, Tl) systems has been suggested elsewhere [39]. The hydrogenation of *m*-DNB can proceed *via* consecutive/parallel steps according to:

$$m\text{-}DNB + 3H_2 \xrightarrow{k_1} m\text{-}NAN + 2H_2O \qquad \textbf{(10.6)}$$

$$m\text{-}NAN + 3H_2 \xrightarrow{k_2} m\text{-}PDM + 2H_2O \qquad \textbf{(10.7)}$$

$$m\text{-}DNB + 6H_2 \xrightarrow{k_3} m\text{-}PDM + 4H_2O \qquad \textbf{(10.8)}$$

and

$$\frac{dN_{m\text{-}DNB}}{d\left(n/F_{m\text{-}DNB}\right)} = -\left(k_1 + k_3\right) \times N_{m\text{-}DNB} \qquad \textbf{(10.9)}$$

$$\frac{dN_{m\text{-}NAN}}{d\left(n/F_{m\text{-}DNB}\right)} = k_1 \times N_{m\text{-}DNB} - k_2 \times N_{m\text{-}NAN} \qquad \textbf{(10.10)}$$

$$\frac{dN_{m\text{-}PDM}}{d\left(n/F_{m\text{-}DNB}\right)} = k_2 \times N_{m\text{-}NAN} + k_3 \times N_{m\text{-}DNB} \qquad \textbf{(10.11)}$$

where N_i represents the molar fraction of the ith compound and k_j is the pseudo-first order rate constant of step j. Combination of **Equations (10.9)** and **(10.10)** gives

$$\frac{dN_{m\text{-}NAN}}{dN_{m\text{-}DNB}} = -L + M \times \left(\frac{N_{m\text{-}NAN}}{N_{m\text{-}DNB}} \right) \qquad \textbf{(10.12)}$$

with

$$L = \frac{k_1}{k_1 + k_3} \quad \therefore \quad M = \frac{k_2}{k_1 + k_3} \qquad \textbf{(10.13)}$$

which, by formal integration, results in:

$$N_{m\text{-}NAN} = \frac{L}{1 - M} \times \left({N_{m\text{-}DBN}}^{M} - N_{m\text{-}DBN} \right) \qquad \textbf{(10.14)}$$

The values of L and M determine the preferred reaction pathway; a stepwise -NO_2 group reduction mechanism (with *m*-NAN as intermediate) should result in a value for L close to unity (k_3~0) and M>1 (k_2>(k_1+k_3)). Indeed, the fit of our experimental results for Au-Ni/Al_2O_3 to **Equation (10.14)** (see **Figure 10.6** III) yields values of L = 1.0 and M = 5.0 that are consistent with a stepwise reaction network.

One unique aspect of this work has been the exclusive production of the partially reduced *m*-NAN product over Au/Al_2O_3, *i.e.* (k_1>>(k_2+k_3)). This level of exclusivity in a continuous process can serve as the basis for the development of a new sustainable route to a range of high value amino-compounds. Moreover, we have provided the first reported catalytic application over an alumina supported Au-Ni alloy in a hydrogenation process. The requirement of a high treatment temperature to form the supported alloy [23] (see Experimental section), which was also applied to Au/Al_2O_3 to facilitate a direct comparison of catalytic performance, has resulted in the formation of larger supported metal particles (see **Table 10.1**, **Figures 10.3** and **10.5**). The dependence of activity and selectivity on particle size in Au catalytic systems is still unclear. It has been proposed that surface defects and smaller Au particle sizes (<10 nm) are required for significant hydrogenation activity [10]. Bailie and co-workers [40], studying the

hydrogenation of but-2-enal over Au/ZnO, proposed that a high selectivity to but-2-en-1-ol required larger Au particles (10-20 nm). Moreover, Hofmeister *et al.* [41] reported lower hydrogenation rates associated with Au particles < 2 nm and ascribed this to quantum size effects that modified the electronic properties of the Au particles. Future work will focus on the role of particle size in selective hydrogenation with a consideration of alternative catalyst formulations, activation and reaction conditions with the goal of delivering enhanced reaction rates while retaining the product exclusivity that we report here.

10.4 Conclusions

The results presented in this communication demonstrate that Au/Al_2O_3 exclusively promotes the partial reduction of *m*-DNB to *m*-NAN in gas phase continuous operation with no detectable catalyst deactivation (up to 4 h on-stream). We have provided, for the first time, evidence of catalytic hydrogenation activity associated with an alumina supported Au-Ni alloy. Alloy formation has been established by XRD (new reflection at $2\theta = 42.8°$) and confirmed by TEM analyses. In addition, the DRS UV-Vis spectrum for $Au\text{-}Ni/Al_2O_3$ did not exhibit the absorption bands that characterised Au/Al_2O_3 and Ni/Al_2O_3. The supported alloy delivered a lower hydrogenation rate (by almost an order of magnitude) and promoted both partial and complete hydrogenation, following a stepwise reaction mechanism.

10.5 References

[10.1] P. F. Vogt, J. J. Gerulis, Ullmann's Encyclopedia of Industrial Chemistry. "Aromatic Amines", Wiley-VCH Verlag GmbH & Co. KGaA, Weinheim, 2005.

[10.2] X. D. Wang, M. H. Liang, J. L. Zhang, Y. Wang, Curr. Org. Chem., 11, 299 (2007)

[10.3] K. R. Westerterp, E. J. Molga, K. B. van Gelder, Chem. Eng. Process., 36, 17 (1997)

[10.4] V. Vishwanathan, V. Jayasri, P. M. Basha, N. Mahata, L. M. Sikhwivhilu, N. J. Coville, Catal. Commun., 9, 453 (2008)

[10.5] Y. X. Liu, J. X. Chen, J. Y. Zhang, Chin. J. Chem. Eng., 15, 63 (2007)

[10.6] M. M. Telkar, J. M. Nadgeri, C. V. Rode, R. V. Chaudhari, Appl. Catal. A: Gen., 295, 23 (2005)

[10.7] Y. Chen, J. Qiu, X. Wang, J. Xiu, J. Catal., 242, 227 (2006)

[10.8] A. Corma, P. Serna, Science, 313, 332 (2006)

[10.9] D. He, H. Shi, Y. Wu, B.-Q. Xu, Green Chem., 9, 849 (2007)

[10.10] P. Claus, Appl. Catal. A: Gen., 291, 222 (2005)

[10.11] M. Boronat, P. Concepción, A. Corma, S. González, F. Illas, P. Serna, J. Am. Chem. Soc., 129, 16230 (2007)

[10.12] F. Cárdenas-Lizana, S. Gómez-Quero, M. A. Keane, ChemSusChem, 1, 215 (2008)

[10.13] F. Cárdenas-Lizana, S. Gómez-Quero, M. A. Keane, Catal. Commun., 9, 475 (2008)

[10.14] T. Joseph, K. V. Kumar, A. V. Ramaswamy, S. B. Halligudi, Catal. Commun., 8, 629 (2007)

[10.15] G. J. Hutchings, Chem. Commun., 2008, p. 1148.

[10.16] J. K. Edwards, A. F. Carley, A. A. Herzing, C. J. Kiely, G. J. Hutchings, Faraday Discuss., 138, 225 (2008)

[10.17] V. I. Pârvulescu, V. Pârvulescu, U. Endruschat, G. Filoti, F. E. Wagner, C. Kübel, R. Richards, Chem. Eur. J., 12, 2343 (2006)

[10.18] B. Pawelec, A. M. Venezia, V. La Parola, S. Thomas, J. L. G. Fierro, Appl. Catal. A: Gen., 283, 165 (2005)

[10.19] A. M. Molenbroek, J. K. Nørskov, J. Phys. Chem. B, 105, 5450 (2001)

[10.20] N. C. Triantafyllopoulos, S. G. Neophytides, J. Catal., 239, 187 (2006)

[10.21] Y.-H. Chin, D. L. King, H.-S. Roh, Y. Wang, S. M. Heald, J. Catal., 244, 153 (2006)

[10.22] G. Yuan, C. Louis, L. Delannoy, M. A. Keane, J. Catal. , 247, 256 (2007)

[10.23] H. Reichert, A. Schöps, I. B. Ramsteiner, V. N. Bugaev, O. Shchyglo, A. Udyansky, H. Dosch, M. Asta, R. Drautz, V. Honkimäki, Phys. Rev. Lett., 95, 235703 (2005)

[10.24] F. Cárdenas-Lizana, S. Gómez-Quero, M. A. Keane, Appl. Catal. A: Gen., 334, 199 (2008)

[10.25] N. Togasaki, Y. Okinaka, T. Homma, T. Osaka, Electrochim. Acta, 51, 882 (2005)

[10.26] G. Tavoularis, M. A. Keane, J. Chem. Technol. Biotechnol., 74, 60 (1999)

[10.27] J. Guzman, B. C. Gates, J. Phys. Chem. B, 107, 2242 (2003)

[10.28] E. Bus, R. Prins, J. A. van Bokhoven, Phys. Chem. Chem. Phys., 9, 3312 (2007)

[10.29] A. C. Gluhoi, N. Bogdanchikova, B. E. Nieuwenhuys, J. Catal., 232, 96 (2005)

[10.30] G. C. Bond, C. Louis, D. T. Thompson, Catalysis by Gold, Imperial College Press, London, 2006.

[10.31] F. Zhao, S.-I. Fujita, J. Sun, Y. Ikushima, M. Arai, Catal. Today, 98, 523 (2004)

[10.32] V. L. Khilnani, S. B. Chandalia, Org. Process Res. Dev., 5, 263 (2001)

[10.33] S. Zhao, H. Liang, Y. Zhou, Catal. Commun., 8, 1305 (2007)

[10.34] J. Barbier, Handbook of Heterogeneous Catalysis. Redox Methods for Preparation of Bimetallic Catalysts, VCH Verlagsgesellschaft mbH, Weinheim (Germany), 1997.

[10.35] Z. Li, Y. Deng, Y. Wu, B. Shen, W. Hu, J. Mater. Sci., 42, 9234 (2007)

[10.36] P. Mulvaney, Langmuir, 12, 788 (1996)

[10.37] B. Pawelec, A. M. Venezia, V. La Parola, E. Cano-Serrano, J. M. Campos-Martin, J. L. G. Fierro, Appl. Surf. Sci., 242, 380 (2005)

[10.38] A. Yu. Vasil'kov, S. A. Nikolaev, V. V. Smirnov, A. V. Naumkin, I. O. Volkova, V. L. Podshibikhina, Mendeleev Commun., 17, 268 (2007)

[10.39] A. Papoutsis, G. Kokkinidis, J. Electroanal. Chem., 371, 231 (1994)

[10.40] J. E. Bailie, H. A. Abdullah, J. A. Anderson, C. H. Rochester, N. V. Richardson, N. Hodge, J. G. Zhang, A. Burrows, C. J. Kiely, G. J. Hutchings, Phys. Chem. Chem. Phys., 3, 4113 (2001)

[10.41] P. Claus, A. Brückner, C. Mohr, H. Hofmeister, J. Am. Chem. Soc., 122, 11430 (2000)

Chapter 11

Gas Phase Hydrogenation of Nitroarenes: A Comparison of the Catalytic Action of Titania Supported Gold and Silver

In the preceding Chapters, exclusive (and time invariant) -NO_2 group reduction has been established for supported Au systems. In the final section of this thesis, a direct comparison of the catalytic behaviour of (TiO_2) supported Au and Ag in the gas phase hydrogenation of a group of *para*-substituted nitroarenes is presented where the catalytic results are correlated using the Hammett equation.

11.1 Introduction

The catalytic hydrogenation of poly-functional nitro-compounds to the corresponding amino-product is of commercial importance in the manufacture of a diversity of herbicides, dyes and pharmaceuticals [1]. Exclusivity in terms of -NO_2 group reduction is difficult to achieve in the presence of other substituents (*e.g.* -Cl, -CH_3 and/or -OH), as has been noted for the hydrogenation of a range of aliphatic [2] and aromatic [3] nitro-compounds in both gas [4,5] and liquid [6,7] phase operation. The conventional synthesis route for amino-derivates, using stoichiometric amounts of Fe in acid media (Béchamp process) is no longer sustainable due to the negative environmental impact associated with toxic by-product formation (*e.g.* iron oxides) [8]. The catalytic (liquid phase) alternative using conventional transition metals (*e.g.* Ni [9] Pd [10] and/or Pt [7]) also exhibits limitations in terms of undesirable toxic secondary reaction products, *i.e.* azo- [11] and/or azoxy-derivates [12]. Various attempts have been reported to enhance selectivity to the target amino-compound, through the use of additives [13], variations in catalyst preparation [9,14] and the incorporation of a second metal [15,16]. Gold and (to a lesser extent) silver have been successfully used in the hydrogenation of CO_2 [17], NO_x [18,19], alkenes [20] and α,β-unsaturated aldehydes [21,22]. Moreover, recent studies of batch liquid phase nitroarene reduction over supported Au [14,23] and Ag [24-26] show potential in terms of high selectivity to amino-compound formation. We have previously demonstrated exclusive -NO_2 group reduction in the hydrogenation of chloro- [4,27-29] and di-nitrobenzene [30] over

supported Au in continuous gas phase operation. To the best of our knowledge, the catalytic action of supported Ag in the gas phase hydrogenation of nitro-compounds has not been reported in the literature. In this study, we compare the catalytic properties of supported Ag with the Au counterpart in the hydrogenation of a series of substituted nitro-compounds that give rise to industrially important amino-derivates.

In general, supported Au [17,31,32] and/or Ag [17,21,33] have exhibited lower hydrogenation activities relative to conventional transition metal catalysts, *e.g.* supported Ni [31], Pd [33], Pt [32] or Rh [21]. There is evidence [22,34-36] of a structure sensitive response in the case of Au where increased efficiency is attributed to smaller particles (≤ 10 nm). Theoretical calculations have demonstrated a high energy barrier for H_2 dissociation on group IB metals [37] and, in the case of Au catalysts, H_2 activation has been associated with step, edge and corner sites on small Au particles [38]. While we could not find any study that explicitly compares the catalytic performance of Au with Ag in nitroarene reduction, we can flag related reports dealing with hydrogen mediated reactions. Deng *et al.* [39] studied the hydrogenation of anthracene with $NaBH_4$ as reducing agent over (unsupported) Ag and Au nanoparticles and found a higher rate over the former for particles below 4 nm, a response that they associated with a higher capacity of silver to generate hydrogen for reaction. Słoczyński *et al.* [17] considered M/($ZnO{\cdot}ZrO_2$) (M = Cu, Au and Ag; mole ratio ZnO/ZrO_2 = 3) and reported a similar yield of methanol (from CO_2) over the Au and Ag catalysts that was lower to that for Cu/($ZnO{\cdot}ZrO_2$), and ascribed this response to a low stabilization of the Ag^+ and Au^+ ions under reaction conditions. In contrast, Wambach and co-workers [40] observed the exclusive formation of methanol over Ag/ZrO_2 while methane, methanol and CO were generated over Au/ZrO_2, a result associated with the distinct nature of the active metal but the authors did not elaborate further. We provide, in this report, a direct comparison of titania supported Au and Ag (at 1 mol % loading) in the selective hydrogenation of a series of *para*-substituted nitroarenes where the catalytic response has been correlated to critical characterization measurements.

11.2 Experimental

11.2.1 Materials and Catalyst Preparation

The TiO_2 (Degussa, P25) support was used as received. Two (1 mol %) TiO_2 supported Au and Ag catalyst precursors were prepared by standard impregnation where

adequate volumes of $HAuCl_4$ (Aldrich, 25×10^{-3} g cm^{-3}, pH = 2) and $AgNO_3$ (Riedel-de Haën, 1×10^{-3} g cm^{-3}) solutions were added to 5 g of support. The slurry was heated (2 K min^{-1}) to 353 K and maintained under constant agitation (600 rpm) in a He purge. The solid residue was dried in a flow of He at 383 K for 3 h and stored under He in the dark at 277 K. Prior to use in catalysis, the samples (sieved into a batch of 75 μm average diameter) were activated in 60 cm^3 min^{-1} H_2 at 2 K min^{-1} to 603 ± 1 K, which was maintained for 2.5 h. After activation, the samples were passivated in 1% v/v O_2/He at room temperature for off-line analysis.

11.2.2 Characterization Analyses

The temperature programmed reduction (TPR) response, BET area and H_2 chemisorptions were recorded using the commercial CHEMBET 3000 (Quantachrome Instrument) unit with data acquisition/manipulation using the TPR Win™ software. The samples were loaded into a U-shaped Pyrex glass cell (100 mm × 3.76 mm i.d.) and heated in 17 cm^3 min^{-1} (Brooks mass flow controlled) 5% v/v H_2/N_2 to 603 K at 2 K min^{-1}. The effluent gas passed through a liquid N_2 trap and changes in H_2 consumption were monitored by TCD (thermal conductivity detector). The reduced samples were swept with 65 cm^3 min^{-1} N_2 for 1.5 h, cooled to room temperature and subjected to H_2 chemisorption using a pulse (10-50 μl) titration procedure. Hydrogen pulse introduction was repeated until the signal area was constant, indicating surface saturation. BET areas were recorded with a 30% v/v N_2/He flow; pure N_2 (99.9%) served as the internal standard. At least two cycles of N_2 adsorption-desorption in the flow mode were used to determine total surface area using the standard single point method. BET surface area and H_2 uptake values were reproducible to within ± 5% and the values quoted in this paper represent the mean. Powder X-ray diffractograms were recorded on a Bruker/Siemens D500 incident X-ray diffractometer using Cu Kα radiation. The samples were scanned at a rate of 0.02º $step^{-1}$ over the range $20º \leq 2\theta \leq 90º$ (scan time = 5 s $step^{-1}$). Diffractograms were identified using the JCPDS-ICDD reference standards, *i.e.* anatase (21-1272), rutile (21-1276), Au (04-0784) and Ag (04-0783). Diffuse reflectance UV-vis (DRS UV-vis) measurements were conducted using a Perkin Elmer Lambda 35 UV-vis Spectrometer with $BaSO_4$ powder as reference; absorption profiles were calculated from the reflectance data using the Kubelka-Munk function. Transmission electron microscopy analysis was conducted using a JEOL JEM 2011 HRTEM unit with a UTW energy dispersive X-ray detector (EDX) detector (Oxford

Instruments) operated at an accelerating voltage of 200 kV and using Gatan DigitalMicrograph 3.4 for data acquisition/manipulation. Samples for analysis were prepared by dispersion in acetone and deposited on a holey carbon/Cu grid (300 Mesh). Up to 400 individual metal particles were counted for each catalyst and the surface area-weighted metal diameter (d_{TEM}) was calculated from

$$d_{TEM} = \frac{\sum_i n_i d_i^3}{\sum_i n_i d_i^2} \qquad \textbf{(11.1)}$$

where n_i is the number of particles of diameter d_i. The size limit for the detection of metal particles on TiO_2 is *ca.* 1 nm.

11.2.3 Catalytic Procedure

Reactions were carried out under atmospheric pressure, *in situ* immediately after activation, in a fixed bed vertical continuous glass reactor (l = 600 mm, i.d. = 15 mm) at T = 473 K. The catalytic reactor, and operating conditions to ensure negligible heat/mass transport limitations, have been fully described elsewhere [41] but some features, pertinent to this study, are given below. A preheating zone (layer of borosilicate glass balls) ensured that the nitroarene reactant was vaporized and reached reaction temperature before contacting the catalyst. Isothermal conditions (± 1 K) were maintained by thoroughly mixing the catalyst with ground glass (75 μm) before insertion into the reactor. The temperature was continuously monitored by a thermocouple inserted in a thermowell within the catalyst bed. Butanolic solutions of the nitroarene reactants were delivered, in a co-current flow of H_2, *via* a glass/teflon air-tight syringe and a teflon line, using a microprocessor controlled infusion pump (Model 100 kd Scientific) at a fixed calibrated flow rate, with an inlet -NO_2 molar flow (F_{-NO_2}) over the range 0.01-0.11 $mmol_{-NO_2}\ h^{-1}$, where the molar metal to inlet molar -NO_2 feed rate ratio spanned the range $2\times10^{-2} - 27\times10^{-2}$ h. The H_2 content was at least 150 times in excess of the stoichiometric requirement, the flow rate of which was monitored using a Humonics (Model 520) digital flowmeter; $GHSV = 2 \times 10^4\ h^{-1}$. In a series of blank tests, passage of each nitroarene in a stream of H_2 through the empty reactor or over the support alone, *i.e.* in the absence of Au or Ag, did not result in any detectable conversion. The

reactor effluent was frozen in a liquid nitrogen trap for subsequent analysis, which was made using a Perkin-Elmer Auto System XL gas chromatograph equipped with a programmed split/splitless injector and a flame ionization detector, employing a DB-1 50 m × 0.20 mm i.d., 0.33 μm film thickness capillary column (J&W Scientific), as described elsewhere [42]. The reactants: nitrobenzene, *p*-nitrophenol, *p*-nitroanisole, *p*-nitrotoluene, *p*-chloronitrobenzene and *p*-dinitrobenzene (Aldrich, ≥ 98%) and the solvent (1-butanol: Riedel-de Haën) were used as supplied without further purification. Repeated catalytic runs with different samples from the same batch of catalyst delivered product compositions that were reproducible to within ± 6%. Hydrogenation activity is expressed in terms of the degree of nitro-group reduction ($x_{\text{-}NO_2}$)

$$x_{\text{-}NO_2} = \frac{[\text{-NH}_2]_{out}}{[\text{-NO}_2]_{in}} \qquad \textbf{(11.2)}$$

where the subscripts *in* and *out* refer to the inlet and outlet streams.

11.3 Results and Discussion

11.3.1 Catalyst Characterization

The results of the BET surface area, room temperature H_2 chemisorption, DRS UV-vis measurement along with the mean metal particle sizes (and range of values) obtained from TEM analysis are given in **Table 11.1**. In terms of TPR analysis, the experimentally determined hydrogen consumption is also given and can be compared with the predicted (or theoretical) values based on the precursor loading. The TPR profiles generated for Au/TiO_2 (AI) and Ag/TiO_2 (BI) are shown in **Figure 11.1**. In the case of Au/TiO_2, hydrogen consumption matched (within 2%) that required for the reduction of $HAuCl_4$ to the metallic form. This result is consistent with reports in the literature where a single reduction step ($Au^{3+} \rightarrow Au^0$) at $T \leq 503$ K has been proposed [27,43-45] for oxide (Al_2O_3 and/or TiO_2) supported Au prepared by impregnation. Hydrogen consumption during TPR in the case of Ag/TiO_2 is consistent with a two step reduction mechanism, *i.e.* $AgNO_3 \rightarrow Ag_2O \rightarrow Ag^0$, as has been suggested for Ag supported on TiO_2 [46], Al_2O_3 [47], SiO_2 [48] and carbon [49]. Bogdanchikova *et al.* [50] examined an Ag/Al_2O_3 precursor prepared by impregnation with $AgNO_3$ and

established (by XRD) that Ag^0 was not present in the precursor, demonstrating metallic Ag formation post-TPR (to 673 K).

Table 11.1: BET surface area, hydrogen consumed (theoretical and experimentally determined) during activation by TPR, H_2 chemisorption values, DRS UV-vis characteristics, metal particle size (mean and range), specific metal surface area and pseudo-first order rate constants for the hydrogenation of nitrobenzene (to aniline) associated with Au/TiO_2 and Ag/TiO_2.

Catalyst	Au/TiO_2	Ag/TiO_2
BET area ($m^2\ g^{-1}$)	47	48
TPR H_2 consumption/ theoretical ($\mu mol\ g^{-1}$)	193	130
TPR H_2 consumption/ experimental ($\mu mol\ g^{-1}$)	195	140
H_2 chemisorption ($\mu mol\ g_{metal}^{-1}$)	15	5
DRS UV-vis A_{max} (nm)	568	450
d_{TEM} (nm)	6.1	7.3
S_{metal} ($m^2_{metal}\ g^{-1}_{metal}$) [a]	53	82
Metal size range (nm)	1-10	1-15
k_{473K} [b] (k'_{473K}) [c]	2 [b] (15×10^{-5}) [c]	1 [b] (12×10^{-5}) [c]

[a] $S_{metal} = 6/(\rho_{metal} \times d_{TEM})$ where $\rho_{Au} = 18.88\ g\ cm^{-3}$; $\rho_{Ag} = 10.50\ g\ cm^{-3}$

[b] units = $mol_{\text{-}NO_2}\ mol^{-1}_{metal}\ h^{-1}$

[c] units = $mol_{\text{-}NO_2}\ m^{-2}_{metal}\ h^{-1}$

The room temperature H_2 chemisorption values recorded for both catalysts were close to the instrument detection limits but the uptake on Ag/TiO_2 was measurably lower. These values are in keeping with the low capacity of Au [4,37] and Ag [51,52] for H_2 uptake due to the completely filled *d*-band [35,53].

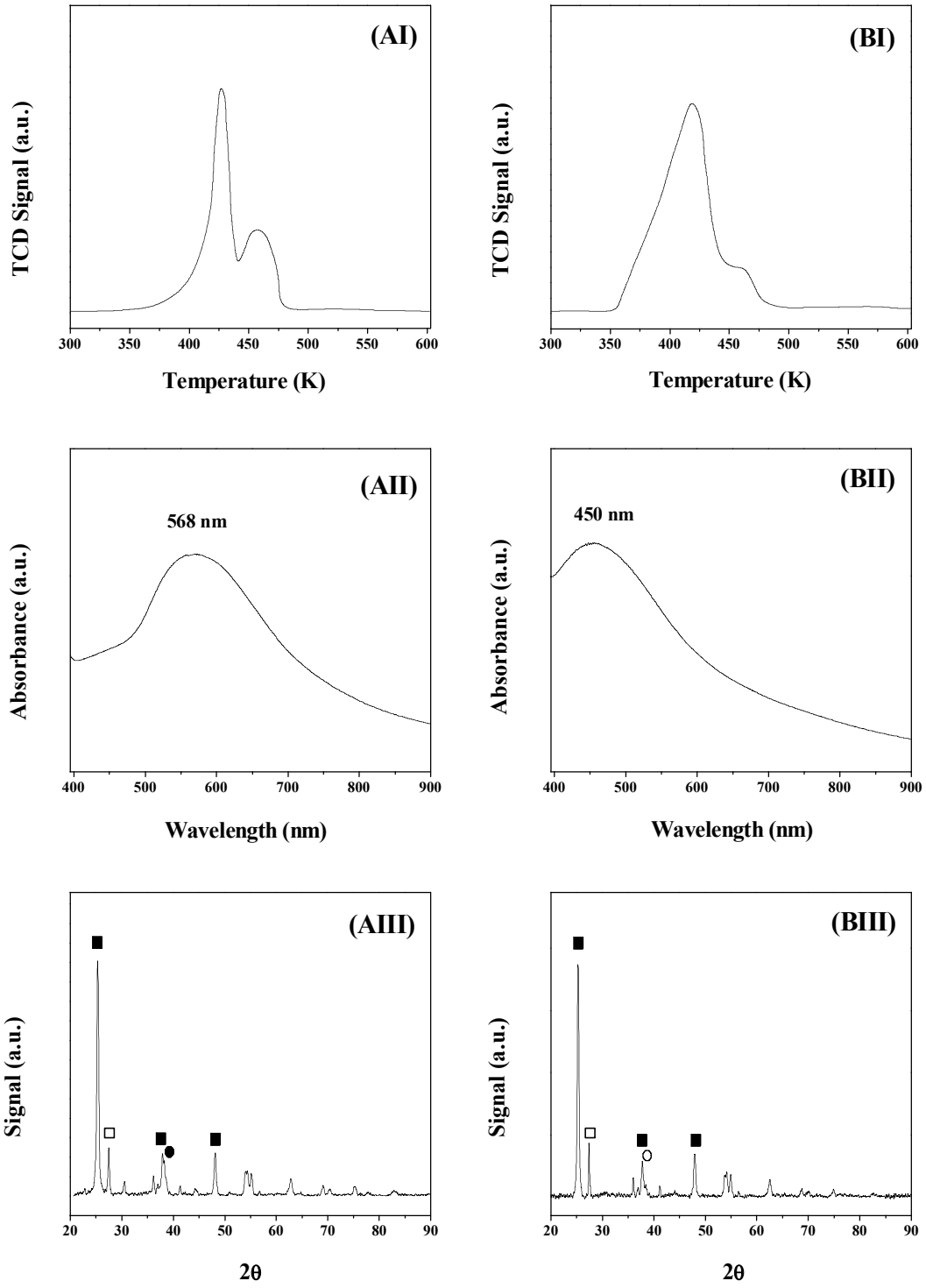

Figure 11.1: Au/TiO_2 (A) and Ag/TiO_2 (B) TPR profiles (I), DRS UV-vis spectra (II) and XRD patterns (III). *Note*: XRD peak assignments based on JCPDS-ICDD reference data: (■) anatase (21-1272); (□) rutile (21-1276); (●) Au (04-0784) and (○) Ag (04-0783).

The DRS UV-vis spectra for the passivated/reduced samples are shown in **Figure 11.1**. The spectrum for Au/TiO_2 (AII) exhibits an absorption band at *ca.* 568 nm characteristic of Au nanoclusters on a titania substrate [54]. The spectrum for Ag/TiO_2 (BII) is dominated by an absorption band at *ca.* 450 nm, which can be linked to the presence of Ag^0. Indeed, wavelengths > 390 nm have been attributed elsewhere [24,50] to the presence of metallic Ag particles. Jia *et al.* [55] have associated a band at 420 nm to absorbance by Ag nano-particles, where a displacement to higher wavelengths was ascribed to an increase in particle size (from 6 nm to 18 nm). The XRD profiles for passivated/reduced Au/TiO_2 (AIII) and Ag/TiO_2 (BIII) are also presented in **Figure 11.1**. Both systems present signals at $2\theta = 25.3°$, 37.8° and 48.1° corresponding to the (101), (004) and (200) planes of tetragonal anatase-phase TiO_2 (JCPDS-ICDD 21-1272). Moreover, the peak at 27.4° suggests the presence of tetragonal rutile-phase TiO_2 (JCPDS-ICDD 21-1276). This XRD response is consistent with a mixture of anatase (80% volume fraction) and rutile forms of TiO_2 in agreement with the reported [56] Degussa P25 composition. It is important to note that only weak signals (overlapping with the (004) anatase peak) due to metallic Au and Ag (2θ = 38.1°) were distinguishable, a result that suggests a highly dispersed metallic phase.

In the case of titania supported metals, the migration of Ti suboxide species on top of the metal particles is known to occur at elevated temperature (≥ 773 K) and is denoted as an encapsulation or decoration [57]. We observed a similar effect in our TEM analysis after prolonged electron beam irradiation. This is illustrated for Au/TiO_2 in **Figure 11.2**. In both images, the encapsulation of Au nano-particles is in evidence. Indeed, in image (II) atomic layers of the support can be seen (see arrows) on top of an isolated Au particle. The diffractogram patterns for selected areas of the support and an Au particle are shown in images (IA) and (IB), respectively. In both cases, the *d*-spacing obtained (*ca.* 0.35 nm) are similar and close to that associated with the characteristic (101) main plane of TiO_2-anatase (JCPDS-ICDD 21-1272). Metal encapsulation as a result of analytical TEM measurements has been previously shown for Au/CeO_2 [58] but we provide here, for the first time, evidence of such an effect for Au/TiO_2. In order to circumvent this response, all images of the catalyst surface were taken at short beam exposure times. Representative high resolution TEM images (I and II) and metal particle size distributions (based on TEM measurements, V) of reduced/passivated Au/TiO_2 (A) and Ag/TiO_2 (B) are given in **Figure 11.3**.

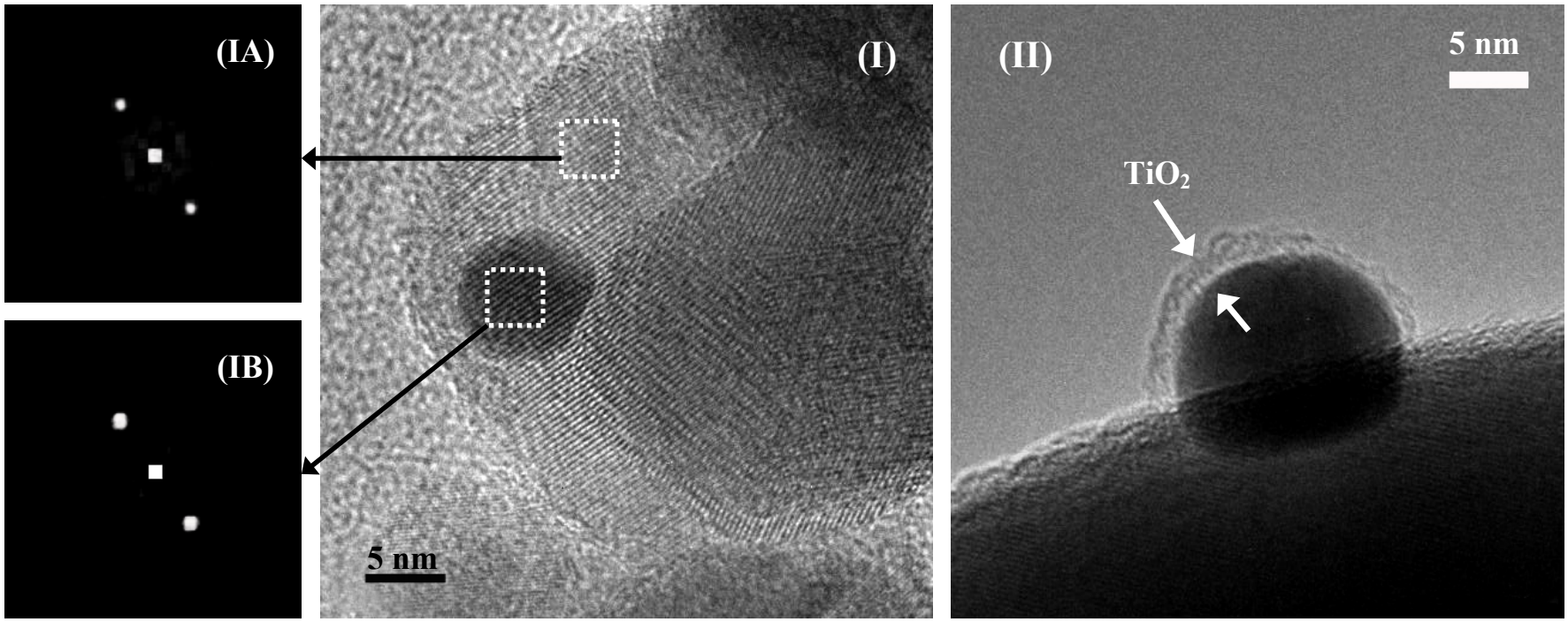

Figure 11.2: Representative TEM images of passivated/reduced (I and II) Au/TiO_2 with diffractrogam patterns (IA and IB) for the selected dashed areas. *Note:* arrows in image (II) indicate TiO_x layer covering Au particle.

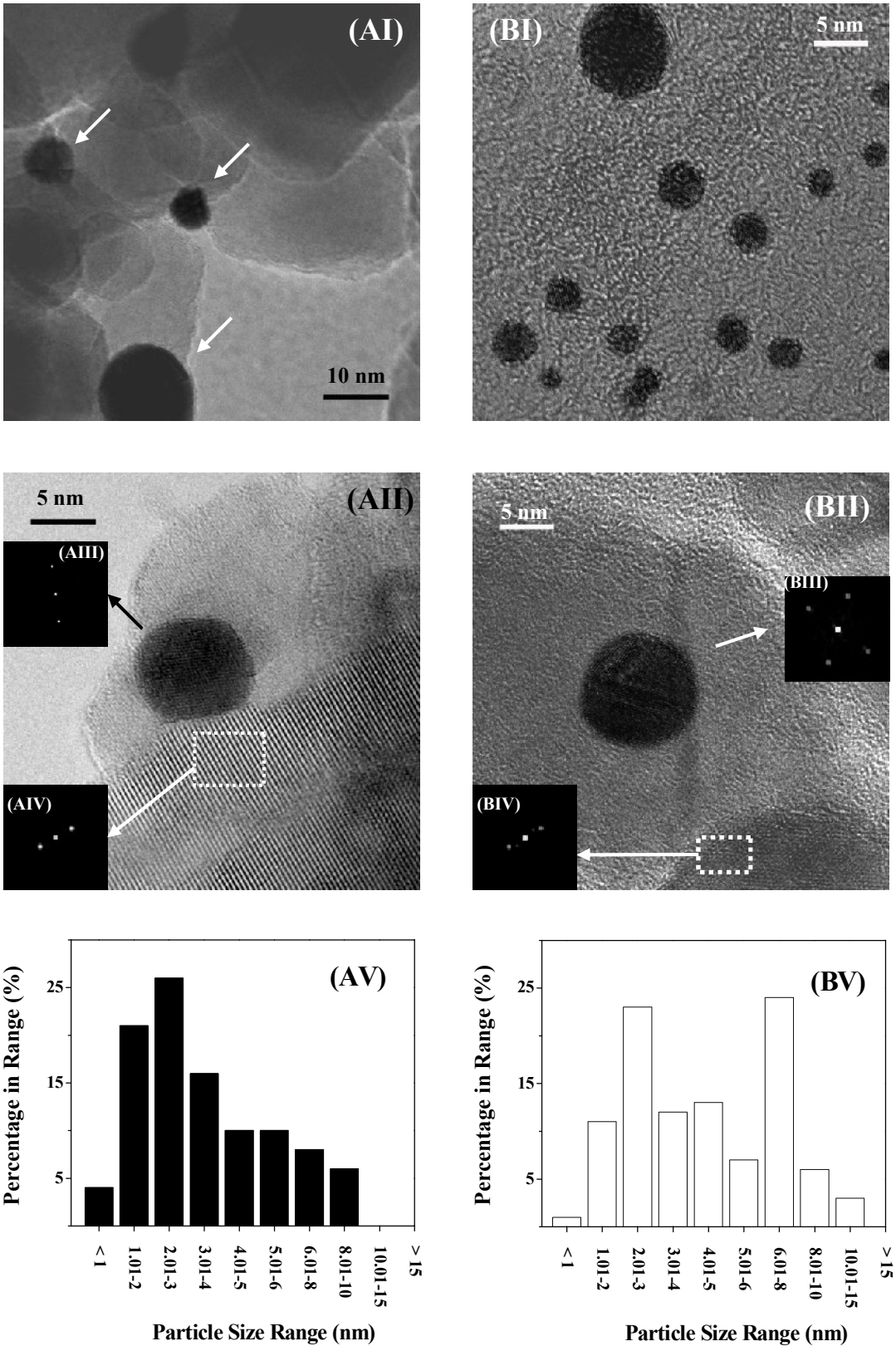

Figure 11.3: Representative high resolution TEM images (I and II) and metal particle size distributions (V) of passivated/reduced Au/TiO_2 (A) and Ag/TiO_2 (B). *Note*: the diffractogram patterns of isolated metal particles (III) and TiO_2 support (IV) are included as insets.

The TEM images of both catalysts show well dispersed nano-scale pseudo-spheroidal metal particles. The diffractogram patterns for individual Au (AIII) and Ag (BIII) particles and the TiO_2 support (AIV and BIV) are included as insets in **Figure 11.3**. The diffractograms for the support are consistent with anatase. The spacings (0.23 nm) between the planes in the atomic lattice for both metal particles are characteristic of the (111) plane of metallic Au (JCPDS-ICDD 04-0784) and Ag (JCPDS-ICDD 04-0783). The metal particles associated with Ag/TiO_2 present a bimodal size distribution while Au/TiO_2 is characterised by a narrower size range. However, both systems present a similar surface area weighted mean particle size (6-7 nm). There is an appreciable component (65 % Au/TiO_2 and 45% Ag/TiO_2) of metal particles with diameters < 5 nm, the particle size proposed to be crucial for catalytic activity in hydrogen mediated reactions over Au [22,35] and Ag [39]. Taken as a whole, the characterisation results demonstrate precursor reduction to the metallic form post-TPR where the Ag and Au particles exhibit a relatively narrow size distribution and similar mean size.

11.3.2 Hydrogenation of Nitrobenzene

In order to compare the catalytic response of Au *vs.* Ag in the gas phase hydrogenation of substituted nitroarenes, we selected nitrobenzene as a reference reactant. Both catalysts promoted the exclusive formation of aniline with no evidence of hydrodenitrogenation and/or aromatic ring reduction, *i.e.* exclusive $-NO_2$ group hydrogenation. This result alone is significant in that aniline is an important chemical used as an additive for rubber production and in the manufacture of several dyes, pigments, pesticides and herbicides [1,59]. About 85% of the global aniline production draws on catalytic nitrobenzene hydrogenation [60] over supported Pt [60,61] or Pd [62,63] catalysts in batch liquid operation where the formation of toxic by-products, *e.g.* nitrosobenzene [64], azobenzene [61], azoxybenzene [60,61,65] and/or phenylhydroxylamine [66], is still a major drawback associated with commercial processes. Furthermore, a time-invariant conversion (for up to 3 h on-stream) was observed for both Au/TiO_2 and Ag/TiO_2 (see **Figure 11.4** (I)). A temporal loss of activity in the gas phase hydrogenation of nitroarenes over supported Pd [5,59,67-69] and Cu [70,71] has been reported and ascribed to the deleterious effect of H_2O as by-product [59,69], metal leaching [68] and coking [5,67,69-71]. Catalyst deactivation is also a documented feature of hydrogenation reactions over supported Au [34,72-76]

and/or Ag [19,24,52] and has been linked to metal sintering [24,34,52,74], leaching [24] and coke formation [19,34,72,75,76].

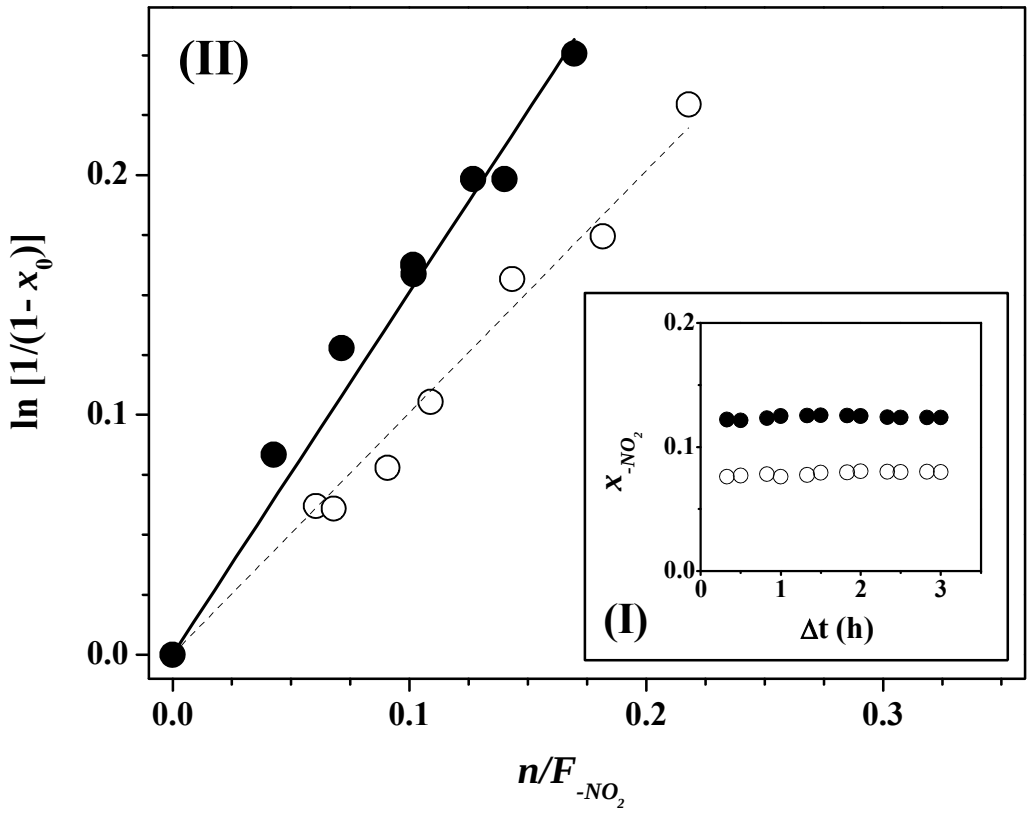

Figure 11.4: Variation of nitrobenzene fractional conversion (x_{-NO_2}) to aniline with time-on-stream over Au/TiO_2 (●) and Ag/TiO_2 (○) (metal/nitrobenzene = 7×10^{-2} mol_{metal} h $mol^{-1}_{-NO_2}$. (II) Pseudo-first order kinetic plot for reaction over Au/TiO_2 (●, solid line) and Ag/TiO_2 (○, dashed line) at T = 473 K.

Catalyst performance was quantified using pseudo-first order kinetics based on the mass balance under continuous flow conditions where

$$\ln\left[1/\left(1-x_{-NO_2}\right)\right] = \mathrm{k}\times\left(n/F_{-NO_2}\right) \qquad \textbf{(11.3)}$$

F_{-NO_2} is the total -NO_2 inlet molar flow, n the moles of metal in the catalyst bed: $\left(n/F_{-NO_2}\right)$ has the physical meaning of contact time. The extracted pseudo-first order rate constants (k, units: $mol_{-NO_2}\, mol^{-1}_{metal}\, h^{-1}$) are given in **Table 11.1**. We have previously demonstrated the applicability of this approach for the hydrogenation of nitroarenes over supported Au catalysts [4,27-30] but establish here that it also applies to data

generated for supported Ag (see **Figure 11.4** (II)). A direct comparison of the performance of both catalysts is only meaningful in terms of specific activities, *i.e.* per m^2 of exposed metal. The Au and Ag metal surface areas were obtained from

$$S_{metal}\ (\mathrm{m}^2_{metal}\ \mathrm{g}^{-1}_{metal}) = \frac{6}{\rho_{metal} \times d_{TEM}} \qquad \textbf{(11.4)}$$

where ρ_{metal} is the metal density and d_{TEM} is the surface area weighted mean particle size as measured by TEM. The specific pseudo-first order rate constants are included in **Table 11.1** where it can be seen that Au delivered a slightly higher (but greater than the associated experimental error) hydrogenation rate when compared with Ag. We can attribute this response to a less effective activation of nitrobenzene and/or hydrogen by Ag/TiO_2 relative to Au/TiO_2. Indeed, Boccuzzi *et al.* [46] studied the water gas shift reaction over Ag/TiO_2 and Au/TiO_2 and ascribed the lack of activity in the case of the former to a limited capacity to activate CO.

11.3.3 Effect of para-Substituents

The hydrogenation of nitroarenes has been proposed to proceed *via* a nucleophilic mechanism [4,7], where a weak nucleophilic agent (hydrogen) attacks the activated $-NO_2$ group with the formation of a negatively charged intermediate. In the previous section, we have noted that aniline was the only product in the hydrotreatment of nitrobenzene over both Au and Ag. In the hydrogenation of substituted nitrobenzenes bearing -OH, $-O-CH_3$, $-CH_3$, -Cl and $-NO_2$ in the *para*- position, both catalysts were again 100% selective in generating the corresponding aminated product. The higher activity observed for Au/TiO_2 (relative to Ag/TiO_2) in the case of nitrobenzene extended to all the substituted nitrobenzenes where, for both catalysts, the following activity sequence was established: *p*-dinitrobenzene > *p*-chloronitrobenzene > nitrobenzene > *p*-nitrotoluene > *p*-nitroanisole > *p*-nitrophenol. In order to assess the dependence of rate on the nature of the *para*-substituent, we have applied the Hammett correlation. The Hammett equation evaluates the effect of a (*meta*- or *para*-) substituent on reaction kinetics and can be used to predict rate and equilibrium constants without prior experimental determination [77,78]. Furthermore, it is a useful tool for the elucidation of reaction mechanisms [79]. In this approach, the rate constants for the substituted reactants (k_i)

can be related to that obtained for the non-substituted (or reference) benzene derivate (k_0) according to

$$\log\left[\frac{k_i}{k_0}\right] = \rho \times \sigma_i \qquad \textbf{(11.5)}$$

The ρ term (reaction constant) is an estimation of the charge development during the course of the reaction and provides a measure of the susceptibility to substituent electronic effects [80,81]. In a nucleophilic attack, the reaction rate is enhanced by electron-withdrawing substituents and $\rho > 0$, while ρ values close to 0 are indicative of a partially charged transition state [81]. The σ_i factor is an empirical parameter (values used in this study were taken from [79,81]) that is dependent on the substituent electron donating/acceptor character [81]. This equation was initially conceived for homogeneous systems where good linear correlations have been established for the hydrogen treatment of substituted acetophenones [82], acetamidoacrylic acid derivatives [78] and aromatic nitro-compounds [83]. The involvement of adsorption phenomena [84], the inhomogeneous distribution/nature of active sites and the greater contribution of steric effects has limited the applicability of the Hammett expression in heterogeneous catalytic systems [85]. Nevertheless, there have been some studies where it has been successfully employed in the gas [86] and liquid [87-92] phase hydrogen-mediated treatment of chlorobenzenes [86], acetophenones [87] and (of direct relevance to this study) nitroaromatics [88-92] over solid catalysts. We provide, in this report, the first example of its application to the gas phase hydrogenation of substituted-nitroarenes. The fit of the experimental rate data to the Hammett relationship is presented in **Figure 11.5**. Both catalysts generated positive reaction constants (ρ), consistent with a nucleophilic reaction mechanism. The higher ρ value generated for Au/TiO_2 (0.93) compared with Ag/TiO_2 (0.22) indicates a greater dependence of rate on the electronic character of the substituent and is diagnostic of a higher charge development in the reactant→intermediate step [81]. This, in turn, can account for the measurably higher specific activities observed for Au/TiO_2. Our ρ values are close to those reported for liquid phase operation (MgFeO, 0.690 [90], iron oxides 0.546 [91] and Pt/SiO_2-$AlPO_4$ 0.1-2.0 [92]), suggesting a common reaction mechanism for the formation of amines promoted by heterogeneous systems.

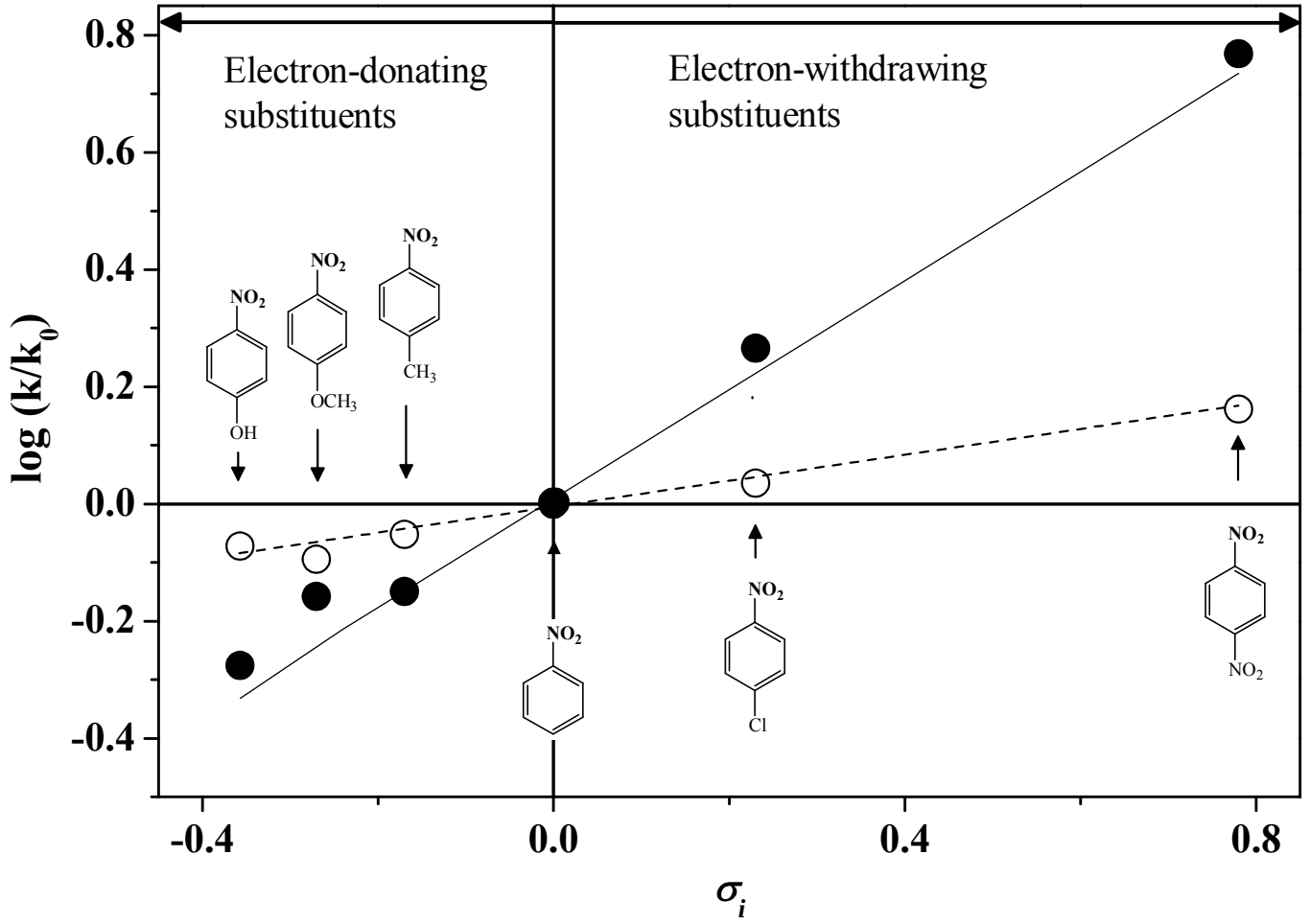

Figure 11.5: Hammett plot for the selective -NO_2 group reduction of *para*-substituted nitroarenes over Au/TiO_2 (●, solid line) and Ag/TiO_2 (○, dashed line) at T = 473 K.

11.4 Conclusions

1 mol % Au and Ag on TiO_2 catalyst precursors were synthesized by impregnation (with $HAuCl_4$ and $AgNO_3$) to deliver (post-TPR) a well dispersed metallic phase, characterised by metal particles in the overall range 1-15 nm and surface area weighted mean values of 6-7 nm. Hydrogen consumption during TPR suggests a single Au^{3+} to Au^0 reduction step while $AgNO_3$ undergoes a stepwise reduction to Ag^0 *via* Ag_2O. Both catalysts promoted exclusive and time invariant -NO_2 reduction for a range of *p*-substituted (-H, -OH, -O-CH_3, -CH_3, -Cl and -NO_2) nitrobenzenes. The reaction proceeds *via* a nucleophilic mechanism where the presence of electron withdrawing ring substituents serves to elevate rate as demonstrated by the linear Hammett relationship. The higher reaction constant (ρ) obtained for Au/TiO_2 (0.93) when compared with Ag/TiO_2 (0.22) indicates a greater dependency of rate on the electronic character of the substituent and we associate this with a more effective reactant activation to generate the negatively charged intermediate leading to a higher specific rate. We provide, in this report, the first direct comparison of the catalytic action of supported (TiO_2) Au and Ag in gas phase nitroarene hydrogenation and establish the viability of both catalytic systems to promote the sustainable (continuous and clean) production of a range of commercially important amino-compounds.

11.5 References

[11.1] P. F. Vogt, J. J. Gerulis, Ullmann's Encyclopedia of Industrial Chemistry. "Aromatic Amines", Wiley-VCH Verlag GmbH & Co. KGaA, Weinheim, 2005.

[11.2] S. G. Harsy, Tetrahedron, 46, 7403 (1990)

[11.3] Y. Zheng, K. Ma, H. Wang, X. Sun, J. Jiang, C. Wang, R. Li, J. Ma, Catal. Lett., 124, 268 (2008)

[11.4] F. Cárdenas-Lizana, S. Gómez-Quero, M. A. Keane, Catal. Commun., 9, 475 (2008)

[11.5] V. Vishwanathan, V. Jayasri, P. M. Basha, N. Mahata, L. M. Sikhwivhilu, N. J. Coville, Catal. Commun., 9, 453 (2008)

[11.6] X. D. Wang, M. H. Liang, J. L. Zhang, Y. Wang, Curr. Org. Chem., 11, 299 (2007)

[11.7] B. Coq, F. Figuéras, Coord. Chem. Rev., 178-180, 1753 (1998)

[11.8] K. R. Westerterp, E. J. Molga, K. B. van Gelder, Chem. Eng. Process., 36, 17 (1997)

[11.9] N. Yao, J. Chen, J. Zhang, J. Zhang, Catal. Commun., 9, 1510 (2008)

[11.10] G. Zhang, L. Wang, K. Shen, D. Zhao, H. S. Freeman, Chem. Eng. J., 141, 368 (2008)

[11.11] A. Corma, P. Serna, Science, 313, 332 (2006)

[11.12] N. S. Chaubal, M. R. Sawant, J. Mol. Catal. A: Chem., 261, 232 (2007)

[11.13] H. Li, Q. Zhao, H. Li, J. Mol. Catal. A: Chem., 285, 29 (2008)

[11.14] A. Corma, P. Serna, P. Concepción, J. J. Calvino, J. Am. Chem. Soc., 130, 8748 (2008)

[11.15] X. X. Han, Q. Chen, R. X. Zhou, J. Mol. Catal. A: Chem., 277, 210 (2007)

[11.16] X. Yang, H. Liu, H. Zhong, J. Mol. Catal. A: Chem., 147, 55 (1999)

[11.17] J. Słoczyński, R. Grabowski, A. Kozłowska, P. Olszewski, J. Stoch, J. Skrzypek, M. Lachowska, Appl. Catal. A: Gen., 278, 11 (2004)

[11.18] L. Ilieva, G. Pantaleo, I. Ivanov, A. M. Venezia, D. Andreeva, Appl. Catal. A: Gen., 65, 101 (2006)

[11.19] K. Theinnoi, S. Sitshebo, V. Houel, R. R. Rajaram, A. Tsolakis, Energy Fuels, 22, 4109 (2008)

[11.20] J. E. Bailie, G. J. Hutchings, Catal. Commun., 2, 291 (2001)

[11.21] P. Claus, Top. Catal., 5, 51 (1998)

[11.22] R. Zanella, C. Louis, S. Giorgio, R. Touroude, J. Catal., 223, 328 (2004)

[11.23] L. Liu, B. Qiao, Y. Ma, J. Zhang, Y. Deng, Dalton Trans., 2008, p. 2542.

[11.24] Y. Chen, C. Wang, H. Liu, J. Qiu, X. Bao, Chem. Commun., 2005, p. 5298.

[11.25] J. Ning, J. Xu, J. Liu, H. Miao, H. Ma, C. Chen, X. Li, L. Zhou, W. Yu, Catal. Commun., 8, 1763 (2007)

[11.26] S. Jana, S. K. Ghosh, S. Nath, S. Pande, S. Praharaj, S. Panigrahi, S. Basu, T. Endo, T. Pal, Appl. Catal. A: Gen., 313, 41 (2006)

[11.27] F. Cárdenas-Lizana, S. Gómez-Quero, M. A. Keane, ChemSusChem, 1, 215 (2008)

[11.28] F. Cárdenas-Lizana, S. Gómez-Quero, N. Perret, M. A. Keane, Gold Bulletin, in press (2009)

[11.29] F. Cárdenas-Lizana, S. Gómez-Quero, A. Hugon, L. Delannoy, C. Louis, M. A. Keane, J. Catal., 262, 235 (2009)

[11.30] F. Cárdenas-Lizana, S. Gómez-Quero, M. A. Keane, Catal. Lett., 127, 25 (2009)

[11.31] T. Osaki, T. Hamada, Y. Tai, React. Kinet. Catal. Lett., 78, 217 (2003)

[11.32] B. C. Campo, S. Ivanova, C. Gigola, C. Petit, M. A. Volpe, Catal. Today, 133-135, 661 (2008)

[11.33] G. C. Bond, A. F. Rawle, J. Mol. Catal. A: Chem., 109, 261 (1996)

[11.34] T. V. Choudhary, C. Sivadinarayana, A. K. Datye, D. Kumar, D. W. Goodman, Catal. Lett., 86, 1 (2003)

[11.35] P. Claus, Appl. Catal. A: Gen., 291, 222 (2005)

[11.36] E. Bus, R. Prins, J. A. van Bokhoven, Catal. Commun., 8, 1397 (2007)

[11.37] B. Hammer, J. K. Nørskov, Nature, 376, 238 (1995)

[11.38] E. Bus, J. T. Miller, J. A. van Bokhoven, J. Phys. Chem. B, 109, 14581 (2005)

[11.39] J.-P. Deng, W.-C. Shih, C.-Y. Mou, J. Phys. Chem. C, 111, 9723 (2007)

[11.40] J. Wambach, A. Baiker, A. Wokaun, Phys. Chem. Chem. Phys., 1, 5071 (1999)

[11.41] G. Tavoularis, M. A. Keane, J. Chem. Technol. Biotechnol., 74, 60 (1999)

[11.42] G. Yuan, M. A. Keane, Chem. Eng. Sci., 58, 257 (2003)

[11.43] E. Bus, R. Prins, J. A. van Bokhoven, Phys. Chem. Chem. Phys., 9, 3312 (2007)

[11.44] C. Baatz, U. Prüße, J. Catal., 249, 34 (2007)

[11.45] C. Baatz, N. Decker, U. Prüße, J. Catal., 258, 165 (2008)

[11.46] F. Boccuzzi, A. Chiorino, M. Manzoli, D. Andreeva, T. Tabakova, L. Ilieva, V. Iadakiev, Catal. Today, 75, 169 (2002)

[11.47] T. Paryjczak, J. Góralski, K. W. Jóźwiak, React. Kinet. Catal. Lett., 16, 147 (1981)

[11.48] V. S. Kumar, B. M. Nagaraja, V. Shashikala, A. H. Padmasri, S. S. Madhavendra, B. D. Raju, K. S. Rama Rao, J. Mol. Catal. A: Chem., 223, 313 (2004)

[11.49] S. P. Ramnani, S. Sabharwal, J. V. Kumar, K. H. P. Reddy, K. S. R. Rao, P. S. S. Prasad, Catal. Commun., 9, 756 (2008)

[11.50] N. Bogdanchikova, F. C. Meunier, M. Avalos-Borja, J. P. Breen, A. Prstryakov, Appl. Catal. B: Environ., 36, 287 (2002)

[11.51] A. Montoya, A. Schlunke, B. S. Haynes, J. Phys. Chem. B, 110, 17145 (2006)

[11.52] M. Bron, D. Teschner, A. Knop-Gericke, F. C. Jentoft, J. Kröhnert, J. Hohmeyer, C. Volckmar, B. Steinhauer, R. Schlögl, P. Claus, Phys. Chem. Chem. Phys., 9, 3559 (2007)

[11.53] G. Lee, E. W. Plummer, Phys. Rev. B, 62, 1651 (2000)

[11.54] L. Armelao, D. Barreca, G. Bottaro, A. Gasparotto, S. Gross, C. Maragno, E. Tondello, Coord. Chem. Rev., 250, 1294 (2006)

[11.55] X. Jia, X. Ma, D. Wei, J. Dong, W. Qian, Colloids Surf., A, 330, 234 (2008)

[11.56] R. I. Bickley, T. Gonzalez-Carreno, J. S. Lees, L. Palmisano, R. J. D. Tilley, J. Solid State Chem., 92, 178 (1991)

[11.57] S. Bernal, J. J. Calvino, M. A. Cauqui, G. A. Cifredo, A. Jobacho, J. M. Rodríguez-Izquierdo, Appl. Catal. A: Gen., 99, 1 (1993)

[11.58] T. Akita, M. Okumura, K. Tanaka, M. Kohyama, M. Haruta, Catal. Today, 117, 62 (2006)

[11.59] P. Sangeetha, P. Seetharamulu, K. Shanthi, S. Narayanan, K.S. Rama Raob, J. Mol. Catal. A: Chem., 273, 244 (2007)

[11.60] C.-H. Li, Z.-X. Yu, K.-F. Yao, S.-F. Jib, J. Liang, J. Mol. Catal. A: Chem., 226, 101 (2005)

[11.61] F. Zhao, Y. Ikushima, M. Arai, J. Catal., 224, 479 (2004)

[11.62] E. A. Gelder, S. D. Jackson, C. M. Lok, Catal. Lett., 84, 205 (2002)

[11.63] X. Yu, M. Wang, H. Li, Appl. Catal. A: Gen., 202, 17 (2000)

[11.64] F. Zhao, R. Zhang, M. Chatterjee, Y. Ikushima, M. Araib, Adv. Synth. Catal., 346, 661 (2004)

[11.65] F. Ragaini, S. Cenini, M. Gasperini, J. Mol. Catal. A: Chem., 174, 51 (2001)

[11.66] M. M. Pérez, S. Martínez de Lecea, A. L. Solano, Appl. Catal., 151, 461 (1997)

[11.67] E. Klemm, B. Amon, H. Redlingshöfer, E. Dieterich, G. Emig, Chem. Eng. Sci., 56, 1347 (2001)

[11.68] K. K. Yeong, A. Gavriilidis, R. Zapf, V. Hessel, Catal. Today, 81, 641 (2003)

[11.69] P. Sangeetha, K. Shanthi, K. S. R. Rao, B. Viswanathan, P. Selvam, Appl. Catal. A: Gen., 353, 160 (2009)

[11.70] S. Diao, W. Qian, G. Luo, F. Wei, Y. Wang, Appl. Catal. A: Gen., 286, 30 (2005)

[11.71] L. Petrov, K. Kumbilieva, N. Kirkov, Appl. Catal., 59, 31 (1990)

[11.72] B. Campo, C. Petit, M. A. Volpe, J. Catal., 254, 71 (2008)

[11.73] C. Milone, M. L. Tropeano, G. Gulino, G. Neri, R. Ingoglia, S. Galvagno, Chem. Commun., 2002, p. 868.

[11.74] X. Zhang, H. Shi, B.-Q. Xu, Catal. Today, 122, 330 (2007)

[11.75] B. Pawelec, A. M. Venezia, V. La Parola, S. Thomas, J. L. G. Fierro, Appl. Catal. A: Gen., 283, 165 (2005)

[11.76] Y. Azizi, C. Petit, V. Pitchon, J. Catal., 256, 338 (2008)

[11.77] L. P. Hammett, J. Am. Chem. Soc., 59, 96 (1937)

[11.78] M. Alamé, M. Jahjah, S. Pellet-Rostaing, M. Lemaire, V. Meille, C. de Bellefon, J. Mol. Catal. A: Chem., 271, 18 (2007)

[11.79] H. H. Jaffé, Chem. Rev., 53, 191 (1953)

[11.80] J. Shorter, Chem. Lysty, 94, 210 (2000)

[11.81] C. D. Johnson, The Hammett Equation, Cambridge University Press, Cambridge, 1973.

[11.82] T. Kamitanaka, T. Matsuda, T. Harada, Tetrahedron Lett., 44, 4551 (2003)

[11.83] V. M. Belousov, T. A. Palchevskaya, L. V. Bogutskaya, React. Kinet. Catal. Lett., 36, 369 (1988)

[11.84] A. Finiels, P. Geneste, C. Moreau, J. Mol. Catal. A: Chem., 107, 385 (1996)

[11.85] M. Kraus, in Advances in Catalysis and Related Subjects: vol. 17. "Linear Correlations of Substrate Reactivity in Heterogeneous Catalytic Reactions", Academic Press Inc., New York, 1967.

[11.86] T. Yoneda, T. Takido, K. Konuma, J. Mol. Catal. A: Chem., 265, 80 (2007)

[11.87] J. R. Ruiz, C. Jiménez-Sanchidrián, J. M. Hidalgo, Catal. Commun., 8, 1036 (2007)

[11.88] B. Coq, A. Tijani, F. Figuéras, J. Mol. Catal., 68, 331 (1991)

[11.89] P. Lu, N. Toshima, Bull. Chem. Soc. Jpn., 73, 751 (2000)

[11.90] P. S. Kumbhar, J. Sanchez-Valente, J. M. M. Millet, F. Figueras, J. Catal. , 191, 467 (2000)

[11.91] M. Lauwiner, P. Rys, J. Wissmann, Appl. Catal. A: Gen. , 172, 141 (1998)

[11.92] M. A. A. Lopidana, V. B. Bolos, C. J. Sanchidrian, J. M. M. Rubio, F. R. Luque, Bull. Chem. Soc. Jpn., 60, 3415 (1987)

Chapter 12

Summary and Future Work

12.1 General Conclusions

The ultimate objective of this PhD research project was the development of a catalyst system for a cleaner alternative route in the production of industrially important aromatic amino-derivates. Gold catalysts have been found to exhibit high stability (up to 80 h on stream) and promote the exclusive nitro-group reduction of a wide range of substituted nitroarenes. Therefore, gold based systems can be considered effective for the production of amino-compounds where catalyst formulation can be modified to control product distribution. The latter feature, *i.e.* controlled selectivity represents a progressive means of sustainable production. The main advantages, from an economic point of view, are the continuous (high throughput) production under mild reaction conditions (P = 1 atm; 393 K $\leq T \leq$ 573 K) and the stability/versatility of the Au systems, which can be applied to produce a range of products of immediate importance in the fine chemical industry.

The results presented in this thesis illustrate that -NO_2 group reduction proceeds *via* a nucleophilic mechanism where the presence of electron-withdrawing substituents is shown to enhance hydrogenation rate. The electronic character of the Au active site plays a critical role in determining the catalytic response, and this can be modified by:

i) Varying the support: the presence of Lewis acid/basic sites promotes the formation of $Au^{\delta+}$/ $Au^{\delta-}$ species *via* metal-support electron transfer that modifies reactant adsorption/activation and ultimately product distribution.

ii) Gold dispersion: nitro-group reduction exhibits structure sensitivity with increasing specific rates associated with smaller Au particle size (from 10.0 to 3.4 nm). Furthermore, there is a dependency of selectivity on Au dispersion with different trends observed for particles larger or smaller than 5 nm. The Au size can be controlled by varying the synthesis method where catalysts prepared by

deposition exhibit smaller particle sizes when compared to those prepared by impregnation.

Introducing a second metal has been established as an effective alternative approach to control catalytic performance. Hydrogenation rate can be significantly enhanced by the formation of bimetallic Au-Pd clusters (as suggested by DRIFTS analysis) where exclusive nitro-group reduction is maintained. Moreover, bimetallic Au based systems can deliver a distinct selectivity response as demonstrated in the case of Au-Ni where surface Au-Ni synergism results from electron transfer from Ni to Au. The data obtained for supported Ag also show promise for selective nitro-group reduction and this represents a challenging area that warrants further research.

12.2 Future Directions

From a consideration of the results generated in this thesis and taking account of the existing gaps in the open literature, the following areas represent possible directions in terms of future work:

12.2.1 Ni-Promoted Selective Nitro-Group Reduction over Al_2O_3 and TiO_2 Supported Au

An exclusive nitro-group reduction over Au with increased activity by (i) using reducible oxides (*Chapter 5*) and (ii) incorporation of Pd (*Chapter 4*) has been shown. Furthermore, a significantly higher nitro-group reduction rate and distinct product distribution was recorded over Ni, relative to Au, in the hydrogenation of *m*-dinitrobenzene (*Chapter 9*). The possible role of Ni as a promoter of Au over non- (*e.g.* Al_2O_3) and reducible (*e.g.* TiO_2) oxides in the hydrogenation of chloro- and di-nitrobenzene is an area that requires investigation. Preliminary results have revealed exclusive nitro-group reduction over Au and Au-Ni where the incorporation of Ni significantly increases hydrogenation rate. Furthermore, catalytic performance appears to be sensitive to the nature of the support, a response that should be examined further.

12.2.2 EXAFS Characterization of Alumina Supported Au, Ni and Au-Ni for the Controlled Nitro-group Reduction of Di- and Tri-Nitrobenzene

Distinct catalytic behaviour in the hydrogenation of *m*-dinitrobenzene over Au-Ni/Al_2O_3 (prepared by reductive deposition of Au onto Ni), compared with monometallic counterparts is discussed in *Chapter 9*. This result has been attributed to a surface Au-Ni synergism as suggested by EDX mapping and XPS analysis. In order to explicitly establish bimetallic particle formation, a more detailed characterization is required. In this respect, EXAFS analyses have been performed and the initial results suggest a significant degree of Au-Ni interaction in the Au-Ni/Al_2O_3 system. This observation requires further development with analysis of the consequences in hydrogenation activity and selectivity: -NO_2 reduction in di- and tri-nitrobenzene reactants is proposed as suitably demanding catalyst testing.

12.2.3 Hematite vs. Magnetite Supported Gold Catalysts for the Gas Phase Hydrogenation of Chloronitrobenzene and Dinitrobenzene

The results generated in *Chapter 7* are consistent with a more facile reduction of Fe_2O_3 (hematite) to Fe_3O_4 (magnetite) during TPR activation in the presence of Au. Moreover, comparison of the catalytic action over (1 mol %) Au supported on Al_2O_3, TiO_2, Fe_2O_3 and CeO_2 and a reference catalyst (Au/TiO_2, World Gold Council) in the hydrogenation of *m*-dinitrobenzene presented in *Chapter 7*, serve to clearly illustrate that the chemistry of the support plays an important role in determining catalyst performance. The effect of the support on catalytic behaviour should be investigated further in the hydrogenation of chloro- and di-nitrobenzene over Au/Fe_2O_3 and Au/Fe_3O_4. Preliminary results suggest a distinct catalytic response that it is dependent on the nature of the iron oxide and final activation temperature (over the range 423 K $\leq$ T $\leq$ 673 K) where differences in catalytic activity for Au/Fe_3O_4 can be associated with metal segregation post-activation at higher temperature as suggested by HRTEM measurements. Such a response can form the basis for a comprehensive study of the catalytic action of Au/Fe_2O_3 and Au/Fe_3O_4.

12.2.4 Fe_2O_3 vs. Fe_3O_4 Supported Silver Catalysts for the Gas Phase Hydrogenation of Chloronitrobenzene and Dinitrobenzene

In the continuous gas phase hydrogenation of a series *p*-substituted nitroarenes over TiO_2 supported Au and Ag, presented in *Chapter 11*, exclusive nitro-group reduction was achieved over both systems where Au/TiO_2 delivered a higher hydrogenation activity. Furthermore, as established in *Chapter 7*, the nature of the support has a considerable impact on catalytic response over Au catalysts. A direct comparison between the catalytic behaviour of iron oxide supported Au *vs.* Ag is a topic that should generate valuable structure/performance correlations.

12.2.5 Gas Phase Hydrogenation of Dinitrobenzene over Carbon Supported Au and Ag

A similar selectivity response but higher hydrogenation rates were recorded for Au/TiO_2 (relative to Ag/TiO_2) in the treatment of a series of aromatic nitrocompounds (*Chapter 11*). As a further examination of the catalytic behaviour of Au *vs.* Ag, the catalytic response over carbon supported systems prepared by deposition-precipitation should be considered. Preliminary results suggest that supported Ag and Au promote exclusive $-NO_2$ group reduction: differences in specific activity and possible structure sensitivity effects will require further work.

12.2.6 Gas Phase Hydrogenation of Nitrocompounds in Aqueous Solution over Au/TiO_2

As established in *Chapter 5*, the nature of the (alcoholic) solvent influences nitro-group reduction rate where a lower activity in pentanol, relative to ethanol, was recorded and attributed to a competitive solvent-reactant adsorption effect. As an extension of this study, the response using water as a more sustainable solvent should be investigated. Preliminary results for the gas phase hydrogenation of nitrobenzene over Au/TiO_2 suggest that the use of aqueous solutions enhances hydrogenation rate while product (aniline) exclusivity is retained.

12.2.7 Preparation of Molybdenum Nitride: Application as a Au Catalyst Support

While supported Au catalysts deliver 100% selectivity in terms of -NO_2 group reduction, hydrogenation rate is still appreciably lower than that delivered by conventional supported transition metal catalysts. This can be attributed to the reduced capacity of Au to dissociatively adsorb hydrogen. One possible approach to raising activity is the use of a support such as molybdenum nitride that is capable of H_2 chemisorption. Preliminary work has been undertaken to synthesis molybdenum nitride with a sufficiently high surface area (≥100 m^2 g^{-1}). Attention was focused on identifying the intermediates in the β-Mo nitride formation via the treatment of MoO_3 with H_2+N_2 as there has been no definitive analysis of the transition from MoO_3 to β-Mo nitride. A combination of surface/bulk characterisation techniques (XRD, SEM, TEM, DRS UV-vis, BET area/porosity and elemental analysis) were used in order to establish the steps involved in the genesis of β-Mo nitride. Preliminary results suggest the following stepwise synthesis mechanism: $MoO_3 \rightarrow MoO_2 \rightarrow Mo \rightarrow \beta\text{-}Mo_2N_{0.78}$ where TPD analysis indicates the presence of H_2 associated with the surface of β-$Mo_2N_{0.78}$ post-thermal treatment. Results suggest that the critical reaction variables governing surface area are (a) heating rate, (b) gas space velocities and (c) N_2 content. Increased surface areas are associated with the (cubic) γ- phase (≥ 40 m^2 g^{-1}) when compared to the β-form (≤ 17 m^2 g^{-1}), a result tentatively linked to the formation of Mo metal as intermediate during treatment of MoO_3. Further work is required to optimise nitride surface area and consider the feasibility of nitride supported Au as an effective hydrogenation catalyst. It is proposed that this work is extended to consider the catalytic action of molybdenum carbide supported Au. This line of research may serve to open a new area of non-oxide supported Au (and Ag) catalysis.

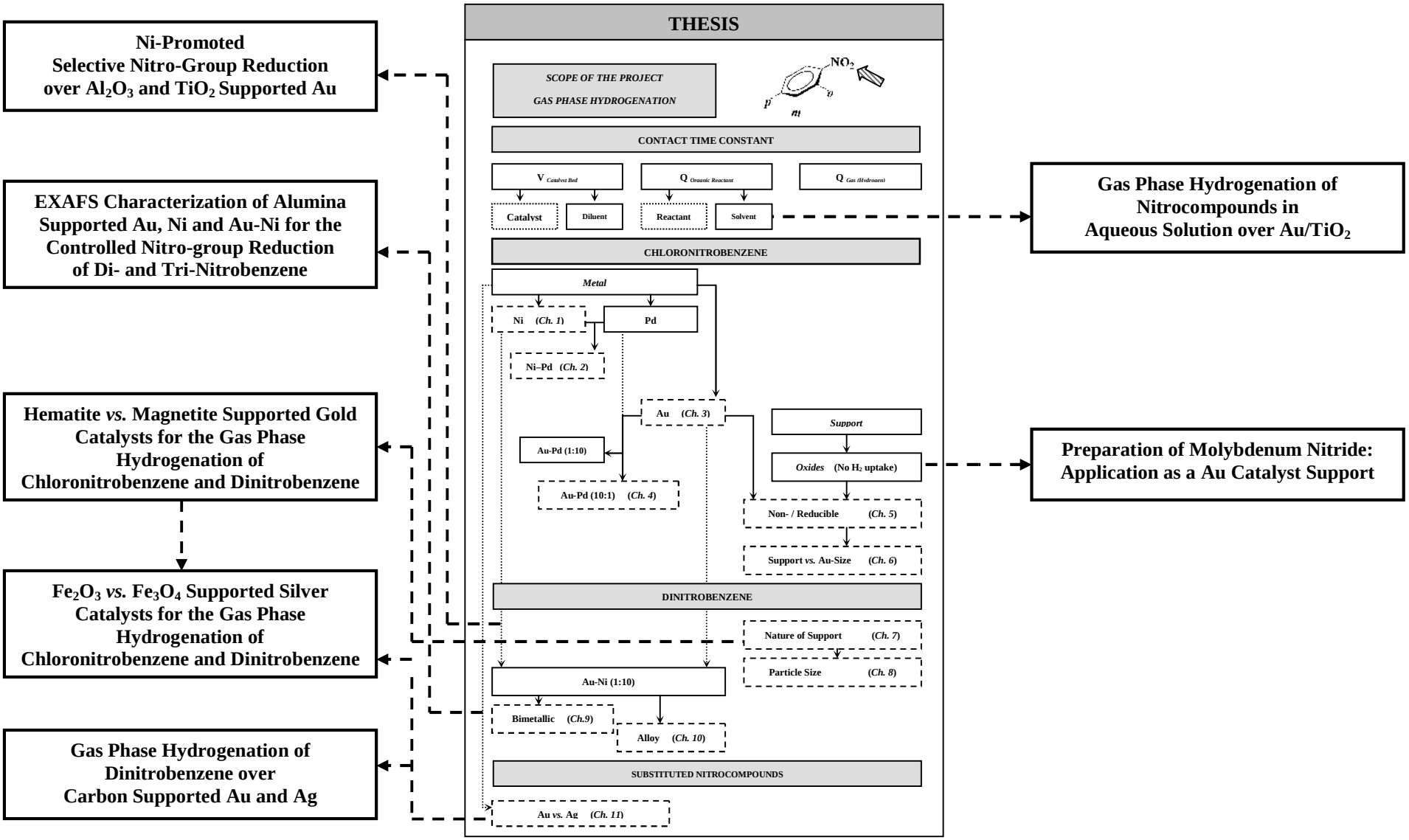
Ni-Promoted
Selective Nitro-Group Reduction
over Al_2O_3 and TiO_2 Supported Au
EXAFS Characterization of Alumina
Supported Au, Ni and Au-Ni for the
Controlled Nitro-group Reduction
of Di- and Tri-Nitrobenzene
Hematite vs. Magnetite Supported Gold
Catalysts for the Gas Phase
Hydrogenation of
Chloronitrobenzene and Dinitrobenzene
Fe_2O_3 vs. Fe_3O_4 Supported Silver
Catalysts for the Gas Phase
Hydrogenation of
Chloronitrobenzene and Dinitrobenzene
Gas Phase Hydrogenation of
Dinitrobenzene over
Carbon Supported Au and Ag
THESIS
SCOPE OF THE PROJECT
GAS PHASE HYDROGENATION
CONTACT TIME CONSTANT
V Catalyst Bed
Q Organic Reactant
Q Gas (Hydrogen)
Catalyst
Diluent
Reactant
Solvent
CHLORONITROBENZENE
Metal
Ni (Ch. 1)
Pd
Ni–Pd (Ch. 2)
Au (Ch. 3)
Au-Pd (1:10)
Au-Pd (10:1) (Ch. 4)
Support
Oxides (No H_2 uptake)
Non- / Reducible (Ch. 5)
Support vs. Au-Size (Ch. 6)
DINITROBENZENE
Nature of Support (Ch. 7)
Particle Size (Ch. 8)
Au-Ni (1:10)
Bimetallic (Ch.9)
Alloy (Ch. 10)
SUBSTITUTED NITROCOMPOUNDS
Au vs. Ag (Ch. 11)
Gas Phase Hydrogenation of
Nitrocompounds in
Aqueous Solution over Au/TiO_2
Preparation of Molybdenum Nitride:
Application as a Au Catalyst Support